Flying Height Control Sliders with Piezoelectric and Thermal Nanoactuators for Ultrahigh Density Magnetic Recording

by

Jia-Yang Juang

B. S. (National Taiwan University, Taiwan) 1997
M. S. (National Taiwan University, Taiwan) 1999

A dissertation submitted in partial satisfaction of the

requirements for the degree of

Doctor of Philosophy
in

Engineering – Mechanical Engineering

in the

GRADUATE DIVISION

of the

UNIVERSITY OF CALIFORNIA, BERKELEY

Committee in charge:

Professor David B. Bogy, Chair
Professor Liwei Lin
Professor Andrew R. Neureuther

Spring 2006

This dissertation of Jia-Yang Juang is approved:

Chair Date

Date

Date

University of California, Berkeley

Spring, 2006

Flying Height Control Sliders with Piezoelectric and Thermal Nanoactuators for Ultrahigh Density Magnetic Recording

by

Jia-Yang Juang

Abstract

Flying Height Control Sliders with Piezoelectric and Thermal Nanoactuators for Ultrahigh Density Magnetic Recording

by

Jia-Yang Juang

Doctor of Philosophy in Engineering- Mechanical Engineering

University of California, Berkeley

The central theme of this dissertation is a comparative study of flying height (FH) control sliders with piezoelectric and thermal actuation as well as a comprehensive study of the design, fabrication, modeling and dynamic control of the piezoelectric nanoactuator for achieving a FH of ~2 nm, which is required for an areal data density of 1 Tbit/in^2, which is the goal on the next generation of hard disk drives.

It is found that the intermolecular and electrostatic forces at the head-disk interface that occur at such small spacing are effectively reduced in both approaches. The thermal protrusion of FH control sliders can be controlled by adjusting the power of the heating elements, but the inherent power-consuming thermal actuation limits the actuation displacement, especially for battery powered mobile applications. The quasi-static nature allows thermal FH control sliders to compensate the static spacing loss. The piezoelectric dynamic control slider shows promising performance of higher bandwidth, larger actuation displacement, and higher power efficiency. However, the

requirement of piezoelectric materials and the modification of the slider design pose challenges for the fabrication process and increase the manufacturing cost.

Even though the protruded area was relatively small for a thermally actuated slider, there was still considerable counter effect of the air bearing, resulting in an actuation efficiency of only ~50 %. A new air bearing surface (ABS) design, called “Scorpion III”, is presented, which demonstrates an overall enhancement, including virtually 100 percent efficiency with significantly less power consumption.

Another ABS design, named “Scorpion IV”, was designed and fabricated for a piezoelectric slider. Dynamic analysis by numerical simulations show that Scorpion IV exhibits an overall enhancement in flying performance, such as track-seeking and dynamic load/unload, due to its remarkably high stiffness and damping. We also propose an inexpensive and low-temperature process for integrating the piezoelectric material in the fabrication of current Al_2O_3-TiC sliders, and we conducted experimental analysis to investigate the flying and actuation performances of the fabricated head-gimbal-assemblies. The FH was successfully reduced from about 10 nm to contact, and a track of considerable lube depletion and carbon wear was observed after the contact tests.

To dynamically suppress the FH modulation (FHM) under intermolecular and electrostatic forces for the actuated air bearing slider we present a new 3-DOF analytic model of an observer-based nonlinear compensator for calculating the required control voltage for the piezoelectric nanoactuator. The nonlinear air bearing stiffness and damping were identified by impulse responses, and these values were used in the model. Numerical simulations show that the response of the model is in good agreement with a

Dynamic Simulator developed in the Computer Mechanics Laboratory. However, the model requires much less computation time, and hence it can be used as a plant for the observer-based nonlinear sliding mode controller. Numerical studies show that the FHM due to disk waviness was effectively controlled and reduced.

The key contributions of this dissertation are the identification of some of the mechanical challenges inherent in ultrahigh density magnetic recording required for the next generation of hard disk drives as well as some solutions to address these challenges.

Professor David B. Bogy

Dissertation Chair

DEDICATION

To my parents, wife and sisters

TABLE OF CONTENTS

LIST OF FIGURES

LIST OF TABLES

ACKNOWLEDGEMENTS

I would like to express my sincere gratitude to my research advisor, Prof. David B. Bogy, for his academic guidance, research advice, encouragement and financial support throughout my career at the Computer Mechanics Laboratory. It is my honor to be the 50th Ph.D. that Prof. Bogy has advised. He has been my mentor not only for his earnest attitude toward research and teaching but also for his respectable personality and great sense of humor. I am fortunate to have had the privilege to study under him and know him personally.

I would also like to thank Dr. C. Singh Bhatia, who has given me professional and personal advice and support throughout my study at Berkeley. I enjoyed the summer internship while I worked with him in Hitachi GST. His enthusiasm and insight have encouraged me to make this research project more complete. I owe my gratitude to all the people who have helped me while working at Hitachi. I am fortunate to have worked with many talented engineers, in particular Mr. Tim Neumann, Mr. Yoshiki Midori, Mr. Nghia Bach, Dr. Cherngye Hwang and Dr. Robert Payne. I cherish the working experience with them.

I wish to thank Prof. Liwen Lin, Prof. J. Karl Hedrick and Prof. Andy Neureuther for their invaluable advice on my research and this dissertation.

It has been a great pleasure to work with my colleagues at CML. Dr. Hong Zhu was especially supportive and has been my good friend since I joined this group. I particularly enjoy working with Rohit Ambekar on many interesting experiments. Thanks also go to Dr. Xinjiang Shen, Dr. Qinghua Zeng, Brendan Cox, Du Chen, Naozumi Tsuda,

Hiroyuki Kubotera, Takeshi Watanabe, Sujit Kirpekar, Vineet Gupta, Puneet Bhargava and Sean Moseley.

I am deeply indebted to my parents, my wife, Li Xu, and my two sisters for their love and support. They have supported me, now support me, and will always support me. Being a Ph. D. student in ME department at Berkeley, Li is not only supporting me as my wife, but also as my colleague and my best friend. I cannot envision life without my family – it forms the backbone from which all my other pursuits grow. I would like to dedicate this dissertation to them.

The research presented in this dissertation was supported by the Computer Mechanics Laboratory at the University of California, Berkeley and supported in part by the Industry Storage Consortium (INSIC). I was also supported by The California State Nanotechnology Fellowship.

Jia-Yang Juang

Berkeley, May 2006

CHAPTER 1
INTRODUCTION

1.1 Magnetic Hard Disk Drives

Among the information storage systems the magnetic hard disk drive (HDD) is the dominant mass storage device for computers ranging from laptops to mainframes, and one of the major storage devices for consumer electronics because of its large storage capacity, low cost per megabyte, fast access time and a relatively mature manufacturing infrastructure. The basic operation principles of magnetic hard disk drives have not changed much since its introduction in 1957 by IBM. However, many technological challenges have been overcome in the evolutionary process, which results in a rapid increase in both the areal density and data transfer rate.

A magnetic disk drive is mainly composed of four parts [1]:

1. Magnetic read/write heads, magnetic disks and head-disk interface (HDI). Each write/read element is located on the trailing edge of a slider. A slider is mounted to the end of a stainless steel gimbal-suspension, forming a head-gimbal assembly (HGA).
2. Data detection electronics and write circuit, mostly located on a print-circuit board.
3. Mechanical servo and control system, including spindles, actuators, suspensions and control chips.
4. Interface to microprocessor, located at one edge of the print-circuit board and through which the microprocessor input information from or output information to the disk drive is achieved.

Fig. 1.1 shows a photograph of a hard disk drive with its cover off, exposing the components. The operation of the head-disk assembly is based on a self-pressurized air bearing between the slider and the spinning disk, which maintains a constant separation (called flying height, FH) between them, as shown in Fig. 1.2. By positioning the slider along the radial direction, different data tracks can be read or written on the disk. The state-of-the-art FH and track width are ~ 10 nm and 250 nm, respectively.

As shown in Fig. 1.3 the areal density of magnetic recording in HDDs has been increased dramatically at an annual compound growth rate of ~ 60 % in the 1990s. This fast pace was mainly due to the introduction of magnetoresistive (MR) heads and the continuous reduction of the FH as shown in Fig. 1.4. In order to increase the areal density, the magnetic data bits have to be packed closer together in both the circumferential and radial directions, corresponding to linear bit density and track density, respectively. The increase of data track density is possible only when the position accuracy of the servo system can be improved while a reduction of FH is required for increasing the linear bit density.

An areal density of 1 Tbit/in^2 is the current goal of academic and industry researchers for future HDDs. Organizations such as the Information Storage Industry Consortium (INSIC) in the US and the Storage Research Consortium (SRC) in Japan are working on research in media and heads (magnetics) signal processing, servo systems and tribology (head-disk interface) to achieve the goal of reaching 1 Tbit/in^2.

1.2 Head-Disk Interface (HDI) and Air Bearing Surface (ABS)

Over the years the technological advancement in the air bearing slider and magnetic read/write elements has enabled the sustained improvement of both mechanical and magnetic performances of HDDs. Figs. 1.4 and 1.5 show a historical overview of the miniaturization of the slider and read/write transducer. The body size of the slider has changed from the full size slider (4.1 × 3.2 × 0.85 mm) to the current femto slider (0.85 × 0.70 × 0.23 mm). The air bearing surface (ABS) is a patterned surface that comes within proximity of the disk surface. The relative motion between the slider and the disk creates a thin air film bearing with a particular pressure distribution. The flying attitude, including FH, pitch and roll angles, of the slider is determined by the force balance of the generated pressure and the applied force from the suspension. The ABS design has evolved to be very complicated to meet many requirements encountered as the FH is continuously decreased.

However, in order to achieve the areal density of 1 Tbit/in^2, the nominal head-media spacing (HMS) has to be reduced to 5 nm. This HMS includes a physical spacing (FH) of 2.5 nm between the read/write element and the surface of the disk, the protective layers–slider and disk diamond-like-carbon overcoats, and lubricants on the disk. The protective overcoats, made of diamond-like carbon and silicon, are necessary to provide wear resistance and to protect the magnetic media and transducer from corrosion. The lubricant is also required for reducing the wear and improving the durability of the overcoats.

A stable and constant FH must also be sustained in the presence of altitude and temperature changes, manufacturing tolerance, and track-seeking motion. Furthermore, slider disk contacts must be avoided during load/unload processes and operational shocks. The dynamic instability caused by FH modulations (FHMs) and nanoscale adhesion forces, such as electrostatic and intermolecular forces, should be minimized. Those challenges make a conventional air bearing surface (ABS) slider an unlikely choice for 1 Tbit/in^2. Major challenges are expected in designing a reliable interface between the read/write head and the magnetic disk or head-disk interface (HDI).

1.3 Research Objectives

The research presented in this dissertation is to study the feasibility of achieving the FH goal for 1 Tbit/in^2 by utilizing FH control sliders with thermal and piezoelectric nanoactuators. In a FH control slider an additional actuator, such as a heating element (for thermal actuation) or a piezoelectric material (for piezoelectric actuation), is mounted in the slider body. The read/write transducer is raised or lowered by the actuator on demand for controlling the FH. This research is aimed at attaining the following five objectives: The first objective is to investigate new phenomena associated with the introduction of the nanoactuators, including the actuation stroke, bandwidth, efficiency and power consumption. The second objective is to study special requirements of the ABS for FH control sliders and to design air bearing sliders with 10-nm FH for both thermal and piezoelectric actuations. We evaluated the static and dynamic flying performance of the designed sliders by numerical modeling and simulation. The third objective is to develop an inexpensive and low-temperature approach for integrating piezoelectric materials in the fabrication of current Al_2O_3-TiC sliders and to conduct experimental measurements and tests for the fabricated prototype sliders. The fourth objective is to develop a lumped-parameter model for the piezoelectric slider and design an observer-based nonlinear compensator for calculating the required control voltage for suppressing the FH modulation and enhancing the dynamic stability of the HDI. The fifth objective is to study the effects of the ABS on thermal actuation and track-seeking motions for ultralow flying sliders.

1.4 Dissertation Organization

This dissertation is organized into eight chapters. Chapter 1 is an introduction that covers the history and operation principles of magnetic hard disk drives, the HDI and air bearing surface, the motivation for this work and the objectives of the research presented. Chapter 2 is a study of two approaches, namely thermal and piezoelectric actuators, for achieving the requirements for an areal density of 1 Tbit/in^2. In Chapter 3, two ABSs designed as FH control sliders with thermal and piezoelectric actuations have been proposed and their flying dynamics have been investigated by numerical simulations. Chapter 4 presents an inexpensive and low-temperature approach for integrating piezoelectric materials in the fabrication of current Al_2O_3-TiC sliders. The fabricated prototype sliders have been tested experimentally. Chapter 5 develops an analytical model and an observer-based nonlinear sliding mode controller for compensating the short range adhesion forces, such as intermolecular and electrostatic forces in the HDI, and suppressing the FH modulation induced by disk morphology. Chapter 6 contains an investigation of the effect of ABS design on the actuation performance of thermal FH control sliders. Chapter 7 presents a quasi-static approximation for modeling the track-seeking motion, which can substantially decrease the computation time over that required for a dynamic analysis. The track-seeking performances of four different ABS designs are numerically investigated and design guidelines are provided. Chapter 8 presents the conclusions of this dissertation.

References

1. S. X. Wang and A. M. Taratorin, *Magnetic Information Storage Technology*, Academic Press, 1999.

Fig. 1.1. Hard disk drive (http://www.seagate.com/).

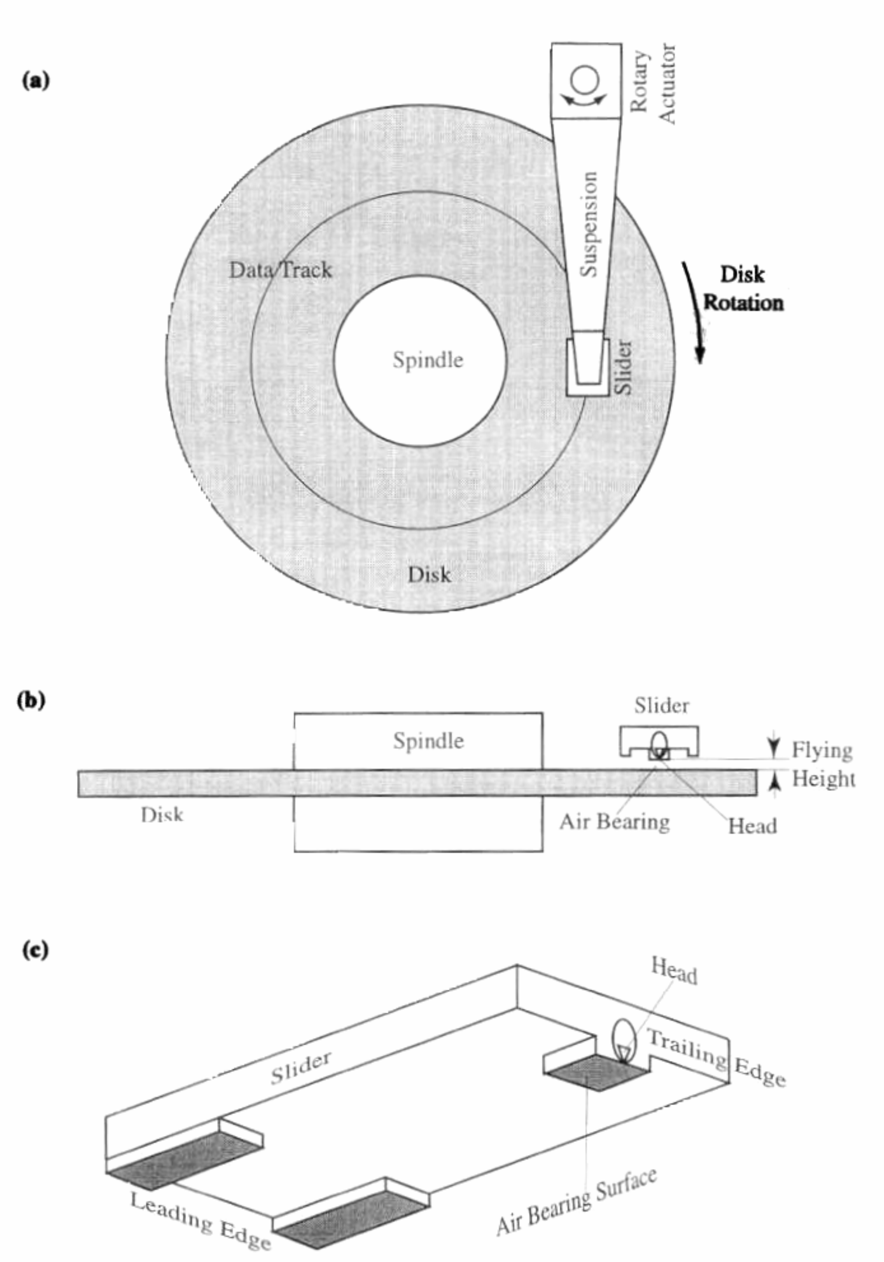

Fig. 1.2. Schematic hard-disk operation: (a) top view; (b) side view; (c) magnified view of a slider. [1].

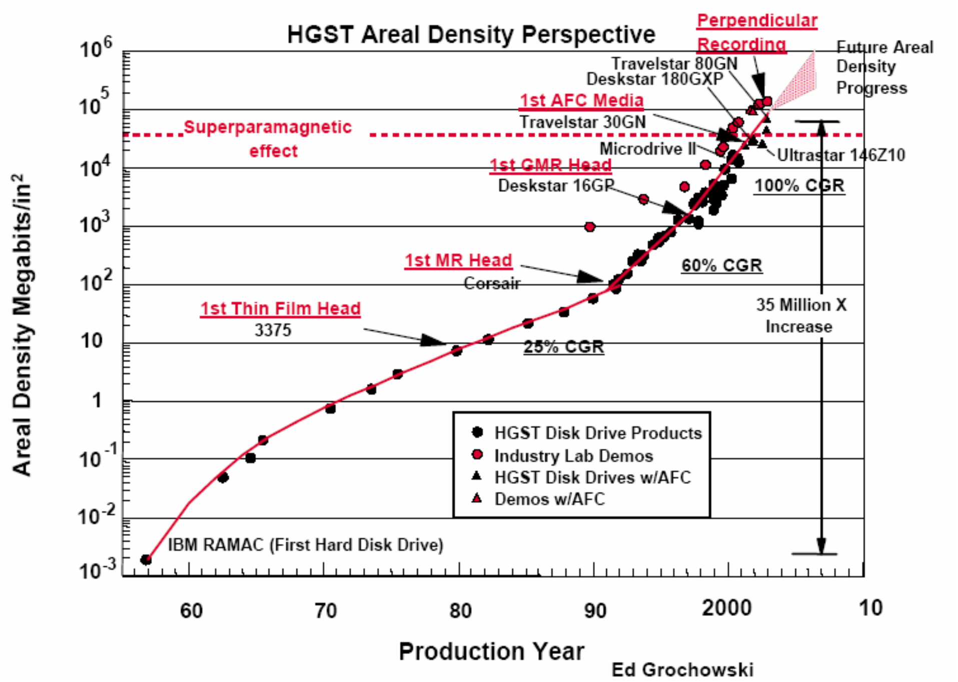

Fig. 1.3. The increase of areal density in the HDDs (http://www.hitachigst.com/).

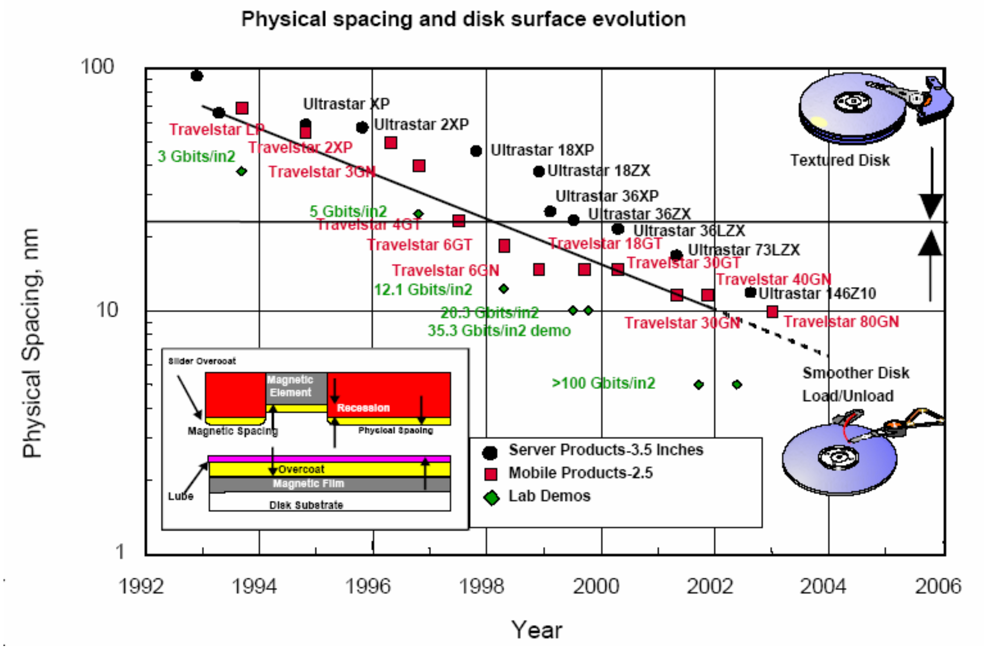

Fig. 1.4. The reduction of the physical spacing (FH) in HDDs for increasing the areal density (http://www.hitachigst.com/).

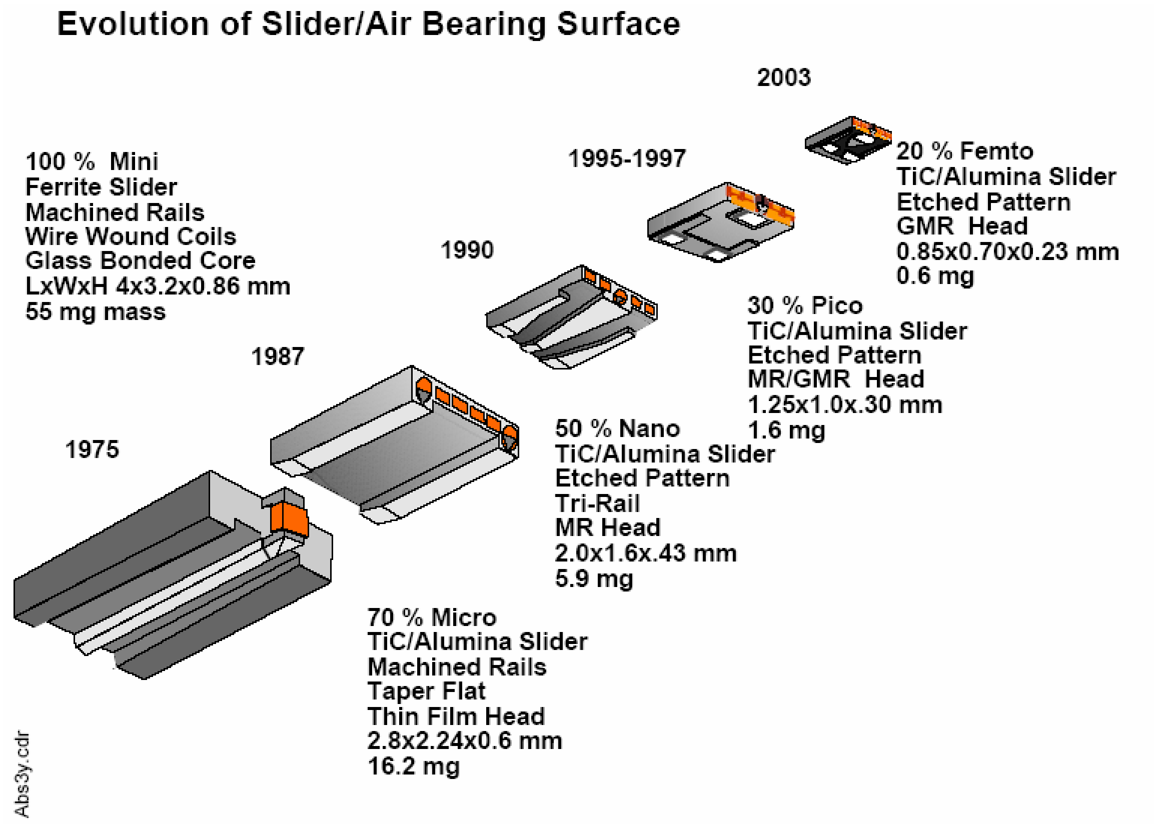

Fig. 1.5. Evolution of slider/air bearing surface (http://www.hitachigst.com/).

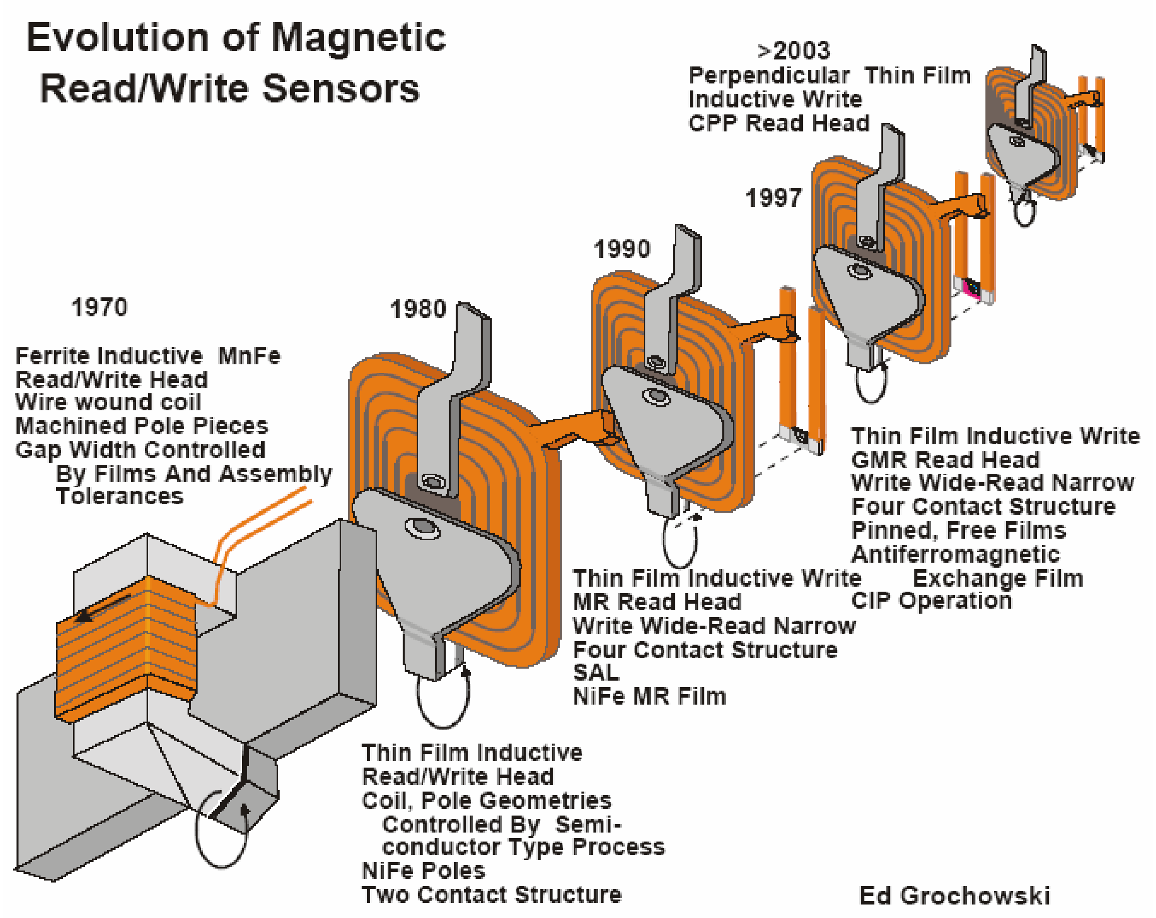

Fig. 1.6 Evolution of magnetic read/write elements (http://www.hitachigst.com/).

CHAPTER 2
TWO NANOACTUATOR DESIGNS FOR AREAL DENSITY OF 1 TBIT/IN^2

To achieve the areal density goal in hard disk drives of 1 Tbit/in^2 the minimum physical spacing or flying height (FH) between the read/write transducer and disk must be reduced to about 2 nm. At such low spacing new nanoscale forces act between the slider and disk, such as intermolecular and electrostatic forces, which must be taken into consideration in the air bearing design. These forces increase the level of flying height modulations (FHMs), which in turn creates dynamic instability and intermittent contact in the flying head slider similar to what has been observed in experiments. Here we present two possible approaches to minimize such forces and/or reduce FHM by FH control, including a thermal flying height control slider and a piezoelectric flying height control slider for hard disk drives.

2.1 Introduction

As the spacing between the slider and the disk decreases in hard disk drives the linear bit spacing of the magnetic recording can decrease, resulting in higher areal density. According to the Wallace spacing loss equation the magnetic signal increases exponentially as the distance decreases between the magnetic media and the transducer. The maximum magnetic signal can be obtained at a spacing of zero, resulting in a contact recording scheme. However, there are trade-offs between reducing the bouncing vibration and wear in such systems [1]. Another significant concern is the thermal stability of both the media and GMR sensors. The read-back signal of GMR sensors can be significantly affected by thermal influences since their electrical resistance is temperature dependent. Continuous high-speed contact generates excessive heat, which undermines the recording performance. The above issues have to be addressed before a reliable contact recording system can be realized.

Instead of contact recording we consider a flying scheme, in which the nominal mechanical spacing (or flying height, FH) between the slider and the disk is reduced to about 2 nm in order to achieve an areal density of 1 Tbit/in^2. On the other hand, due to this reduction in spacing between the slider and the disk, the threshold of new nanoscale phenomena will be crossed. In particular, short range forces between the slider and disk come into play, such as intermolecular and electrostatic forces. A study of the effect of intermolecular forces and electrostatic forces was presented in previous papers, e.g. [2]. The intermolecular and electrostatic forces do not have a significant effect on the flying characteristics of high flying sliders (spacings greater than 10 nm), but they become increasingly important at low spacings (below 5 nm). These forces are attractive in nature and hence result in a reduction in fly height as compared to what would be the case without them. It is also found that these highly nonlinear forces increase the level of disk morphology induced FHM, which in turn creates dynamic instability and intermittent contact in the flying head slider.

Some indications of dynamic instability have been observed experimentally for ultra low flying sliders, such as different take-off and touch-down disk speeds (hysteresis) for flying sliders [3]. Various models have been used to explain the instability that results from the intermolecular forces and charge buildup at the HDI. With the decrease in the head-media spacing (HMS) in order to achieve higher areal density the contribution of intermolecular and electrostatic forces to the force balance at the HDI can no longer be neglected. Hence it is important to investigate alternate air bearing slider designs that can minimize nanoscale short range forces and/or reduce FHM by FH control. To minimize these forces the area of the sliders in close proximity of disks has to be reduced. This can be achieved by reducing the size of the central trailing pads and using higher flying sliders with actuation that can move the read/write transducer closer to the disk on demand. To reduce the FHM by FH control, the bandwidth of actuation has to be high enough to compensate the air bearing dynamics.

In this chapter, we present two approaches to sustain a more stable HDI for low (transducer) FH sliders, including a thermal flying height control slider and a piezoelectric flying height control slider for hard disk drives. This chapter is organized as follows. First, a thermal FH control slider with an additional heating element near the read/write transducer is presented. Finite-element analysis and CMLAir are used to predict the magnitudes of thermal protrusion, FH reduction, intermolecular forces, actuation bandwidth and power consumption. Then, the actuation bandwidth of a piezoelectric slider is calculated by finite-element analysis and measured by Laser Doppler Vibrometer (LDV). Further, the advantages and disadvantages of these two solutions are discussed.

2.2 Two Approaches for Flying Height Control Sliders

2.2.1 Thermal Nanoactuator

The read/write elements of a magnetic head slider consist of thin layers of different materials including write poles, sensor, shields, undercoat, overcoat, coil, insulation layer and the substrate. Due to the mismatch of the coefficients of thermal expansion of the various materials the pole-tip of the write pole protrudes beyond the ABS plane when the ambient temperature varies and/or when an internal heat source is generated by Joule heating of the write current. These temperature-induced (T-PTP) and write-induced (W-PTP) pole-tip protrusions adversely reduce the FH by several nanometers and increase the risk of head-disk contact. Several groups have numerically and/or experimentally investigated the effects of T-PTP and W-PTP [4]-[12].

Based on this concept Meyer *et al.* [13] deposited a resistance heating element (heater) near the read/write elements and the gap FH was reduced by applying a current through the heater to deliberately induce the pole-tip protrusion. Fig. 2.1(a)-(c) illustrate the head-gimbal assembly (HGA) and the location of read/write elements on the slider. The dimension of the slider is 1.25 mm × 1.00 mm × 0.3 mm. Fig. 2.1(d)-(f) show the various layers of materials and the reduction of FH due to the thermal protrusion.

2.2.1.1 Numerical Analysis

In order to determine the magnitudes of the short range forces and the bandwidth of the actuation at flying conditions, a finite-element model of a thermal FH control slider was created as shown in Fig. 2.2. The heating element, coil, write poles, shields, photoresist layer, undercoat insulation layer, and overcoat were modeled in detail to study the effects of the heating power on the flying attitude. The material properties and thickness of each layer are shown in Table 2.1. The thermal conductivities of thin layers are higher than the bulk values due to the heat carrier-boundary scattering and the altered microstructure of thin films [14].

The cooling effect of the air bearing plays a key role in this 3-D heat transfer problem. We first used CMLAir to obtain the nominal FH, pitch, roll, and air pressure distribution of a 5-nm FH ABS slider as shown in Fig. 2.3. The effect of intermolecular forces was included with a nominal value of the Hamaker constant ($A = 1\times10^{-19}$ J). Then we calculated the heat flux through the air bearing based on the model developed by Chen *et al.* [15]. The temperature distributions and pole-tip protrusions were then calculated based on the model and boundary conditions. Since the thermal protrusion causes deformation of the ABS and hence changes the flying attitudes, an iteration approach is used to obtain an equilibrium solution.

2.2.1.2 Results and Discussions

Fig. 2.4 shows that the steady-state FH and thermal protrusion were obtained after several numerical iterations at a heating power of 30 mW. The disk rotational speed, radial position of the head, and skew angle were 7200 rpm, 23 mm, 9.1 degrees, respectively. The FH was reduced from 4.62 to 1.96 nm with a thermal protrusion of 4.2 nm. The ratio of FH reduction to protrusion was 63 %. The loss of 37 % FH reduction was mainly attributed to the increased lift force and the reduced pitch angle as shown in Table 2.2. More importantly, the intermolecular force (IMF) was found to be much smaller than that of conventional sliders with similar FHs due to the fact that only a small region of the slider was protruded in the proximity of the disk.

The protrusion profiles on the ABS and along the center line across the read/write transducer are shown in Figs. 2.5 (a) and (b), respectively. Fig. 2.6 shows the FH reduction along the center line of the ABS. In the case with thermal protrusion the air pressure near the read/write transducer significantly increases, and this lifts the slider upwards, reducing the pitch angle. This highly concentrated air pressure induces extremely high heat flux through the air bearing surface as shown in Fig. 2.7.

Fig. 2.8 shows the temperature distribution over the ABS and around the read/write transducer at a heating power of 30 mW. A temperature valley is observed near the read/write element, which is caused by the extremely concentrated pressure effect on the heat transfer in the air bearing. A similar “butterfly shape” of temperature distributions was experimentally measured by Xu *et al*. [16]. A lower temperature increase is beneficial for GMR sensors which are sensitive to temperature variation.

A transient thermal study was conducted to investigate the bandwidth of the slider. The power to the heating element was set to 30 mW from 0 to 2.5 ms and was turned off at 2.5 ms. The temperature changes of both the GMR sensor and write gap were monitored as shown in Fig. 2.9. It requires about 1 ms for the read/write transducer to reach its steady-state values, corresponding to a bandwidth of 1 kHz. This is too slow for active control of FHM.

2.2.2 Piezoelectric Nanoactuator

The bandwidth of thermal actuation is much lower than the air bearing frequencies, which may be up to 200 kHz. For this reason thermal FH control sliders have little control over FHM and other dynamic losses of FH. The inherent high power consumption of thermal actuation also limits the stroke of protrusions. Several research groups [17]-[21] have presented the FH control using a piezoelectric unimorph cantilever actuator. Some of their results are summarized in Table 2.3. However, their studies were focused on compensating for static spacing loss caused by design tolerances and ambient pressure changes. Neither short range forces nor suppression of FHM was considered. Liu *et al.* [22] investigated an active FH control method for suppressing FHM by bonding a layer of piezoelectric film on one side of the suspension and using real-time spacing variation signals derived from the read-back signal as feedback. However, the short range forces were not considered and since the active element was located on the suspension, the bandwidth was limited by the suspension dynamics.

Juang and Bogy designed a nonlinear compensator for piezoelectric sliders for dynamic active control of FH [23], [24] in the presence of short range forces, where the piezoelectric unimorph cantilever was used as the actuator and the read-back signal was used as feedback. A schematic of this concept is shown in Fig. 2.10. The FH of the read/write elements is adjusted by applying an electrical voltage to the central portion of the piezoelectric material. In order to suppress the FHM due to the air bearing dynamics an actuation bandwidth of 400 kHz may be required. There is no inherent frequency limit for piezoelectric materials. In practice the frequency limits of application are usually determined by resonances associated with the physical structure of the actuators. In order to investigate the resonance frequencies of piezoelectric sliders we attached a 127 μm thick PZT layer on a silicon pico-slider as shown in Fig. 2.11. It was then bonded on a substrate and an LDV apparatus was used to measure the vibration of the cantilever as illustrated in Fig. 2.12(a). Sinusoidal voltages with frequencies from 0 to 1 MHz were applied to the central PZT layer. The first observed resonance frequency was about 610 kHz as shown in Fig. 2.12(b).

A finite-element analysis was also carried out for comparison. The results show that the first natural frequency is about 470 kHz for two different boundary conditions as shown in Fig. 2.13. The higher value of the measured frequency may be caused by an amount of epoxy dispensing on the slider body in the experimental setup.

2.3 Discussions

A brief summary of the advantages and disadvantages for each approach is given in Table 2.3. The quantitative values may vary from one design to another but the qualitative properties should be the same. It is found that the intermolecular forces at a transducer FH of 2 nm were reduced in both approaches. The thermal protrusion of FH control sliders can be controlled by adjusting the power of the heating elements, but the inherent power-consuming thermal actuation limits the actuation displacement, especially for battery powered mobile applications. The quasi-static nature allows thermal FH control sliders to compensate the static spacing loss. The piezoelectric dynamic control slider shows promising performance of higher bandwidth, larger actuation displacement, and higher power efficiency. However, the requirement of piezoelectric materials and modification of the slider design poses challenges in integration of the fabrication process and increases the manufacturing cost.

2.4 Conclusion

While nanoscale design has been used in hard disk drives for several years, only recently have new phenomena arisen that are associated with nanoscale dimensions. As the hard disk drive industry advances toward the areal density of 1 Tbit/in^2 the physical spacing between the air bearing slider that carries the read/write transducer and the top surface of the magnetic disk will be reduced to ~2 nm. In this spacing range new forces, such as intermolecular and electrostatic forces, act and can increase the level of FHM and cause dynamic instability of the flying head slider. Two possible approaches were studied to minimize such forces for flying sliders, including a thermal quasi-static control slider and a piezoelectric dynamic active control slider for hard disk drives. The advantages and disadvantages for each one are also discussed.

References

1. M. Yanagisawa, A. Sato, K. Ajiki, and F. Watanabe, “Design Concept of Contact Slider for High-Density Recording,” *Electronics and Communications in Japan*, part 2, vol.80, pp.43-48, 1997.

2. V. Gupta and D. B. Bogy, “Dynamics of sub-5nm air bearing sliders in the presence of electrostatic and intermolecular forces at the head disk interface,” *IEEE Trans. Magn*., vol. 41, pp. 610-615, 2005.
3. R. Ambekar, V. Gupta, and D.B. Bogy, “Experimental and numerical investigation of dynamic instability in head disk interface at proximity,” *ASME J. of Tribol*., vol. 127, pp. 530-536, 2005.
4. B. K. Gupta, K. Young, S. K. Chilamakuri, and A. K. Menon, “On the thermal behavior of giant magnetoresistance heads,” *ASME J. of Tribol.*, vol. 123, pp. 380-387, 2001.
5. L. Pust, C. J. T. Rea, and S. Gangopadhyay, “Thermo-mechanical head performance,” *IEEE Trans. Magn.*, vol. 38, pp. 101-106, 2002.
6. W. Yan, “Thermal pole tip protrusion finite element analysis of thin film inductive recording heads,” *J. of Applied Physics*, vol. 91, pp. 7571-7573, 2002.
7. R. H. Wang, X. Z. Wu, W. Weresin, and Y. S. Ju, “Head protrusion and its implications on head-disk interface reliability,“ *IEEE Trans. Magn.*, vol. 37, pp. 1842-1844, 2001.
8. J. Xu, M. Kurita, and M. Tokuyama, “Thermal analysis of a magnetic head,” *IEEE Trans. Magn*., vol. 40, pp. 3142-3144, 2004.
9. Y. S. Ju, “Self-heating in thin-film magnetic recording heads due to write currents,” *IEEE Trans. Magn*., vol. 41, pp. 4443-4448, 2005.
10. K. Aoki, T. Hoshino, T. Iwase, T. Imamura, and K. Aruga, “Thermal pole-tip protrusion analysis of magnetic heads for hard disk drives,” *IEEE Trans. Magn*., vol. 41, pp. 3043-3045, 2005.

11. V. Nikitin, S. Gider, J. Tabib, D. Hsiao, M. Salo, G. Sui, S. Yuan, N. A. Satoh, J. Xu, and Y. Maruyama, “Spatial and temporal profiling of protrusion in magnetic recording heads,” *IEEE Trans. Magn.*, vol. 40, pp. 326-331, 2004.
12. E. Jang, G. Wang, K. Y. Cho, and H. Lee, “Heating and cooling effect of giant magnetoresistive heads during writing operations,” *J. Applied Physics*, vol. 91, pp. 8769-8771, 2002.
13. D. W. Meyer, P. E. Kupinski, and J. C. Liu, “Slider with temperature responsive transducer positioning,” U. S. Patent 5991113, Nov. 23, 1999.
14. Y. Yang, S. Shojaeizadeh, J. A. Bain, J. G. Zhu, and M. Asheghi, “Detailed modeling of temperature rise in giant magnetoresistive sensor during an electrostatic discharge event,” *Journal. Of Applied Physics,* vol. 95, pp. 6780-6782, 2004.
15. L. Chen, D. B. Bogy, and B. Strom, “Thermal dependence of MR signal on slider flying state,” *IEEE Trans. Magn.*, vol. 36, pp. 2486-2489, 2000.
16. J. Xu, M. Kurita, and M. Tokuyama, “Thermal analysis of a magnetic head,” *IEEE Trans. Magn.* vol. 40, pp. 3142-3144, 2004.
17. C. E. Yeack-Scranton, V. D. Khanna, K. F. Etzold, and A. P. Praino, “An active slider for practical contact recording,” *IEEE Trans. Magn.,* vol. 26, pp. 2478-2483, 1990.
18. M. Kurita and K. Suzuki, “Flying-height adjustment technologies of magnetic head sliders,” *IEEE Trans. Magn.*, vol. 40, pp. 332-336, 2004.

19. K. Suzuki, R. Maeda, J. Chu, T. Kato, and M. Kurita, “An active head slider using a piezoelectric cantilever for in situ flying-height control,” *IEEE Trans. Magn.,* vol. 39, pp. 826-831, 2003.

20. N. Tagawa, K. Kitamura, and A. Mori, “Design and fabrication of MEMS-based active slider using double-layered composite PZT thin film in hard disk drives,” *IEEE Trans. Magn.*, vol. 39, pp. 926-931, 2003.

21. L. Su, M. Kurita, J. Xu, K. Kato, K. Adachi, and Y. Miyake, “Static and dynamic characteristics of active-head sliders,” *Tribology International*, vol. 38, pp. 717-723, 2005.

22. X. Liu, A. Li, W. Clegg, D. F. L. Jenkins, and P. Davey, “Head-disk spacing variation suppression via active flying height control,” *IEEE Trans. Instrum. Meas.*, vol. 51, pp. 897-901, 2002.

23. J. Y. Juang and D. B. Bogy, “Design of controlled flying proximity sliders for head-media spacing variation suppression in ultra-low flying air bearings,” *IEEE Trans. Magn*., vol. 41, pp. 3052-3054, 2005.

24. J. Y. Juang and D. B. Bogy, “Nonlinear compensator design for active sliders to suppress head-disk spacing modulation in hard disk drive,” *IEEE/ASME Trans. Mechatron*., to be published.

TABLE 2.1 Material Properties used in the FEA

Layer and Material		Young's modulus (GPa)	Thermal conductivity (W/m.K)	Coefficient of thermal expansion (x 10^{-6}/ °C)	Poisson's ratio
Slider substrate	Al_2O_3-TiC	390	20	7.1	0.22
Under-coat (1.2 μm)	Al_2O_3 (thin layer)	138	1.8	7.8	0.25
Shields (2.0 μm)	Ni-Fe	200	35	12.8	0.3
Bottom pole (1.0 μm)	Ni-Fe	200	35	12.8	0.3
Coil (2 μm)	Cu	130	400	15.4	0.34
Heater (250 nm)	Ni-Fe (thin layer)	200	30	12.8	0.3
Coil insulation (5 μm)	Photo-resist	7	0.209	51	0.2
Top pole (1.0 μm)	Ni-Fe	200	35	12.8	0.3
Over-coat (23 μm)	Al_2O_3	138	25	7.8	0.25

TABLE 2.2 Comparison of Flying Attitudes

	Protrusion (nm)	FH (nm)	Pitch (μrad)	Roll (μrad)	IMF (gf)	Max. pressure (atm)
Before protrusion	0	4.62	215	0.7	0.037	16
After protrusion	4.2	1.96	212	0.4	0.065	30

TABLE 2.3 Comparison of Three Approaches

	Micro-trailing pad slider	Thermal quasi-static control slider	Piezoelectric dynamic control slider
FH control or adjustment	N/A	Yes (thermal expansion)	Yes (piezoelectricity)
Intermolecular forces	Minimize (0.19 gf)	Minimize (0.065 gf)	Compensate (0.03 gf [17], [18])
Actuation bandwidth	N/A	Low (1 kHz)	High (610 kHz; >100 kHz [13]; 700 kHz [14]; 243 kHz [15])
Actuation displacement (non-flying condition)	N/A	Low (0.14 nm/mW)	High (9 nm/V [12]; 17.5 nm/V [13]; 15 nm/V [14]; 1.5 nm/V [15])
Power consumption	N/A	High (30 mW)	Low
Manufacturing complexity	Low	Medium	High

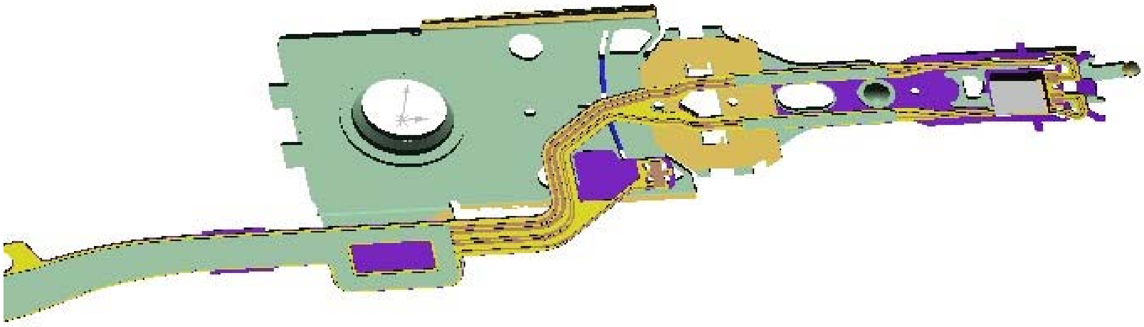

(a) Head gimbal assembly (HGA). The ABS is not shown for simplicity.

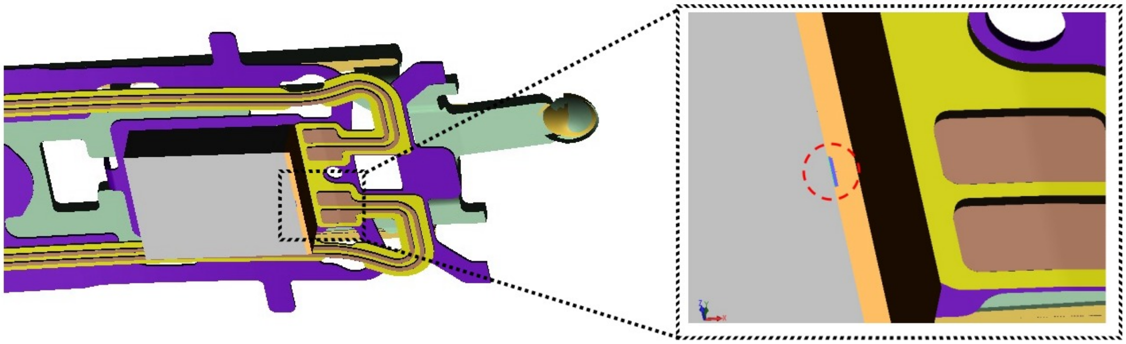

(b) Enlarged view of the slider

(c) Enlarged view near the trailing edge

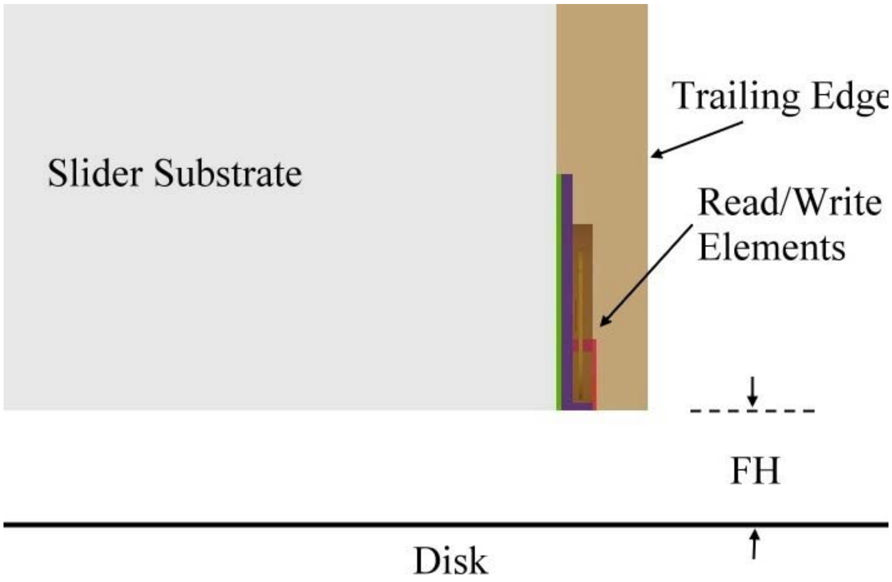

(d) Cross-section view of part of a slider without thermal actuation

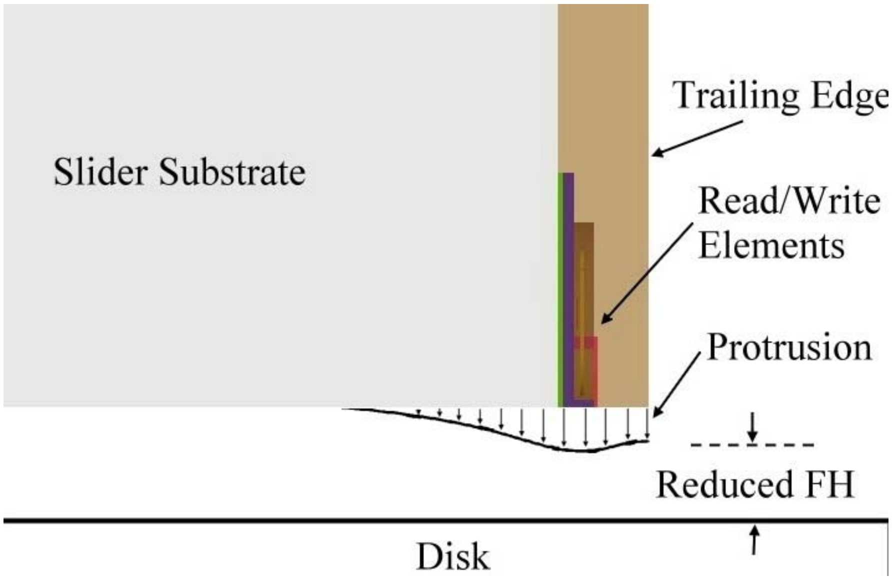

(e) the actuated pole-tip protrusion and the reduced FH

Fig. 2.1. Schematic diagrams of the actuated pole-tip protrusion of read/write elements.

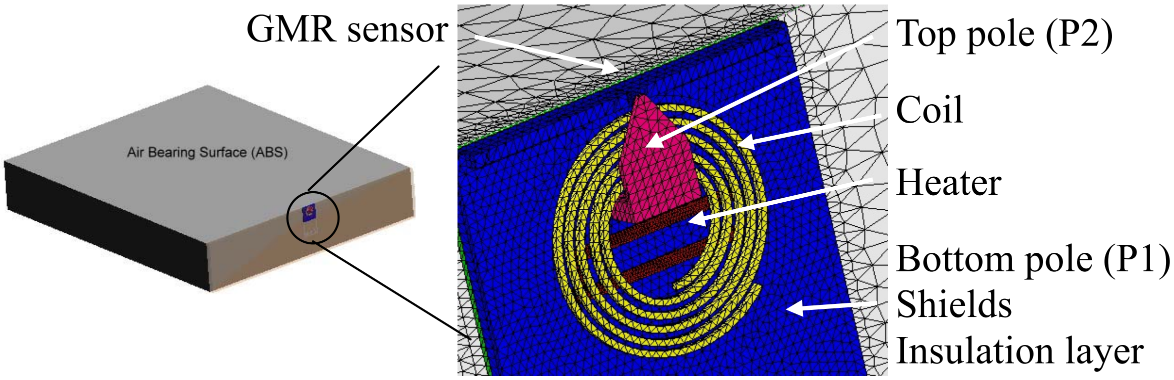

Fig. 2.2. The finite-element model of a TFC slider. The overcoat and photoresist are not shown for a clear view of the read/write transducer.

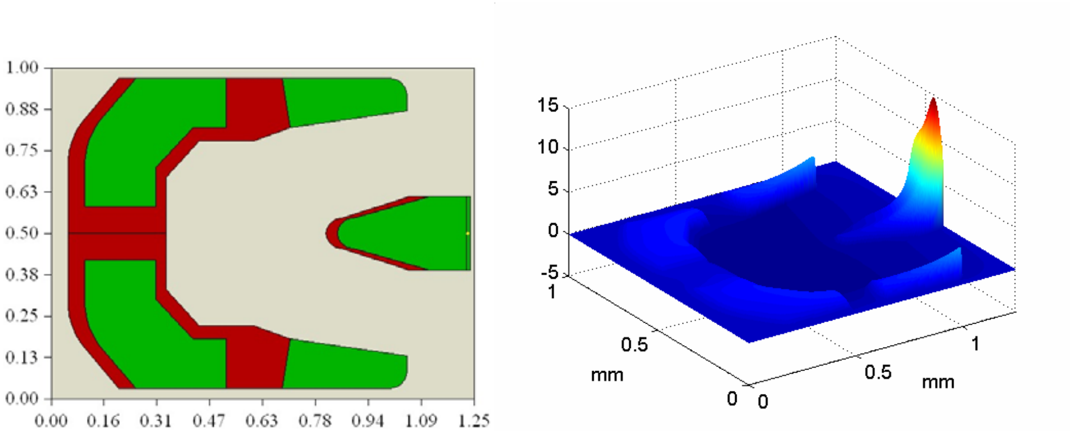

(a) (b)

Fig. 2.3. (a) An ABS design used in this study; (b) the air pressure distribution of this ABS. The scale displayed is normalized to ambient pressure: (p - pa)/pa.

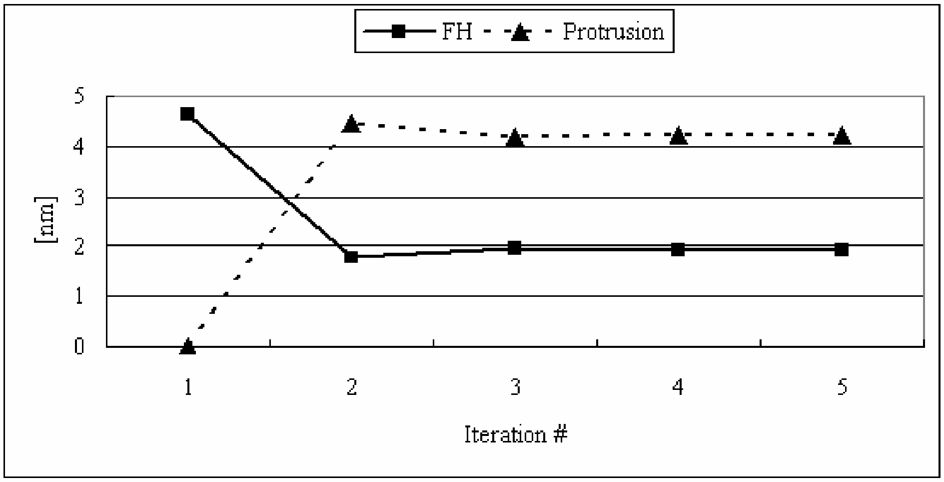

Fig. 2.4. Steady-state FH and thermal protrusion were obtained after several numerical

iterations at a heating power of 30 mW.

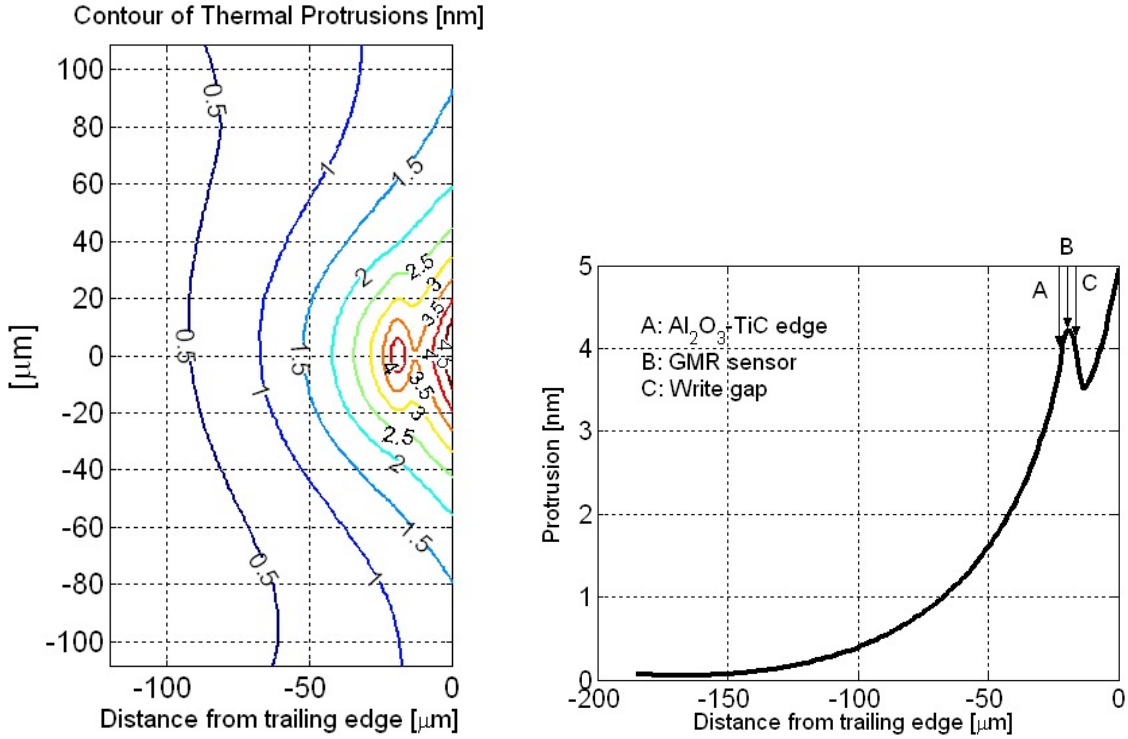

(a) (b)

Fig. 2.5. Thermal protrusion profiles on the ABS (a) and along the center line across the read/write transducer. The distances of the write gap and GMR sensor from the trailing edge are 16.3 and 19.8 μm, respectively.

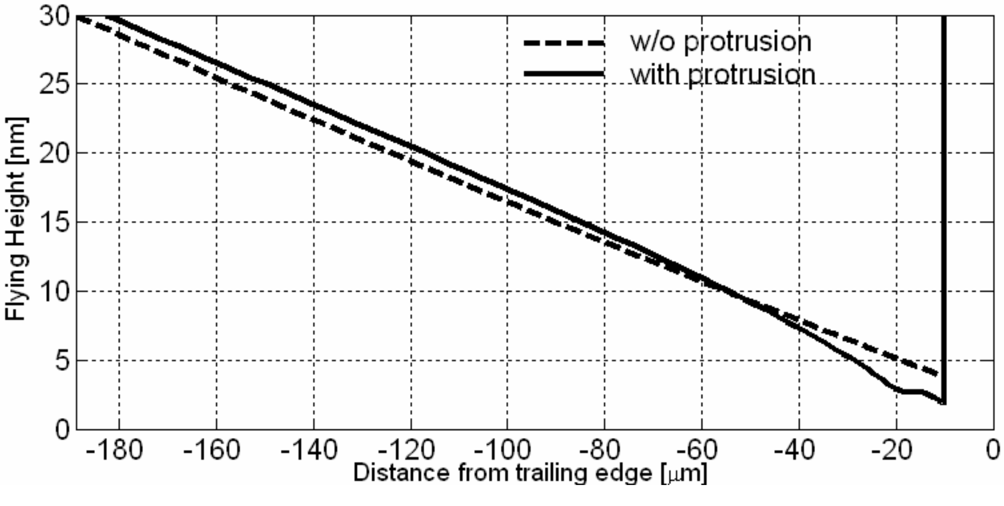

Fig. 2.6. Comparison of FH profiles along the center line of ABS. The distances of the write gap and GMR sensor from the trailing edge are 16.3 and 19.8 μm, respectively.

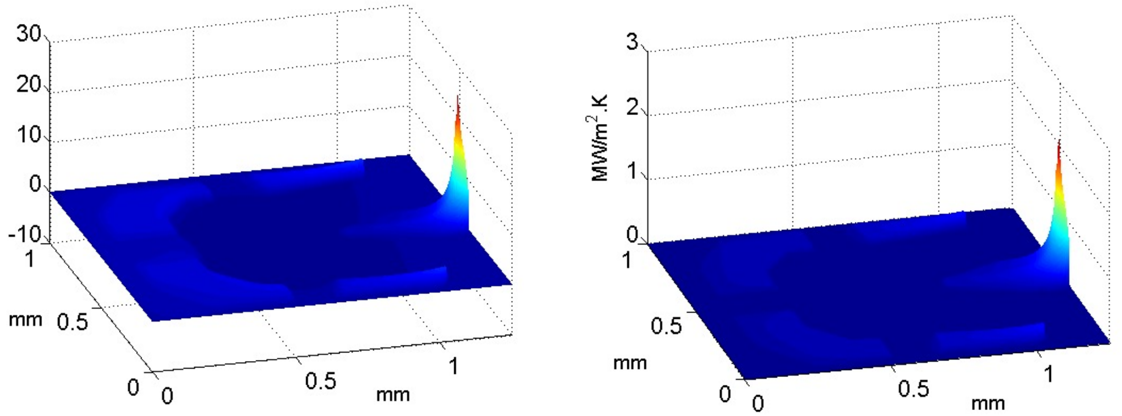

(a) (b)

Fig. 2.7. The air pressure distribution (a) and the distribution of the heat transfer film coefficient across the ABS with thermal deformation.

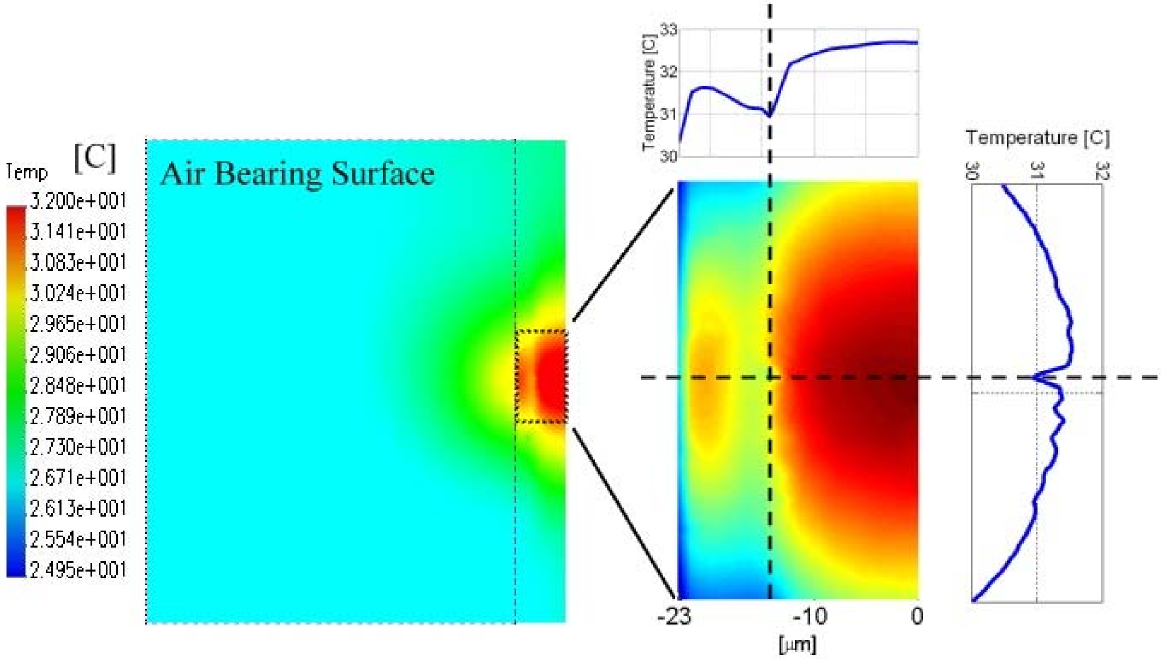

Fig. 2.8. Temperature distributions of a flying slider with thermal protrusion at a heating power of 30 mW. Line distributions show a clear temperature valley near the read/write head.

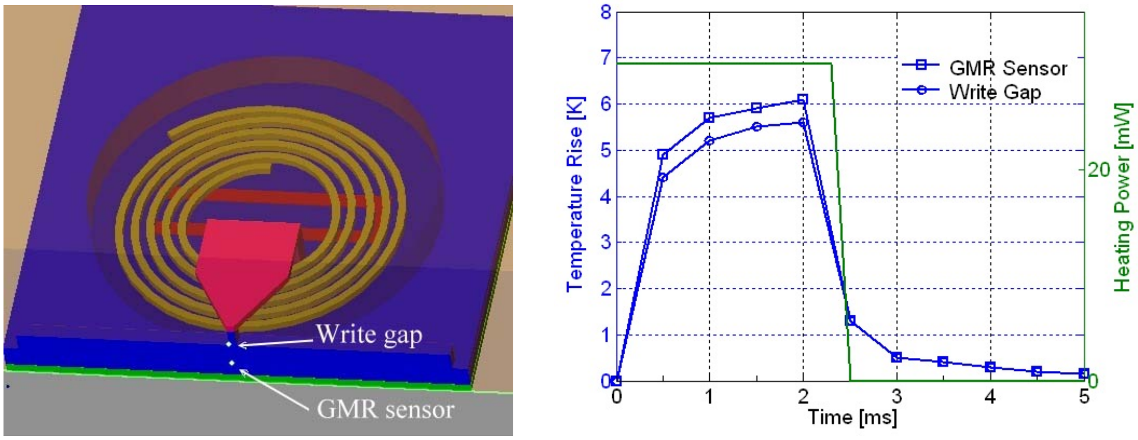

(a) (b)

Fig. 2.9. Transient temperature changes of a flying slider with a varying heating power.

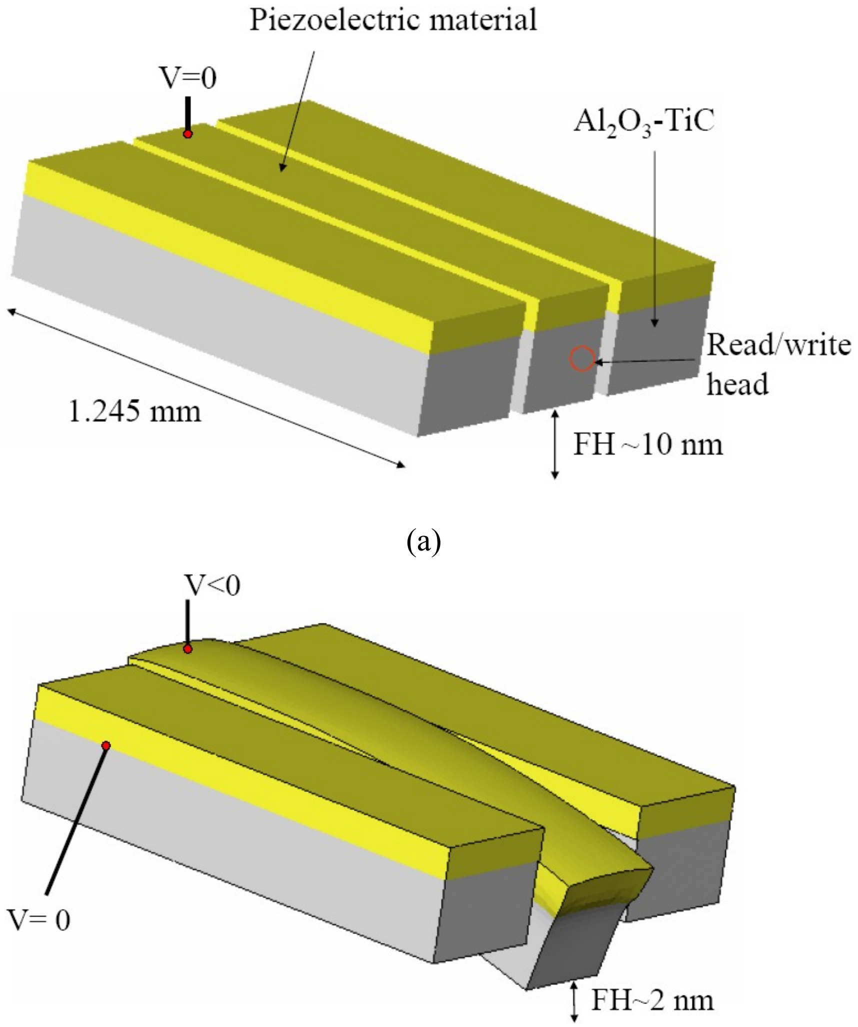

(a)

(b)

Fig. 2.10. Two operational modes of a FH control slider with piezoelectric actuation. (a) passive mode; (b) active mode.

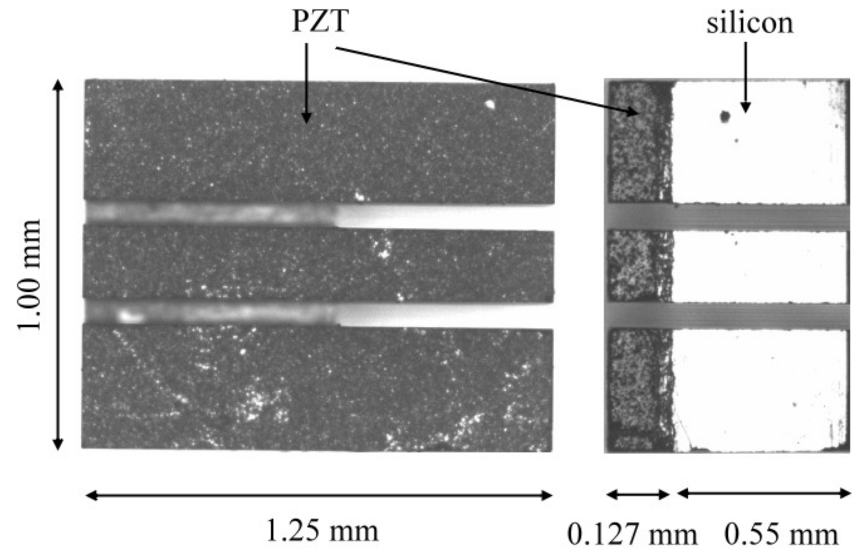

Fig. 2.11. A piezoelectric pico-slider used to determine the actuation bandwidth.

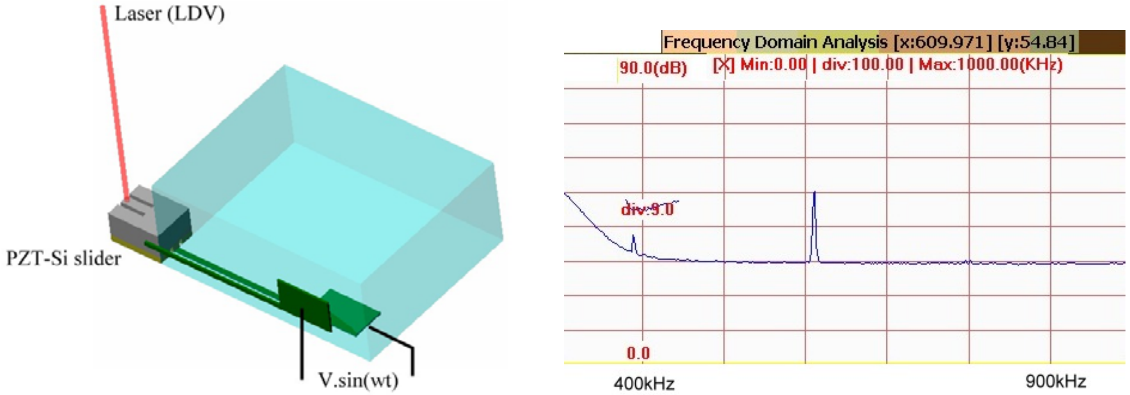

(a) (b)

Fig. 2.12. (a) Experimental set-up; (b) the first measured resonance frequency is about 610 kHz.

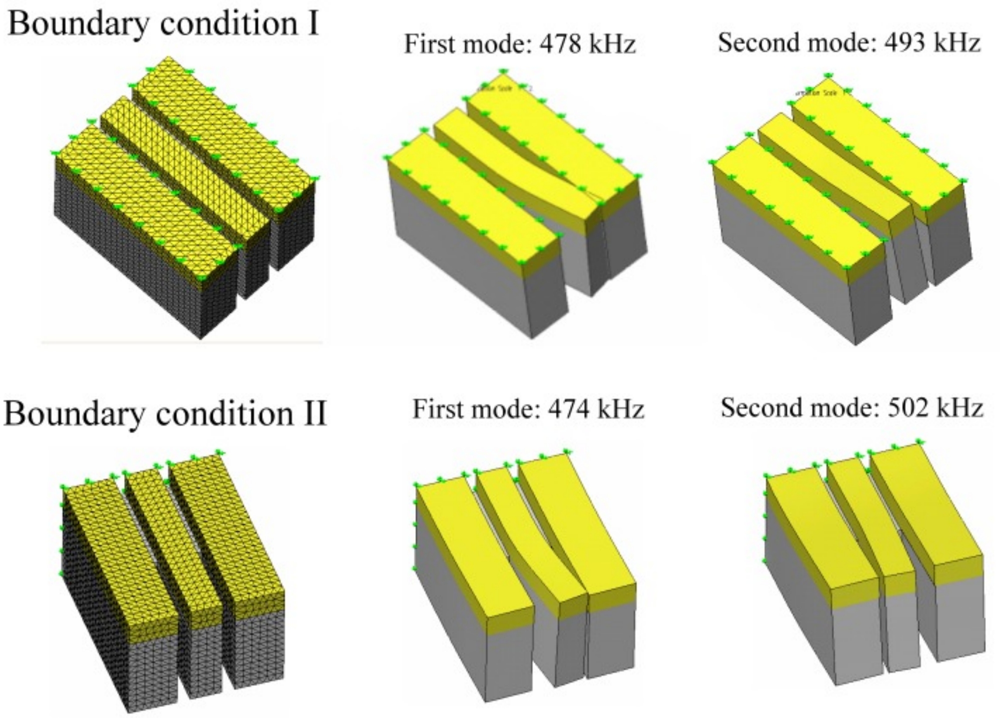

Fig. 2.13. Finite-element models and the first two modes and natural frequencies for two different boundary conditions.

CHAPTER 3
AIR BEARING DESIGNS AND FLYING DYNAMICS OF FH CONTROL SLIDERS

To achieve the areal density goal in hard disk drives of 1 Tbit/in^2 the minimum physical spacing or flying height (FH) between the read/write element and disk must be reduced to ~2 nm. A brief review of several FH adjustment schemes is first presented and discussed. Two ABS designs, Scorpion III and IV, for a FH control slider with thermal and piezoelectric nanoactuators, respectively, are proposed to achieve virtually 100 percent actuation efficiency (defined as the ratio of the FH reduction to the unloaded stroke). A numerical study is conducted to investigate both the static and dynamic performances of the Scorpion sliders, such as uniformity of gap FH with near-zero roll over the entire disk, ultrahigh roll stiffness and damping, low nanoscale adhesion forces, uniform FH track-seeking motion, dynamic load/unload and FH modulation (FHM). The Scorpion sliders are found to exhibit an overall enhancement in performance, compared with several conventional ABS designs.

3.1 Introduction

As the spacing between the slider and the disk decreases in hard disk drives the linear bit spacing of the magnetic recording can decrease, resulting in a higher areal density. According to the Wallace spacing loss equation the magnetic signal increases exponentially as the distance decreases between the magnetic media and the transducer. The maximum magnetic signal can be obtained at a mechanical spacing of zero, resulting in a contact recording scheme. However, there are trade-offs between reducing the bouncing vibration and wear in such systems [1]. Another significant concern is the thermal stability of both the media and GMR sensors. The read-back signal of GMR sensors can be significantly affected by thermal influences since their electrical resistance is temperature dependent. Continuous high-speed contact generates excessive heat, which degrades the recording performance. Also, the air bearing shear force and friction caused by slider-disk contact may affect the tracking ability of these sliders. The above issues have to be addressed before a reliable contact recording system can be realized.

Instead of contact recording we consider a flying scheme in which the nominal head-media spacing (HMS) has to be reduced to 5 nm for an areal density of 1 Tbit/in^2. This HMS includes a physical spacing (or gap flying height, gap FH) of 2.5 nm between the read/write element and the surface of the disk, the protective layers–slider and disk diamond-like-carbon overcoats, and lubricants on the disk. A stable and constant gap FH must also be sustained in the presence of altitude and temperature changes, manufacturing tolerance, and track-seeking motion. Furthermore, slider disk contacts must be avoided during load/unload processes and operational shocks. The dynamic instability caused by FH modulations (FHMs) and nanoscale adhesion forces, such as electrostatic and intermolecular forces should be minimized. Those challenges make a conventional air bearing surface (ABS) slider an unlikely choice for 1 Tbit/in^2. One potential solution is a FH adjustment or controlled slider that is capable of adjusting its gap FH. Table 3.1 summarizes the challenges of the head-disk-interface (HDI) for ultrahigh density recording and potential solutions provided by a FH control slider. Several approaches have been reported for FH adjustment or control as shown in Table

3.2 [2]-[20]. They are categorized into five major principles of actuation with four different actuation mechanisms. The effect of air bearing coupling indicates whether one particular actuation is coupled with the air bearing. Such effect has to be minimized to increase the actuation efficiency (defined as the ratio of FH reduction to actuation stroke). Khanna *et al*. [11] in 1991 and then Zhang *et al.* [12] in 2005 reported a method of FH adjustment by bonding a bulk piezoelectric material on the backside of a slider body. The FH was adjusted by applying a voltage to the piezoelectric material and thereby changing the crown and/or camber of the slider body. The structure of such sliders is simpler and it is relatively easy to fabricate but the fact that the actuation is coupled with the air bearing significantly limits the actuation stroke and efficiency. Instead of piezoelectric materials Dietzel *et al.* [13] used a microfabricated thermal actuator to deform the slider body. Besides the disadvantage of air bearing coupling, the power consumption was very high compared to the operating power of an HDD, especially for battery powered mobile applications. Another principle of actuation is to apply an electrostatic force in the HDI [16], [17] or to change the pattern of air flow by ducts and valves [18]. Besides the disadvantage of air bearing coupling, the former also significantly increases the risk of electrostatic discharge (ESD) across the interface and the latter has difficulty achieving a high resolution FH adjustment. Another approach is to bond a layer of piezoelectric material to one side of the suspension and change the FH by bending the suspension [19], [20]. Besides the strong coupling of the actuation and the air bearing, the bandwidth of actuation is limited by that of the suspension dynamics, which is much lower than that of the air bearing. Another concept of actuation is to drive the read/write elements so that they have relative displacement to the slider body. Due to the minute area that the read/write element occupies on the slider air bearing surface the effect of air bearing coupling could be minimized. Chen *et al.* [15] designed a micromachined monolithic electrostatic actuator for adjusting FH. However, such an actuator was susceptible to particle contamination due to the complex structure of the multiple parallel plates and the electrostatic attraction force. The concept of adjusting the transducer FH by the thermal expansion of materials was first demonstrated by Meyer *et al.* [14] in which a resistance heating element (heater) was mounted to the slider body near the read/write element. When a current is applied through the heater a portion of the head protrudes due to the mismatch of the coefficients of thermal expansion of the various materials. Such protrusion reduces the FH. In Chapter 2 we found that even though the protruded area was relatively small, there was still considerable air bearing coupling with the resulting actuation efficiency of only 63 %, which suggested that the ABS played a key role in reducing the air bearing coupling. Another approach that can potentially exhibit high actuation bandwidth, low power-consumption, and less air bearing coupling is to utilize piezoelectrically actuated unimorph cantilever sliders. Yeack-Scranton *et al.* [9] proposed an active slider for contact recording, where a piezoelectric material was inserted in a channel that ran across the full width of the slider at its top rear. They experimentally demonstrated movement of the read/write element from ~ 200 nm to contact, but the proposed structure of piezoelectric actuator was difficult to implement in the smaller currently used pico- or femto-sized sliders and the effect of the air bearing was not discussed. In a previous study [10] we numerically and experimentally studied an Al_2O_3-TiC slider with a unimorph piezoelectric cantilever. We used a conventional ABS and found that the actuation efficiency was very low due to the highly pressurized central trailing pad. Several papers, such as Kurita *et al.* [2], [3], Tagawa *et al.* [5], Suzuki *et al.* [4], and Su *et al*. [6], have presented active sliders made of silicon with piezoelectric unimorph cantilevers. The slider structure was simpler and could be fabricated by silicon microfabrication technology. An ABS design with less air bearing coupling effect was also proposed, which was achieved by a small central trailing pad. The increase of aerodynamic lift force caused by the bending of the cantilever was minimized such that the flying attitude of the slider body was hardly changed during the head actuation. However, the use of silicon as the slider material makes it difficult to integrate with current fabrication technology. Also, the two slots that defined the cantilever significantly reduced the amplitude of the negative pressure of their subambient ABS sliders and the negative pressure is known to be a key attribute for high performance sliders. Since such sliders have several merit features over other FH control schemes, it is important to study and design an ABS for such sliders with high negative pressure and other required characteristics.

In this chapter we present novel ABS designs for FH control sliders with thermal and piezoelectric nanoactuators, which can achieve high actuation efficiency (or little air bearing coupling), high negative pressure, high air bearing stiffness, and damping. Numerical studies of the static and dynamic performances, including flying attitude, actuation efficiency, nanoscale adhesion forces, track-seeking motion, dynamic load/unload and FHM, are carried out and discussed. The results are also compared with conventional ABS designs.

3.2 Design Concept

In order to control the gap FH, we consider FH control sliders with thermal and piezoelectric nanoactuators as described in Chapter 2. For a piezoelectrically actuated slider the FH is about 10 nm in the off duty cycle (passive mode) and is reduced to ~2 nm during reading and writing (active mode) by applying a voltage to the central piece of piezoelectric material (Fig. 2.10). The actuation stroke is a function of the applied voltage, the air bearing force generated by the central trailing pad, the actuator geometry and materials [7], [8]. For a thermally actuated slider the FH is reduced by actuated pole-tip protrusion (A-PTP) as illustrated in Fig. 2.1. Such reduction of FH of several nanometers is expected to permit the increase in the areal density from less than 100 Gbit/in^2 to 1 Tbit/in^2. Two ABS designs, called Scorpion III and IV, were designed for thermal and piezoelectric sliders, respectively. As illustrated in Fig. 3.1(a) Scorpion IV has four levels of etching steps. The recessed areas with 1.7 μm and 600 nm etch depths create a subambient pressure zone and a negative pressure distribution (suction force), “pulling” the slider towards the disk surface. The two side trailing pads generate a positive pressure distribution (lift force), “pushing” the slider away from the disk surface (Fig. 3.1(b)). Those negative and positive pressure distributions balance with the applied gram-load and together determine the flying attitude, such as FH, pitch and roll, and other important characteristics, including air bearing stiffness and damping. The read/write element is located near the center of the trailing pad of the slider body. The targeted gap FH (without actuation) is 10 nm at a disk velocity of 15000 rpm. Based on a similar concept, Scorpion III was also designed as shown in Fig. 3.2. The Scorpion ABSs were designed to achieve high actuation efficiency (low air bearing coupling) and to meet the following requirements: (1) constant FH profile from the inner diameter (ID) to the outer diameter (OD) with skews, (2) high roll stiffness and damping, (3) reduced effect of nanoscale adhesion forces in the HDI, (4) minimal FH changes during track-seeking motions, (5) better dynamic load/unload performance, and (6) comparable FHM. The features of Scorpion IV include the two slots defining the cantilever, the microtrailing pad, the cavity walls enclosing half of the two 600-nm side etch levels, and the stripes on the two leading pads. The slider is primarily supported by the positive force generated by the two side-trailing pads as seen in Fig. 3.1(b). The two slots allow the cantilever to move upwards or downwards, *i. e.*, to adjust the FH. The reduced area of the microtrailing pad effectively minimizes the air bearing coupling effect and the nanoscale adhesion forces, such as electrostatic and intermolecular forces. The cavity walls hold the negative pressure without it leaking to the slots and hence increase the stiffness. The multiple stripes create pressure gradients and increase the air film damping [21]. A conventional ABS, Slider A, is used for comparison (Fig. 3.3). Those results are shown and discussed in the following sections.

3.3 Static Analysis

3.3.1 Flying Attitude and Actuation Efficiency

Numerical simulations were performed using the CML Static Air Bearing Simulator, which solved the generalized Reynolds equations and determined the steady-state flying attitude, including FH, pitch, and roll. The disk radius/skew range is 17.87 mm/-15.62° to 29.89 mm/7.22° with a disk velocity of 15000 rpm. The simulation conditions and air bearing specifications for Scorpion III and IV are summarized in

Tables 3.3 and 3.4, respectively. In Figs. 3.4 - 3.7 it is seen that a nearly uniform 10-nm FH is achieved with minimal loss at high altitude (4500 m) and a roll angle less than 3 μrad over the disk for both designs. A relatively high negative (suction) force is also preserved, which is needed to maintain high stiffness and low sensitivity to ambient pressure change.

Fig. 3.8 shows the simulated FH as a function of actuation stroke for Scorpion IV. Due to the small area of the central trailing pad and the support of the two side trailing pads the actuation is not coupled with the air bearing pressure and a high actuation efficiency (= FH reduction/stroke) of 98.75 % is achieved. It is seen that the reduction of gap FH is essentially proportional to the stroke, and the FH of the rest of the slider is nearly unchanged. A small increase of air bearing pressure is observed when the slider has an 8-nm actuation stroke (Fig. 3.9). Similarly, the FH reduction as a function of the heating power for Scorpion III is plotted in Fig. 3.10. Almost 100 % actuation efficiency is also achieved. It is seen that the reduction of the gap FH is nearly proportional to the power, and the FH of the rest of the slider is nearly unchanged. Little increase in air bearing pressure near the center trailing pad is observed when the slider has a 7.5-nm actuated pole-tip protrusion (A-PTP) as shown Fig. 3.11.

3.3.2 Stiffness and Damping of the Air Bearing

The air bearing stiffness and damping of a particular slider design are primarily determined by the geometry of the air bearing surface. It has been shown that high stiffness and damping are desired for a reliable and stable HDI. Modal analysis and the system identification method were used to calculate the frequency responses and obtain the modal parameters, such as modal stiffness, damping ratios and nodal lines, of the air bearing sliders [21]. Fig. 3.12 shows the frequency responses of Scorpion III, IV and Slider A. It is seen that Slider A exhibits a typical three-peak curve, corresponding to the roll, first pitch and second pitch modes. Scorpion III shows two peaks, which clearly indicates that the damping ratio for the roll mode is very large. It is noted that Scorpion IV shows only one peak as a result of large damping ratios for the roll and second pitch modes. Comparisons of the modal frequencies, stiffness and damping ratios with published data in [22], [23] are shown in Fig. 3.13 and Table 3.5. Among the five ABS designs, Scorpion IV shows a remarkable increase of 52 %, 506 %, and 237 % in damping ratios over the second most highly-damped conventional ABS II for the first pitch, second pitch, and roll modes, respectively (Fig. 3.13). As listed in Table 3.5 Scorpion IV exhibits 694 % increase in the roll stiffness over Slider A but it shows 24 % and 28 % decrease of the first and second pitch stiffnesses, respectively. Similarly, Scorpion III shows a remarkable increase of 294 % in damping ratio over ABS II for the roll mode. It will be demonstrated in the Dynamic Analysis section that the dynamical performances of the Scorpion designs are greatly enhanced, which is primarily attributed to the significant increase of the roll stiffness and damping.

3.3.3 Nanoscale Adhesion Forces

Nanoscale adhesion forces, such as electrostatic and intermolecular forces, can cause dynamical instability in the HDI of ultralow flying sliders [24]. Even though those forces cannot be completely attenuated their effect can be reduced by simply decreasing the effective slider area within proximity of the disk. For a FH control slider, this reduction in area is achieved by flying at a higher FH and bending the microsized central trailing pad close to the disk. Numerical simulations were performed to investigate the effect of such forces on the flying attitude of the Scorpion sliders. Fig. 3.14 shows the minimum FH as a function of electrostatic potential between the slider and the disk for four different ABS designs, where the 4.5-nm and 5-nm minimum FHs of Scorpion III and Scorpion IV at zero voltage are obtained with a 4-nm actuation stroke. It is seen that the breakdown voltage of Scorpion IV (with 108 μrad pitch) is 27 % and 43 % higher than the high-pitch slider (245 μrad) and low-pitch slider (190 μrad), respectively. The breakdown voltage of Scorpion III (with 123 μrad pitch) is even higher due to its small area of thermal protrusion. Similarly, in comparing the intermolecular force, Scorpion III and IV exhibited 30–40 % and 24–28 % decreases, respectively, within the 2–4 nm FH region as shown in Fig. 3.15.

3.4 Dynamic Analysis

The air bearing film and slider body form a complex coupled nonlinear dynamic system. The CML Dynamic Air Bearing Simulator is used to solve the generalized Reynolds equations coupled with the dynamics of the slider body and a lumped parameter suspension, where the suspension is represented by flexure stiffnesses and damping coefficients. By using the simulator we can obtain dynamic responses of a slider subject to various dynamic inputs, including the flying characteristics during track-seeking motion and FHM over measured disk morphology. The CML Load/Unload & Shock Simulator, developed by Bhargava and Bogy [25], is used to simulate complex dynamic responses of a slider in the load/unload process and under operational shock. This simulator is based on the Dynamic Simulator and uses more sophisticated finite-element models for the suspension and disk.

3.4.1 Flying Characteristics during Track-seeking Motion

Track-seeking is the process for a slider to move from one track to another. During this process the FH changes as a result of the skew angle and the relative disk velocity as well as the inertia force due to the slider's acceleration or deceleration in the cross track direction. Track access time is one of the important hard drive performance indices. Increasing the seek acceleration can reduce the access time. However, it also leads to larger inertial effects and adversely increases FH drops. Fig. 3.16 shows the track-seeking profile used in this study. The maximum acceleration is 65 G, and it takes 11 ms for seeking from the ID to the OD or vice versa. The effective skew angle is the angle between the slider's longitudinal direction and the relative disk velocity (or air flow velocity) which is the resultant vector of the disk track linear velocity and the slider's seek velocity. The FH changes of Slider A and the Scorpion sliders during the seek motion are shown in Fig. 3.17. It is seen that Scorpion III and IV exhibit remarkably flat FHs during the entire seek profile with a maximum FH difference of less than 0.2 nm, as compared with the 0.75-nm FH difference of Slider A near the MD. Since the Scorpion ABSs have ultrahigh roll stiffness, their sensitivity to the skew angle change is significantly reduced, hence, resulting in a more uniform FH profile.

3.4.2 Dynamic Load/Unload Performance

Dynamic load/unload (L/UL) has been widely used in recent hard disk drives for achieving better shock resistance, lower power consumption as well as lower wear and debris formation. Previous research showed that the ABS design significantly affects the L/UL performance [26], [27]. The main design objectives of L/UL are no slider-disk contact during the entire L/UL and a smooth and short unloading process. Challenges exist in both the loading and unloading processes. During the loading process sliders may hit the disk especially at high loading velocities. In the unloading process the air bearing positive pressure quickly responds to changes in FH and pitch, while the negative pressure generated by subambient cavities is relatively resistant to change. This results in a negative net force, which in turn causes slider-disk contact. The negative pressure therefore plays a key role in the L/UL processes. While the likelihood of contact can be decreased or eliminated by reducing the negative force, this force is beneficial to maintain high stiffness and low fly sensitivity. Another potential solution is to use a slider with burnished or rounded corners [28]. However, this additional corner rounding can cause sensitivity of the FH to tolerances associated with the manufacturing process. Another solution is to design an ABS with high roll stiffness so that it can avoid the undesirable roll motion during unloading. It has been shown in the previous section that the Scorpion ABSs has much higher roll stiffness than the other conventional ABS designs. The CML L/UL & Shock Simulator was used to investigate the L/UL of Scorpion III and IV with a finite element model for the suspension (Fig. 3.18). The simulator models actuator rotation over a prescribed ramp profile. The unloading process takes place at the OD (29.89 mm, 7.22^{o}) and 15000 rpm. The displacements and the minimum clearances of Scorpion III and IV during unloading at 50 mm/s and 150 mm/s are shown in Figs. 3.19(a) and 3.20(a), respectively. The minimum clearance drops due to the unloading process are illustrated in Figs. 3.19(b) and 3.20(b). It is seen that the minimum clearance drops merely 0.3 nm even at a high velocity (Figs. 3.21 and 3.22). Fig. 3.23 shows the air bearing forces of Scorpion III during unload. The lift-off forces are -0.83 and -1.17 gf at 50 mm/s and 150 mm/s, respectively. The lift-off forces of Scorpion IV are -0.74 and -0.79 gf at 50 mm/s and 150 mm/s, respectively as shown in Fig. 3.24. The displacement, minimum clearance and air bearing forces during the loading process are shown in Fig. 3.25 and 3.26. Similarly, there is no contact observed in the process.

3.4.3 Flying Height Modulation

In order to quantitatively compare the FHM of the ABS designs, we measured the topography of a current “super-smooth” disk surface by laser Doppler vibrometer (LDV) and used it as external excitation in the simulations. Fig. 3.27 shows the measured disk morphology used in the simulations at three radial positions. The peak-to-peak and standard deviation (σ) of the disk roughness are 1.76 and 0.31 nm, respectively. The FHMs of Scorpion III and IV are compared with that of Slider A as shown in Figs. 3.28 and 3.29. The quantitative results are summarized in Tables 3.6 and 3.7, which include peak-to-peak values and standard deviations. The two Scorpion designs behaved similarly in FHMs. The maximum peak-to-peak FHMs of Scorpion III and Slider A are found to be 0.35 nm (at the ID) and 0.47 nm (at the OD), respectively. Scorpion III exhibits a lower ratio of the maximum to minimum peak-to-peak value than Slider A. In cross-comparing ABS designs at different radial positions, Scorpion III is found to have

54−62 % less FHM than Slider A at the MD and the OD but has 94 % more FHM at the ID. The higher FHM of Scorpion III at the ID is due to the relatively higher skew (-15.62°) and the very small positive pressure under the central trailing pad. Such FHM can be further suppressed by the dynamic feedback controller proposed by Juang and Bogy [7], [8]. However, due to the low bandwidth of thermal actuation, the FHM of Scorpion III can not be suppressed by the actuator.

3.5 Conclusions

This chapter proposes novel ABS designs, Scorpion III and IV, for FH control sliders with a thermal and a piezoelectric nanoactuator, respectively. It was found that the Scorpion sliders exhibit virtually 100 percent actuation efficiency (or little air bearing coupling), which indicates that the gap FH can be efficiently reduced by the actuator. A uniform FH and near-zero roll angle were achieved across the disk. The FH losses at a high altitude (4500 m) were found to be ~20 % and ~30 % for Scorpion III and IV, respectively, which can be readily compensated by the actuators with a pressure sensor. The Scorpion designs showed a remarkable increase in damping ratios and roll stiffness compared to several conventional designs, which was beneficial to better track-seeking and L/UL processes. The FH drop was reduced to less than 0.2 nm during the track-seeking motion. Even though the Scorpion sliders have rather high negative forces (-3.1 gf for Scorpion IV and -4.8 gf for Scorpion III), the minimum clearance dropped only 0.3 nm even at a high unloading velocity. The peak-to-peak FHMs of the Scorpion sliders simulated with a measured disk topography were found to be 0.17−0.36 nm. The higher value at the ID was due to the relatively higher skew (-15.62°) and the small positive pressure under the central trailing pad. Furthermore, the nanoscale adhesion forces, such as electrostatic and intermolecular forces, were found to be much less compared to conventional designs due to the fact that the FH control slider flies relatively higher with the miniature microtrailing pad in the close proximity of the disk surface.

References

1. M. Yanagisawa, A. Sato, K. Ajiki, and F. Watanabe, “Design Concept of Contact Slider for High-Density Recording,” *Electronics and Communications in Japan*, part 2, vol.80, pp.43-48, 1997.
2. M. Kurita, T. Yamazaki, H. Kohira, M. Matsumoto, R. Tsuchiyama, J. Xu, T. Harada, Y. Inoue, L. Su, and K. Kato, “An active-head slider with a piezoelectric actuator for controlling flying height ,” *IEEE Trans. Magn.,* vol. 38, pp. 2102-2104, 2002.
3. M. Kurita and K. Suzuki, “Flying-height adjustment technologies of magnetic head sliders,” *IEEE Trans. Magn.,* vol. 40, pp. 332-336, 2004.
4. K. Suzuki, R. Maeda, J. Chu, T. Kato, and M. Kurita, “An active head slider using a piezoelectric cantilever for in situ flying-height control,” *IEEE Trans. Magn.,* vol. 39, pp. 826-831, 2003.
5. N. Tagawa, K.-I. Kitamura, and A. Mori, “Design and fabrication of MEMS-based active slider using double-layered composite PZT thin film in hard disk drives,” *IEEE Trans. Magn.,* vol. 39, pp. 926-931, 2003.

6. L. Su, M. Kurita, J. Xu, K. Kato, K. Adachi, and Y. Miyake, “Static and dynamic characteristics of active-head sliders,” *Tribol. Intl.,* vol. 38, pp. 717-723, 2005.
7. J. Y. Juang and D. B. Bogy, “Controlled-flying proximity sliders for head-media spacing variation suppression in ultralow flying air bearings,” *IEEE Trans. Magn.,* vol. 41, pp. 3052-3054, 2005.
8. J. Y. Juang and D. B. Bogy, “Nonlinear compensator design for active sliders to suppress head-disk spacing modulation in hard disk drive,” *IEEE/ASME Trans. Mechatron.*, to be published.
9. C. E. Yeack-Scranton, V. D. Khanna, K. F. Etzold, and A. P. Praino, “ An active slider for practical contact recording,” *IEEE Trans. Magn.,* vol. 26, pp. 2478-2483, 1990.
10. J. Y. Juang, D. B. Bogy and C. S. Bhatia, “Numerical and experimental studies of an Al_2O_3-TiC slider with a piezoelectric nanoactuator,” *2006 ASME/JSME joint Conf. on Micromechatronics for Information and Precision Equipment*, June 21-23, 2006, Santa Clara, CA..
11. V. D. Khanna, F. Hendriks, and A. P. Praino, “ Programmable air bearing sliders,” *IEEE Trans. Magn.,* vol. 27, pp. 5145-5147, 1991.
12. M. Zhang, S. Yu, J. Liu, and B. Liu, “Flying height adjustment by slider’s air bearing surface profile control,” *J. Applied Physics,* vol. 97, 10P309, 2005.
13. A. Dietzel, R. Berger, P. Mächtle, M. Despont, W. Häberle, R. Stutz, G. K. Binnig, and P. Vettiger, “In situ slider-to-disk spacing on a nanometer scale

controlled by microheater-induced slider deformations," *Sensors and Actuators A,* vol. 100, pp. 123-130, 2002.

14. D. W. Meyer, P. E. Kupinski, and J. C. Liu, "Slider with temperature responsive transducer positioning," U. S. Patent 5,991,113, Nov. 23, 1999.
15. F. Chen, H. Xie, and G. K. Fedder, "Microactuator for ultra-low magnetic disk head fly height control," *IEEE Trans. Magn.,* vol. 37, pp. 1915-1918, 2001.
16. D. Song, D. Schnur, and Z.-E. Boutaghou, "Discharge mechanism for electrostatic fly control," *IEEE Trans. Magn.,* vol. 40, pp. 3162-3164, 2004.
17. Z. Feng, C. Y. Shih, C.-S. F. Poon, and V. K. Gubbi, "Method for controlling flying height of a magnetic head," U.S. Patent 6,529,342 B1, March 4, 2003.
18. T. R. Albrecht, R. E. Fontana, Jr., P. Kasiraj, E. H. Klaassen, R. N. Payne, and T. C. Reiley, "Flying height adjustment for air bearing sliders," U. S. Patent 6,344,949, Feb. 5, 2002.
19. D. L. Good, J. E. Mason, and H. H. Ottesen, "Fly height servo control of read/write head suspension," U.S. Patent 5,377,058, December 27, 1994.
20. X. Liu, A. Li, W. Clegg, D. F. L. Jenkins, and P. Davey, "Head-disk spacing variation suppression via active flying height control," *IEEE Trans. Instrum. Meas.*, vol. 51, pp. 897-901, 2002.
21. Q. H. Zeng and D. B. Bogy, "Stiffness and damping evaluation of air bearing sliders and new designs with high damping," *ASME J. Tribo.*, vol. 121, pp. 341-347, 1999.
22. B. H. Thornton and D. B. Bogy, "A numerical study of air-bearing slider form-factors," *ASME J. Tribol.*, vol. 126, pp. 553-558, 2004.

23. Z.-E. Boutaghou, W. Qian, M. Olim, A. Sannino, J. Zhu, and C. Serpe, "Disc head slider with subambient pressure cavity bottom surfaces of different depths," U.S. Patent 6,934,122 B2, August 23, 2005.
24. V. Gupta and D. B. Bogy, "Dynamics of sub-5nm air bearing sliders in the presence of electrostatic and intermolecular forces at the head disk interface," *IEEE Trans. Magn.*, vol. 41, pp. 610-615, 2005.
25. P. Bhargava and D. B. Bogy, "Numerical simulation of load/unload in small form factor hard disk drives," Technical Dissertation No. 2005-011, Computer Mechanics Lab., Department of Mechanical Engineering, University of California, Berkeley.
26. Q. H. Zeng and D. B. Bogy, "Slider air bearing designs for load/unload applications," *IEEE Trans. Magn.,* vol. 35, pp. 746-751, 1999.
27. D. B. Bogy and Q. H. Zeng, "Design and operating conditions for reliable load/unload systems," *Tribol. Intl.,* vol. 33, pp. 357-366, 2000.
28. M. Suk and D. Gillis, "Effect of slider burnish on disk damage during dynamic load/unload," *ASME J. Tribol.,* vol. 120, pp. 332-338, 1998.

TABLE 3.1 Challenges of Ultra-low Flying Sliders And Potential Solutions Provided by a Controlled FH Slider

Challenges	Potential Solutions
FH drop due to altitudes	FH adjustment (with a pressure sensor)
FH drop during seek motions	High roll stiffness
Manufacturing tolerance (σ)	FH adjustment
Load/Unload process	- Retract the read/write element while loading/unloading - High roll stiffness and damping
Operational shock	- Retract the read/write element during shocks (with a accelerometer) - High stiffness and damping
FHM and nanoscale adhesion forces (such as electrostatic and intermolecular forces)	- Reduce those forces by reducing the area of central trailing pads - FHM suppression by dynamic feedback control (with a feedback of readback signals)

TABLE 3.2 Comparison of FH Adjustment/Control Sliders [2]-[20]

Principle of Actuation	Actuation Mechanism	Air Bearing Coupling	Authors
Unimorph cantilever	Piezoelectricity	No	Kurita [2],[3]; Suzuki [4], Tagawa [5], Su [6], Juang [7],[8]
	Piezoelectricity	Yes	Yeack-Scranton [9], Juang [10]
Change of Crown/Camber	Piezoelectricity	Yes	Khanna [11], Zhang [12]
	Thermal expansion	Yes	Dietzel [13]
Relative displacement of read/write elements	Thermal expansion	N/A	Meyer [14]
	Thermal expansion	Yes	Juang (Chapter 2)
	Thermal expansion	No	Juang (this Chapter)
	Electrostatic force	N/A	Chen [15]
Forces in HDI	Electrostatic force	Yes	Song [16], Feng [17]
	Change of air flow by ducts and valves	Yes	Albrecht [18]
Suspension bending	Piezoelectricity	Yes	Good [20], Liu [20]

TABLE 3.3 Air Bearing Specifications and Flying Attitudes For Scorpion III

Slider Size (mm): 1.245 ×1.000×0.300
Crown: 9.3 nm
Camber: -2 nm
Suspension Load: 2.0 gf
Disk RPM: 15000

Radial Position (mm)	17.87 (ID)	21	23.88 (MD)	27	29.89 (OD)
Skew (°)	-15.62	-8.197	-2.56	2.768	7.22
Pitch (μrad)	115.79	119.85	121.33	121.40	120.52
Roll (μrad)	0.60	0.31	-0.39	-1.22	-2.09
Gap FH (nm)	9.79	9.95	9.99	10.04	10.12
Minimum FH (nm)	7.34	7.47	7.24	6.99	6.77
Negative Force (gf)	-4.67	-4.73	-4.77	-4.81	-4.85

TABLE 3.4 Air Bearing Specifications and Flying Attitudes For Scorpion IV

Slider Size (mm): 1.245 ×1.000×0.300
Crown: 9.3 nm
Camber: -2 nm
Suspension Load: 2.0 gf
Disk RPM: 15000

Radial Position (mm)	17.87 (ID)	21	23.88 (MD)	27	29.89 (OD)
Skew (°)	-15.62	-8.197	-2.56	2.768	7.22
Pitch (μrad)	103.03	107.64	108.55	107.39	105.16
Roll (μrad)	-2.07	-0.24	-0.32	-1.25	-2.58
Gap FH (nm)	9.77	10.01	10.05	10.13	10.33
Minimum FH (nm)	7.81	8.69	8.70	8.45	8.18
Negative Force (gf)	-2.92	-3.02	-3.09	-3.17	-3.24

TABLE 3.5 Comparison of Air Bearing Stiffness of Various ABS Designs. The data of Scorpion III, IV and Slider A were evaluated at The MD

	Scorpion III	Scorpion IV	Slider A	Multi-Level Cavity [23]	ABS I [22]
Form factor	pico	pico	pico	pico	pico
Gap FH (nm)	9.99	10.05	10.65	10.23	4.80
Pitch (μrad)	121	109	126	230	214
Roll (μrad)	-0.4	-0.3	-1.4	0.5	0.8
k_z (gf/nm)	0.328	0.182	0.239	0.164	0.178
k_p (μN.m/μrad)	1.036	0.517	0.715	0.49	0.537
k_r (μN.m/μrad)	0.403	0.246	0.031	N/A	0.059
Negative force (gf)	-4.8	-3.1	-4.0	-3.9	-3.1

TABLE 3.6 SIMULATIONS OF FHM WITH ACTUAL MEASURED DISK TOPOGRAPHY FOR SCORPION III AND SLIDER A

	Air Bearing Design		
	Scorpion III	Slider A	Scorpion III/Slider A
ID: Peak-to-Peak (nm)	0.35	0.18	194 %
ID: σ (nm)	0.05	0.03	167 %
MD: Peak-to-Peak (nm)	0.12	0.26	46 %
MD: σ (nm)	0.02	0.04	50 %
OD: Peak-to-Peak (nm)	0.18	0.47	38 %
OD: σ (nm)	0.03	0.07	43 %
Max. p-p/min. p-p	292 %	261 %	
Max. σ/min. σ	250 %	233 %	

TABLE 3.7 Simulations of FHM with Actual Measured Disk Topography for Scorpion IV and Slider A

	Air Bearing Design		
	Scorpion IV	Slider A	Scorpion IV/Slider A
ID: Peak-to-Peak (nm)	0.36	0.18	200 %
ID: σ (nm)	0.06	0.03	200 %
MD: Peak-to-Peak (nm)	0.17	0.26	65.38 %
MD: σ (nm)	0.02	0.04	50.00 %
OD: Peak-to-Peak (nm)	0.23	0.47	48.94 %
OD: σ (nm)	0.03	0.07	42.86 %
Max. p-p/min. p-p	212 %	261 %	
Max. σ/min. σ	300 %	233 %	

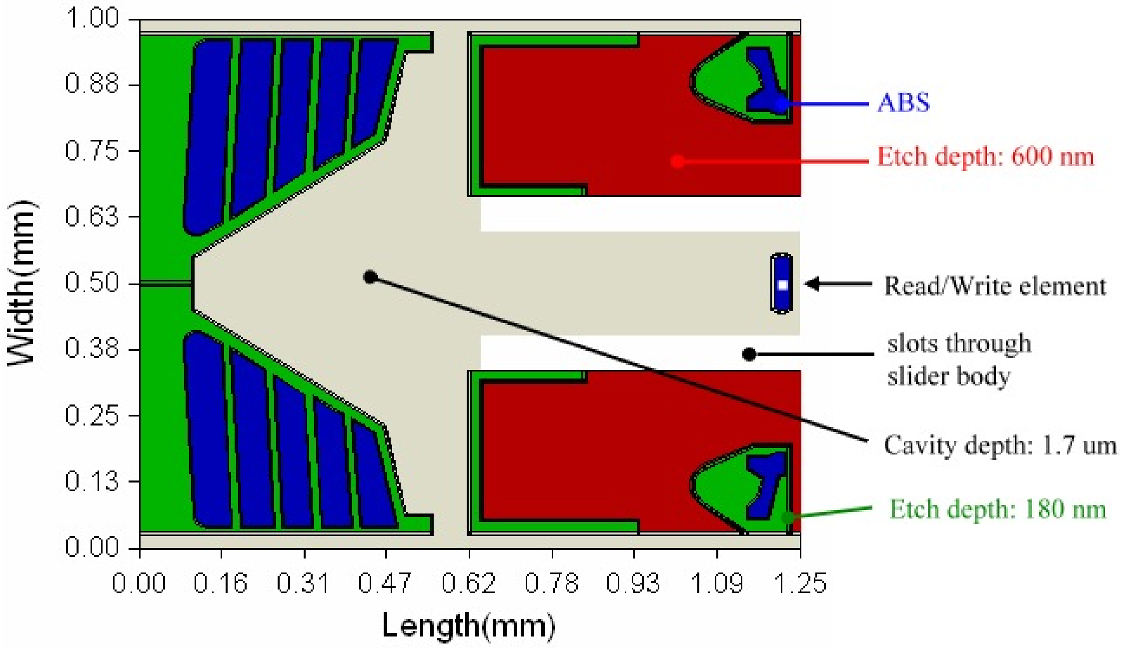

(a)

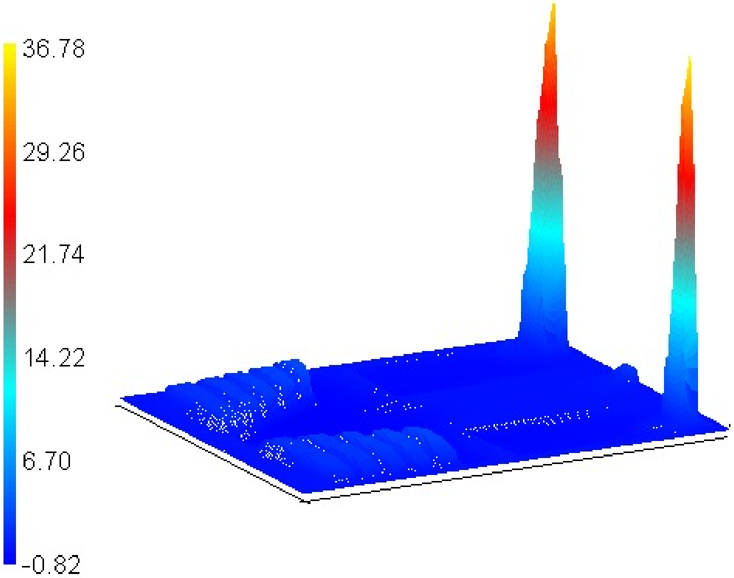

(b)

Fig. 3.1. (a) Air bearing surface design, Scorpion IV; (b) Air bearing pressure profile at the MD (radial position 23.88 mm, skew: -2.56°). The scale displayed is normalized to ambient pressure: $(p - p_a)/p_a$.

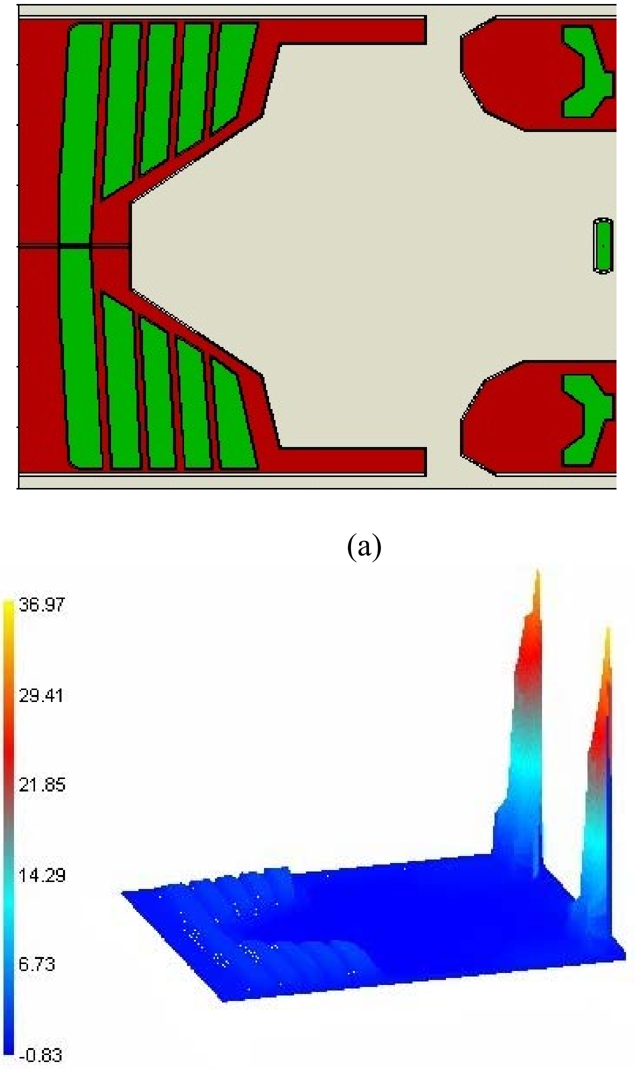

(a)

(b)

Fig. 3.2. (a) Air bearing surface design, Scorpion III; (b) Air bearing pressure profile at the MD (radial position 23.88 mm, skew: -2.56°). The scale displayed is normalized to ambient pressure: $(p - p_a)/p_a$.

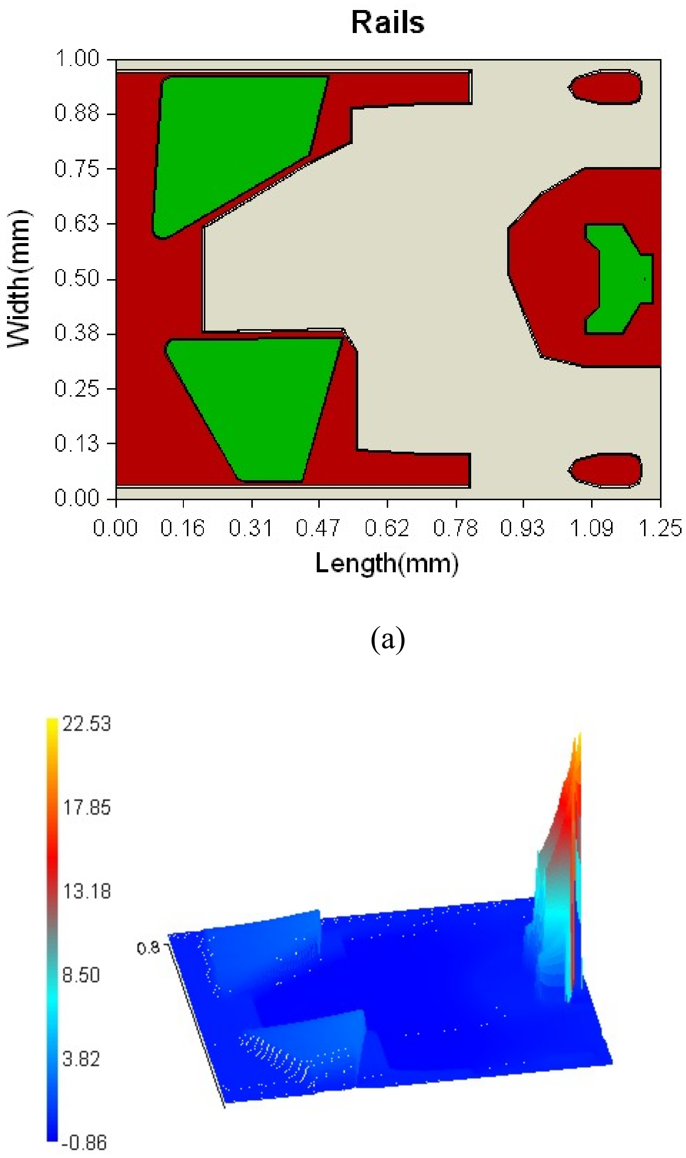

(a)

(b)

Fig. 3.3. (a) A conventional pico-slider ABS, Slider A, used for comparison; (b) Air bearing pressure profile at radial position 23.88 mm. The scale displayed is normalized to ambient pressure: $(p - p_a)/p_a$.

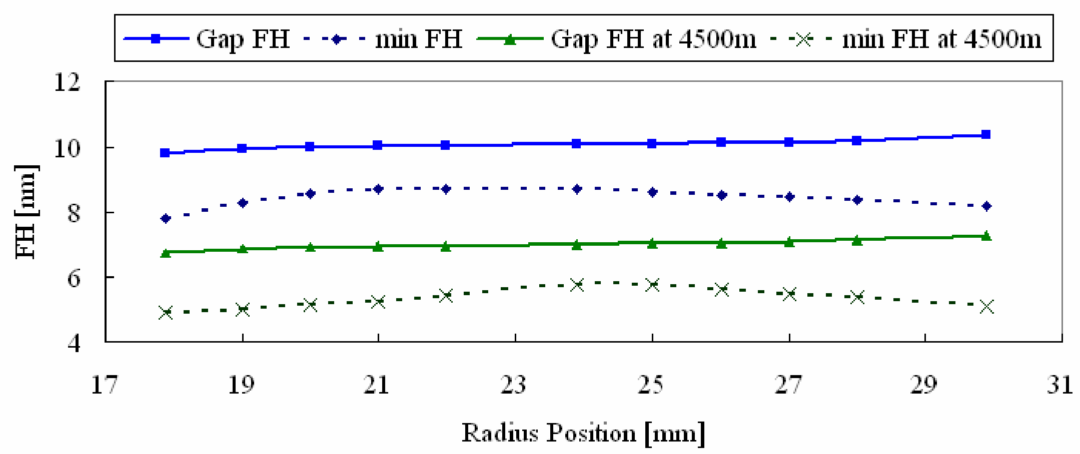

Fig. 3.4. Simulation of gap FH and minimum FH profiles of Scorpion IV at sea level, 0 m, and high altitude, 4500 m.

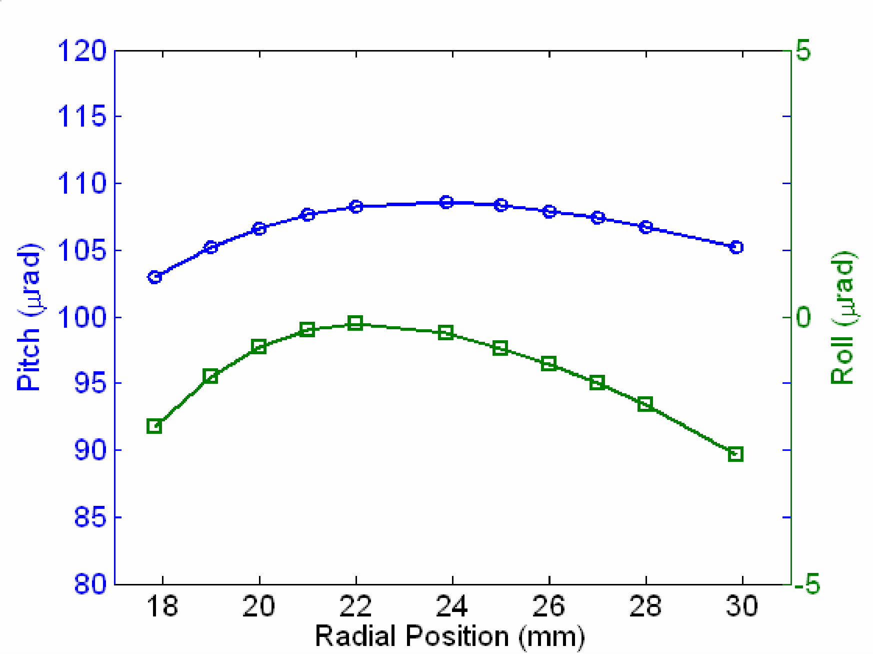

Fig. 3.5. Simulation of pitch and roll profiles of Scorpion IV at sea level, 0 m.

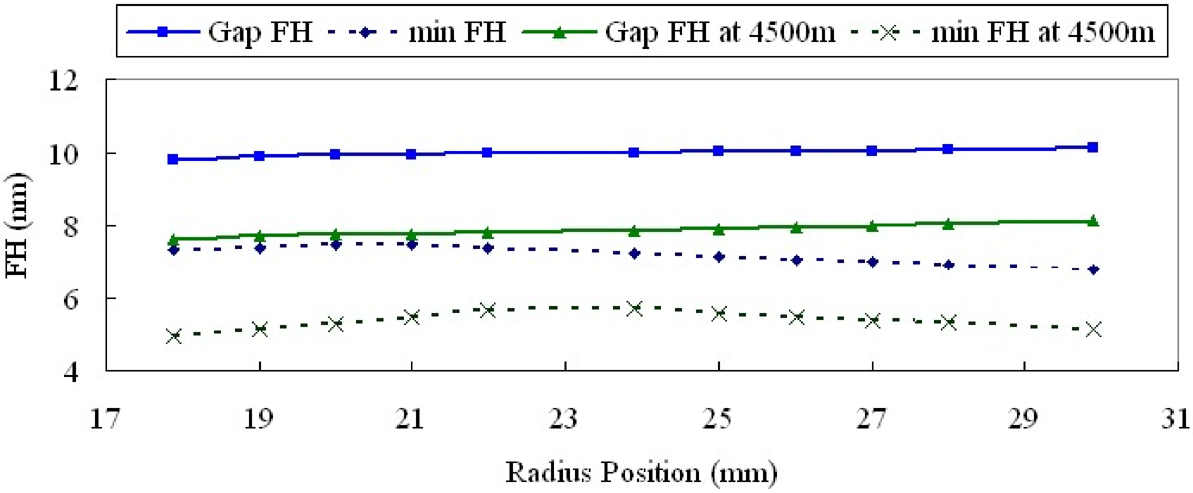

Fig. 3.6. Simulation of gap FH and minimum FH profiles of Scorpion III at sea level, 0 m, and high altitude, 4500 m.

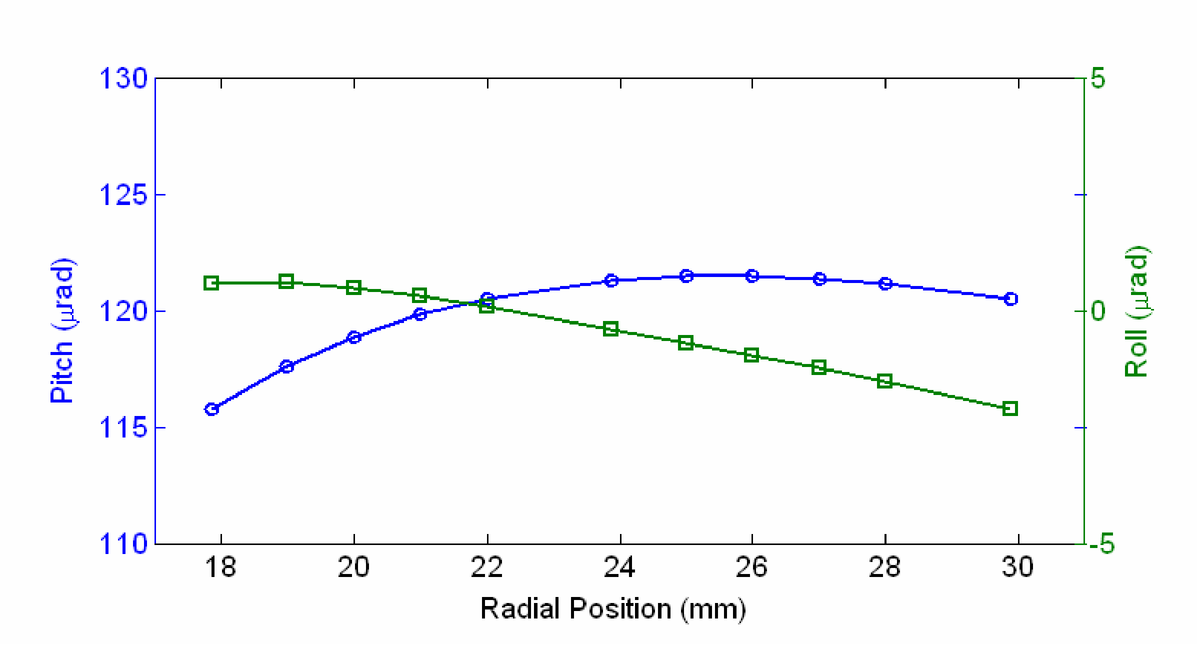

Fig. 3.7. Simulation of pitch and roll profiles of Scorpion III at sea level, 0 m.

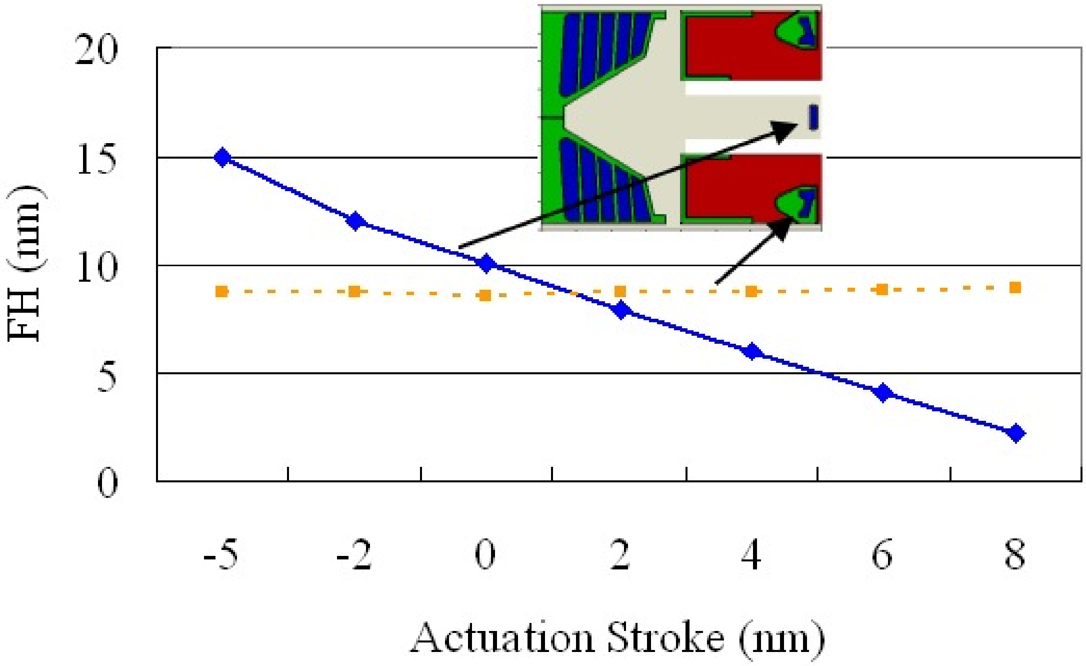

Fig. 3.8. Simulated FHs at the read/write transducer and one point on one of the side ABS rails. The radial position is at the MD.

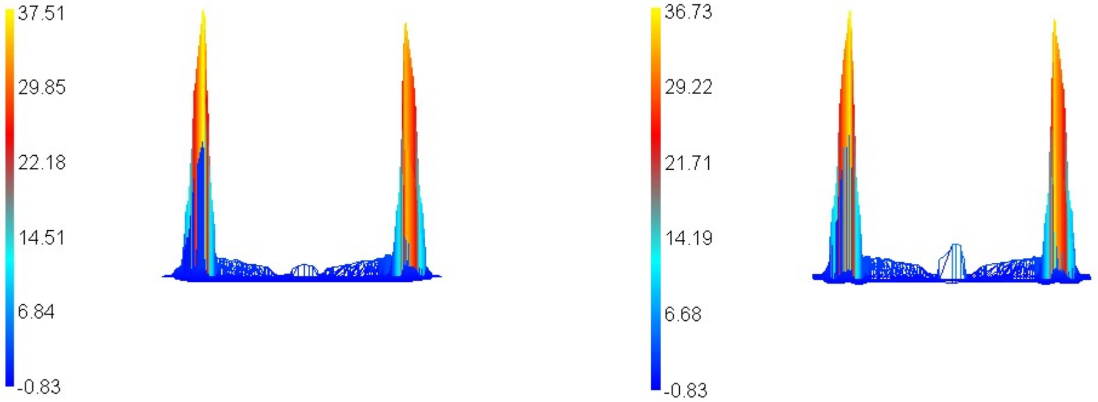

(a)

(b)

Fig. 3.9. Air pressure distributions before (a) and after (b) a 8-nm actuation stroke.

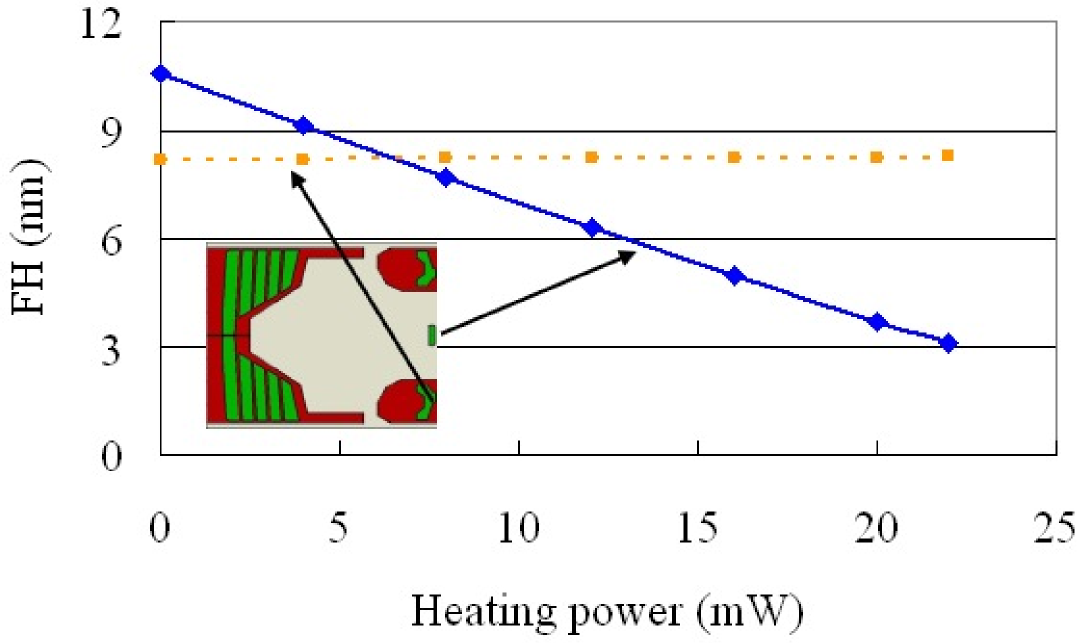

Fig. 3.10. Simulated FHs at the read/write transducer and one point on one of the side ABS rails. The radial position is at the MD.

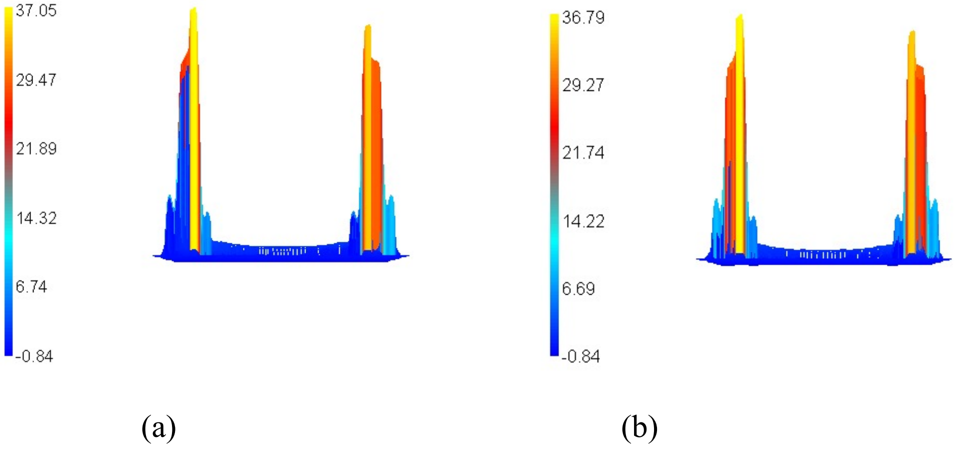

Fig. 3.11. Air pressure distributions before (a) and after (b) a 7.5-nm actuation stroke.

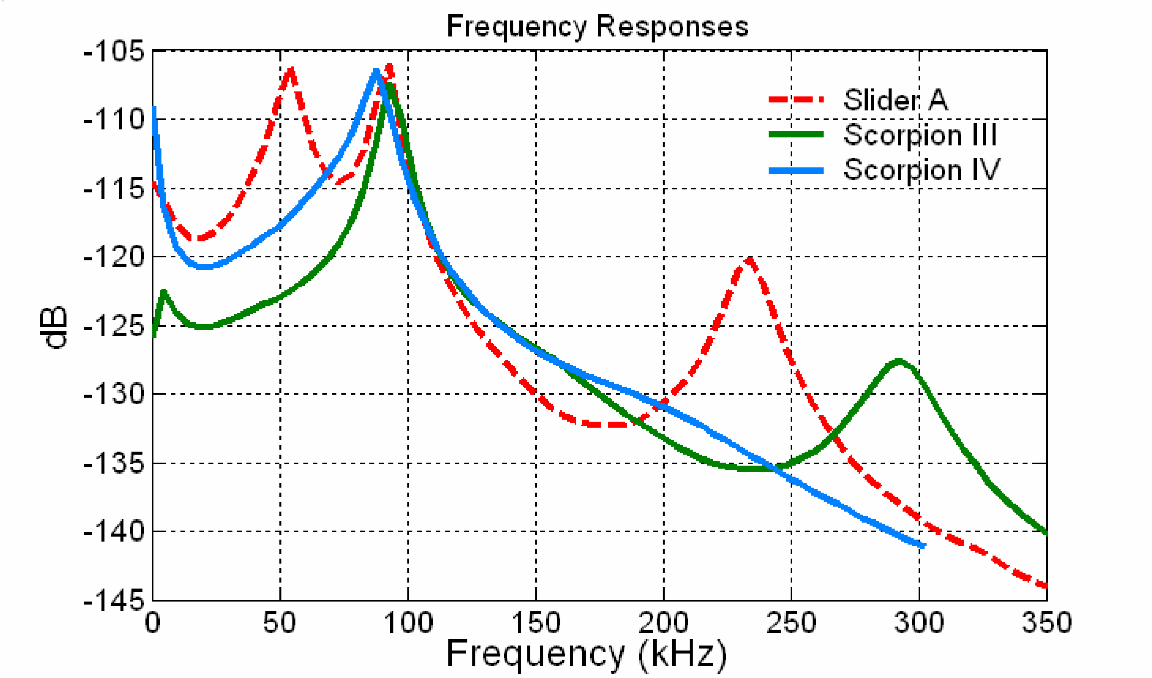

Fig. 3.12. Frequency responses of the air bearings of Scorpion III, IV and Slider A.

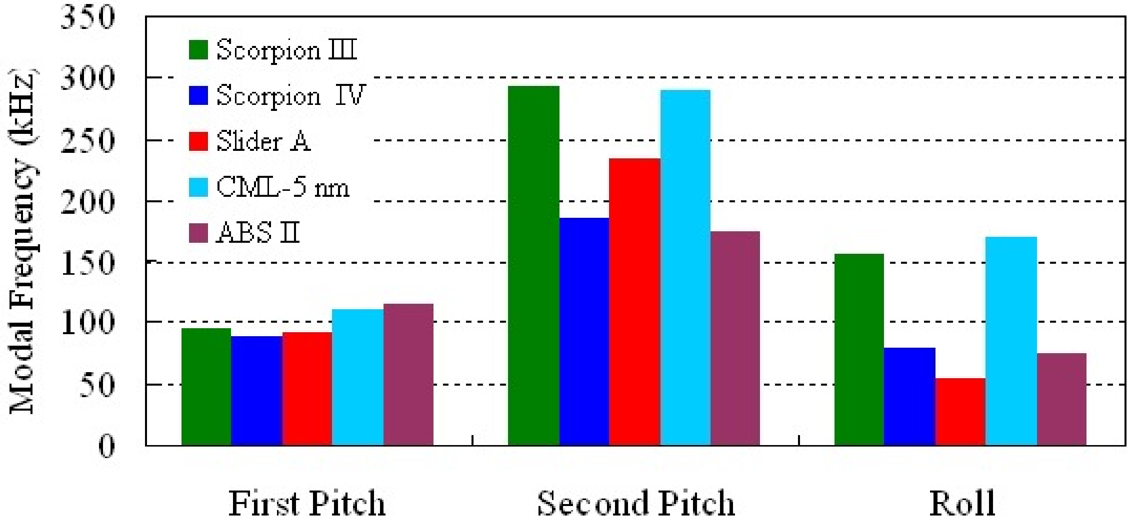

(a)

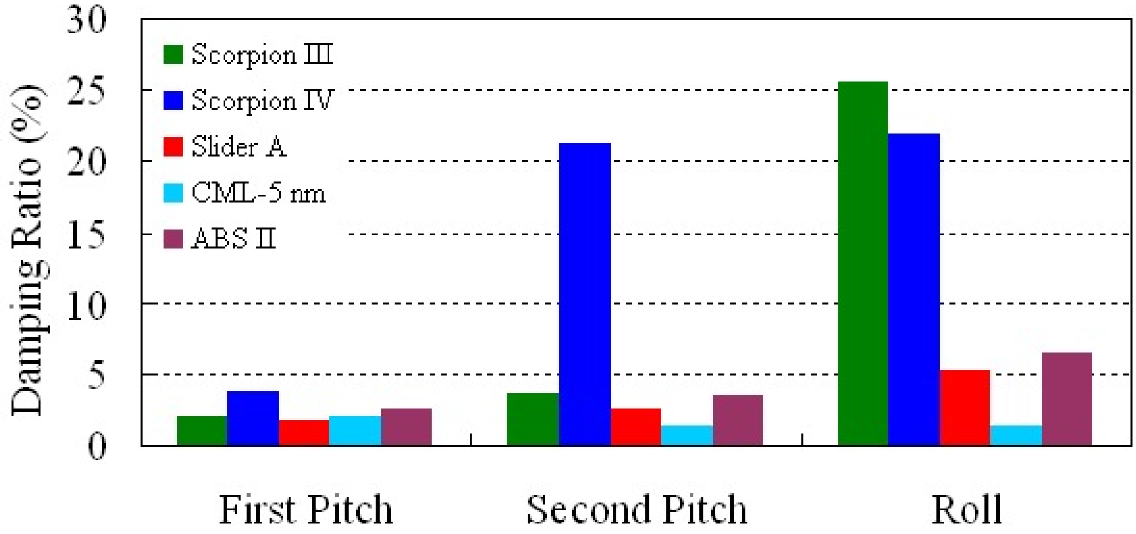

(b)

Fig. 3.13. Comparison of modal frequencies and damping ratios of various ABS designs. The data of Scorpion III, IV and Slider A were evaluated at the MD. The data of ABS I and ABS II were obtained from [24].

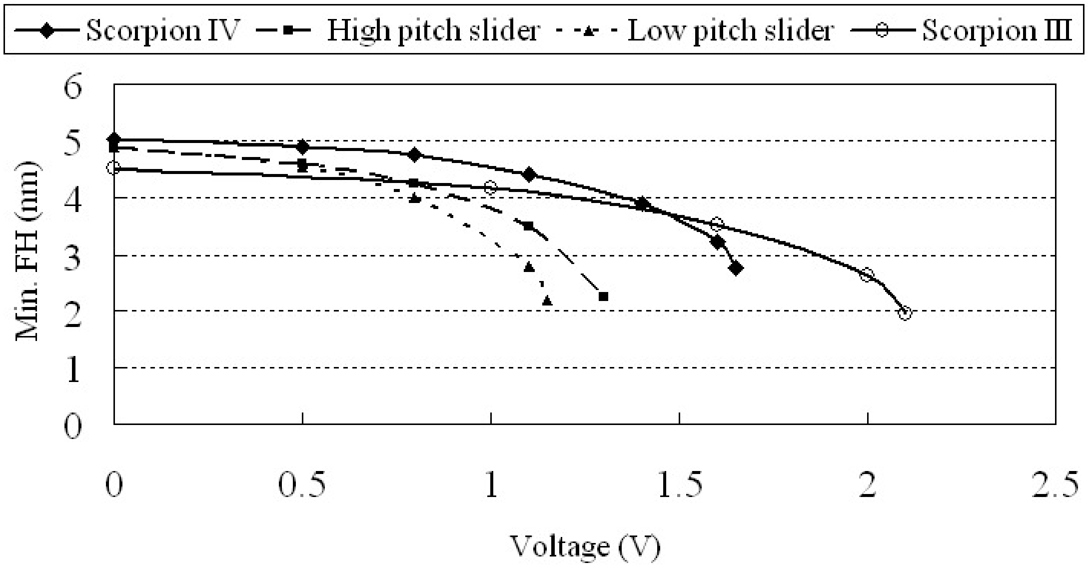

Fig. 3.14. The drop of minimum FH caused by the electrostatic potential across the HDI. The actuation stroke of Scorpion III and IV is 4 nm. The pitches of Scorpion III and IV are 123 and 108 μrad, respectively, at zero voltage. The results of the high-pitch slider (245 μrad) and low-pitch slider (190 μrad) are from [26].

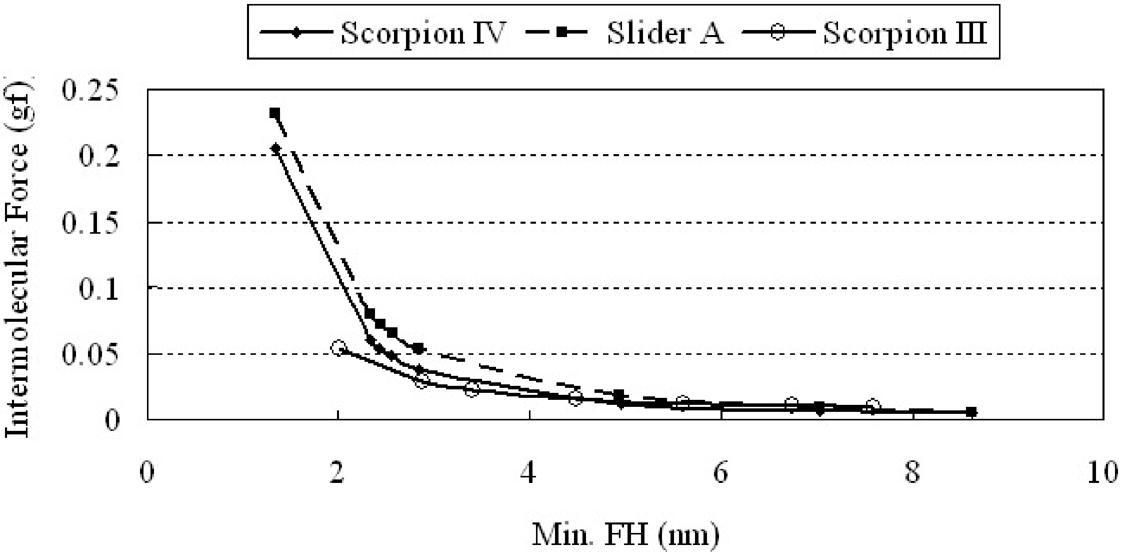

Fig. 3.15. Comparison of magnitudes of intermolecular adhesion forces of Scorpion III, IV and Slider A as functions of minimum FH. The FH of Scorpion IV was reduced by actuating the central trailing pad toward the disk and the obtained flying attitudes (min. FH, pitch, and roll) were then used to calculate the intermolecular forces of Slider A.

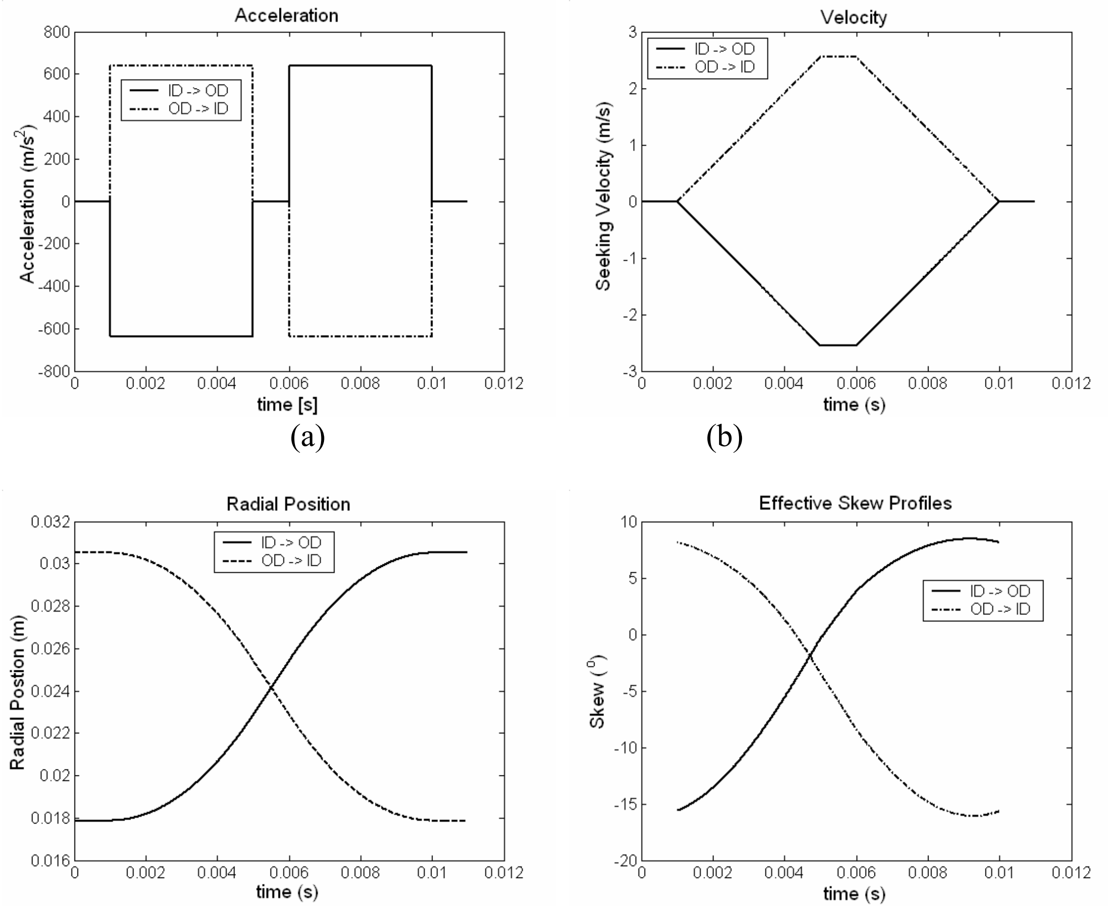

(a) (b)

(c) (d)

Fig. 3.16. Track-seeking profiles. The maximum acceleration is 65 G.

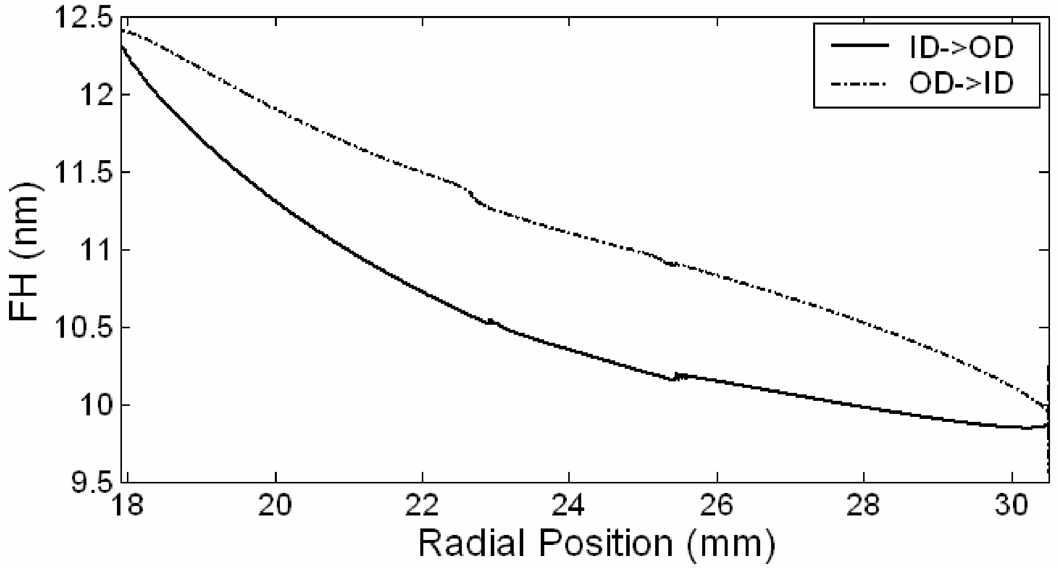
12.5
12
11.5
11
10.5
10
9.5
FH (nm)
18
20
22
24
26
28
30
Radial Position (mm)
ID->OD
OD->ID

(a)

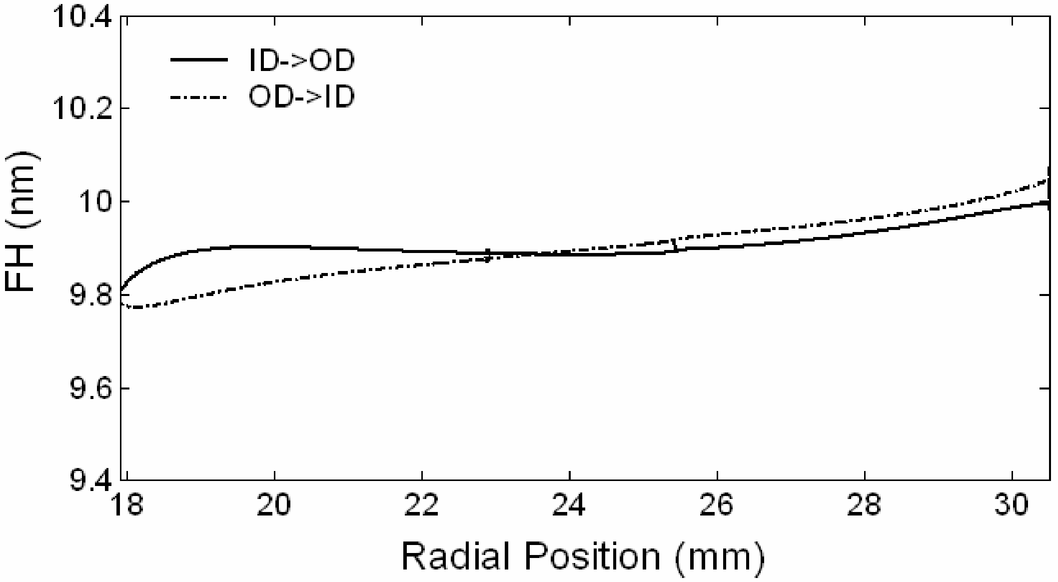
10.4
10.2
10
9.8
9.6
9.4
FH (nm)
18
20
22
24
26
28
30
Radial Position (mm)
ID->OD
OD->ID

(b)

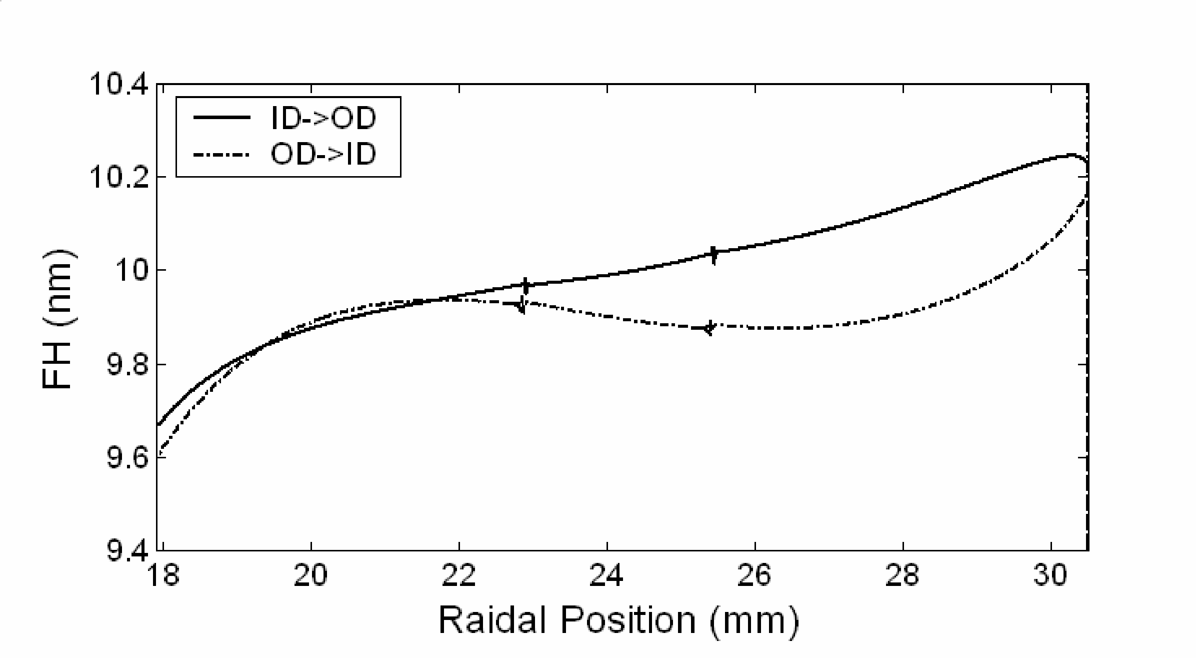

(c)

Fig. 3.17. Gap FH changes due to the seek motion for (a) Slider A (with a maximum difference of ~0.75 nm near the MD); (b) Scorpion III (with a maximum difference of ~0.1 nm near the ID); (c) Scorpion IV (with a maximum difference of ~0.2 nm near the OD).

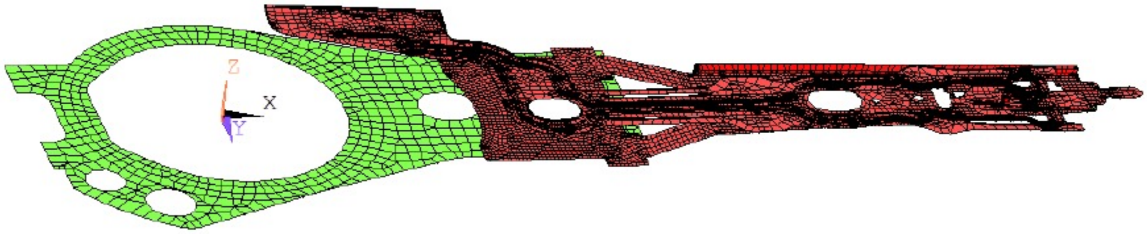

Fig. 3.18. Suspension model used in the dynamic load/unload simulation [27].

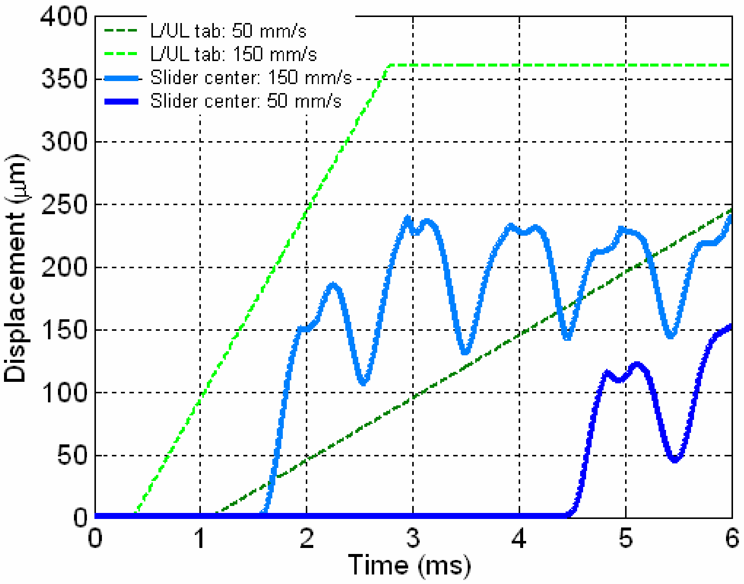

(a)

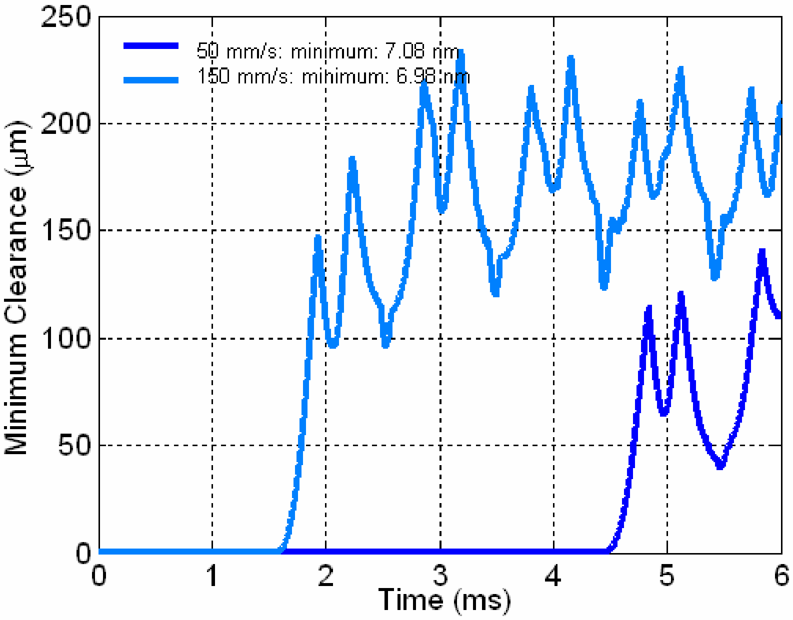

(b)

Fig. 3.19. Comparison of the displacement and minimum clearance histories of Scorpion III during the unloading processes with two unloading velocities, 50 mm/s and 150 mm/s, at the OD (7.22° skew) and 15000 rpm.

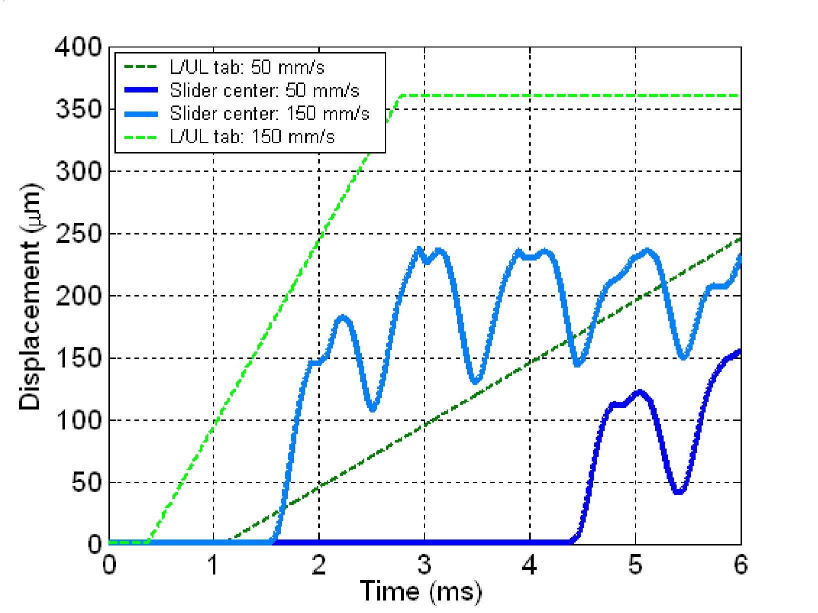

(a)

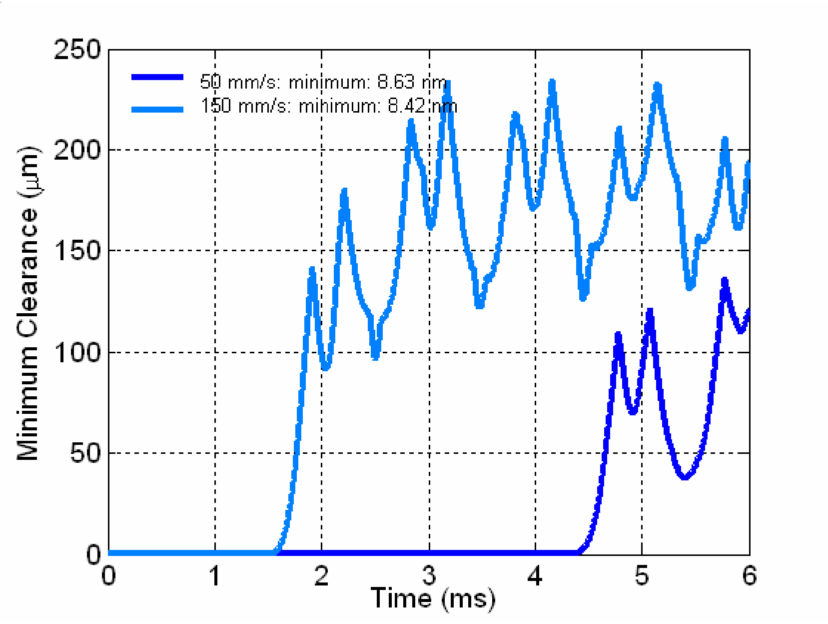

(b)

Fig. 3.20. Comparison of the displacement and minimum clearance histories of Scorpion IV during the unloading processes with two unloading velocities, 50 mm/s and 150 mm/s, at the OD (7.22° skew) and 15000 rpm.

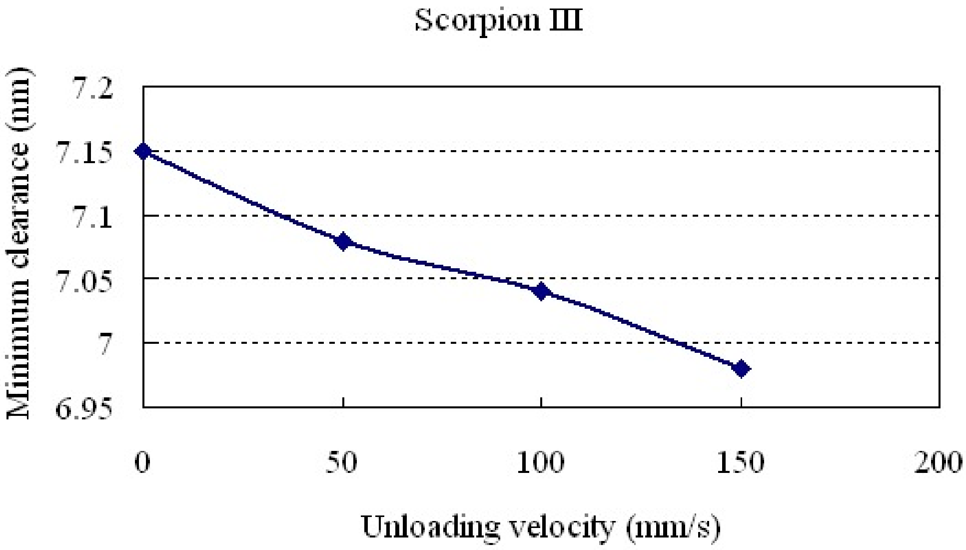

Fig. 3.21. The minimum clearances of Scorpion III during the unloading process as a function of unloading velocity.

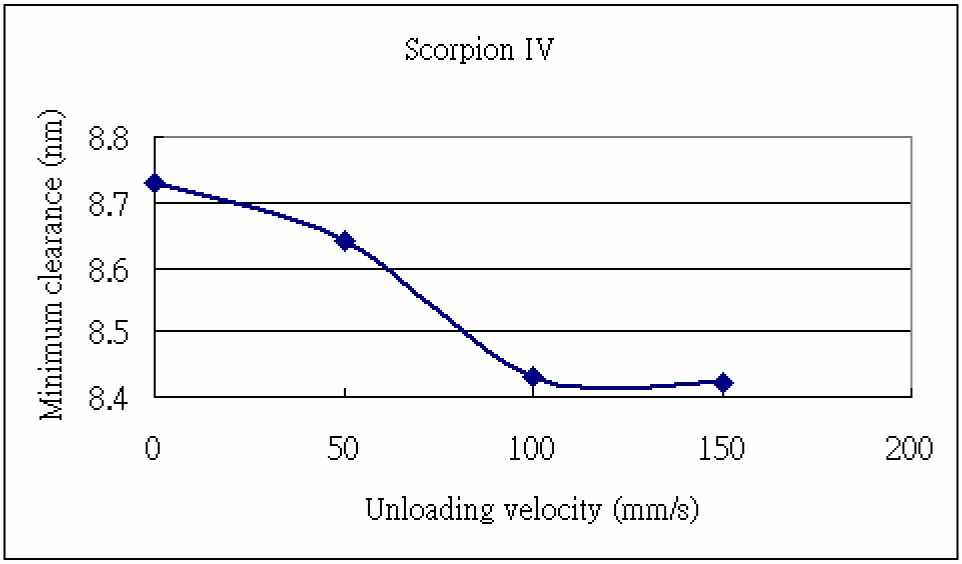

Fig. 3.22. The minimum clearances of Scorpion Iv during the unloading process as a function of unloading velocity.

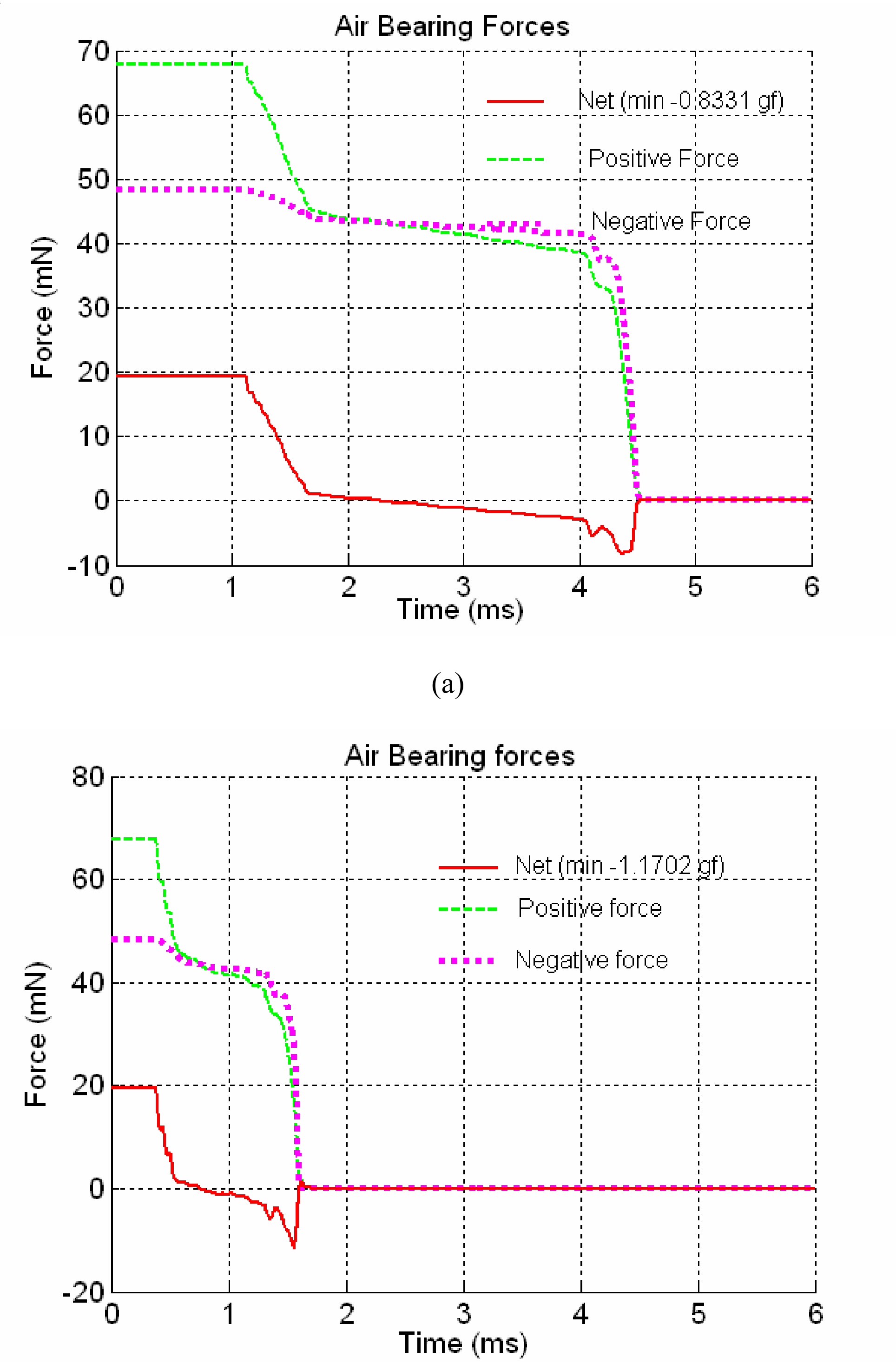

(a)

(b)

Fig. 3.23. Air bearing force histories of Scorpion III during unloading processes at the OD. (a) unloading velocity: 50 mm/s; (b) 150 mm/s.

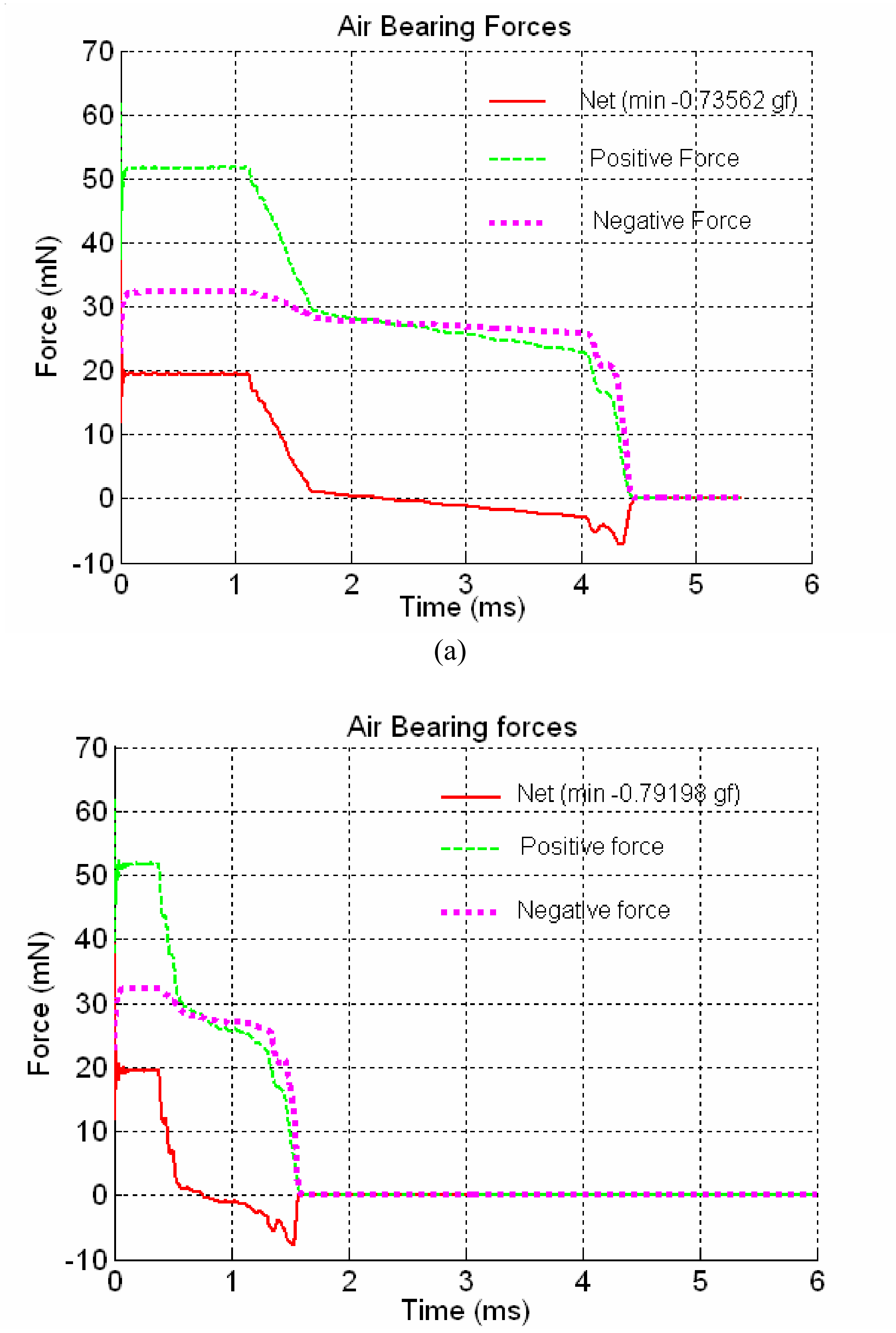

(a)

(b)

Fig. 3.24. Air bearing force histories of Scorpion IV during unloading processes at the OD. (a) unloading velocity: 50 mm/s; (b) 150 mm/s.

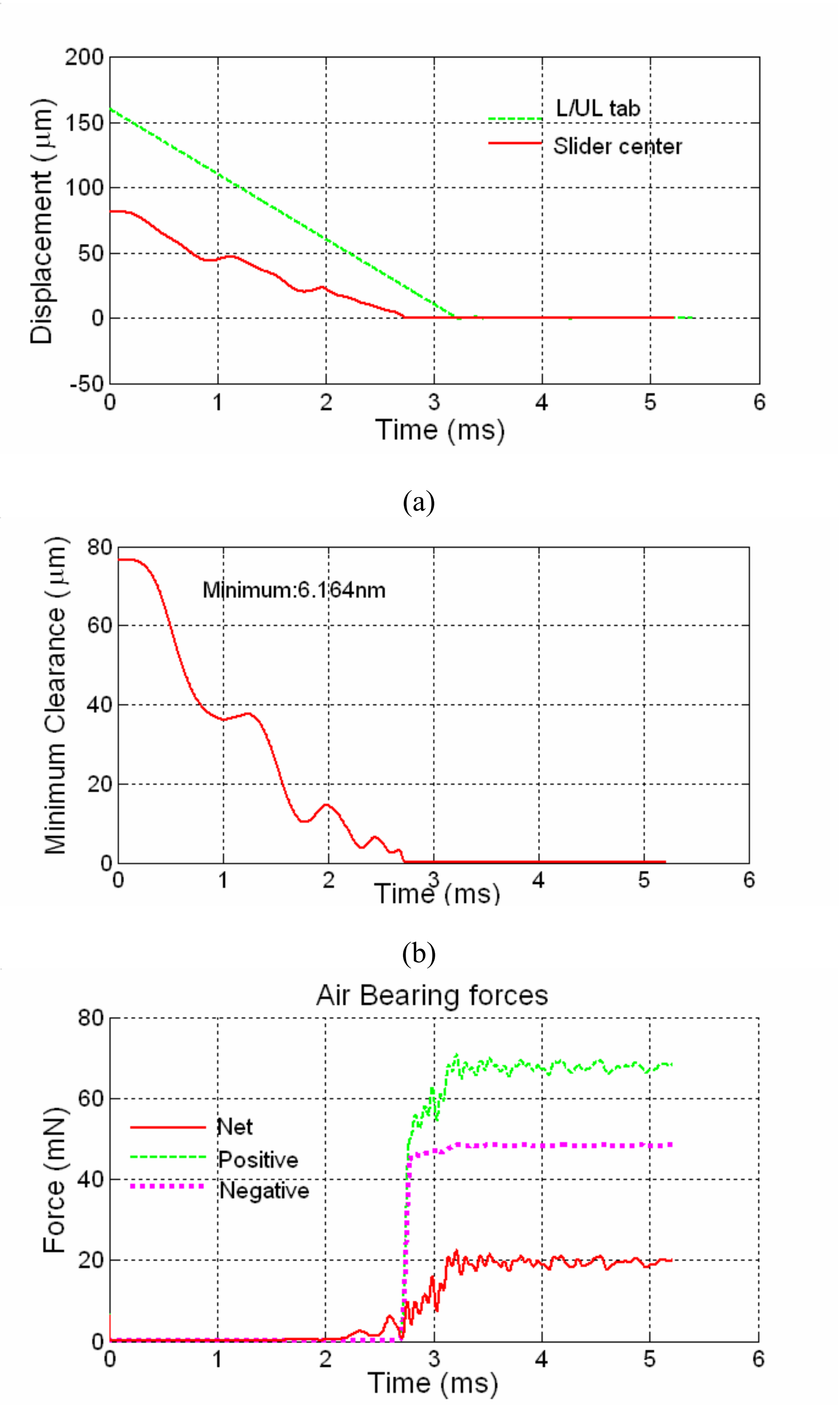

(a)

(b)

(c)

Fig. 3.25. Displacement, minimum clearance and force histories of Scorpion III during loading at the OD with 50 mm/s loading velocity and 15000 rpm disk velocity.

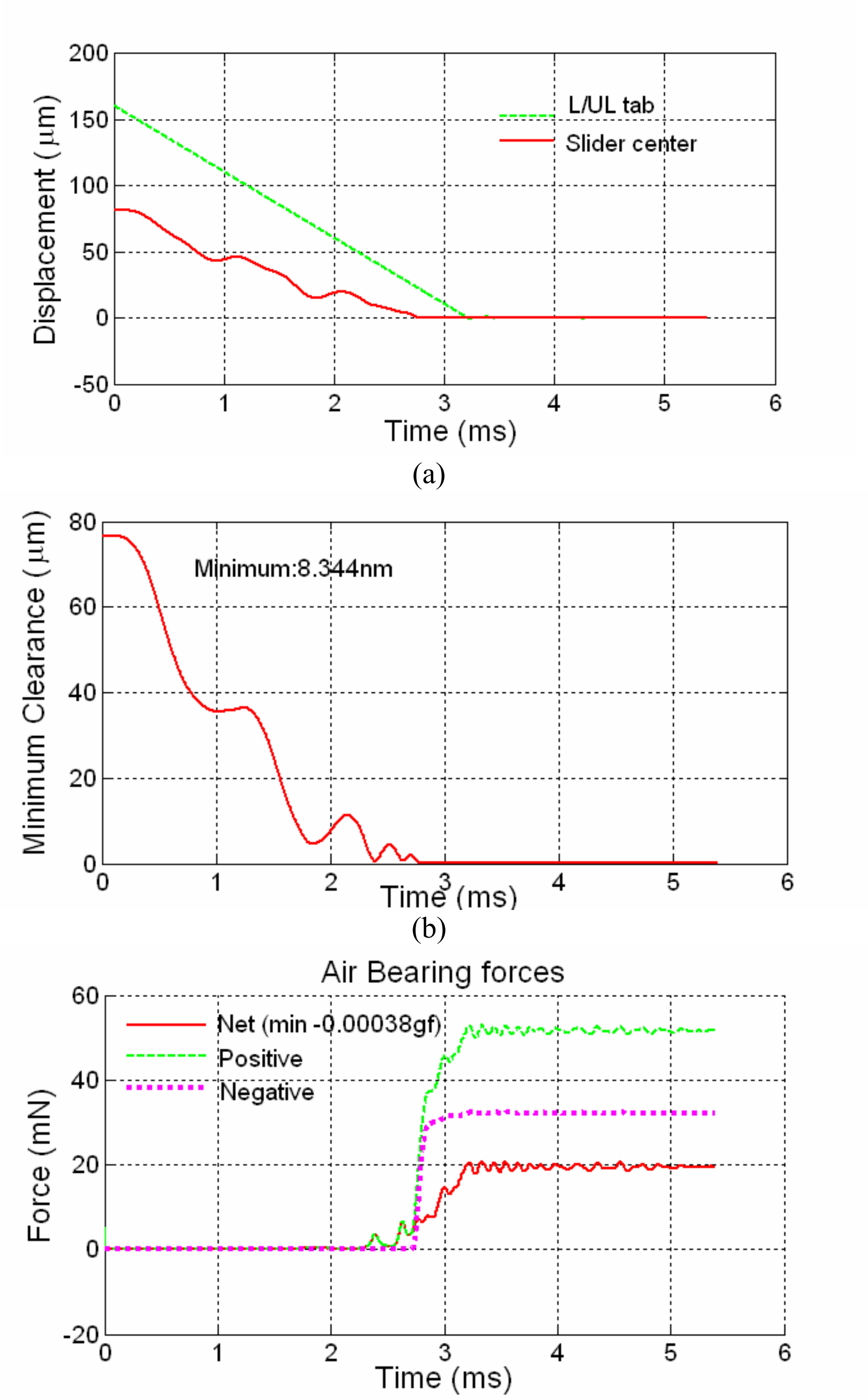

(a)

(b)

(c)

Fig. 3.26. Displacement, minimum clearance and force histories of Scorpion IV during loading at the OD with 50 mm/s loading velocity and 15000 rpm disk velocity.

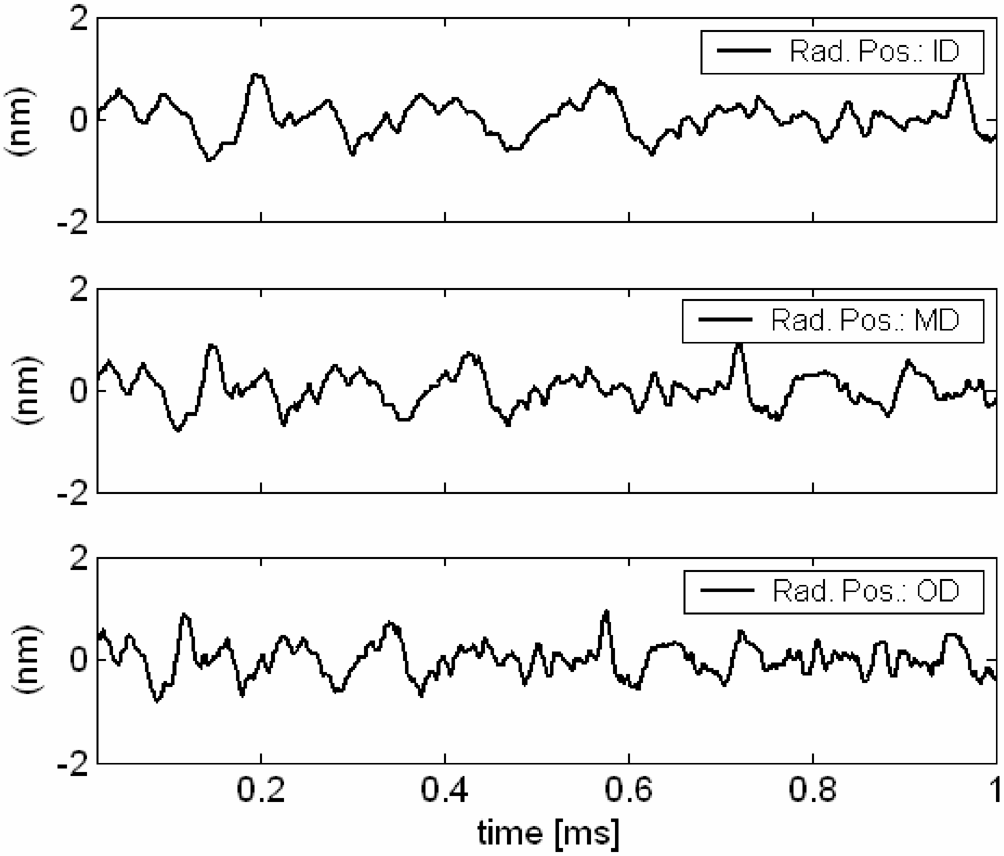

Fig. 3.27. Measured disk morphology used in the simulation at three radial positions, ID, MD, and OD. The peak-to-peak and standard deviation of the disk roughness are 1.76 nm and 0.31 nm, respectively.

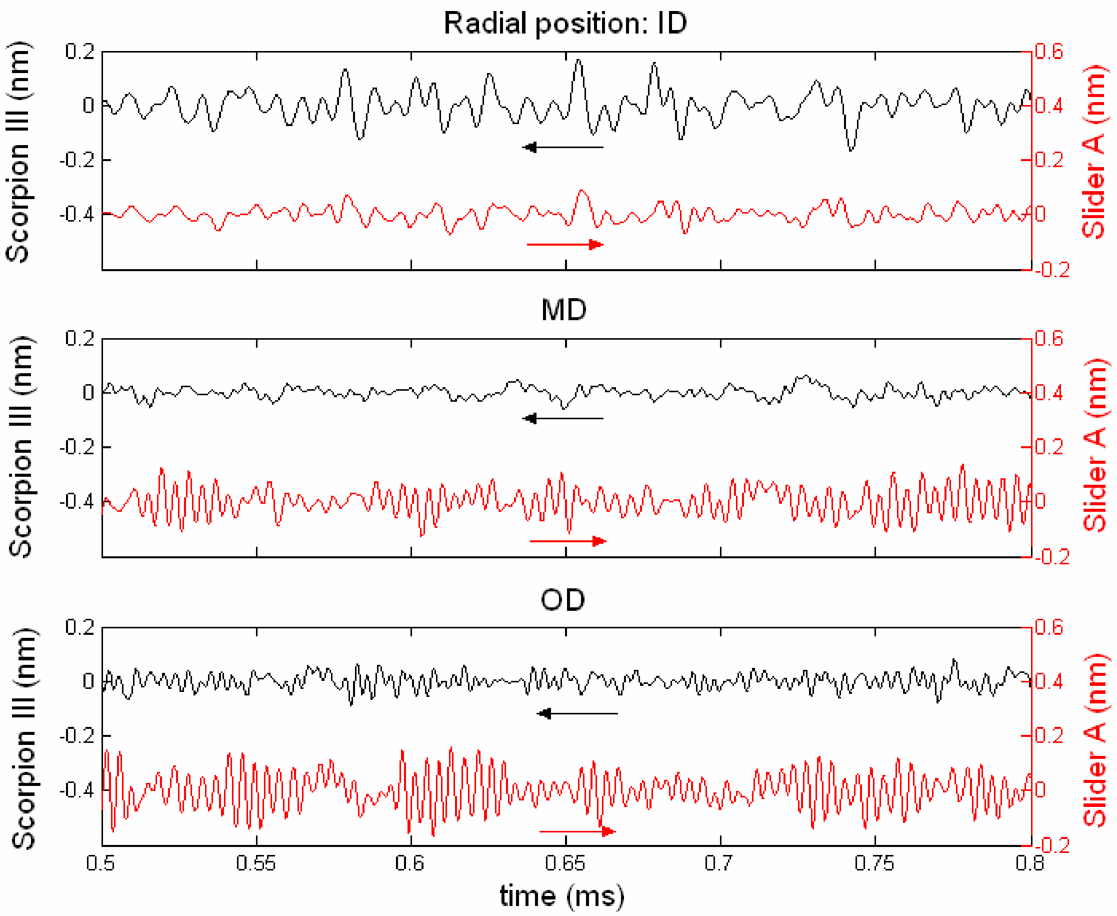

Fig. 3.28. Comparison of FHMs of Scorpion III and Slider A at three radial positions, ID, MD, and OD with skews -15.62°, -2.56°, and 7.22°, respectively.

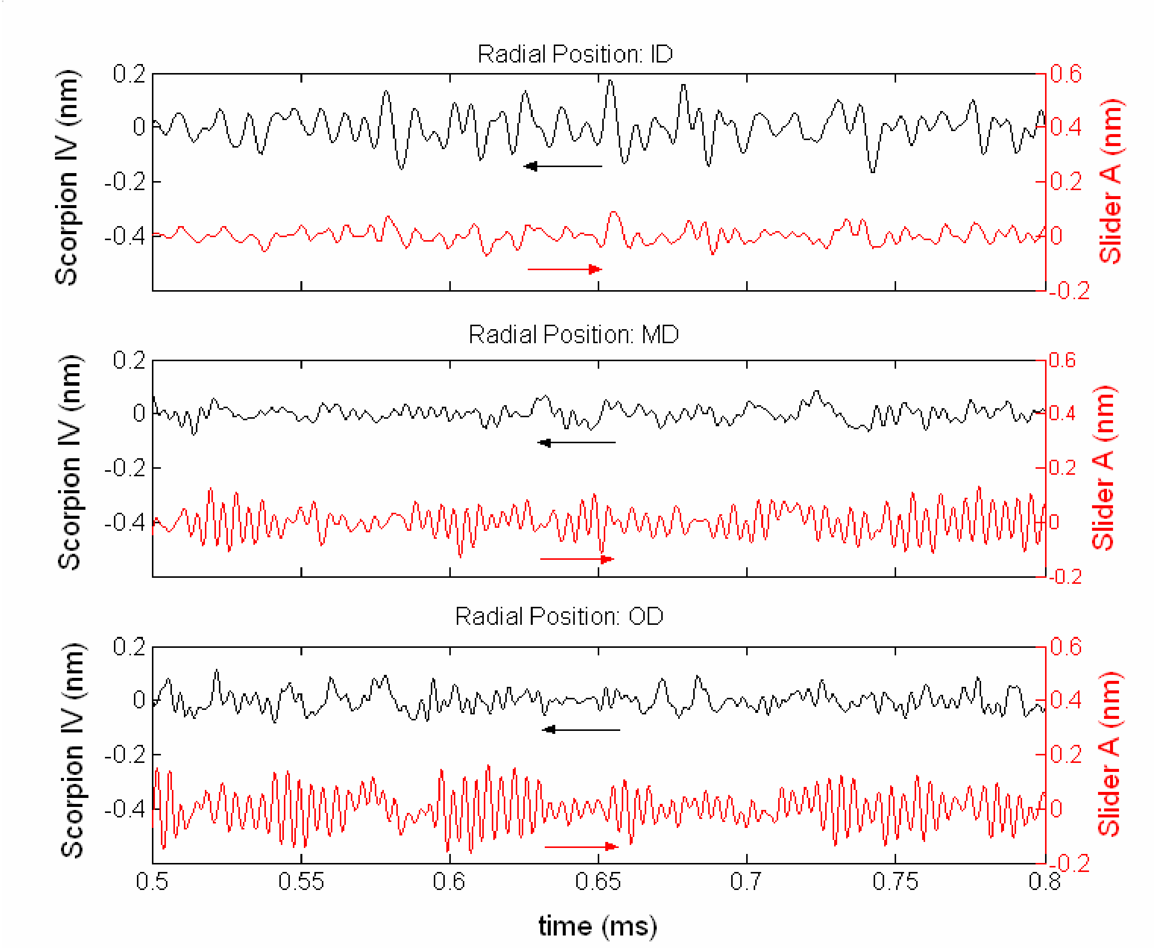

Fig. 3.29. Comparison of FHMs of Scorpion IV and Slider A at three radial positions, ID, MD, and OD with skews -15.62°, -2.56°, and 7.22°, respectively.

CHAPTER 4

FABRICATION AND EXPERIMENTAL STUDY OF FLYING AND CONTACT DYNAMICS OF AN AL_2O_3-TIC SLIDER WITH A PIEZOELECTRIC NANOACTUATOR

In this chapter we report on the design and fabrication of Al_2O_3-TiC sliders with a special ABS design and piezoelectric actuator for achieving high actuation efficiency. We demonstrate an inexpensive and low-temperature approach for integrating piezoelectric materials in the fabrication of current Al_2O_3-TiC sliders. A bulk PZT sheet is bonded onto the back of row-bars, and the sliders are separated by a standard dicing process. The process requires no deep reactive-ion etching (DRIE) or high temperature processes and is suitable for mass production. The fabricated prototype sliders have been tested experimentally. The measured nonflying actuated stroke exhibits a linear relationship with the applied voltage with a rate of ~ 0.8 nm/V. The FHs of two different sliders, designed for the actuated center pad and actuated side pads schemes, were successfully reduced from 15.5 nm and 8.5 nm to contact with applied voltages of 20 V and 10 V, respectively, which demonstrates high actuation efficiency. The AE measurements show clear spikes when the center pad is brought into contact with the disk by the actuator. The pattern of the AE signals during contact is different from the one observed in conventional sliders during “touchdown-takeoff tests” where there is a pronounced increase in the AE amplitude upon contact. This difference is attributed to the sustained air bearing even when the intermittent contacts occur in the head-disk interface. It is also found that the dominant air bearing mode shifts from the first pitch to the second pitch as a result of the intermittent contacts. In addition, a track of considerable lube depletion and carbon wear was observed after the contact tests.

4.1 Introduction

As the spacing between the slider and the disk decreases in hard disk drives the linear bit spacing of the magnetic recording can decrease, resulting in a higher areal density. A gap flying height of less than 5 nm between the read/write element and the surface of the disk is required for the next generation of magnetic recording. A stable and constant FH must also be sustained in the presence of altitude and temperature changes, manufacturing tolerance, and track-seeking motion. Furthermore, the dynamic instability caused by FH modulations (FHMs) and nanoscale adhesion forces, such as electrostatic and intermolecular forces, should be minimized. Those challenges make a conventional air bearing surface (ABS) slider an unlikely choice for an areal density of 1 Tbit/in^2. One potential solution is a FH adjustment or control slider that is capable of adjusting its gap FH with sub-nanometer resolution.

Due to its quick response and low power consumption piezoelectric materials have been proposed as active elements for adjusting the FH. Yeack-Scranton *et al.* [1] proposed an active slider for contact recording, where a piezoelectric material was inserted in a channel that ran across the full width of the slider at its top rear. They experimentally demonstrated movement of the read/write element from ~ 200 nm to contact, but the proposed structure of piezoelectric actuator is difficult to implement in the smaller currently used pico- or femto-sized sliders. Another approach is to bond a layer of piezoelectric material to one side of the suspension and change the FH by bending the suspension [2], [3]. The bandwidth of actuation is limited by that of the suspension dynamics, which is much lower than that of the air bearing. Khanna *et al.* [4] in 1991 and then Zhang *et al.* [5] in 2005 reported a method of FH adjustment by bonding a bulk piezoelectric material on the backside of a slider body. The FH was adjusted by applying a voltage to the piezoelectric material and thereby changing the crown and/or camber of the slider body. The structure of such sliders is simpler and it is relatively easy to fabricate, but the fact that the FH is adjusted by changing the crown and/or camber contradicts the ABS design rule of reducing sensitivity of flying attitudes to these two parameters. Another approach is to utilize piezoelectrically actuated unimorph cantilever sliders. Several papers, such as Kurita *et al.* [6], [7], Tagawa *et al.* [8], Suzuki *et al.* [9], and Su *et al.* [10], have presented active sliders made of silicon with piezoelectric unimorph cantilevers. The slider structure was simple and could be fabricated by silicon microfabrication technology. However, the use of silicon as the slider material and the requirement of high temperature processes make it difficult to integrate with current fabrication technology. Juang *et al.* [11] developed a low-temperature and inexpensive process for fabricating and integrating Al_2O_3-TiC sliders with piezoelectric nanoactuators using a conventional ABS. They found that the actuation efficiency was only 7 % due to the strong counter effect of the air bearing.

In this chapter we propose an approach for integrating piezoelectric materials in the fabrication of current Al_2O_3-TiC sliders and conduct numerical and experimental analyses to investigate their performance. We designed and fabricated Al_2O_3-TiC sliders with a special ABS for achieving high actuation efficiency. Experiments using a Zygo optical profiler, dynamic FH tester (DFHT), acoustic emission sensor (AE), laser Doppler vibrometer (LDV) and optical surface analyzer (OSA) were carried out to study the actuation and flying performance as well as the slider dynamics when the center pad is actuated to contact the disk.

4.2 Fabrication

A schematic diagram of the controlled-FH slider with an unimorph piezoelectric nanoactuator is shown in Fig. 4.1. The slider carries a layer of piezoelectric material, which is located between the slider body and the suspension flexure. The two slits near the trailing edge are created to form a cantilever. The piezoelectric layer is separated into three parts by a dicing process. The read/write element is located on the air bearing surface near the end of the cantilever. There are two operational schemes: actuated center-pad and actuated side-pads. For the actuated center-pad scheme an electric voltage is applied to the middle portion of the piezoelectric material and the cantilever bends down or up depending on the polarity of the induced electric field, resulting in a decrease or increase of the gap FH. For the actuated side-pads scheme an electrical voltage is applied to the piezoelectric layers on the two sides and the FH is reduced when the two side-pads are bent up, causing a relative downward displacement of the center pad with respect to the ABS. According to the sign convention in this study a positive stroke is the one that reduces the FH and vice versa.

Fig. 4.2 illustrates the fabrication process of Al_2O_3-TiC sliders with piezoelectric actuators. The process starts from dicing wafers into quads and cutting them into row-bars, followed by lapping of the row-bars to the desired slider thickness. The ABS is then defined and etched by photolithography and dry-etch processes such as ion-milling and reactive-ion etching. A thin layer of diamond-like carbon (DLC) is deposited on the entire ABS to protect the read/write element from corrosion and wear. The row-bars are then bonded with 127-μm thick commercially available lead-zirconate-titanate (PZT) sheets (Piezo Systems, Inc.) by silver epoxy (Transene Company, Inc.). Thin vacuum sputtered nickel electrodes have been deposited on both surfaces of the PZT sheets to produce extremely low current leakage and low magnetic permeability. A standard dicing process is used to separate the PZT and to cut the row-bars into individual sliders. Since there are no deep reactive-ion etching or high temperature processes involved the cost introduced by these additional steps can be kept at a minimum, and the previously deposited read/write element will not be damaged. The sliders are then mounted onto suspensions by the use of conductive and nonconductive glues to complete the head-gimbal assembly (HGA). The electrodes on the suspension flexure for read/write heads are used to apply voltages to the actuator. Two prototypes, Slider #1 and Slider #2 were assembled and studied for the actuated center pad and side-pads scheme, respectively. Examples of a fabricated Al_2O_3-TiC slider with a layer of PZT and a completed HGA are shown in Fig. 4.3 and Fig. 4.4, respectively.

4.3 Experiments

An ABS design named Scorpion is used in this study. As illustrated in Fig. 4.5(a) it has four levels of etching steps and was designed for piezoelectric sliders with high air bearing stiffness and damping [12]. The targeted gap FH (without actuation) is 12 nm at a disk velocity of 15000 rpm. Fig. 4.5(b) shows the pressure distribution of the Scorpion

ABS. Instead of being supported by a center pressure peak the slider is primarily supported by the high pressures generated at the side trailing pads, which significantly increases the actuation efficiency. The two white rectangles are slits that run through the entire slider thickness and have dimensions of 65×600 μm.

These tests were conducted on a Candela OSA spin-stand with a dual-channel LDV for monitoring slider dynamics and an AE sensor for detecting contact. One channel of the LDV was focused on the slider backside and measured the slider's velocity in the Z-direction. This was integrated to obtain the slider's displacement over time. To capture the repeatable part of the slider displacements the second channel of the LDV was used as a trigger to the data acquisition system, which averaged the slider velocity channel accurately over 300 disk revolutions. The trigger was obtained from a scratch on the disk edge, which gives a very accurate trigger [13]. Three measurements of slider displacements were taken corresponding to each voltage, which was varied from 0V to 60V in steps on 10V.

A smooth disk (rms 0.2 nm) with 12 Å Zdol 4000 lube was used for conducting the tests. After each voltage cycle of 0V-60V-0V, the disk was monitored for lubricant depletion.

4.4 Results and Discussions

4.4.1 Nonflying Stroke

The unimorph actuator, composed of a piece of piezoelectric material and a portion of the slider, deflects under an electric voltage *V* and an external vertical force *F* exerted on the tip. The constitutive equation of the tip deflection subject to a voltage and a force can be described as follows [14]:

$$\delta = aF + bV \tag{4.1}$$

$$a = \frac{1}{k_s} = \frac{4L^3}{E_p w t_p^3} \frac{\alpha\beta(1+\beta)}{\alpha^2\beta^4 + 2\alpha\left(2\beta + 3\beta^2 + 2\beta^3\right) + 1}$$

$$b = \frac{3L^2}{t_p^2} \frac{\alpha\beta(1+\beta)}{\alpha^2\beta^4 + 2\alpha\left(2\beta + 3\beta^2 + 2\beta^3\right) + 1} d_{31}$$

$$\alpha = {}^{E_s}\!/_{E_p}, \qquad \beta = {}^{t_s}\!/_{t_p}$$

where the subscripts *s* and *p* stand for the slider and piezoelectric materials, respectively. E and t are the Young's modulus and beam thickness, respectively. L and w represent the length and width of the composite beam. k_s is the bending stiffness of the cantilever. d_{31} is the piezoelectric coefficient.

According to Eq. (4.1) the actuated stroke as a function of the cantilever length was calculated without an external force. The thicknesses of the PZT and Al_2O_3-TiC layers are 127 and 300 μm, respectively. The material properties are E_p = 62 GPa, E_s = 398 GPa, $d_{31} = -320\times10^{-12}$ m/V. It is seen that the stroke increases as the actuator length increases and is about 0.6 nm/V for a length of 600-μm.

The nonflying actuated stroke of the prototype sliders at the pole-tip as a function of applied voltage was measured by a Zygo optical profiler (NewView interferometer, Zygo Corporation). Fig. 4.7 shows an example of a measurement obtained by the instrument. The topography of a portion of the slider near the trailing edge was measured and analyzed. The profile along the direction of the slider's width is plotted in Fig. 4.7(b). It is observed that there are three etching steps (four levels) with etch depths of about 191 nm, 1.38 μm and 1.88 μm. The actuation stroke was measured as the height difference between the center pad and the two side-pads when an electrical voltage is applied to the piezoelectric materials. It is noted that an initial stroke of several nanometers was observed even when no voltage was applied, which may be attributed to the cutting/bonding process and/or the mismatch of coefficients of thermal expansion of the PZT and Al_2O_3-TiC. Further investigation is required for minimizing and eliminating the initial stroke.

The actuated stroke was obtained by subtracting the initial surface profile (without voltage) from the actuated one (with voltage). Fig. 4.8 shows the stroke of Slider #1 when the voltage is increased from 0 to 40 V and returned to 0 V. A stroke of 32 nm is obtained with a voltage of 40 V, corresponding to a rate of 0.8 nm/V. A slight hysteresis is also observed. The measured stroke is 0.2 nm/V larger than the calculated value of 0.6 nm/V at a length of 600 μm, and it fits the calculated stroke when the actuator length is 700 μm. This result indicates that the effective actuation length is 100 μm longer than the cutting length of the slits.

Similarly, the actuated stroke of Slider #2 was measured. The driving voltage was gradually increased from 0 to 60 V, returned to 0 V, decreased to -60 V and returned to 0 V to form a complete loop as shown in Fig. 4.9(a). A hysteresis of 5 nm is observed due to the relatively high driving voltage. The measurement data and a linear fit for the branch from 0 to 60 V are shown in Fig. 4.9(b). The stroke is found to be proportional to the applied voltage with a rate of 0.72 nm/V. It is observed that Slider #1 and #2 have initial strokes of -6 and 0 nm, respectively, which have to be included in the FH measurements.

4.4.2 Flying Heights: Measurements and Simulations

We used an optical dynamic FH tester (DFHT4, KLA-Tencor Corporation) to measure the FH of the fabricated suspended sliders. In the tests the sliders were flown over a glass disk at three radial positions (ID, MD, and OD) at a rotational speed of 15000 rpm and a skew angle of 0 degree. The FHs were measured at the outer trailing pad (Point A) and the inner trailing pad (Point B). The FH at the center trailing pad was not measured since the light spot of the instrument (~30 μm) was larger than the available area of the center pad. Instead of direct measurements the FHs at the center pad were estimated by averaging the FHs at the two side-pads and taking the initial stroke into account. Fig. 4.10 shows the measured FH of Point A at the MD as a function of degree (360 degrees per revolution). The average and standard deviation are 9.11 and 0.14 nm, respectively. The experimental results are compared with numerical ones simulated by using the CML Air Bearing Simulator as shown in Table. 4.1. The measured values are 2 to 5 nm smaller than those obtained by simulations. Such a discrepancy may be due to the measurement error and/or to the simulation model, which may not be accurate under ultralow flying conditions. Based on the results the gap FHs of Slider #1 and #2 are estimated to be 15.5 nm (9.5 nm + 6 nm) and 8.5 nm (8.5 nm + 0 nm), respectively.

4.4.3 Contact Tests

Contact tests were conducted on a Candela OSA spin-stand with an AE sensor for detecting contact. Slider #1 was loaded on the disk at a radial position of 26 mm and a linear speed of 38 m/s. The slider body was electrically grounded and a voltage was applied to the top electrode of the PZT actuator. The voltage was gradually increased from 0 to 60 V in increments of 5 V. The process was repeated at a new radial position of 25 mm. Figs. 4.11(a) and 4.11(c) show the time histories of the AE signal when no voltage was applied to the piezoelectric actuator, which indicates that the slider flew well and no contact was detected by the AE sensor. Isolated spikes were observed when a voltage of 60 V was applied to the actuator as shown in Figs. 4.11(b) and 4.11(d). These spikes were caused by the intermittent contacts of the center pad and the disk. However, such a pattern of the AE signals during contact is different from the one observed in the conventional sliders during "touchdown-takeoff tests" [15] where there was a pronounced increase in the amplitude of the AE signal upon contact. Thus, during controlled contact (as is the case here) only a small portion of the slider comes into contact with the disk while the rest of the ABS is supported by the air bearing. There is no loss of air bearing as the voltage increases to increase the intensity of contact. Therefore the corresponding AE signal showed only an increase in the frequency of contacts but not an AE avalanche, which occurs in case of conventional sliders at touchdown due to complete loss of the air bearing.

Fig. 4.12 shows the number of hits (spikes) and FH as functions of the applied voltage. A contact event that has an AE amplitude over ±500 mV was counted as a hit. The gap FH was obtained by the measured FHs at the two side-pads and the measured initial stroke with consideration of the actuated stroke. At the radial position of 26 mm no contact was detected when the applied voltage was less than 20 V, corresponding to an estimated FH of -0.5 nm, and contact events were first detected when the applied voltage was increased to 25 V, corresponding to a FH of about -4.5 nm. A monotonic increase in the number of hits was observed as the voltage was increased, which indicated that the event of intermittent contacts became more frequent when the actuated stroke of the center pad was increased. It is noted that the contact was first detected at a FH between -0.5 nm and -4.5 nm, which was less than the take-off height (~ 2 nm). There are two possible reasons: one may be attributed to the AE sensor which may not be sensitive enough to detect the slight contact. The other may be the push-back lifting force generated by the center trailing pad, which may reduce the actuation stroke as compared to the case without flying. A similar trend was also observed when a second test was conducted on a new track (25 mm). It is seen that the intermittent contacts were detected at a smaller voltage (15 V). Such reduction of slider stability may be attributed to the lubricant pickup after the first test. Lubricant pickup decreases the slider's stability. Further, it also causes ABS contamination, which in turn may collect miniscule debris particles and cause wear at the head-disk interface [15].

We carried out contact tests for Slider #2 for the actuated side-pads scheme. Similarly, the contact event was detected by the AE sensor at a FH of about 0 nm. Fig. 4.13 shows the comparison of the nonflying strokes measured before and after the contact test, which demonstrates good repeatability of piezoelectric actuation even after contact.

4.4.4 Flying Height Modulation

Intermittent contacts due to increase in actuation voltage also cause a change in slider dynamics. To investigate this we measured the fly height modulation for Slider #2 as described in the previous section. From Fig.4.14 we see that the peak-to-peak and standard deviation (3σ) of the slider displacements gradually increase as the voltage is increased. However, the increase is not substantial and signifies a gradual increase in the slider-disk contact as the center trailing pad is lowered due to the voltage increase. The repeatability of this data was also found to be good, as seen from the small error bars.

Figs. 4.15(a) and 4.15(b) show the repeatable part of the slider's displacement without slider-disk contact at 0 V and during slider-disk contact at 60 V, respectively. Comparing (a) and (b) we see the increased amplitude of slider displacements in the latter case. Similar to the AE measurements, the difference is not as sharp compared to a conventional slider where there is a pronounced increase in the amplitude of slider displacements upon contact due to the complete loss of air bearing.

Figs. 4.16(a)-(f) show the frequency content of slider displacements as the voltage is increased from 0 to 60 V. The CML Parameter Identification Program was used to identify the air bearing frequencies and mode shapes of the Scorpion sliders in Chapter 3. The first pitch and the second pitch modes were found to be near 100 kHz and 200 kHz, respectively. The nodal lines shown indicate that the axes of the first and second pitch modes lie near the trailing and the leading edges, respectively. Using this information we can identify the dominant ABS frequencies in Figs. 4.16 (a)-(f). The arrows shown in Figs. 4.16(a) and 4.16(f) indicate the first and second pitch modes. It is seen by traversing the plots (a-f) that as the voltage (intensity of contact) increases, the second pitch mode gradually becomes more dominant. This can be explained as follows: When the slider is flying the trailing edge flies much closer to the disk than the leading edge. Thus, the stiffness associated with the trailing edge is much more and the modulations in the leading edge flying height due to disk forcing are much more than at the trailing edge due to which the slider pitch mode is close to the trailing edge. Hence, the first pitch mode is dominant when there is no slider-disk contact. As the trailing pad protrudes due to an increase in the voltage the trailing edge flies higher, and the slider pitch is also lowered. Further, only the trailing edge gets significant forcing due to impact force. Due to this the modulations of the trailing pad are much higher than at the leading pad so that the second pitch mode is dominant during slider-disk contact. This hypothesis can be readily tested using the LDV to monitor the dynamics of multiple points on the slider.

From Figs. 14(a-f) we also see an increase of about 14 dB (5 times) in the peak frequency components during slider-disk contact.

FHM is defined as the difference between slider and disk displacements, *i.e.* the modulation of mechanical fly height over time. During the experiments the disk was scratched during slider disk contact, due to which its topography was changed substantially. Hence, the FHM as a function of applied voltage is not reported here and further tests need to be carried out to examine the same.

4.4.5 Controlled Contact Effect on Lubricant

The effect of controlled contact on the lube was also monitored during the full voltage cycle 0V-60V-0V, during which the trailing pad was forced in and out of contact. When one such test was conducted substantial lube depletion was seen below the side rails and the trailing pad, as indicated by the arrows in Fig. 4.17, which plots the average lube depletion in the radial direction. Since the trailing pad was brought into contact the depletion under it was more (5 Å) than that under the side rails (1 Å - 3 Å). Overall the depletion was relatively high due to which, when the controlled contact test was repeated the second time, there was considerable wear, and a wear track was seen on the disk. Fig 4.18 shows the track. From the OSA analysis total lubricant depletion was seen in the dark area. This area measured about 250 μm in width, slightly wider than the cantilever width (200 μm). The central white portion in the dark area was the only place where there was only lubricant depletion and no carbon wear, while the rest of the dark area had carbon wear and the generation of debris particles. There was also considerable wear of the ABS surface as seen in Fig. 4.19.

More tests need to be conducted to determine the reliability of the interface during partial contact using the Scorpion design. It is believed that the disk showed accelerated wear due to excessive increase in voltage (60 V) to the cantilever which increased the contact intensity.

4.5 Conclusions

This chapter presented fabrication and experimental results of flying and contact dynamics of Al_2O_3-TiC sliders with piezoelectric nanoactuators. We fabricated and assembled prototype sliders using an inexpensive and low-temperature process. The measured nonflying actuated stroke exhibited a linear relationship with the applied voltage with a rate of ~ 0.8 nm/V. However, a hysteresis was observed when excessive voltages (± 60 V) were applied to the piezoelectric actuators. The FHs of two different sliders were successfully reduced from 15.5 nm and 8.5 nm to contact with applied voltages of 20 V and 10 V, respectively, which demonstrated high actuation efficiency. The AE measurements showed clear spikes when the center pad was brought into contact with the disk by the actuator. However, such a pattern of the AE signals during controlled contact is different from the one observed in the conventional sliders during "touchdown-takeoff tests" where there is a pronounced increase in the AE amplitude upon contact. This is attributed to the sustained air bearing even when the intermittent contacts occur in the head-disk interface. It is also found that the dominant air bearing mode shifted from the first pitch to the second pitch as a result of the intermittent contacts. In addition, a track of considerable lube depletion and carbon wear was observed after the contact tests.

References

1. C. E. Yeack-Scranton, V. D. Khanna, K. F. Etzold, and A. P. Praino, “ An active slider for practical contact recording,” *IEEE Trans. Magn.,* vol. 26, pp. 2478-2483, 1990.
2. D. L. Good, J. E. Mason, and H. H. Ottesen, “Fly height servo control of read/write head suspension,” U.S. Patent 5,377,058, December 27, 1994.
3. X. Liu, A. Li, W. Clegg, D. F. L. Jenkins, and P. Davey, “Head-disk spacing variation suppression via active flying height control,” *IEEE Trans. Instrum. Meas.*, vol. 51, pp. 897-901, 2002.
4. V. D. Khanna, F. Hendriks, and A. P. Praino, “ Programmable air bearing sliders,” *IEEE Trans. Magn.,* vol. 27, pp. 5145-5147, 1991.
5. M. Zhang, S. Yu, J. Liu, and B. Liu, “Flying height adjustment by slider’s air bearing surface profile control,” *J. Applied Physics,* vol. 97, 10P309, 2005.
6. M. Kurita, T. Yamazaki, H. Kohira, M. Matsumoto, R. Tsuchiyama, J. Xu, T. Harada, Y. Inoue, L. Su, and K. Kato, “An active-head slider with a piezoelectric actuator for controlling flying height ,” *IEEE Trans. Magn.,* vol. 38, pp. 2102-2104, 2002.
7. M. Kurita and K. Suzuki, “Flying-height adjustment technologies of magnetic head sliders,” *IEEE Trans. Magn.,* vol. 40, pp. 332-336, 2004.
8. K. Suzuki, R. Maeda, J. Chu, T. Kato, and M. Kurita, “An active head slider using a piezoelectric cantilever for in situ flying-height control,” *IEEE Trans. Magn.,* vol. 39, pp. 826-831, 2003.

9. N. Tagawa, K.-I. Kitamura, and A. Mori, “Design and fabrication of MEMS-based active slider using double-layered composite PZT thin film in hard disk drives,” *IEEE Trans. Magn.,* vol. 39, pp. 926-931, 2003.

10. L. Su, M. Kurita, J. Xu, K. Kato, K. Adachi, and Y. Miyake, “Static and dynamic characteristics of active-head sliders,” *Tribol. Intl.,* vol. 38, pp. 717-723, 2005.

11. J. Y. Juang, D. B. Bogy and C. S. Bhatia, “Numerical and experimental studies of an Al_2O_3-TiC slider with a piezoelectric nanoactuator,” *2006 ASME/JSME Joint Conf. on Micromechatronics for Information and Precision Equipment*, June 21-23, Santa Clara, CA.

12. J. Y. Juang, D. B. Bogy and C. S. Bhatia, “Design and dynamics of flying height control slider with piezoelectric actuation,” *ASME J. of Tribol.*, submitted for publication.

13. Q. H. Zeng, B. H. Thornton, D. B. Bogy, and C. S. Bhatia, “Flyability and flying height modulation measurement of sliders with sub-10nm flying heights,” *IEEE Trans. Magn.,* vol. 37, pp. 894-899, 2001.

14. Smits, J. G. and Choi, W.-S., “The Constituent Equations of Piezoelectric Heterogeneous Bimorphs,” *IEEE Trans. Ultrason., Ferroelect., Freq. Contr.*, vol. 38, no. 3, pp. 256-270, 1991.

15. R. P. Ambekar and D. B. Bogy, “Effect of slider lubricant pickup on stability at the head-disk interface,” *IEEE Trans. Magn.,* vol. 41, pp. 3028-3030, 2005.

TABLE 4.1 Comparisons of the Simulated and Measured FHs at Point A (outer trailing pad) and B (inner trailing pad). The values in the Parentheses are the Standard Deviations.

	OD		MD		ID	
	Sim. (nm)	Exp. (nm)	Sim. (nm)	Exp. (nm)	Sim. (nm)	Exp. (nm)
Point A	13.31	11.64 (0.2)	13.43	10.04 (0.18)	13.11	11.01 (0.18)
Point B	13.23	8.08 (0.1)	13.60	9.11 (0.14)	13.63	8.78 (0.16)

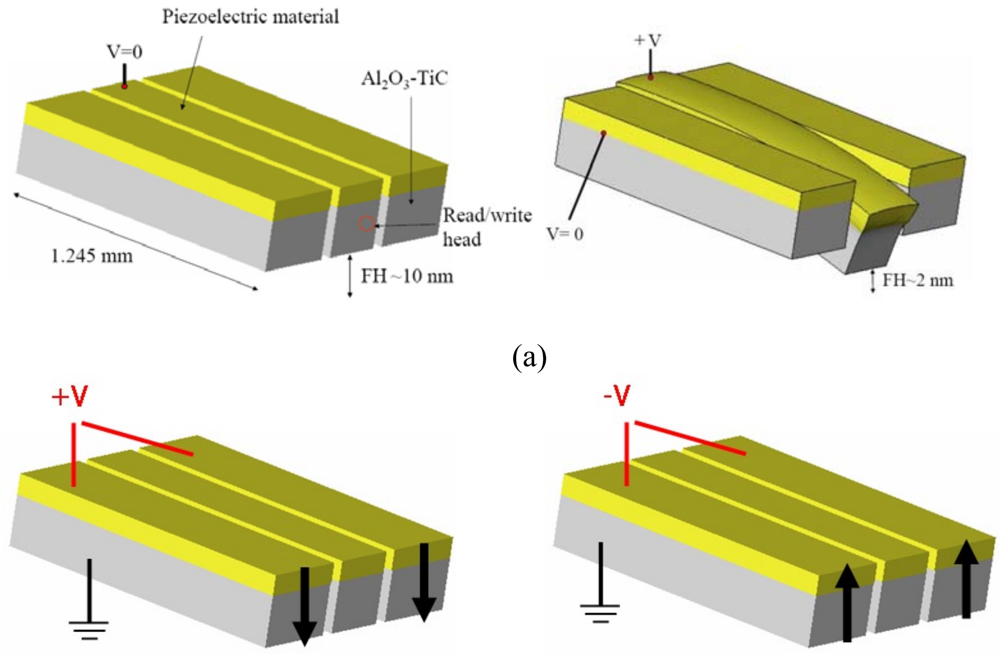

(a)

(b)

Fig. 4.1. Two operational schemes of a FH control slider with piezoelectric actuation. (a) actuated center-pad; (b) actuated side-pads.

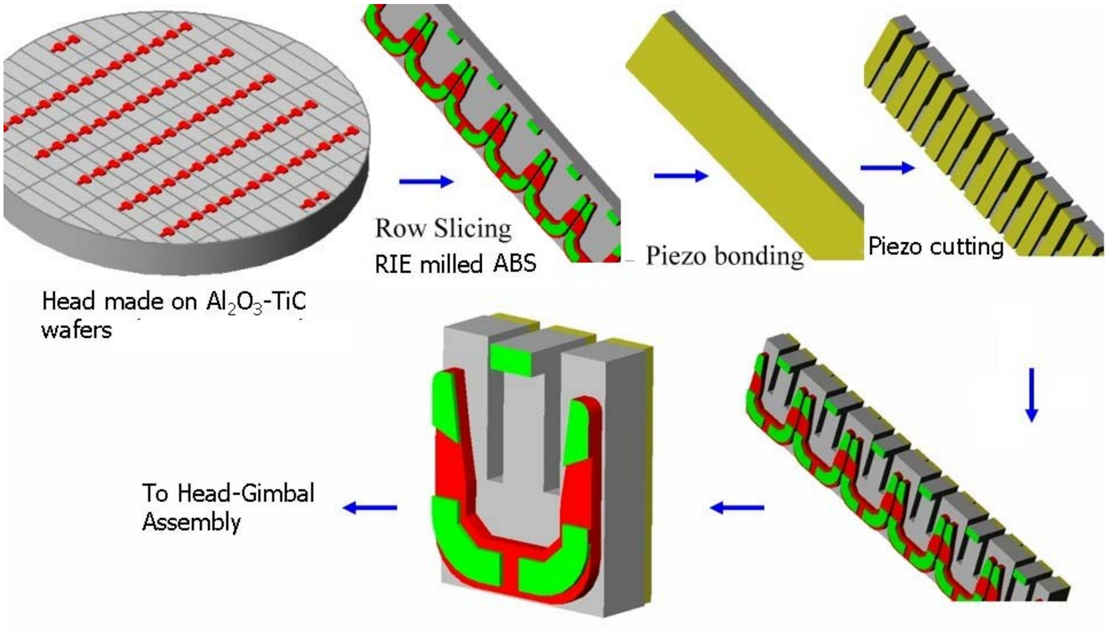

Fig. 4.2. Schematic diagram of the process flow.

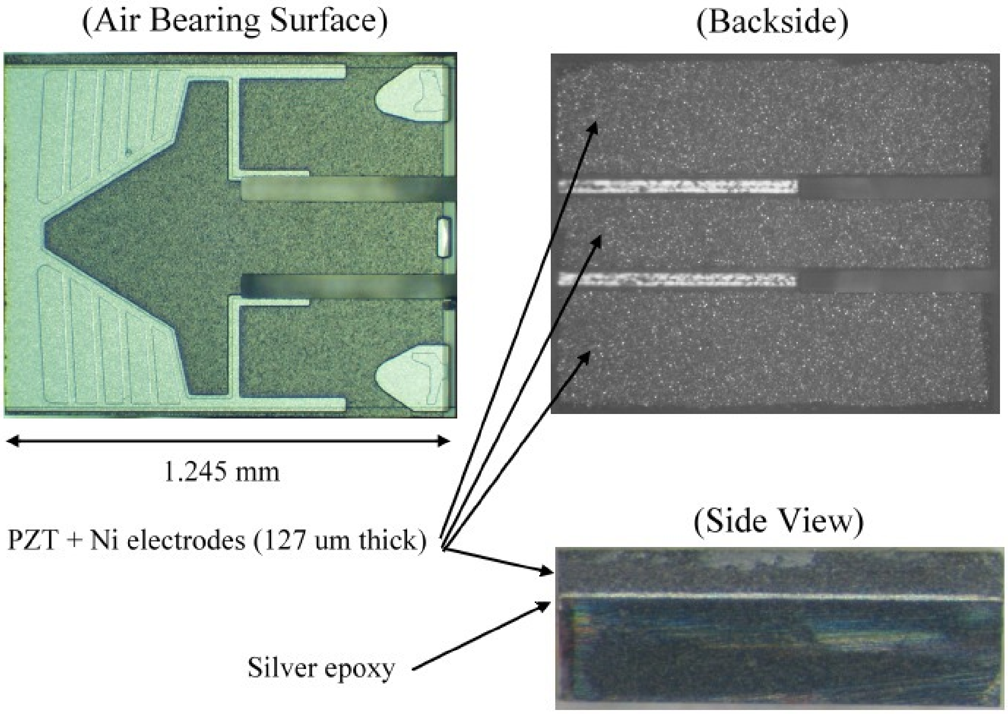

Fig. 4.3. Fabricated Al_2O_3-TiC slider with a layer of piezoelectric material bonded on the back-side.

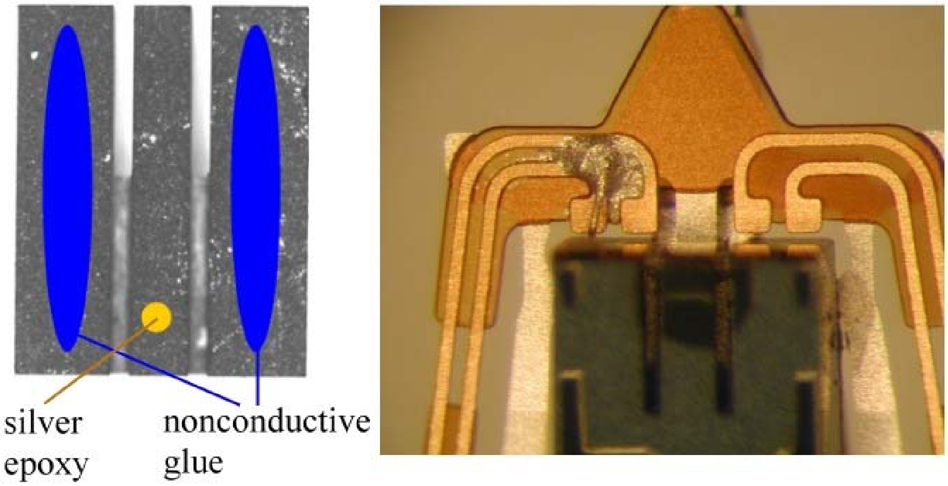

(a) (b)

Fig. 4.4. HGA of the fabricated slider

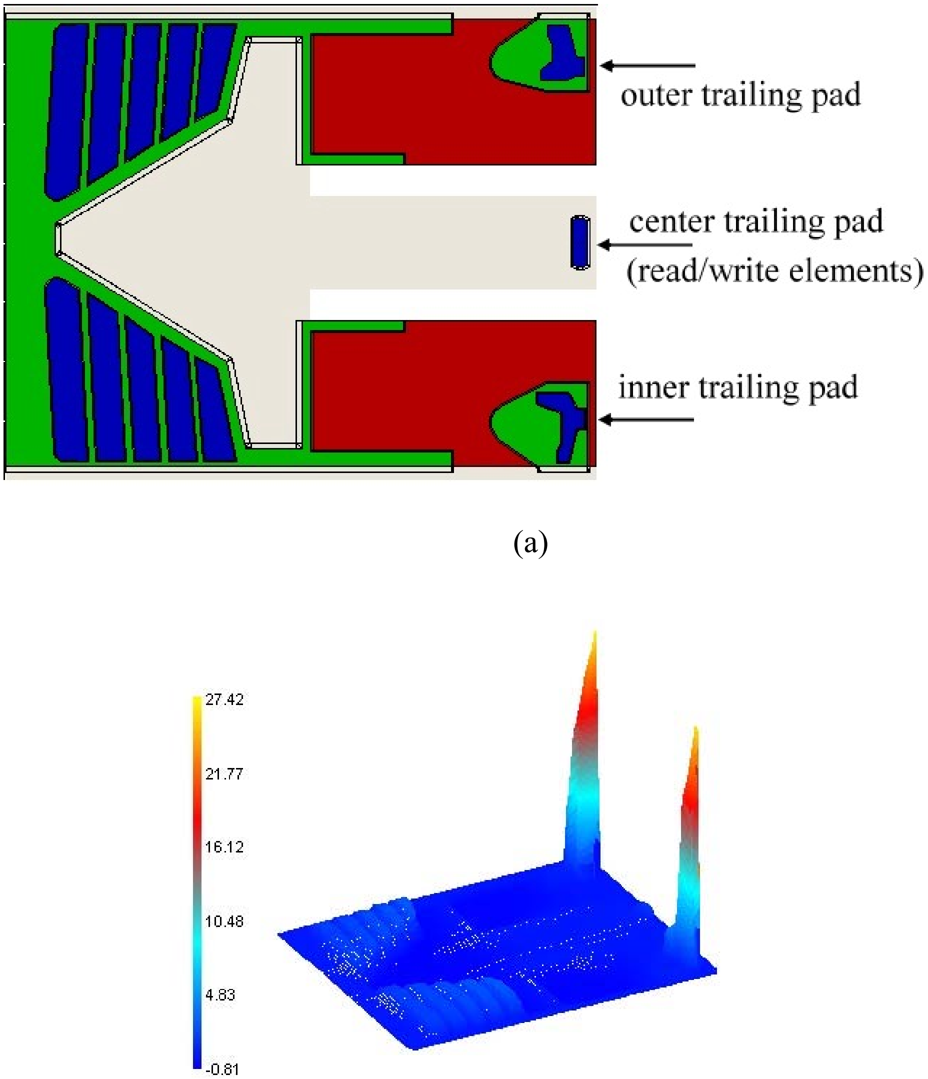

(a)

(b)

Fig. 4.5. (a) A pico-slider ABS used in this study. The two white rectangles are slits through the entire thickness of the slider; (b) Air bearing pressure profile at radial position 29.89 mm, 0 degree skew. The scale displayed is normalized to ambient pressure: $(p - p_a)/p_a$.

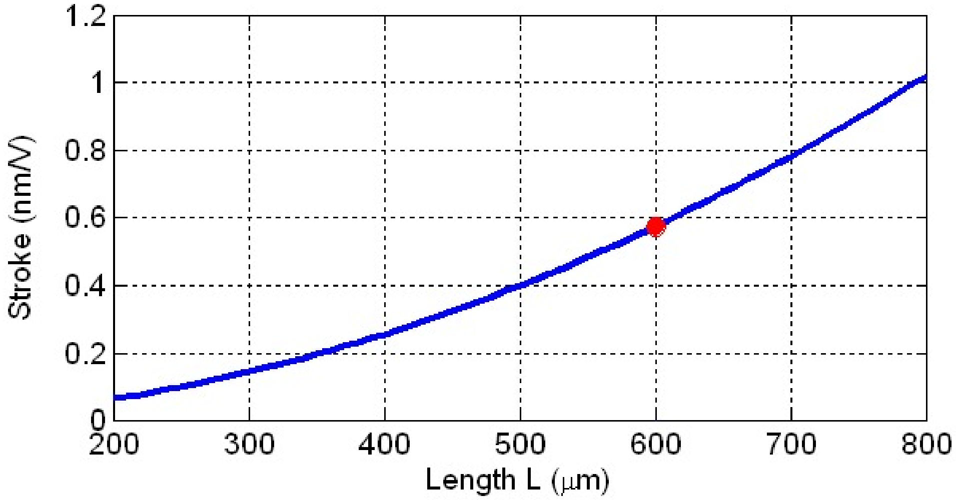

Fig. 4.6. The actuated stroke of a piezoelectric unimorph actuator under 1 V. The thicknesses of the piezoelectric and Al_2O_3-TiC layers are 127 and 300 μm, respectively. The material properties are E_p = 62 GPa, E_s = 398 GPa, d_{31} = -320x10^{-12} m/V. The stroke is about 0.6 nm/V for a 600-μm long cantilever.

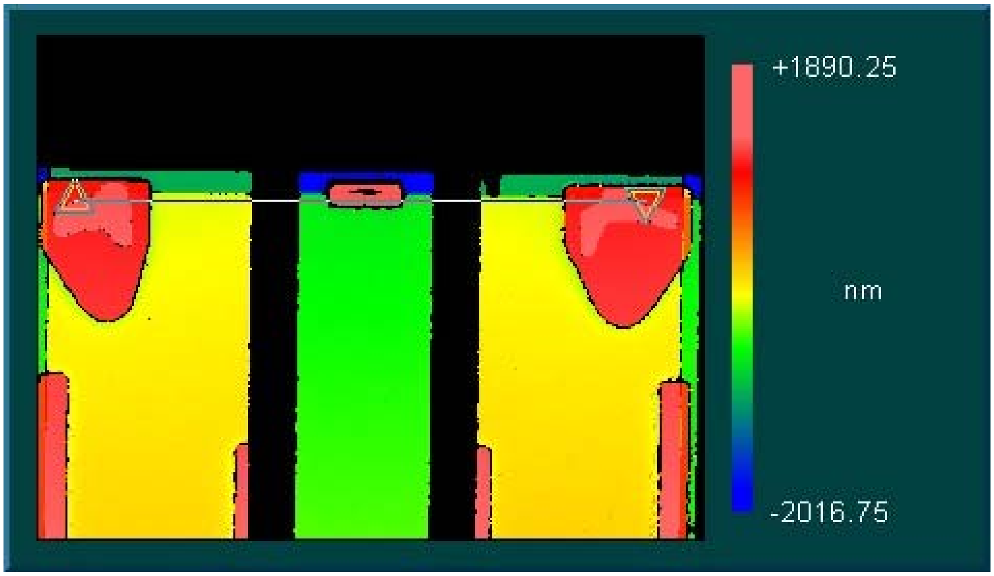

(a)

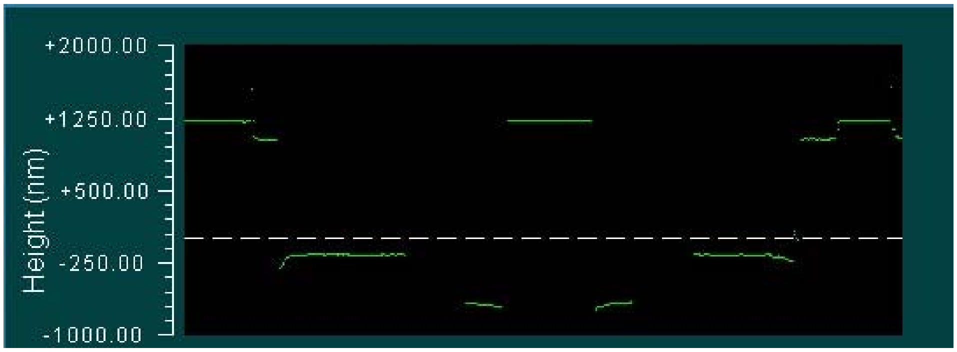

(b) profile

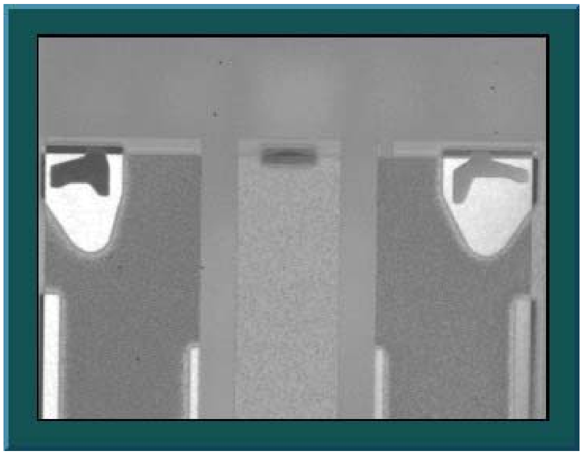

(c) Intensity data

Fig. 4.7. An example of the air bearing topography measured by a Zygo optical profiler.

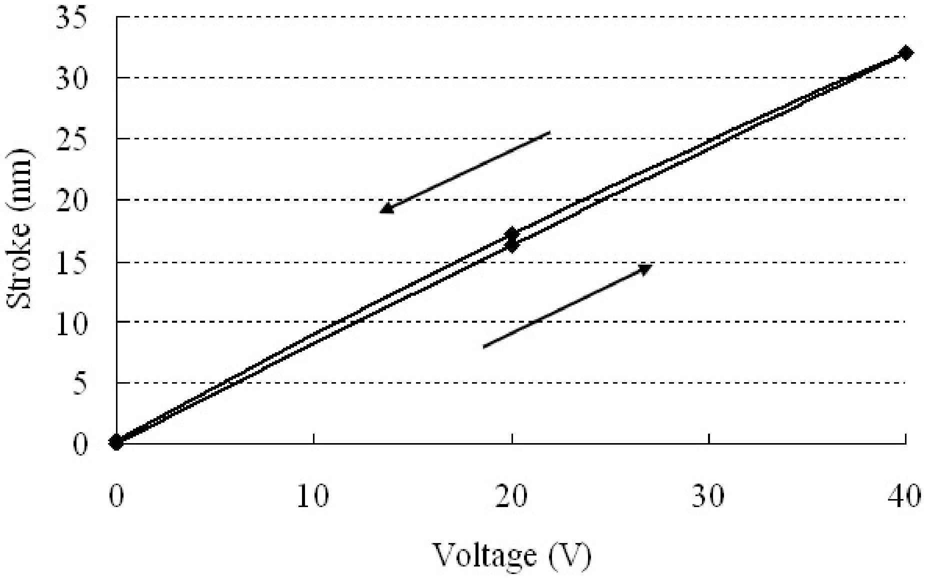

Fig. 4.8. The measured nonflying stroke as a function of the applied voltage for Slider #1.

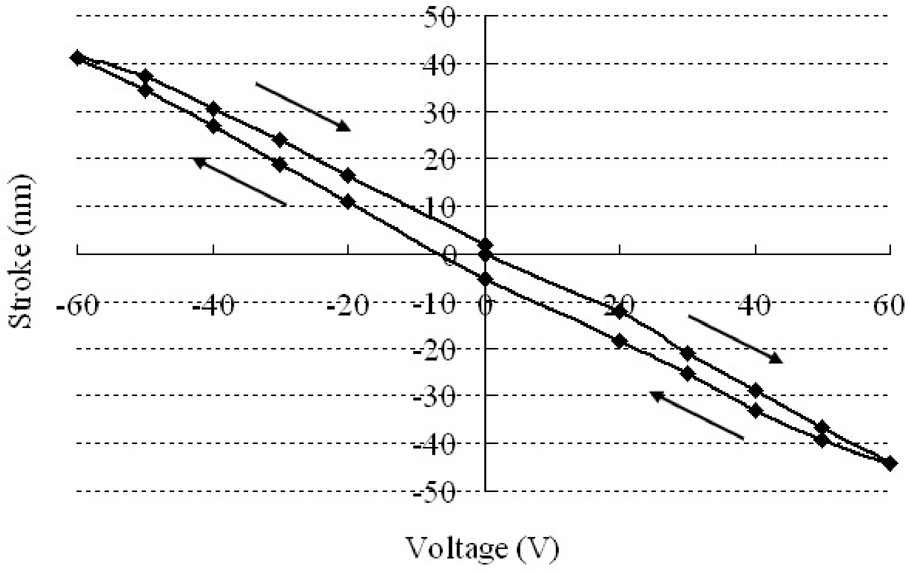

(a)

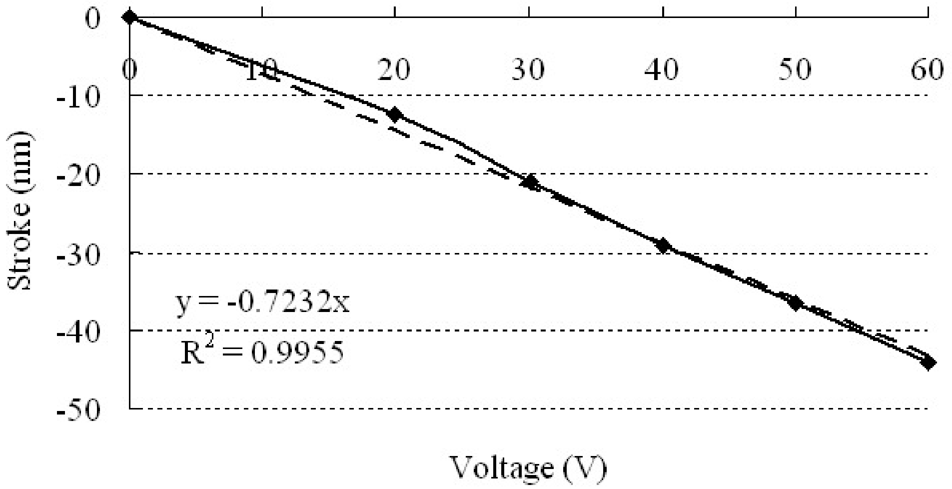

(b)

Fig. 4.9. The measured nonflying stroke as a function of the applied voltage. (a) The voltage was gradually increased from 0 to 60 V, returned to 0 V, decreased to -60 V and returned to 0 V; (b) A linear fit of a rate of 0.72 nm/V is found to fit the measurement data from 0 to 60 V. The minus sign indicates that a negative voltage is required for a positive stroke in the actuated side-pads scheme.

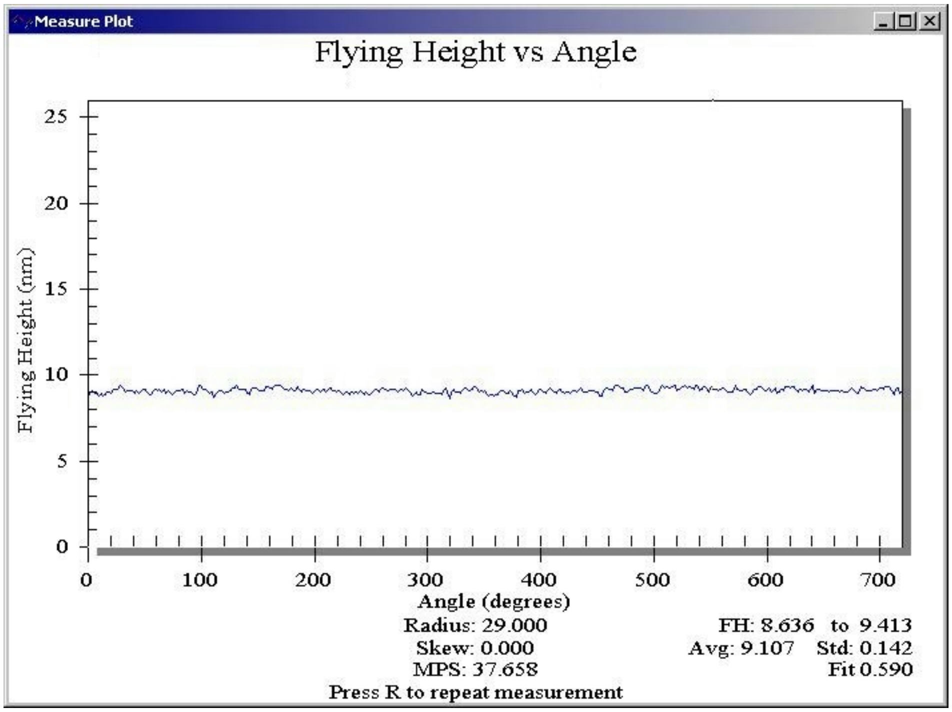

Radius: 29.000
Skew: 0.000
MPS: 37.658

FH: 8.636 to 9.413
Avg: 9.107 Std: 0.142
Fit 0.590

Press R to repeat measurement

Fig. 4.10. The measured FH at Point A (the inner trailing pad) at the MD as a function of degree.

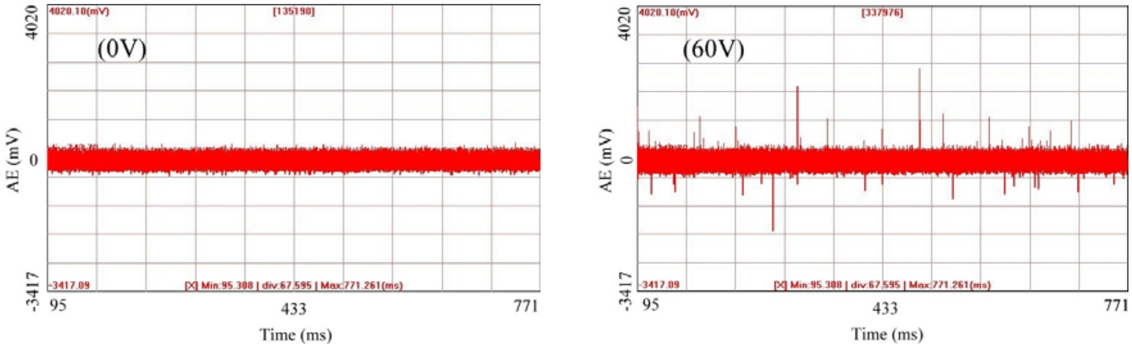

(a) Radial position: 26 mm

(b) Radial position: 26 mm

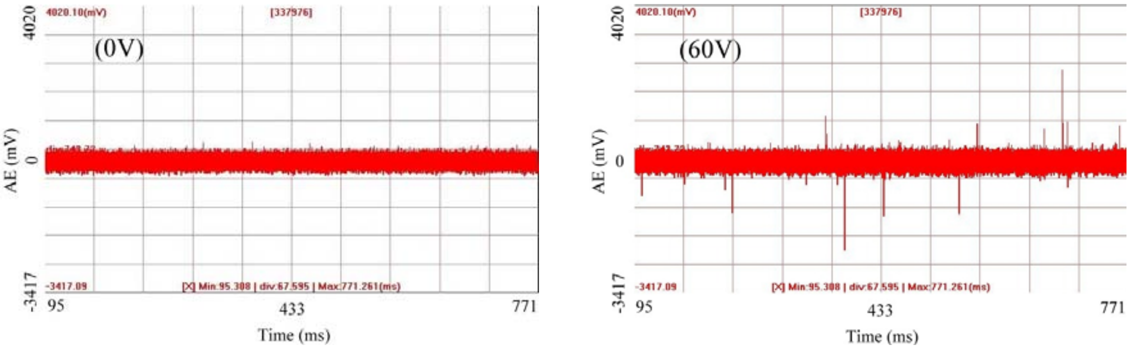

(c) Radial position: 25 mm

(d) Radial position: 25 mm

Fig. 4.11. The time histories of the AE signals: (a) 0 V at 26 mm; (b) 60 V at 26 mm; (c) 0 V at 25 mm; (d) 60 V at 25mm.

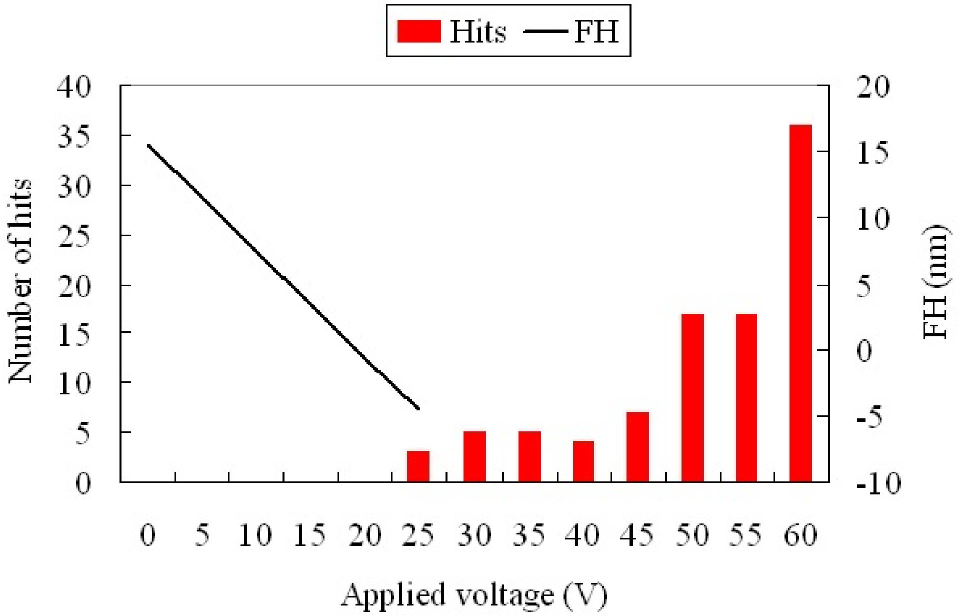

(a) Radial position: 26 mm

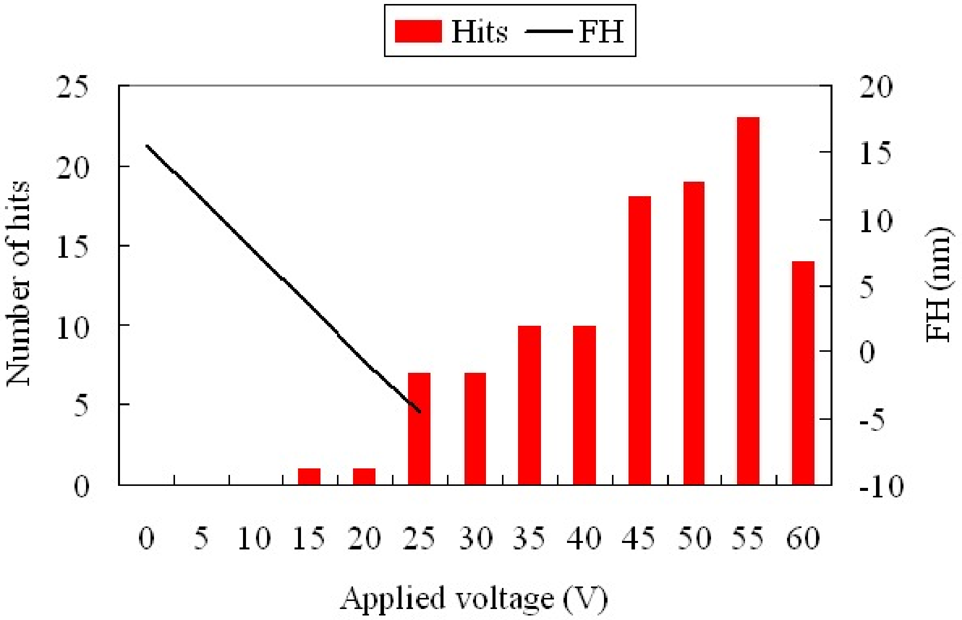

(b) Radial position: 25 mm

Fig. 4.12. The number of hits (spikes) and the estimated FH as functions of the applied voltage. The contact event that has an AE amplitude over ±500 mV was counted as a hit.

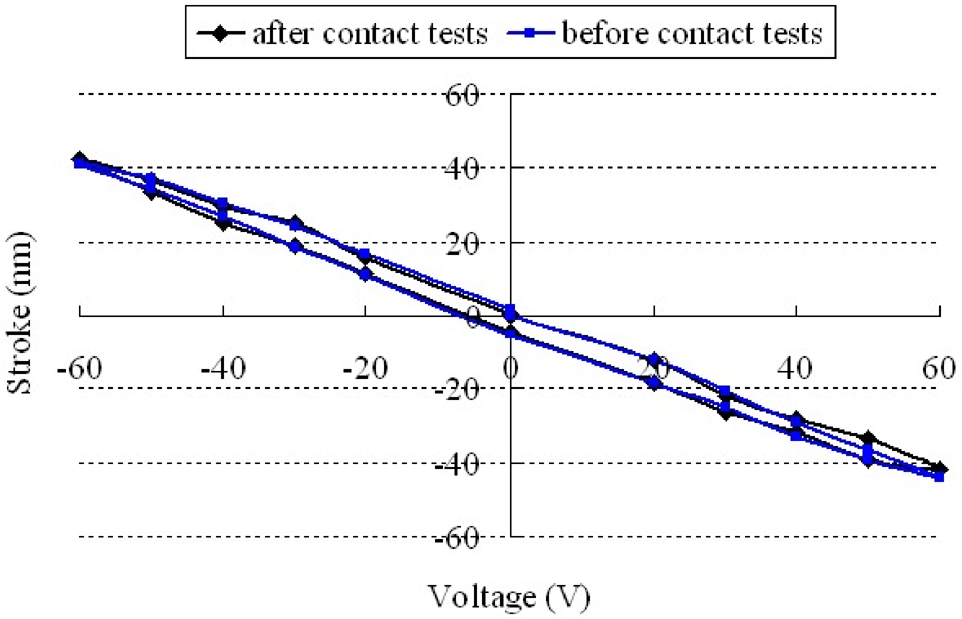

Fig. 4.13. Comparison of the nonflying actuated strokes measured before and after the contact test, which demonstrated good repeatability.

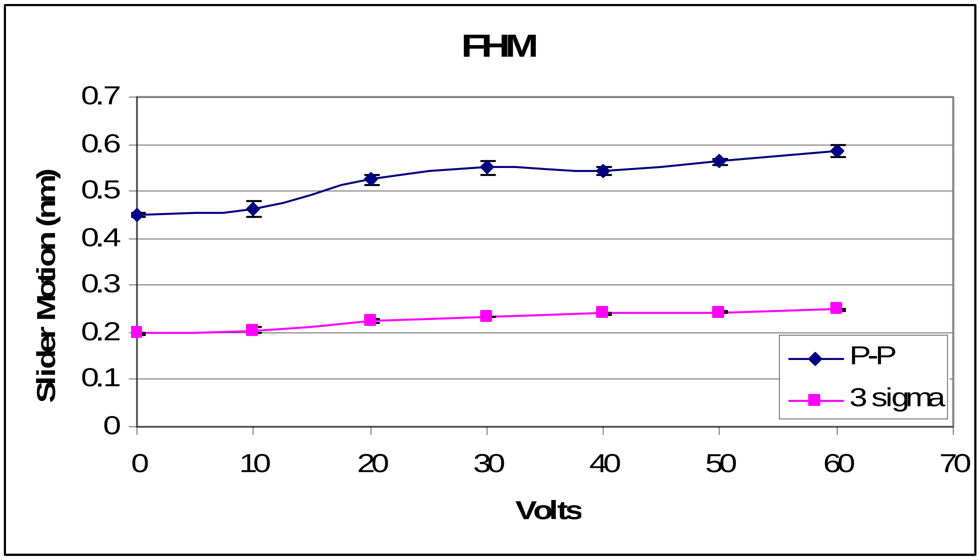

Fig. 4.14. Peak-to-peak and standard deviation (3σ) of slider displacements as a function of applied voltage.

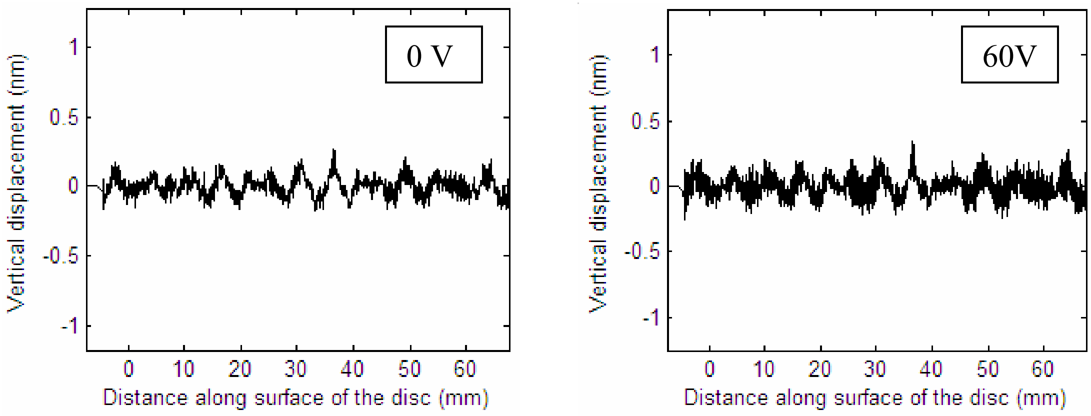

(a) (b)

Fig. 4.15. Repeatable part of slider displacements: (a) when no slider-disk contact occurs; (b) when slider-disk contact occurs.

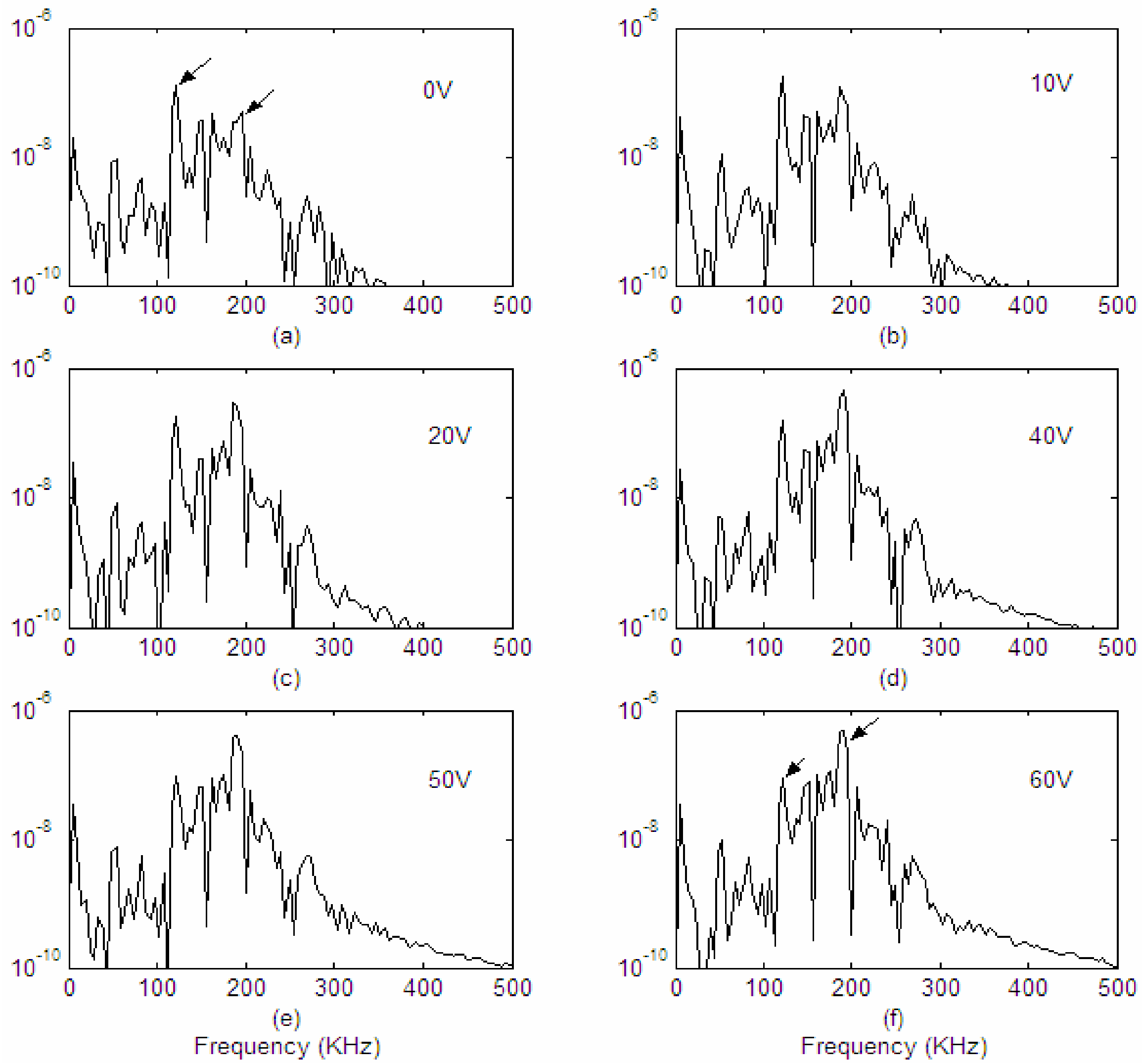

Fig. 4.16. Shift in the frequency response due to change in intensity of contact.

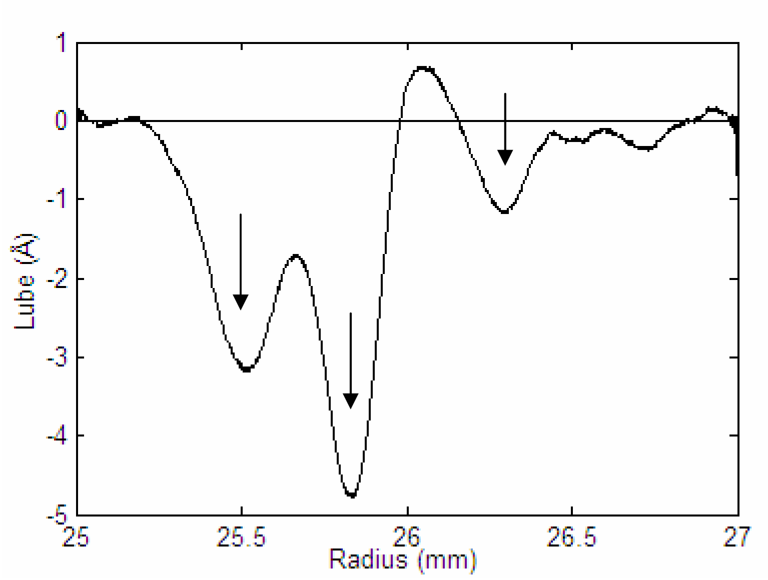

Fig. 4.17. Average lube height as a function of radius on an experimental track.

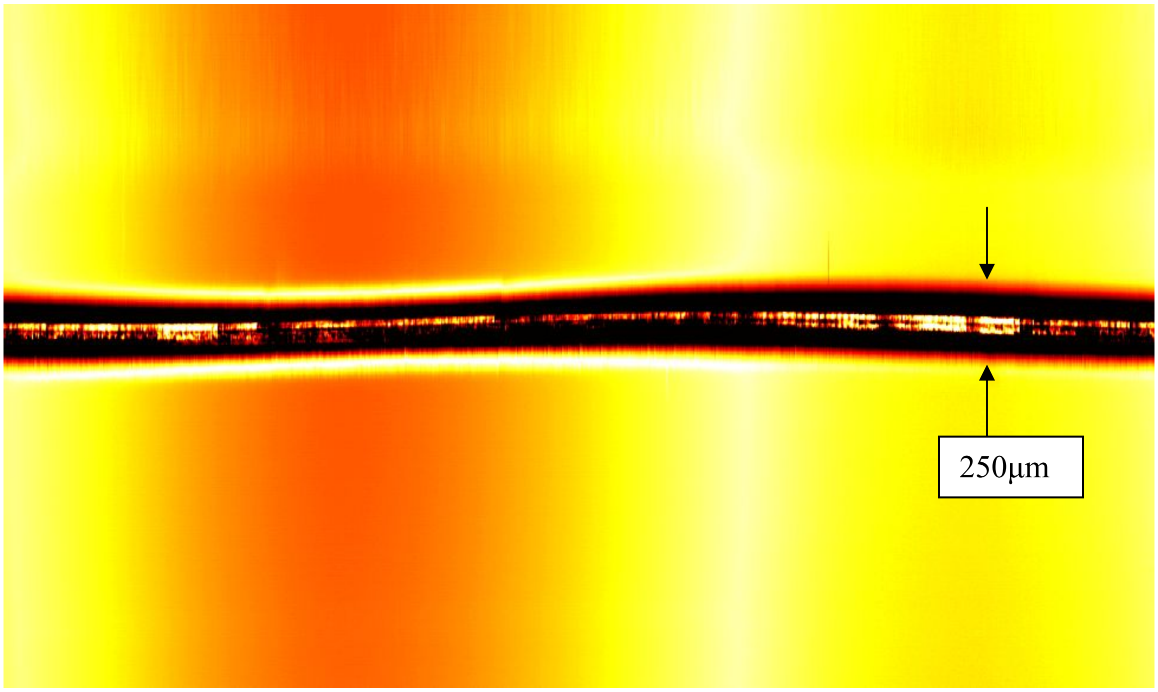

Fig. 4.18. OSA scan of experimental track showing lube depletion and carbon wear.

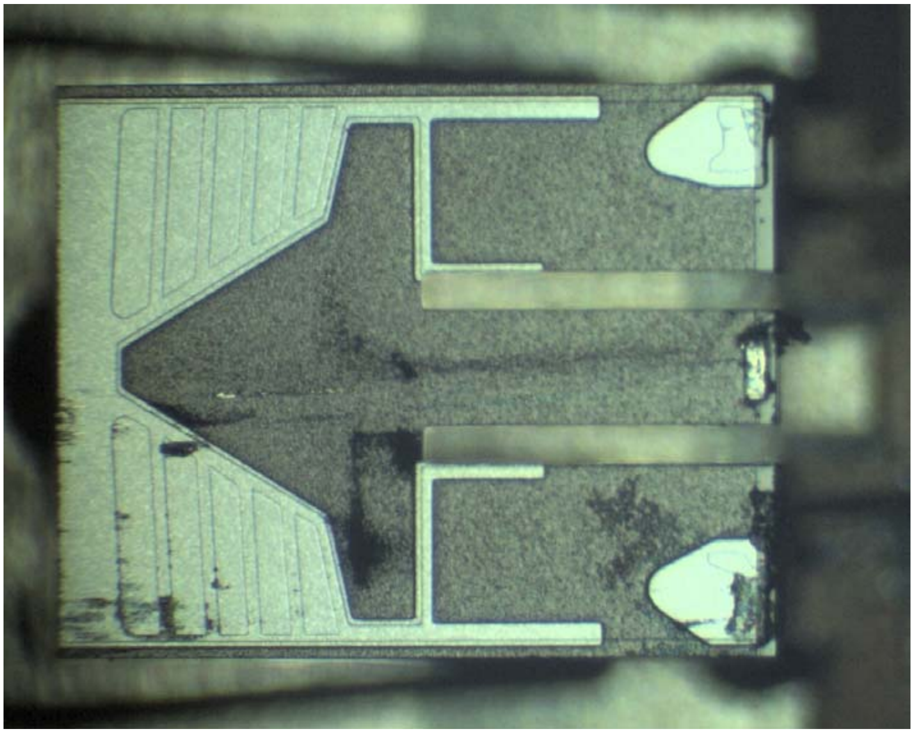

Fig. 4.19. Photograph of the piezoelectric slider after contact tests. Considerable amount of debris and particles were accumulated on the ABS, especially near the center and inner trailing pads.

CHAPTER 5
MODELING AND DYNAMIC CONTROL FOR FLYING HEIGHT MODULATION SUPPRESSION IN ULTRALOW FLYING AIR BEARINGS

As the slider flying height (FH) continues to be reduced in hard disk drives, the flying height modulation (FHM) due to disk morphology and interface instability caused by highly nonlinear attractive forces becomes significant. Based on the concept that the FH of a portion of the slider that carries the read/write element can be adjusted by a piezoelectric actuator located between the slider and suspension and that the FH can be measured by use of a magnetic signal, a new 3-DOF analytic model and an observer-based nonlinear compensator are proposed to achieve ultra-low FH with minimum modulation under short range attractive forces. Numerical simulations show that the FHM due to disk waviness is effectively controlled and reduced.

5.1 Introduction

The areal density of magnetic recording in hard disk drives has been increasing at a multiple of 1.6 per year since the late 90's. This achievement has been enabled mechanically by decreasing the distance between the read/write transducer and the rotating disks. According to the Wallace spacing loss equation the magnetic signal increases exponentially as the distance decreases between the magnetic media and the transducer. Therefore, the maximum magnetic signal can potentially be obtained at a spacing of zero, resulting in a contact recording scheme. However, when the slider comes into contact with the disk, other considerations must be addressed to assure a stable contact interface with minimum wear and contact bouncing vibration. Yanagisawa *et al.*

[1] used a 0.3 mm diameter glass ball to study contact sliding experimentally, and they showed that the wear of the spherical contact slider decreased as the gram load decreased, but the bouncing vibrations increased. In other words, there was a trade-off between reducing the bouncing and wear.

Ono *et al.* [2] numerically studied the effects of several parameters on the bouncing vibrations of a 1-DOF slider model and found that bouncing vibrations can be reduced by decreasing the contact stiffness and increasing the contact damping as well as applied load. Ono and Takahashi [3, 4] used a 2-DOF model for a tri-pad contact slider and showed that in order to achieve minimum bouncing it is necessary to design the contact pad such that its penetration depth is greater than the amplitude of the disk surface waviness. Such high penetration causes a relatively severe wear of the disk or slider. The effects of the front and rear air bearing stiffnesses, as well as the friction coefficient, on the contact force and bouncing vibrations were analyzed numerically with a 2-DOF tri-pad slider model in Iida *et al.* [5]. It was found that the rear air bearing stiffness should be larger than the front air bearing stiffness in order to reduce the vibration. However, contact forces may be increased if the rear air bearing is too stiff. Accordingly, there is an optimum rear air bearing stiffness in terms of both stable contact and wear durability.

In [6, 7], Ono and Iida used a 1-DOF model to investigate the design conditions of a contact slider over a random wavy disk surface. Assuming a uniform contact pressure their simulation results showed that a larger contact pad area is better for wear durability because the contact stiffness and applied load necessary to attain contact sliding increases in proportion to the square root of the contact area. Asperity contact and bulk deformation were considered in Yamane *et al.* [8] to evaluate contact forces, contact stiffness, and contact pressure in the near-contact regime as a function of separation between the contact pad and disk surface. They showed that the mean contact force and spacing variation increased with an increase in the rms value of micro-waviness of the disk surface. The short range attractive forces between the slider and disk in the proximity regime have to be considered in both flying and contact sliders. These forces are strongly related to lubricant thickness, surface roughness, and slider/disk materials. More significant bouncing vibrations and flying height hysteresis have been observed experimentally when smoother disks or a thicker lubricant are used.

Additionally, Iida and Ono [4, 5] included the meniscus attractive force in their random asperity contact simulations. They observed similar touch-down and take-off hysteresis as observed in experiments and showed that the attractive force could be significantly reduced if the rms value of asperity heights was increased or the asperity density was reduced. However, the attractive force increased with an increase in lubricant thickness. Yamane *et al.* [8] studied the bouncing vibrations experimentally and by numerical simulation using a 2-DOF dynamic model considering the adhesive force of the lubricant as well as the friction force. The frequency spectra of the trailing edge bouncing vibrations after touch-down and before take-off showed some similarity between experimental and numerical results, but the vibration amplitudes had considerable disagreement between the two cases. The bouncing vibrations observed in the numerical simulations were self-excited vibrations caused by the combination effect of a relatively large short range attractive force and the friction force between the disk and slider when the contact occurred. These self-excited vibrations were negligible if the friction coefficient or the attractive force was small. The authors concluded that a contact slider with minimum self-excited bouncing can be achieved by use of a stiffer air bearing and with minimum friction coefficient and attractive force. Even though several design considerations have been proposed to design a contact slider in the literature, it is still unclear how those designs can be implemented into a real system, namely the design of the air bearing surface (ABS) and the selection of lubricants.

As the flying height (FH) is reduced in a flying head slider to the sub 3-nm regime in ultra-high density hard disk systems, the flying height modulation (FHM) induced by the disk morphology and dynamic instability due to short range attractive forces become more significant. Gupta and Bogy [9] conducted a numerical study of the effect of intermolecular and electrostatic forces on the stability of the HDI, and they showed that those short range attractive forces may cause an instability of the HDI at such low flying heights. This effect must be considered in the design of the ABS.

In order to achieve reliable reading and writing of magnetic data it is required that the transducer location on the slider vibrate less than ±10 % of the nominal FH, or about ±0.3 nm, in future systems for 1 Tbit/in^2 areal density. Furthermore, considerable FHM may cause instability of the interface due to adhesive forces. The concept of FH adjustment by piezoelectric material has been proposed in [10-12], but the main purpose in those papers was to decrease the effects of manufacturing tolerances and environmental variations on the FH. Those authors utilized silicon microfabrication technology to fabricate the sliders. However, the use of silicon as the slider material may cause other issues in slider fabrication and HDI tribology. Li *et al.* [13] presented a real-time FH detection method by using readback or thermal signals and in [14] they developed a real-time feedback control method to suppress the FHM. In this case, the actuator was a piezoelectric film attached to the suspension. The actuation bandwidth was limited by the suspension dynamics. The effect of short range attractive forces was not taken into consideration in these studies.

In this chapter a new 3-DOF analytic model is proposed to describe the dynamics of the piezoelectric actuated slider. The air bearing parameters, such as stiffness and damping, are identified by a modal analysis method developed in the Computer Mechanics Laboratory (CML) [15, 16]. Then, an observer-based nonlinear sliding mode controller [17] is designed to compensate the short range attractive forces and to suppress the FHM of ultra-low flying height air-bearing sliders in proximity, in which the magnetic signal is used for real-time FHM measurement. The attractive forces are included in the model as a highly nonlinear term and the effect of disk morphology is modeled as unknown but bounded disturbances. The performance of the controller is investigated by numerical simulations.

5.2 Nonlinear 3-DOF Lumped Parameter Model of Controlled Flying Sliders

A schematic diagram of the FH control slider with a piezoelectric nanoactuator is shown in Fig. 5.1. The FH is about 20 nm in the off duty cycle and is reduced to about 3 nm during reading and writing. Figure 5.2 shows the five-pad ABS design example used in this chapter. The gap FH is adjusted by the deflection of the cantilever actuator. The deflection is achieved by grounding the slider and applying a negative voltage to the top electrode of the central piezoelectric material.

There are two modes of operation. In the passive mode, there is no external voltage applied to the piezoelectric material so the active cantilever rests in the original position. The gap flying height in this case may be designed to be between 10 and 20 nm, depending on the ABS design. In the active mode the cantilever is bent into close proximity of the disk with the application of a negative DC voltage to the middle portion of the piezoelectric material. Meanwhile, an AC computed control voltage is superposed on the DC voltage so that the FHM is minimized. The active mode is used only when the read/write head is in operation. The duty cycle for a practical head is rather low. Most of the time of the head is spent in non-read/write conditions, such as latency, seeking, or idle. Thus the wear and power consumption can be greatly reduced by simply operating the piezoelectric slider in the passive mode. The air bearing pressure distributions in both modes are shown in Fig. 5.3, where the additional pressure peak is seen when the central pad is deflected into close proximity to the disk.

The slider is modeled as a nonlinear 3-DOF lumped model in which the cantilever actuator and the air bearing dynamics are modeled as 1-DOF and 2-DOF, respectively.

5.2.1 1-DOF Lumped Model of the Piezoelectric Unimorph Nanoactuator

The cantilever actuator, composed of a piece of piezoelectric material and a portion of the slider, deflects under an electric voltage *V* and an external vertical force *F* exerted on the tip as shown in Fig. 5.4(a). *V* and *F* are the control voltage and air bearing force in our application. The equation for the tip deflection when it is subject to a voltage and a force can be written as follows [18]:

$$\delta = aF + bV \tag{5.1}$$

$$a = \frac{1}{k_c} = \frac{4L^3}{E_p w t_p^3} \frac{\alpha\beta(1+\beta)}{\alpha^2\beta^4 + 2\alpha\left(2\beta + 3\beta^2 + 2\beta^3\right) + 1}$$

$$b = \frac{3L^2}{t_p^2} \frac{\alpha\beta(1+\beta)}{\alpha^2\beta^4 + 2\alpha\left(2\beta + 3\beta^2 + 2\beta^3\right) + 1} d_{31}$$

$$\alpha = {E_s}/{E_p}, \qquad \beta = {t_s}/{t_p}$$

where the subscripts *s* and *p* stand for the slider and piezoelectric materials, respectively. *E* and *t* are the Young's modulus and beam thickness, respectively. *L* and *w* represent the length and width of the composite beam. k_c is the bending stiffness of the cantilever. d_{31} is the piezoelectric coefficient.

The deflections of the cantilever of three different slider thicknesses (0.3, 0.23, and 0.2 mm) per volt (without external force) were calculated according to Eq. (5.1) and were simulated by finite element analysis (FEA) with the results as shown in Fig. 5.5. It was found that an optimal thickness of the PZT exists for which the deflection is maximized for a given voltage and slider thickness.

According to Eq. (5.1) the cantilever is modeled as a single DOF mass-damper-spring system with (bending) stiffness k_c and damping c_c as shown in Fig. 5.4(b). k_c is determined by Eq. (5.1) and c_c is assumed to be zero in the calculation. The equivalent mass m_{eq} is calculated by the following equation,

$$m_{eq} = \frac{k_c}{\omega_n^2} \tag{5.2}$$

where ω_n is the first natural frequency of the cantilever obtained by finite element analysis. ω_n is about 3380 rad/s for a pico-sized slider with 300 μm thickness and 80 μm PZT plate as shown in Fig. 5.6. Since the bandwidth of the PZT itself is very high the bandwidth of cantilever actuator is primarily limited by the first resonant frequency of the structure, *i.e.* about 500 kHz in this case.

5.2.2 2-DOF Lumped Model of the Air Bearing and Its Parameter Identification

In this section we focus on the air bearing dynamics while the cantilever is fixed without moving relative to the rest of slider. For symmetric ABS designs and flying at 0° skew, the motion of the slider in the roll direction makes little contribution to the system response. However, the two pitch modes contribute to the slider's dynamics at the R/W transducer. This can be modeled as a 2-DOF system as shown in Fig. 5.7(a). The equation of motion of this model for free vibration can be expressed in the following form,

$$[m]\{\ddot{x}\} + [c]\{\dot{x}\} + [k]\{x\} = \{0\} \tag{5.3}$$

where

$$\{x\} = \begin{bmatrix} z_M \\ \theta \end{bmatrix}; \quad [m] = \begin{bmatrix} M & 0 \\ 0 & I_\theta \end{bmatrix};$$

$$[c] = \begin{bmatrix} c^* + c_l & -(d_t c^* - d_l c_l) \\ -(d_t c^* - d_l c_l) & d_t^2 c^* + d_l^2 c_l \end{bmatrix}$$

$$[k] = \begin{bmatrix} k^* + k_l & -(d_t k^* - d_l k_l) \\ -(d_t k^* - d_l k_l) & d_t^2 k^* + d_l^2 k_l \end{bmatrix},$$

in which z_M and θ are the displacement of the slider's mass center and the pitch angle of the slider with zero mean values, respectively. The slider's mass M and moment of inertia I_θ are 1.6x10^{-6} kg and 2.2x10^{-13} kg.m^2, respectively. The parameters that need to be identified are described as follows: k_l and k^* are the air bearing stiffness. c_l and c^* are the air bearing damping. d_l and d_t are the distance from the resultant air bearing force to the mass center of the slider. Index l or * represents the value at the leading (two pads) or trailing edge (three pads).

A linear modal analysis program developed in CML [15, 16] is used to identify the parameters. The method uses impulse responses of the slider to obtain the air bearing modal parameters, such as modal frequencies, damping ratios, mode shapes, and physical matrices (mass, stiffness, and damping). The impulse response is calculated by the constrained CML Dynamic Simulator, in which the slider's moment of inertia in the roll direction I_φ is increased to prohibit the slider from rolling and the linear disk velocity is 15 m/s. The initial impulse has to be extremely small to avoid nonlinearity. The deflection of the cantilever is implemented in the CML Dynamic Simulator by setting the relative heights of the central trailing pad and the other four pads.

Figure 5.8 shows the dynamic characteristics of the piezoelectric slider at a gap FH of 3 nm (with the cantilever actuator deflection of 24 nm). It shows the nodal lines of the two mode shapes, two modal frequencies and two damping ratios. The frequencies and damping ratios at several different FH's are shown in Table 5.1. The six parameters k^*, k_l, c^*, c_l, d_t, and d_l were determined algebraically by equating the six elements in the matrices [c] and [k] and those identified by the linear modal analysis approach. The calculated results are shown in Table 5.2. It is observed that only k^* and c^* exhibit significant nonlinearities. For the other four parameters, the linearized values about FH_{pt}= 2.35 nm are used in the following sections.

In the active mode of operation the cantilever actuator is expected to deflect dynamically. Hence, the central trailing pad, located at the end of the cantilever, has relative motion with respect to the other two trailing pads. A more realistic model is shown in Fig. 5.7(b), where k^* and c^* are decomposed into two parts, resulting in four parameters k_t, c_t, k, and c. k_t and c_t are the air bearing stiffness and damping coefficient at the two side trailing pads of the slider body. k and c are the stiffness and damping of the central trailing pad, which is located at the end of the cantilever actuator. l (= 0.595 mm) is the distance from the slider mass center to the read/write transducer. Since the FH at the two side trailing pads is usually more than 40 nm the linearized values of k_t and c_t are used. Table 5.3 shows the set of parameters for the 2-DOF model shown in Fig. 5.7(b). k and c are the only nonlinear elements and c_t is set to zero for simplicity. Figures 5.9 (a) and (b) show plots of *k* and *c* as functions of FH at the pole tip (PT). Among the three curve fitting laws, a natural logarithm curve is found to be the best fit to the stiffness within the range of interest, giving a $k(FH_{pt})$ in units of N/m as a function of FH at the PT (FH_{pt}) in units of nm

$$k(FH_{pt}) = \beta_k \cdot \ln(FH_{pt}) + \alpha_k \tag{5.4}$$

The coefficients β_k and α_k for this fit are determined to be -211456 and 460671, respectively.

The damping coefficient *c* is almost constant for FH_{pt} between 3 and 9. A linear curve fit is applied to *c* for FH_{pt} less than 3 nm, giving a $c(FH_{pt})$ in units of N.sec/m as a function of FH at the PT (FH_{pt}) in units of nm

$$c(FH_{pt}) = \beta_c \cdot FH_{pt} + \alpha_c \tag{5.5}$$

The coefficients β_c and α_c for this fit are determined to be 0.0044 and 0.005, respectively.

This nonlinear 2-DOF model was compared to the CML Dynamic Simulator by looking at impulse responses of the slider. The results for FHpt of 2.35nm are shown in Figs. 5.10 and 5.11 in both the time and frequency (FFT) domains. *H11* and *H21* are the responses in the z_M and θ directions due to an impulse in the z_M direction, respectively. The results for FHpt of 3 nm are also shown in Figs. 5.12 and 5.13. In both cases there is good agreement between the 2-DOF model and the CML Simulator.

5.2.3 Intermolecular and Electrostatic Forces

Due to the reduction in the spacing between the slider and the disk the threshold for new nanoscale phenomena will be crossed. In particular, new forces between the slider and disk come into play, such as intermolecular and electrostatic forces. A study of the effects of intermolecular forces and electrostatic forces was presented in Gupta and Bogy [9]. The intermolecular and electrostatic forces do not have a significant effect on the flying characteristics of high flying sliders (spacings greater than 10 nm), but they become increasingly important at low spacings (below 5 nm). These forces are attractive in nature and hence result in a reduction in fly height as compared to what would be the case without them. Experimental investigations have indicated that these short range forces are one of the major instability factors in ultra low HDI.

These short range attractive forces are considered to act on the cantilever tip, *i.e.*, the 1-DOF cantilever actuator.

$$F_{act} = F_{imf} + F_{elec}$$

where

$$F_{imf} = -\frac{A'}{\left(FH_{pt}\right)^3} + \frac{B'}{\left(FH_{pt}\right)^9} \tag{5.6}$$

$$F_{elec} = -\frac{1}{2}\varepsilon_0 k_e A_{eq} \frac{V^2}{\left(FH_{pt}\right)^2} \tag{5.7}$$

and where the constants α' and β' depend on the ABS design while A' ($1.8\text{x}10^{-30}$) and B' ($2.7\text{x}10^{-88}$) are related to the material properties of the slider and disk. In this paper, the values in Thornton [19] are used. The electrostatic force due to the electrical potential across the slider and disk is shown in Eq. (5.7). ε_o, k_e and V are the permittivity constant

(8.85×10^{-12} farad/m), dielectric constant of the medium (1 for air) and the potential difference between the slider and the disk. The constant A_{eq} in Eq. (5.7) is chosen such that the force agrees with that simulated by the CML Static Simulator. A comparison of the electrostatic forces between the CML Simulator and the model is shown in Fig. 5.14.

5.2.4 Nonlinear 3-DOF Lumped Model

Based on the analysis in the previous sections a nonlinear 3-DOF model is constructed as shown in Fig. 5.15 and the equation of motion is written as follows:

$$[m]\{\ddot{x}\} + [c]\{\dot{x}\} + [k]\{x\} = \{F\} \tag{5.8}$$

where

$$\{x\} = \begin{bmatrix} z_M \\ \theta \\ z_m \end{bmatrix}; \ [m] = \begin{bmatrix} M & 0 & 0 \\ 0 & I_\theta & 0 \\ 0 & 0 & m \end{bmatrix};$$

$$[c] = \begin{bmatrix} c_t + c_l + c_c & -(d_t c_t - d_l c_l - l c_c) & -c_c \\ -(d_t c_t - d_l c_l - l c_c) & d_t^2 c_t + d_l^2 c_l + d_c^2 c_c & l c_c \\ -c_c & l c_c & c + c_c \end{bmatrix}$$

$$[k] = \begin{bmatrix} k_t + k_l + k_c & -(d_t k_t - d_l k_l - l k_c) & -k_c \\ -(d_t k_t - d_l k_l - l k_c) & d_t^2 k_t + d_l^2 k_l + d_c^2 k_c & l k_c \\ -k_c & l k_c & k + k_c \end{bmatrix}$$

$$\{F\} = \begin{bmatrix} f_{dt} + f_{dl} \\ d_l f_{dl} - d_t f_{dt} \\ F_{act} - u + f_d \end{bmatrix} = \begin{bmatrix} k_t z_{dt} + c_t \dot{z}_{dt} + k_l z_{dl} + c_l \dot{z}_{dl} \\ -d_t\left(k_t z_{dt} + c_t \dot{z}_{dt}\right) + d_l\left(k_l z_{dl} + c_l \dot{z}_{dl}\right) \\ F_{act} - u + (k z_d + c \dot{z}_d) \end{bmatrix}$$

Note that the disk profile quantities z_{dt}, z_{dl}, and z_d are assumed unknown but bounded.

Numerical simulations were conducted to calculate the responses of the system over a harmonic wavy disk. The cantilever actuator is deflected at the FH_{pt} of 2.35 nm. The peak-to-peak amplitude of the waviness is assumed to be 2 nm, and three wavelengths are simulated: 1mm, 0.5mm, and 0.2mm, corresponding to frequencies of 15, 30, and 75 kHz at a linear disk velocity of 15 m/s. The FHM is obtained by subtracting z_d from z_m. Figure 5.16 shows the responses without including the short range forces. However, when the forces are included in the model, severe contacts were indicated and the slider could not fly stably.

5.3 Design of Nonlinear Compensators

The short range forces and disk waviness cause instability of the HDI and increase the FHM. It is desirable to compensate the forces and to suppress the modulation by feedback control. Because of the nonlinear components and uncertain disturbance in the air bearing systems, an observer-based nonlinear control or nonlinear compensator design approach is used [17]. A schematic diagram of the controller is shown in Fig. 5.17. Assuming that the real-time FH can be measured we first built an observer for the state estimation and designed a sliding control law using the observer as the plant.

Equation (5.8) is transformed into a state-space representation as follows:

$$\begin{cases} \dot{x} = Ax + Bu + f(x) + f_d \\ y = Cx \end{cases} \tag{5.9}$$

The control goal is to push the FHM to zero. If z_m is used as a state this will be a tracking problem, $z_m \rightarrow z_d$. However, the future z_d is unknown. In order to resolve this, a new state $z = z_m - z_d$ is used. The states of the system are

$$x = [x_1\ x_2\ x_3\ x_4\ x_5\ x_6]^T = [z_M\ \dot{z}_M\ \theta\ \dot{\theta}\ z\ \dot{z}]^T$$

And

$$A = \begin{bmatrix} 0 & 1 & 0 & 0 & 0 & 0 \\ -\frac{1}{M}(k_t + k_l + k_c) & -\frac{1}{M}(c_t + c_l + c_c) & -\frac{1}{M}(-d_t k_t + d_l k_l - l k_c) & -\frac{1}{M}(-d_t c_t + d_l c_l - l c_c) & \frac{k_c}{M} & \frac{c_c}{M} \\ 0 & 0 & 0 & 1 & 0 & 0 \\ -\frac{1}{I}(-d_t k_t + d_l k_l - l k_c) & -\frac{1}{I}(-d_t c_t + d_l c_l - l c_c) & -\frac{1}{I}(d_t^2 k_t + d_l^2 k_l + l^2 k_c) & -\frac{1}{I}(d_r^2 c_r + d_f^2 c_f + l^2 c_c) & -\frac{l k_c}{I} & -\frac{l c_c}{I} \\ 0 & 0 & 0 & 0 & 0 & 1 \\ \frac{k_c}{m} & \frac{c_c}{m} & -\frac{l k_c}{m} & -\frac{l c_c}{m} & -\frac{(k + k_c)}{m} & -\frac{(c + c_c)}{m} \end{bmatrix}$$

$$B = [0 \quad 0 \quad 0 \quad 0 \quad 0 \quad -\frac{1}{m}]^T; \quad C = [0 \quad 0 \quad 0 \quad 0 \quad 1 \quad 0]$$

$$f(x) = [0 \quad 0 \quad 0 \quad 0 \quad 0 \quad \frac{1}{m} F_{act}]^T$$

$$f_d = \begin{bmatrix} 0 \\ k_c z_d + c_c \dot{z}_d + \frac{1}{M}(k_t z_{dt} + c_t \dot{z}_{dt} + k_l z_{dl} + c_l \dot{z}_{dl}) \\ 0 \\ -l k_c z_d - l c_c \dot{z}_d + \frac{d_l}{I}(k_l z_{dl} + c_l \dot{z}_{dl}) - \frac{d_t}{I}(k_t z_{dt} + c_t \dot{z}_{dt}) \\ 0 \\ -\ddot{z}_d - \frac{1}{m}(k_c z_d + c_c \dot{z}_d) \end{bmatrix}$$

The observer is designed as

$$\dot{\hat{x}} = A\hat{x} + Bu + f(\hat{x}) + L(y - C\hat{x}) \tag{5.10}$$

The error dynamic is obtained by subtracting $\dot{x}$ from $\dot{\hat{x}}$

$$\dot{\tilde{x}} = \dot{\hat{x}} - \dot{x} = (A - LC)\tilde{x} - f_d \tag{5.11}$$

Note that ***f(.)*** and $\boldsymbol{f_d}$ represent the nonlinear components and disturbances, respectively.

The observer gain matrix ***L*** is chosen as in a Luenberger observer [20] so as to place the poles of (***A***-***LC***) at desired locations.

The sliding surface is defined as

$$s = \dot{\hat{x}}_5 + \lambda \hat{x}_5 \tag{5.12}$$

We then have

$$\begin{aligned} \dot{s} &= \dot{\hat{x}}_6 + \lambda \dot{\hat{x}}_5 \\ &= \frac{1}{m}[k_c\hat{x}_1 + c_c\hat{x}_2 - lk_c\hat{x}_3 - lc_c\hat{x}_4 - (k+k_c)\hat{x}_5 - (c+c_c)\hat{x}_6 + \\ &\quad F_{act} - u] + L_6(x_5 - \hat{x}_5) + \lambda[\hat{x}_6 + L_5(x_5 - \hat{x}_5)] \end{aligned} \tag{5.13}$$

The control law is designed as

$$\begin{aligned} u &= k_c\hat{x}_1 + c_c\hat{x}_2 - lk_c\hat{x}_3 - lc_c\hat{x}_4 - (k+k_c)\hat{x}_5 - (c+c_c)\hat{x}_6 + \\ &\quad F_{act} + m\lambda[\hat{x}_6 + L_5(x_5 - \hat{x}_5)] + mL_6(x_5 - \hat{x}_5) + m\eta s \end{aligned} \tag{5.14}$$

such that

$$\dot{s}s = -\eta s^2 < 0 \tag{5.15}$$

Eq. (5.15) guarantees that s approaches zero based on Lyapunov theory and drives the estimated FHM $\hat{x}_5$ to zero exponentially according to Eq. (5.12).

To investigate the controller's performance we conducted a large number of numerical simulation experiments. Figure 5.18 shows the results of FHM suppression with the same conditions as used in Fig. 5.16. The required AC control voltages are shown in Fig. 5.19. It is seen that the FHM is reduced almost to zero. The effects of intermolecular and electrostatic forces (0.5 V) are then included in the model. The histories of the cantilever deflection and short range attractive forces are shown in Figs. 5.21 and 5.22, respectively. Figure 5.20 shows that the FHM can be effectively suppressed even with an electrostatic potential of 0.5 V between the disk and slider (which is an unstable system without control). The applied control voltage is also shown in Fig. 5.20 (b). The observer performance is demonstrated by the comparison of the estimated and true FHM in Fig. 5.23 where it is seen that the error between the true and estimated values is very small.

When the electrostatic potential between the slider and disk increases from 0 V to 1 V (*i.e.* electrostatic forces increase), the mean control voltage shifts from 0 to about 3.3 V to compensate the increased electrostatic forces, as shown in Fig. 5.24. This DC shift can actually decrease the applied DC control voltage required to bring the cantilever into the active operational mode.

5.4 Conclusions

Due to the effects of short range forces and disk morphology it is unlikely that a passive air bearing slider will be able to form a reliable head-disk interface at a spacing much less than 5 nm. Substantial research has been carried out on contact recording, in which the slider is expected to be in full contact with the disk. Several design considerations have been given in the literature, but it is still unclear how to implement such systems, namely ABS design, lubricant, and protective overcoat.

In this chapter, a new 3-DOF dynamic model is proposed to model a FH control slider with a piezoelectric nanoactuator. A linear modal analysis is used to identify the air bearing parameters. Good agreement is obtained for the air bearing dynamics between the model and the CML Dynamic Simulator. An observer-based nonlinear sliding mode controller is designed based on the model. Numerical studies show that a FH below 3 nm is achieved and the FHM due to disk waviness is effectively reduced in the presence of short range attractive forces.

References

1. Yanagisawa, M., Sato, A., Ajiki, K., and Watanabe, F., "Design Concept of Contact Slider for High-Density Recording," *Electronics and Communications in Japan*, part 2, vol.80, pp.43-48, 1997.
2. Ono K., Iida K., and Takahashi K., "Effects of Design Parameters on Bouncing Vibrations of a Single-DOF Contact Slider and Necessary Design Conditions for Perfect Contact Sliding," *Journal of Tribology,* vol.121, no.3, pp.596-603, 1999.
3. Ono, K. and Takahashi, K., "Analysis of Bouncing Vibrations of a 2-DOF Tripad Contact Slider Model With Air Bearing Pads Over a Harmonic Wavy Disk Surface," *Journal of Tribology*, vol. 121, pp. 939-947, 1999.
4. Iida, K. and Ono, K., "Analysis of Bouncing Vibrations of a 2-DOF Model of Tripad Contact Slider Over a Random Wavy Disk Surface," *Journal of Tribology*, vol. 123, pp. 159-167, 2001.

5. Iida, K., Ono, K., and Yamane, M., "Dynamic Characteristics and Design Consideration of a Tripad Slider in the Near-Contact Regime," *Journal of Tribology*, vol.124, pp.600-606, 2002.
6. Ono K. and Iida K., "Statistical Analysis of Perfect Contact and Wear Durability Conditions of a Single-DOF Contact Slider," *Journal of Tribology*, vol.122, no.1, pp.238-245, 2000.
7. Iida, K. and Ono, K., "Design Consideration of Contact/ Near-Contact Sliders Based on a Rough Surface Contact Model," *Journal of Tribology,* vol.125, no.3, pp.562-570, 2003.
8. Yamane, M., Ono, K., and Yamaura, H., "2-DOF Analysis of Friction-Induced Slider Vibrations in a Near-Contact Regime," *Proceedings of STLE/ASME Int. Joint Tribology Conf*., Oct., 26-29 2003. TRIB-0046, 2003.
9. Gupta, V. and Bogy, D.B., "Dynamics of Sub-5nm Air Bearing Sliders in the Presence of Electrostatic and Intermolecular Forces at the Head Disk Interface," *IEEE Transactions on Magnetics*, vol. 41, pp. 510-615, 2005.
10. Kurita, M. and Suzuki, K., "Flying-Height Adjustment Technologies of Magnetic Head Sliders," *IEEE Transactions on Magnetics,* vol. 40, no. 1, pp. 332-336, 2004.
11. Kurita, M., Tsuchiyama, R., Tokuyama, M., Xu, J., Yoshimura, Y., Kohira, H., Su, L. Z., and Kato, K., "Flying-Height Adjustment of a Magnetic Head Slider with a Piezoelectric Micro-Actuator," *Intermag Conf.*, Boston, MA, pp. GP-06, 2003.

12. Tagawa, N., Kitamura, K., and Mori, A., "Design and Fabrication of MEMS-Based Active Sliders Using Double-Layered Composite PZT Thin Films in Hard Disk Drives," *IEEE Transactions on Magnetics*, vol. 39, no. 39, pp. 926-931, 2003.
13. Li, Amei, Liu, Xinqun, Clegg, W., Jenkins, D. F. L., and Donnelly, T., "Real-Time Method to Measure Head Disk Spacing Variation Under Vibration Conditions," *IEEE Trans. Instru. And Measur.*, vol. 52, no. 3, pp. 916-920, 2003.
14. Liu, Xinqun, Li, Amei, Clegg, W., Jenkins, D. F. L., and Davey, P., "Head-Disk Spacing Variation Suppression via Active Flying Height Control," *IEEE Trans. Instru. And Measur.*, vol. 51, no. 5, pp. 897-901, 2002.
15. Zeng, Q. H., Chen, L. S., and Bogy, D. B., , "A Modal Analysis Method for Slider-Air Bearings in Hard Disk Drives," Technical Chapter No. 96-021, Computer Mechanics Lab., Dept. of Mechanical Engineering, University of California at Berkeley 1996.
16. Zeng, Q. H. and Bogy, D. B., " The CML Slider-Air Bearing Parameter Identification Program," Technical Chapter No. 97-006, Computer Mechanics Lab., Dept. of Mechanical Engineering, University of California at Berkeley, 1997.
17. Song, B. and Hedrick, J. K., "Observer-Based Dynamic Surface Control for Lipschitz Nonlinear Systems," *42nd IEEE International Conference on Decision and Control*, Piscataway, NJ, USA, pp. 874-9, 2003.

18. Smits, J. G. and Choi, W.-S., “The Constituent Equations of Piezoelectric Heterogeneous Bimorphs,” *IEEE Trans. Ultrason., Ferroelect., Freq. Contr.*, vol. 38, no. 3, pp. 256-270, 1991.
19. Thornton, B. H. and Bogy, D. B., “A Parametric Study of Head-Disk Interface Instability Due to Intermolecular Forces,” *IEEE Transactions on Magnetics*, vol. 40, no. 1, pp. 337-344, 2004.
20. Ogata, K., 1967, “State Space Analysis of Control Systems,” Englewood Cliffs, N.J., Prentice-Hall.

Table 5.1. The results of parameter identification of 2-DOF air bearing at five flying heights.

FH_{pt} (nm)	Deflection (nm)	pitch (μrad)	Frequency 1 (kHz)	Frequency 2 (kHz)	Damping ratio 1 (%)	Damping ratio 2 (%)
0.41	35	209.52	70	232	4.7817	0.4452
0.70	33	212.32	70	217	4.7304	0.6563
2.35	26	221.19	69	175	4.8100	1.4600
3.07	24	223.34	69	165	4.8500	1.7500
20.22	0	235.10	68	112	5.2300	2.6800

Table 5.2. The results of parameter identification of 2-DOF air bearing at five flying heights.

FH_{pt} (nm)	k (MN/m)	c (N.sec/m)	k_t (MN/m)	k_l (MN/m)	c_l (N.sec/m)	d_l (mm)	d_t (mm)
0.41	0.69	0.00650	0.3	0.194725	0.04386	0.2717	0.5358
1.75	0.35	0.01300	0.3	0.194725	0.04386	0.2717	0.5358
2.35	0.28	0.01554	0.3	0.194725	0.04386	0.2717	0.5358
3.07	0.225	0.01800	0.3	0.194725	0.04386	0.2717	0.5358
5.75	0.105	0.01900	0.3	0.194725	0.04386	0.2717	0.5358
9.02	0.04	0.01900	0.3	0.194725	0.04386	0.2717	0.5358

Table 5.3. The identified k and c1 at several flying heights with other parameters as in the case of 2.35 nm. The value of c is set to be zero.

FH_{pt} (nm)	k (MN/m)	c (N.sec/m)	k_t (MN/m)	k_l (MN/m)	c_l (N.sec/m)	d_l (mm)	d_t (mm)
0.41	0.69	0.00650	0.3	0.194725	0.04386	0.2717	0.5358
1.75	0.35	0.01300	0.3	0.194725	0.04386	0.2717	0.5358
2.35	0.28	0.01554	0.3	0.194725	0.04386	0.2717	0.5358
3.07	0.225	0.01800	0.3	0.194725	0.04386	0.2717	0.5358
5.75	0.105	0.01900	0.3	0.194725	0.04386	0.2717	0.5358
9.02	0.04	0.01900	0.3	0.194725	0.04386	0.2717	0.5358

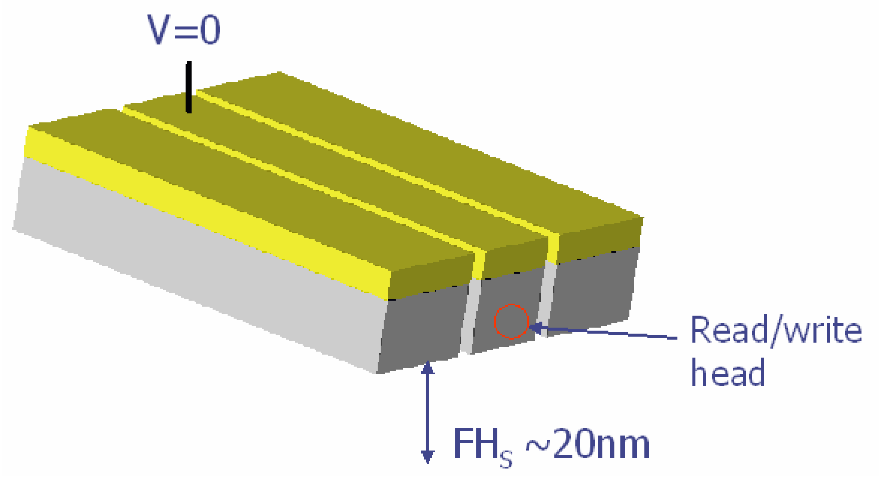

(a) Passive mode (no control algorithm is applied)

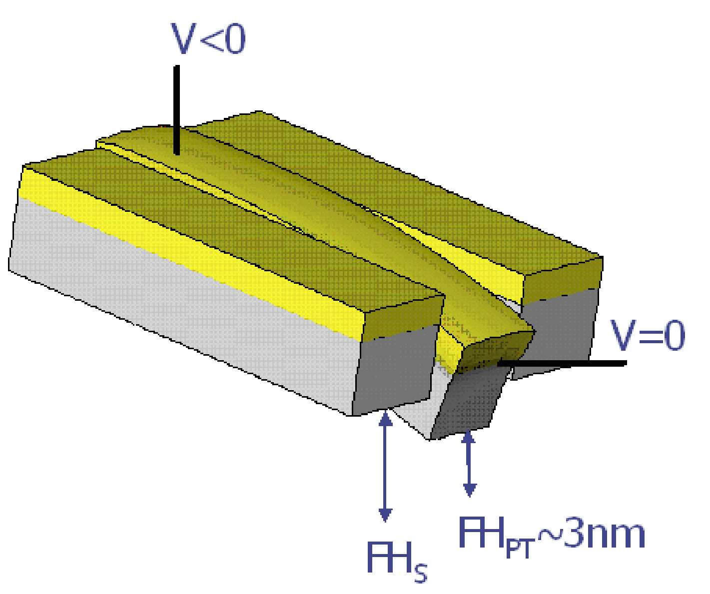

(b) Active mode (control algorithm is applied)

Fig. 5.1. Two operational modes of a controlled flying proximity slider with PZT actuation. The R/W transducer is not shown in this diagram.

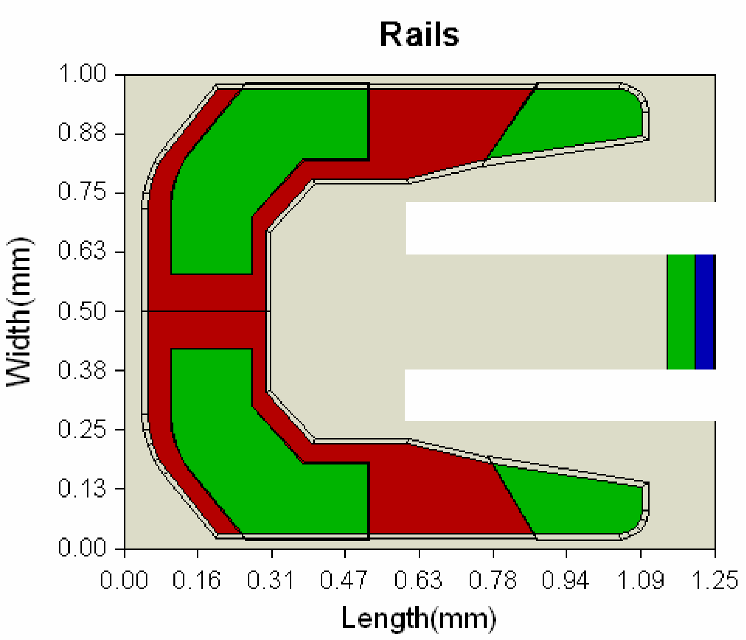

Fig. 5.2 An ABS design of CFP sliders

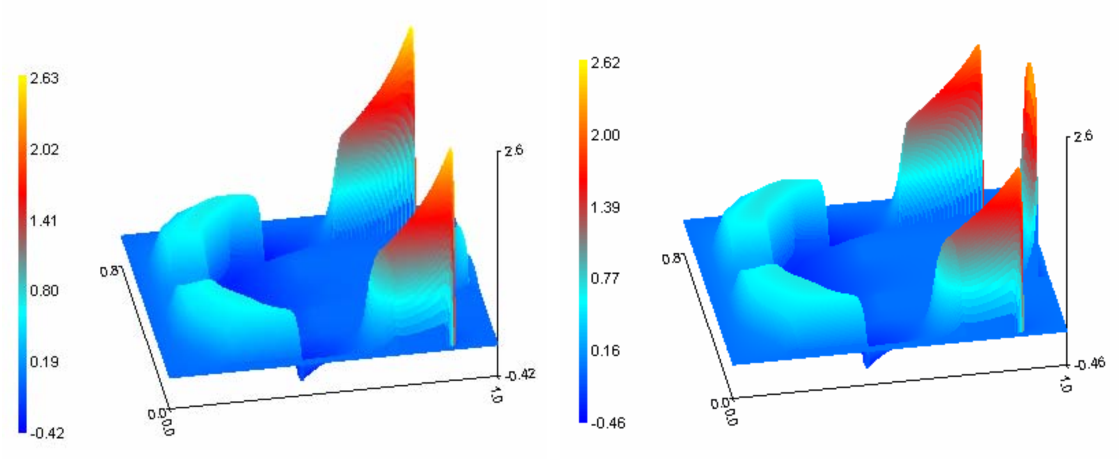

(a) (b)

Fig. 5.3. Air pressure distributions of the ABS in Fig. 5.2. (a) passive mode and (b) active mode. The gap flying height has been reduced from 20 nm to 2.35 nm.

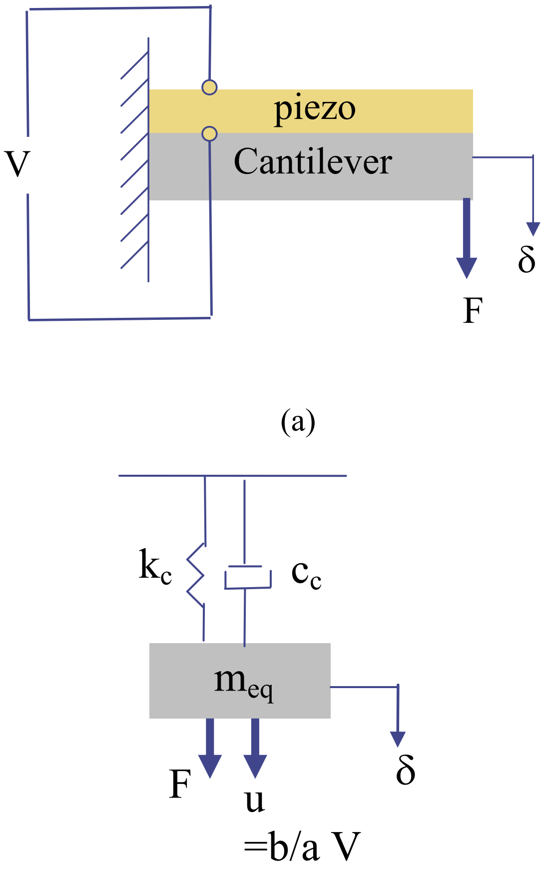

(a)

(b)

Fig. 5.4. Schematic diagram of a piezoelectric composite beam actuator (a) and the 1-DOF model.

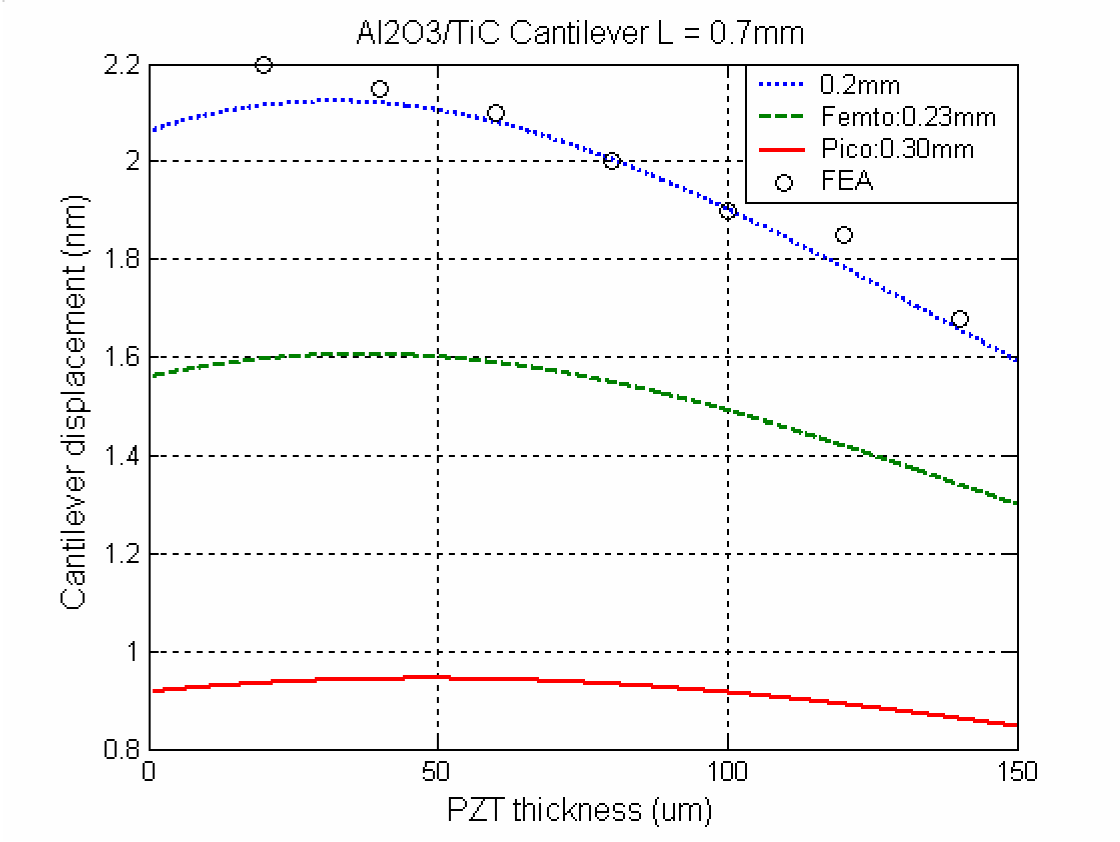

Fig. 5.5. The deflection of the cantilever tip under 1V. The solid line is for a pico-slider thickness, the dash line is for the femto slider thickness. FEA shows the results carried out by finite element analysis. E_p=62GPa, E_c=398GPa, d_{31}=-360x10^{-12}m/V.

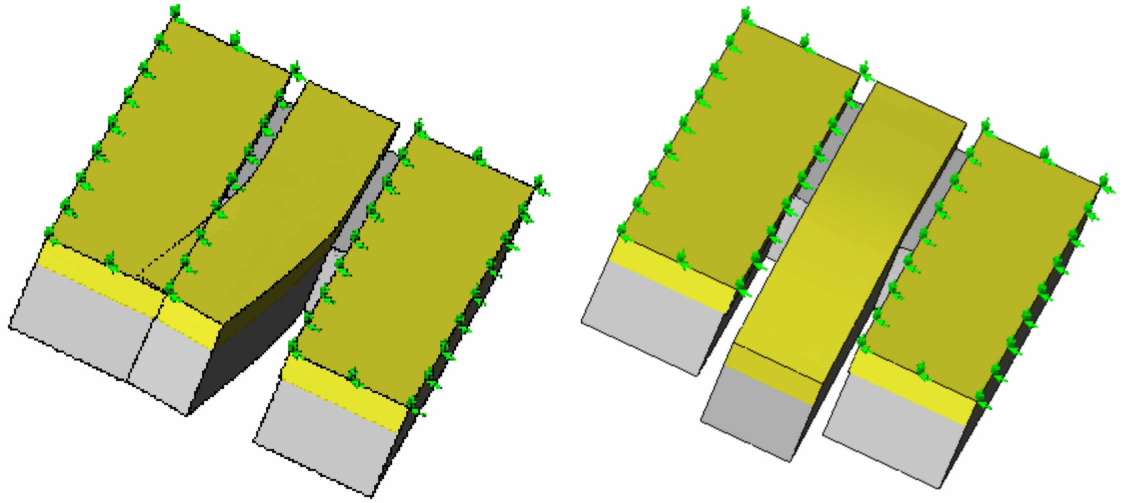

(a) the first mode (in-plane) (b) the second mode (out-of-plane)

Fig. 5.6. The first two modes of a pico-sized CFP slider simulated by finite element analysis (COSMOSDesignSTAR®). The natural frequencies are 538 and 550 kHz. (Slider thickness=300 μm, PZT thickness=80 μm).

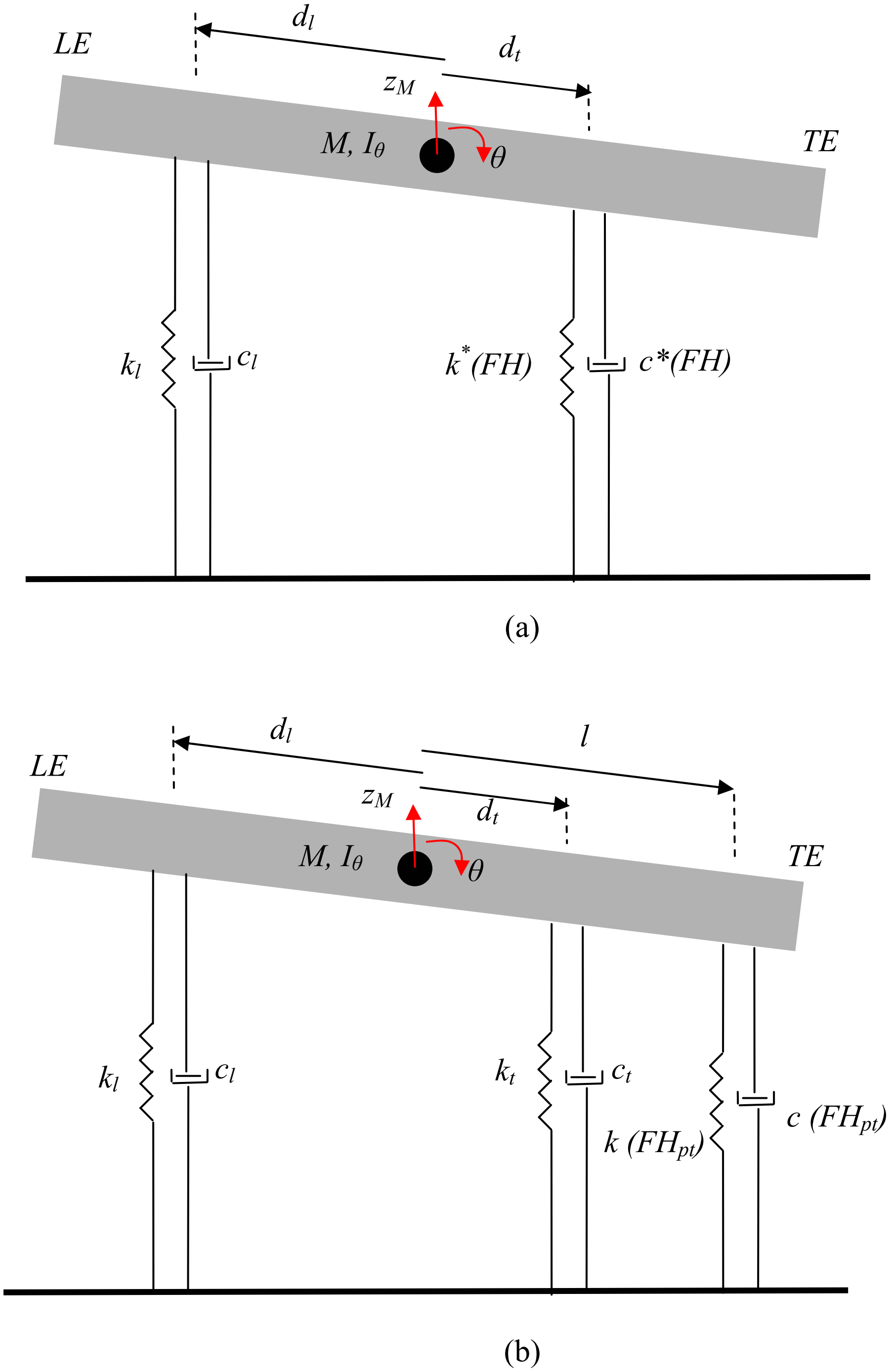

Fig. 5.7. Schematic diagram of 2-DOF dynamic model of CFP sliders. The cantilever is fixed such that there is no relative motion between the slider and the cantilever.

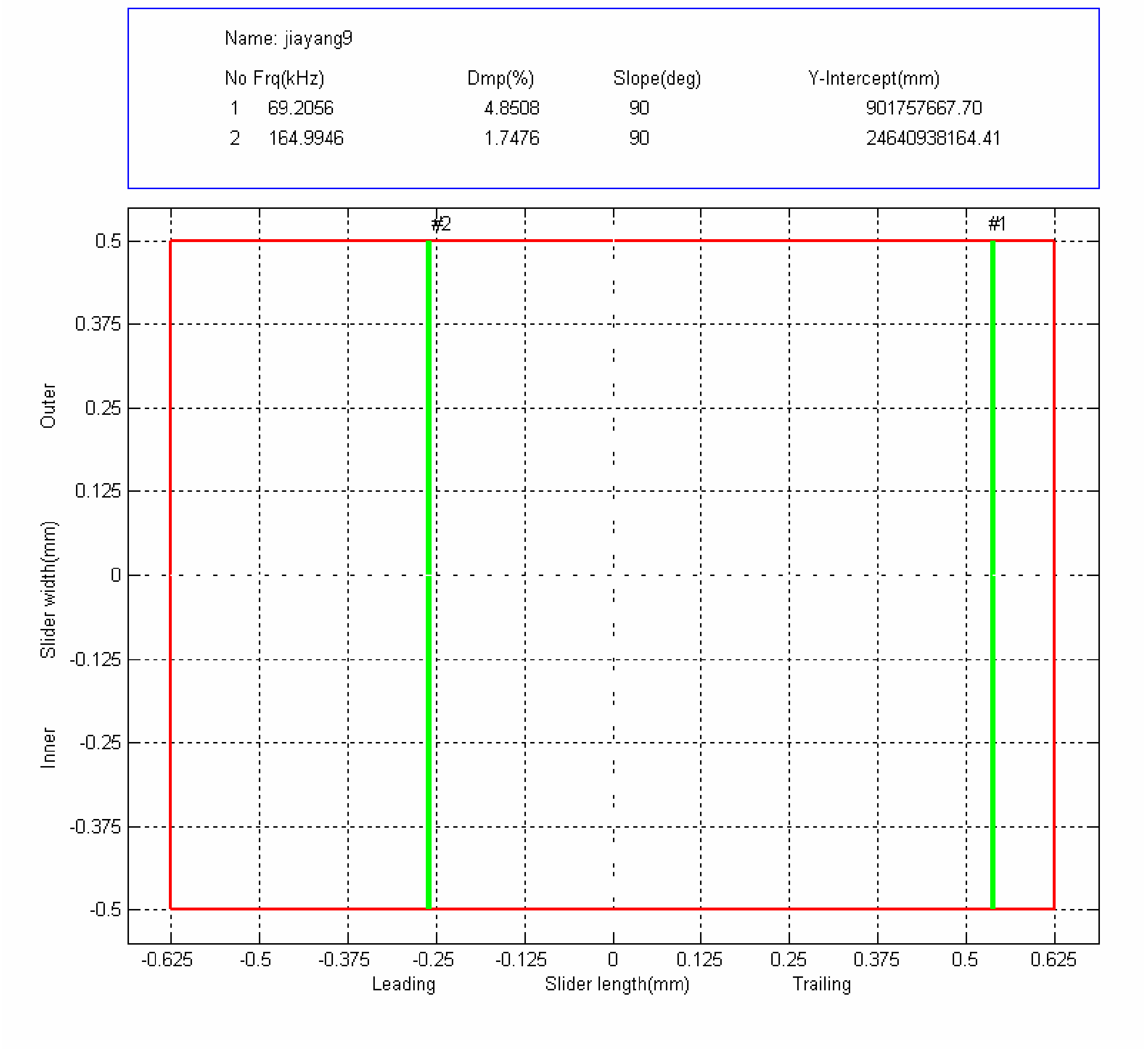

Name: jiayang9

No	Frq(kHz)	Dmp(%)	Slope(deg)	Y-Intercept(mm)
1	69.2056	4.8508	90	901757667.70
2	164.9946	1.7476	90	24640938164.41

Fig. 5.8. Dynamic characteristics of the CFP slider at FHpt = 3.07 nm.

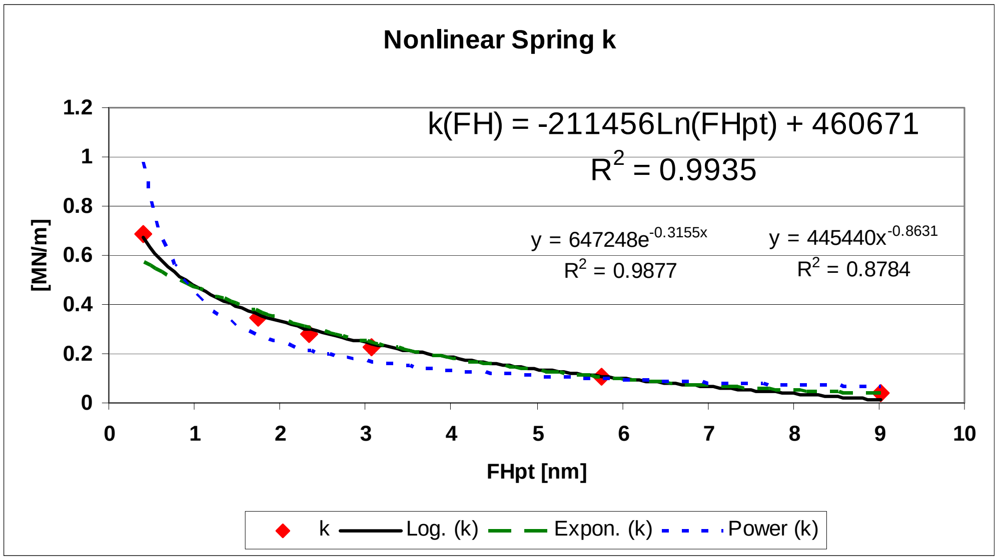

(a)

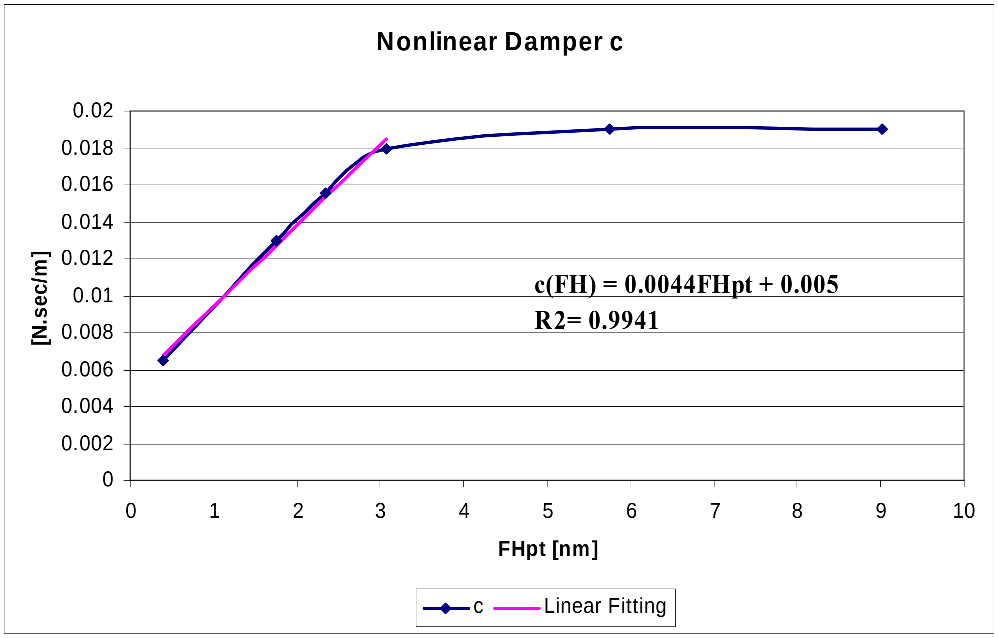

(b)

Fig. 5.9. (a) Nonlinear stiffness k and (b) nonlinear damping c1 as a function of FH at the PT.

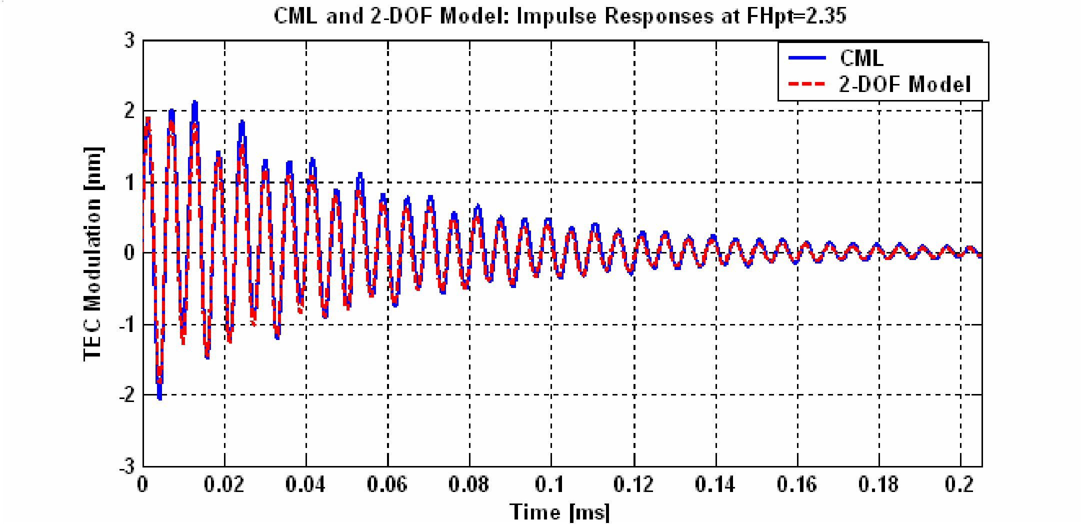

(a)

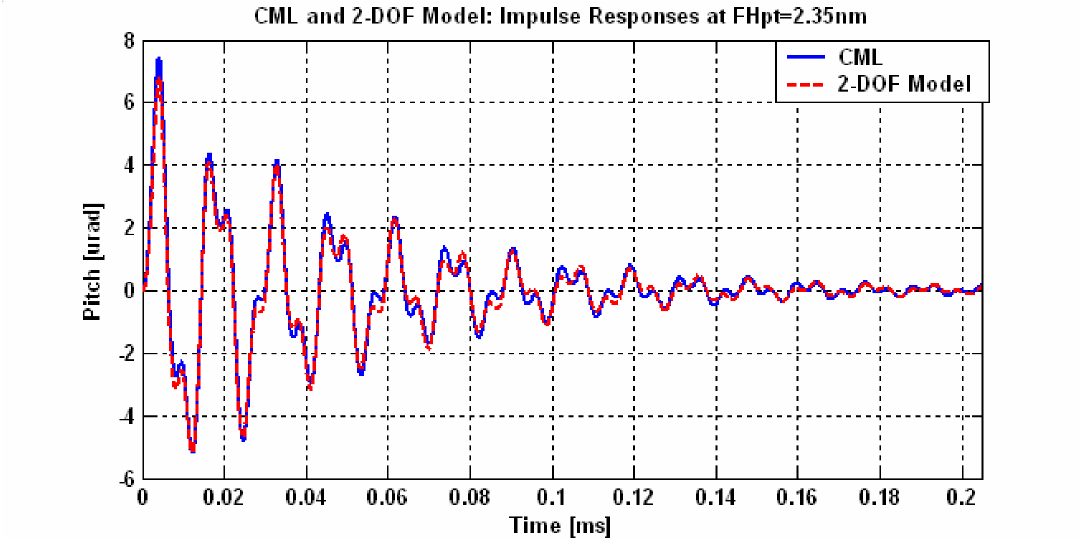

(b)

Fig. 5.10. Impulse responses (initial velocity 0.002 m/s in z direction) of CFP slider simulated by the 2-DOF model and the CML Dynamic Simulator: (a) TEC FH modulation and (b) pitch modulation about the equilibrium of FH_{pt} = 2.35nm.

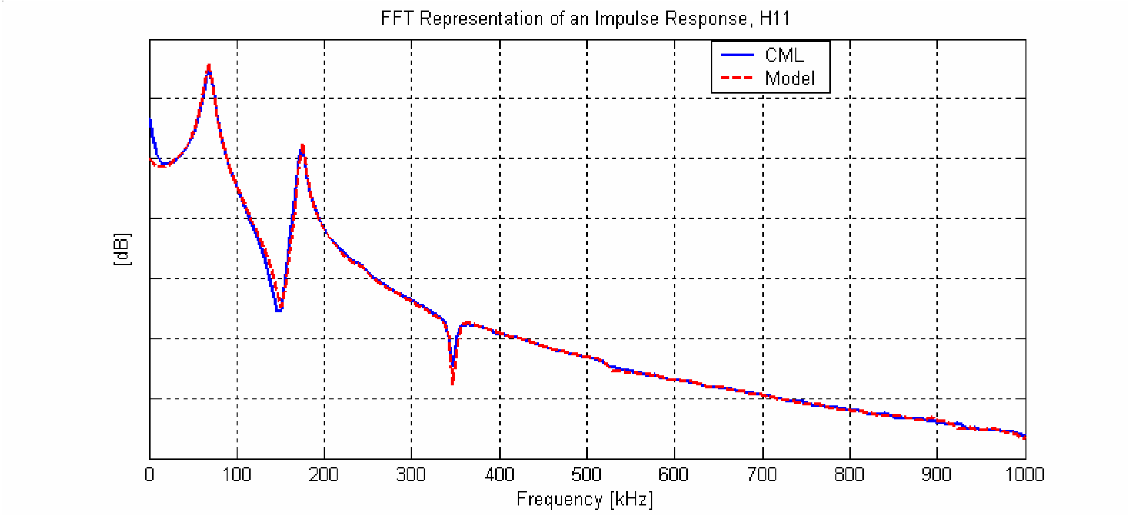

(a)

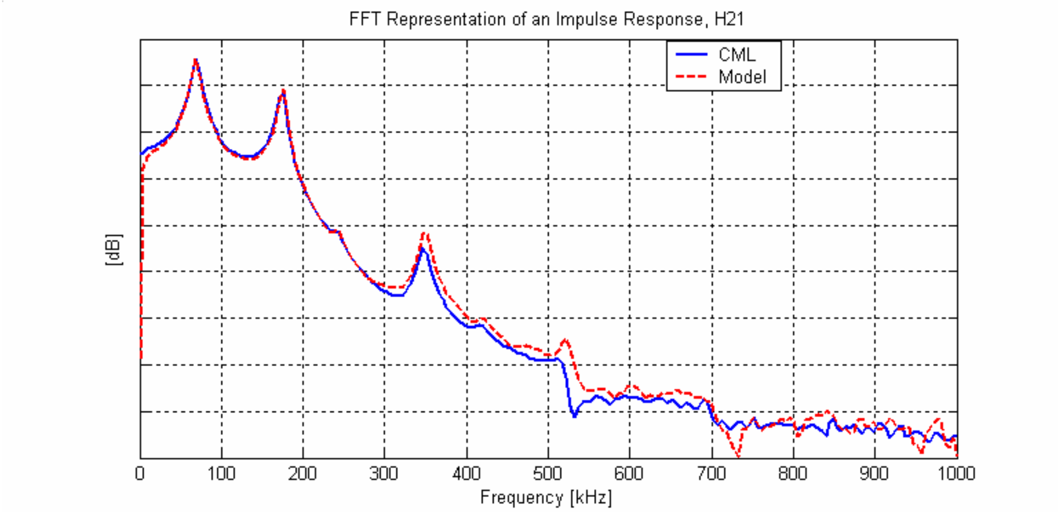

(b)

Fig. 5.11. Impulse responses (initial velocity 0.002 m/s in z direction) of CFP slider simulated by the 2-DOF model and the CML Dynamic Simulator shown in the frequency (FFT) domains: (a) the response of TEC FH and (b) the response of pitch about the equilibrium of FHpt = 2.35nm.

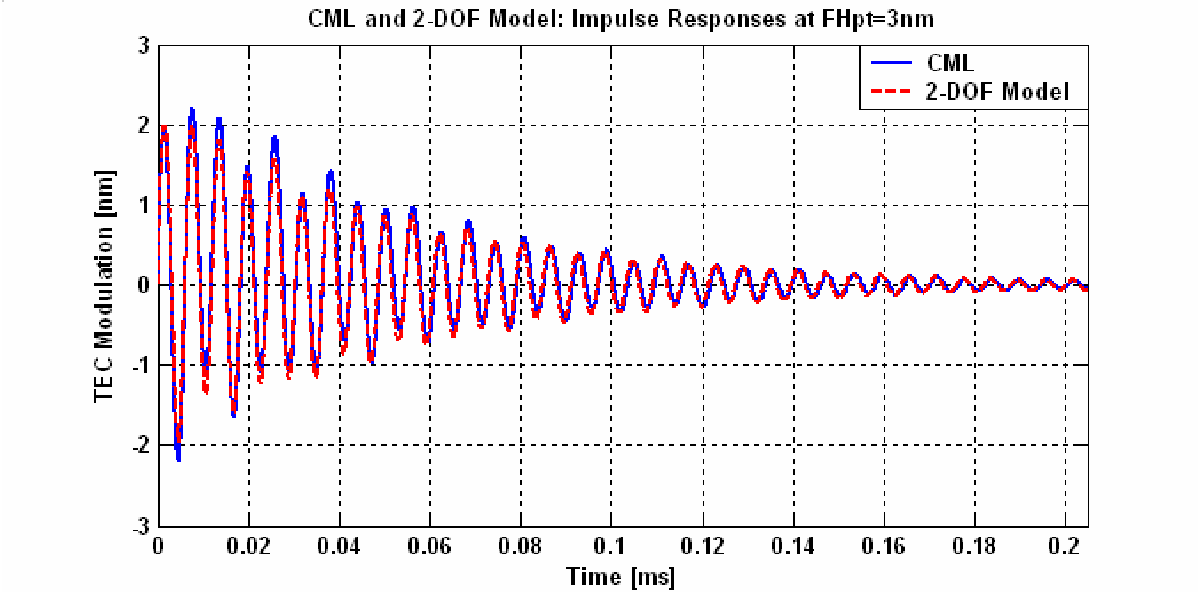

(a)

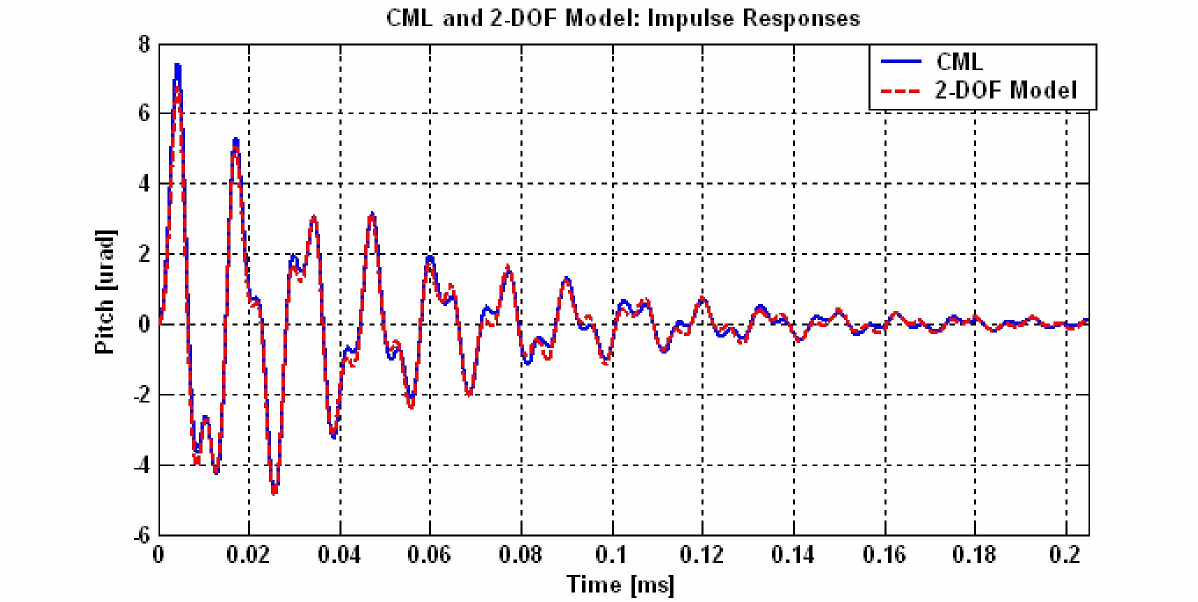

(b)

Fig. 5.12. Impulse responses (initial velocity 0.002 m/s in z direction) of CFP slider simulated by the 2-DOF model and the CML Dynamic Simulator: (a) TEC FH modulation and (b) pitch modulation about the equilibrium of FH_{pt} = 3.07nm.

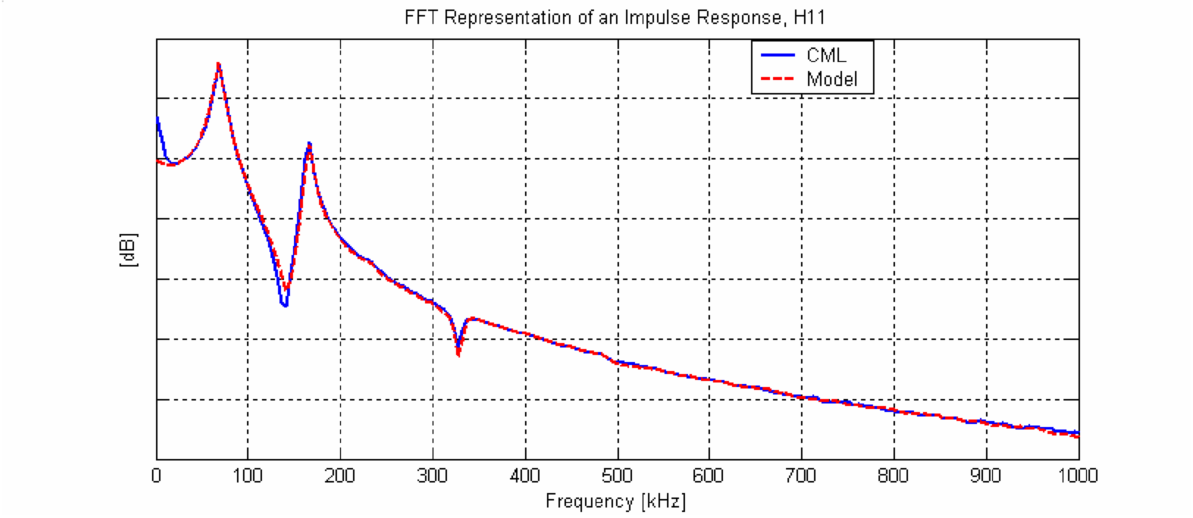

(a)

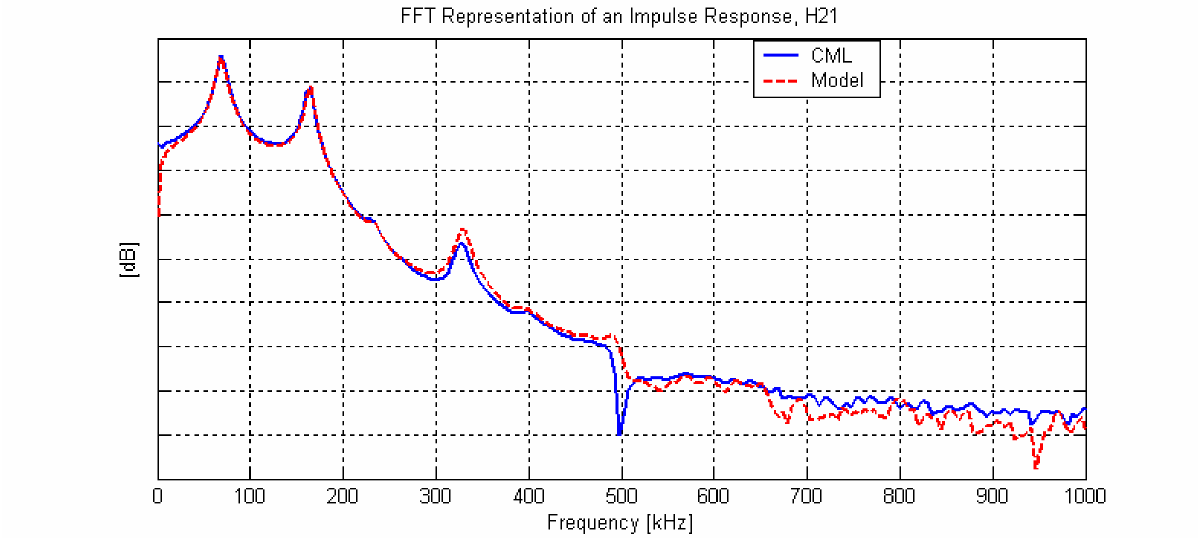

(b)

Fig. 5.13. Impulse responses (initial velocity 0.002 m/s in z direction) of CFP slider simulated by the 2-DOF model and the CML Dynamic Simulator shown in the frequency (FFT) domains: (a) the response of TEC FH and (b) the response of pitch about the equilibrium of FHpt = 3.07nm.

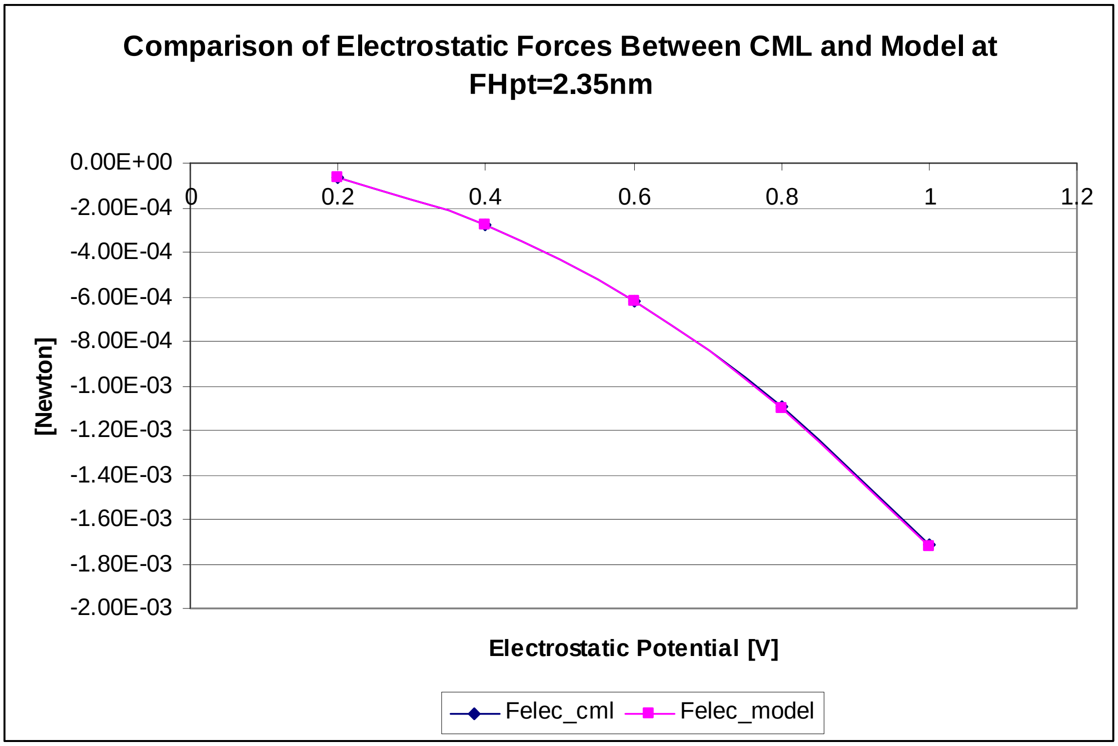

Fig.5.14 . Comparison of electrostatic forces between CML Simulator and model. The forces are calculated when the slider is fixed at FHpt = 2.35 nm and pitch = 221 μrad.

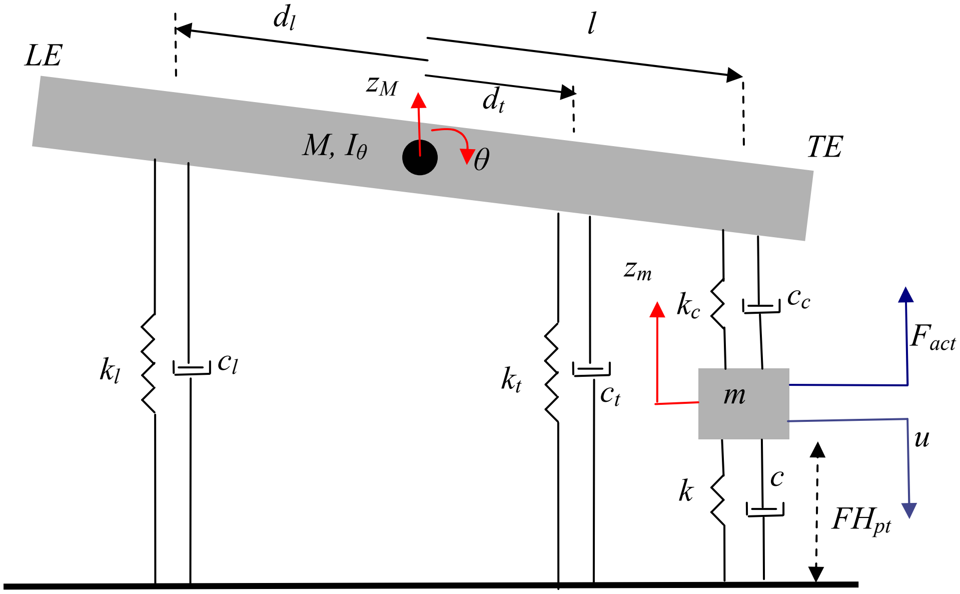

Fig. 5.15. Schematic diagram of 3-DOF dynamic model of CFP sliders.

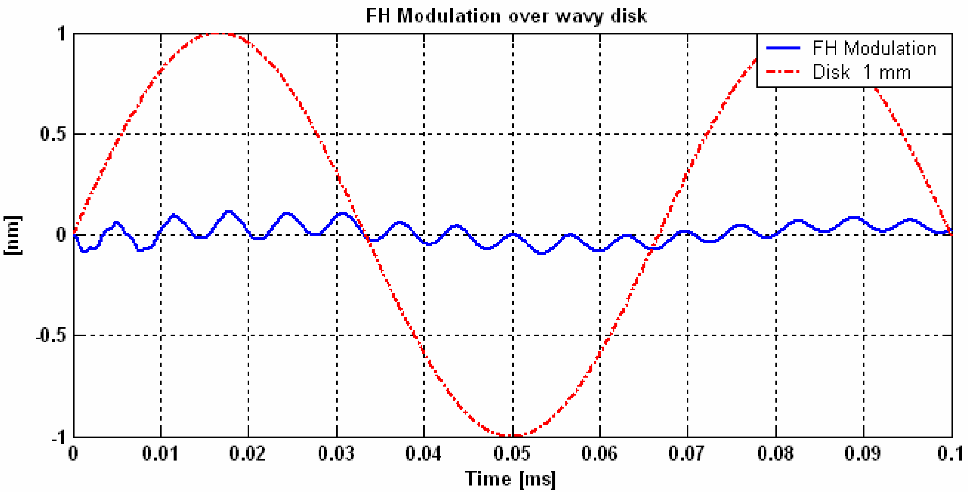

(a) The wavelength of disk waviness: 1 mm

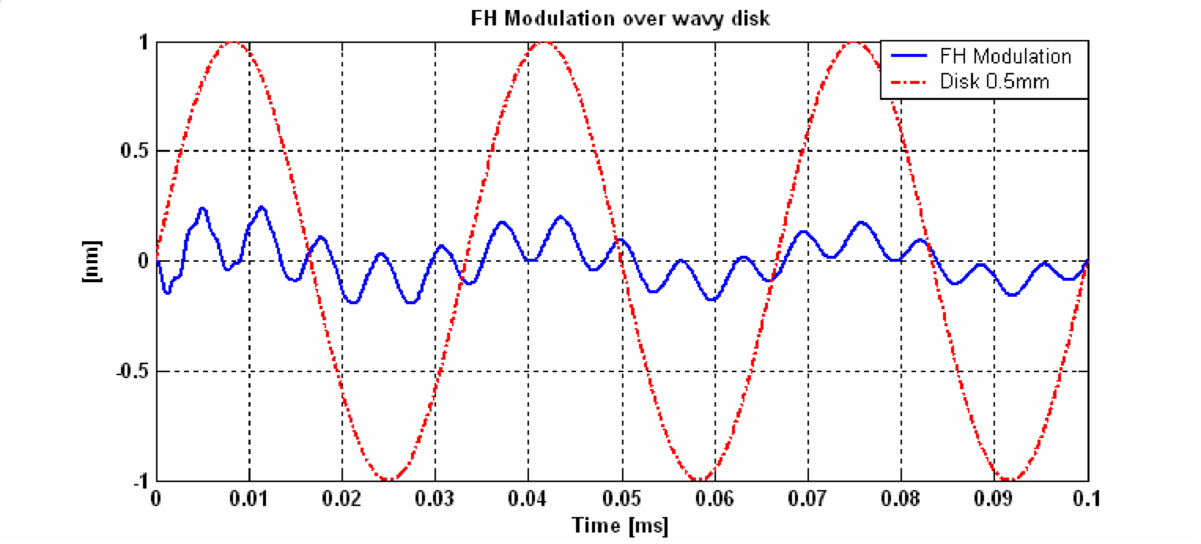

(b) The wavelength of disk waviness: 0.5 mm

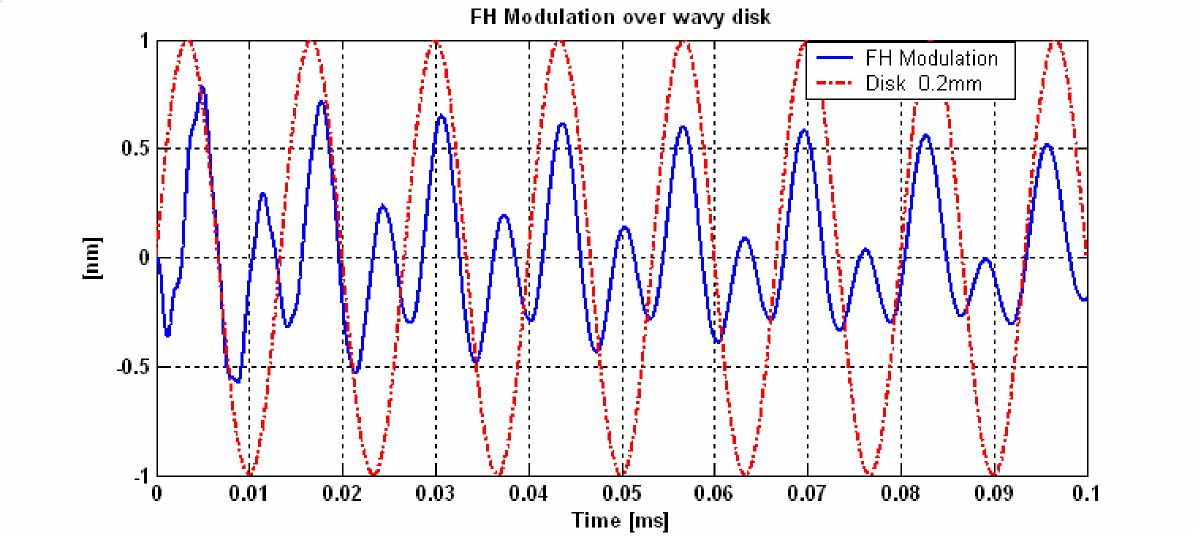

(c) The wavelength of disk waviness: 0.2 mm

Fig. 5.16. FHM of 3-DOF over three disk wavelengths without short range forces.

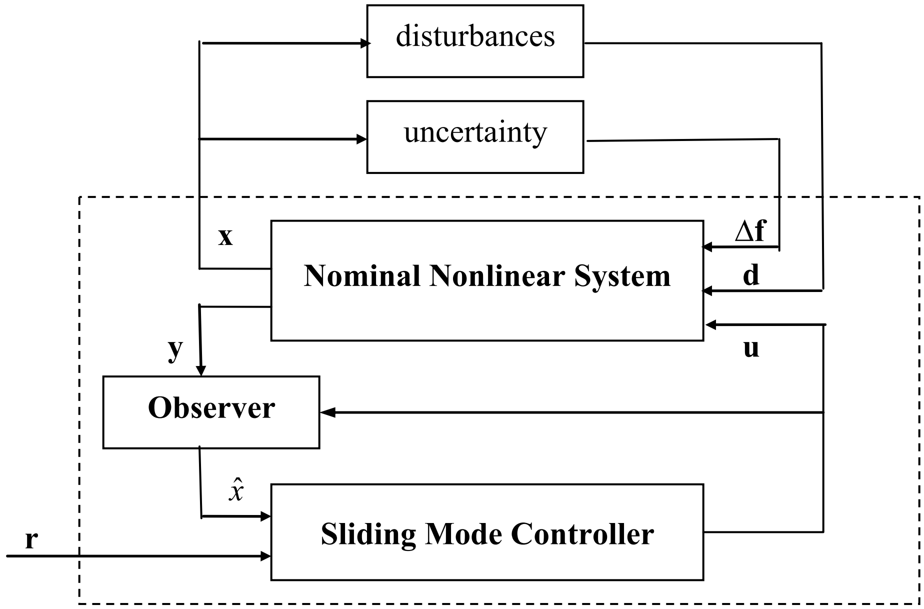

Fig. 5.17. Schematic framework of observer-based sliding mode controller.

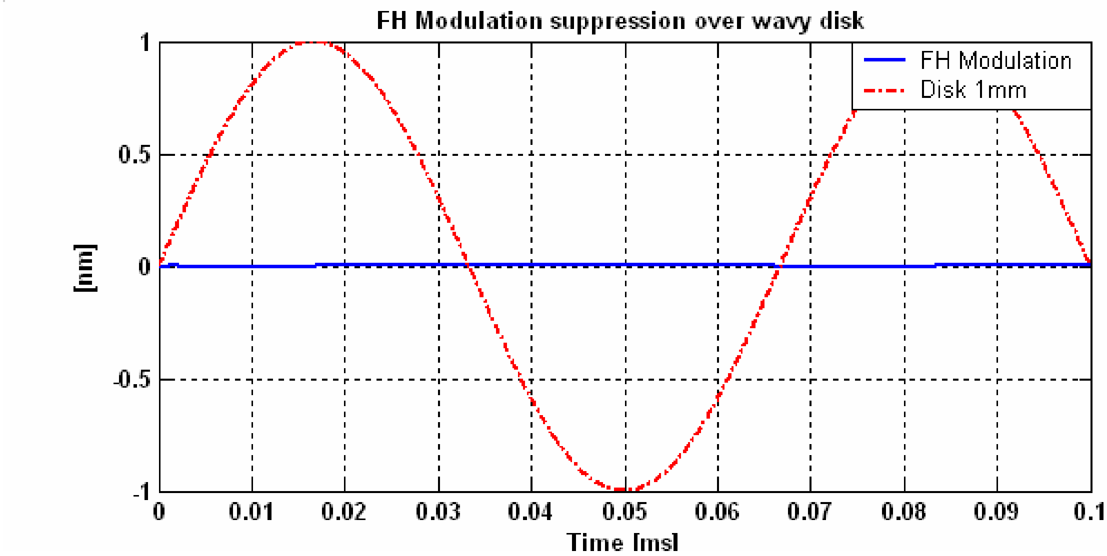

(a) The wavelength of disk waviness : 1 mm

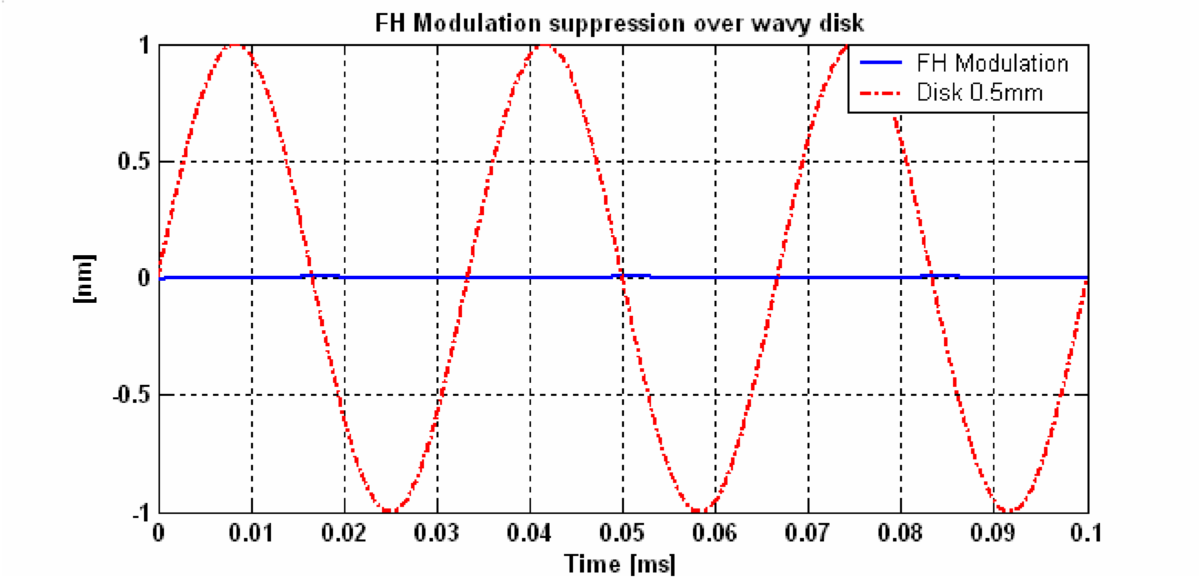

(b) The wavelength of disk waviness: 0.5 mm

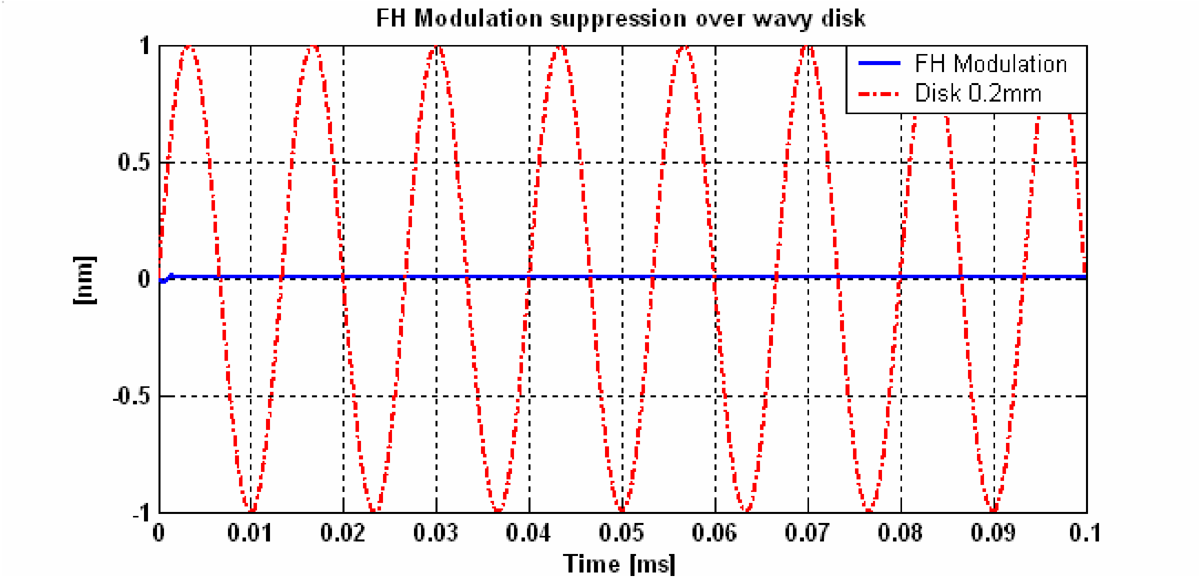

(c) The wavelength of disk waviness: 0.2 mm

Fig. 5.18. The results of FHM suppression of the CFP slider. Simulations conditions are the same as those in Fig. 5.16.

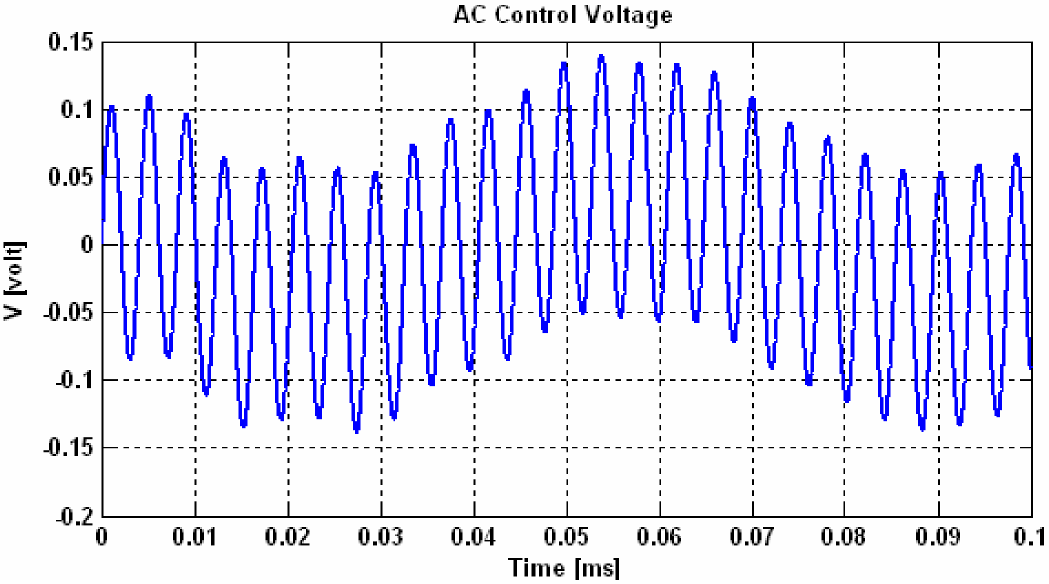
AC Control Voltage
V [volt]
0.15
0.1
0.05
0
-0.05
-0.1
-0.15
-0.2
0
0.01
0.02
0.03
0.04
0.05
0.06
0.07
0.08
0.09
0.1
Time [ms]

(a)

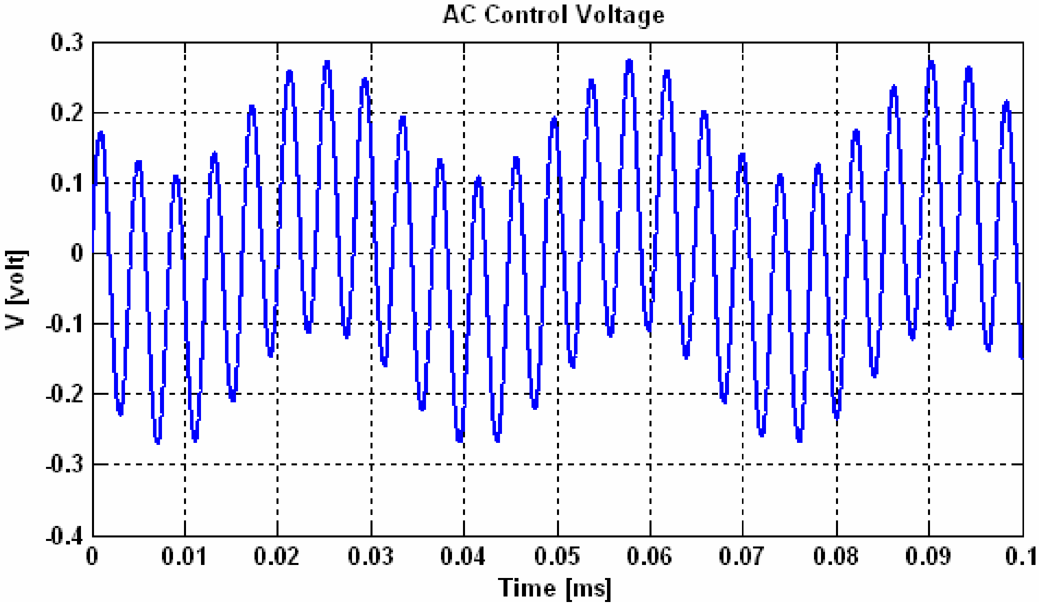
AC Control Voltage
V [volt]
0.3
0.2
0.1
0
-0.1
-0.2
-0.3
-0.4
0
0.01
0.02
0.03
0.04
0.05
0.06
0.07
0.08
0.09
0.1
Time [ms]

(b)

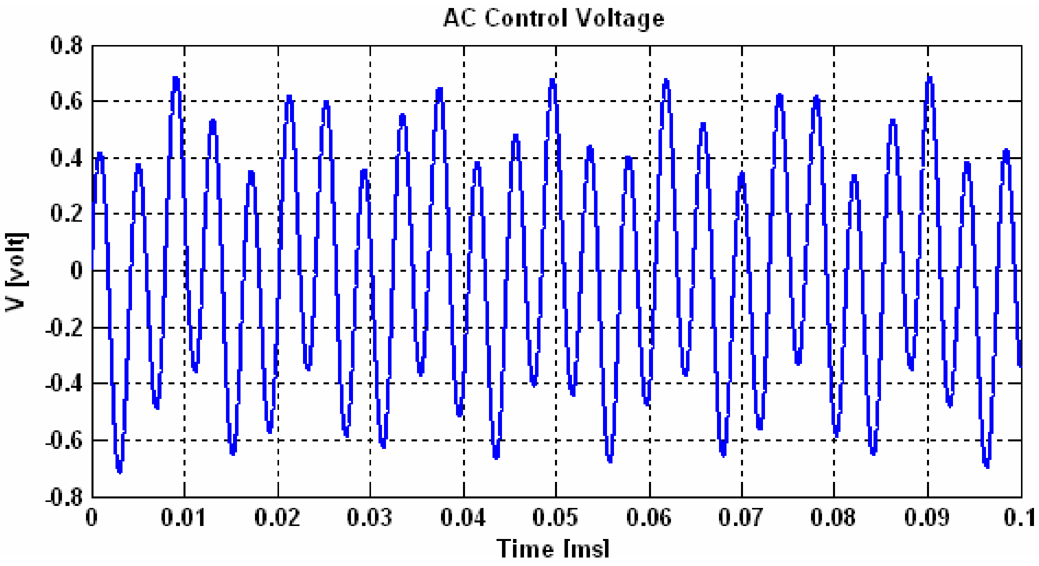

(c)

Fig. 5.19. The voltage determined by the control law for cases in Fig. 5.18.

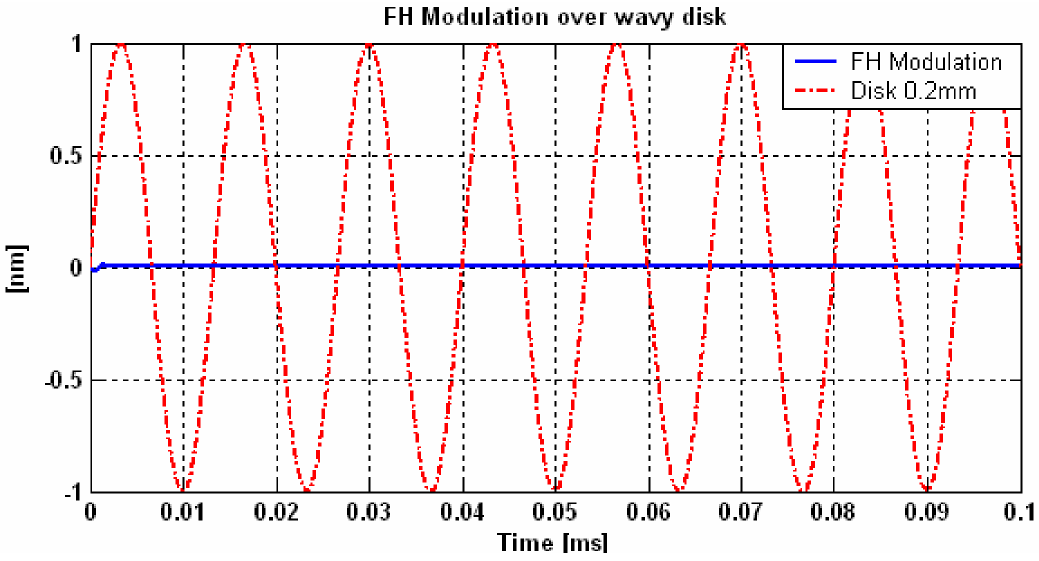

(a)

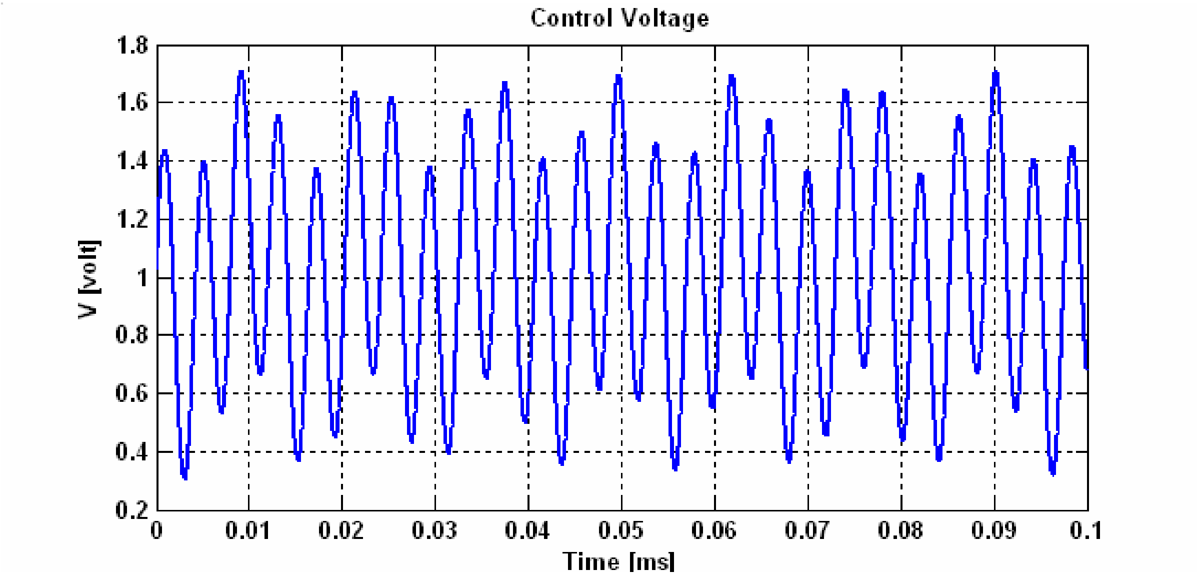

(b)

Fig. 5.20. (a) The results of FHM suppression of the CFP slider in the presence of intermolecular and electrostatic forces (0.5 V). The disk waviness wavelength is 0.2 mm. (b) the control voltage.

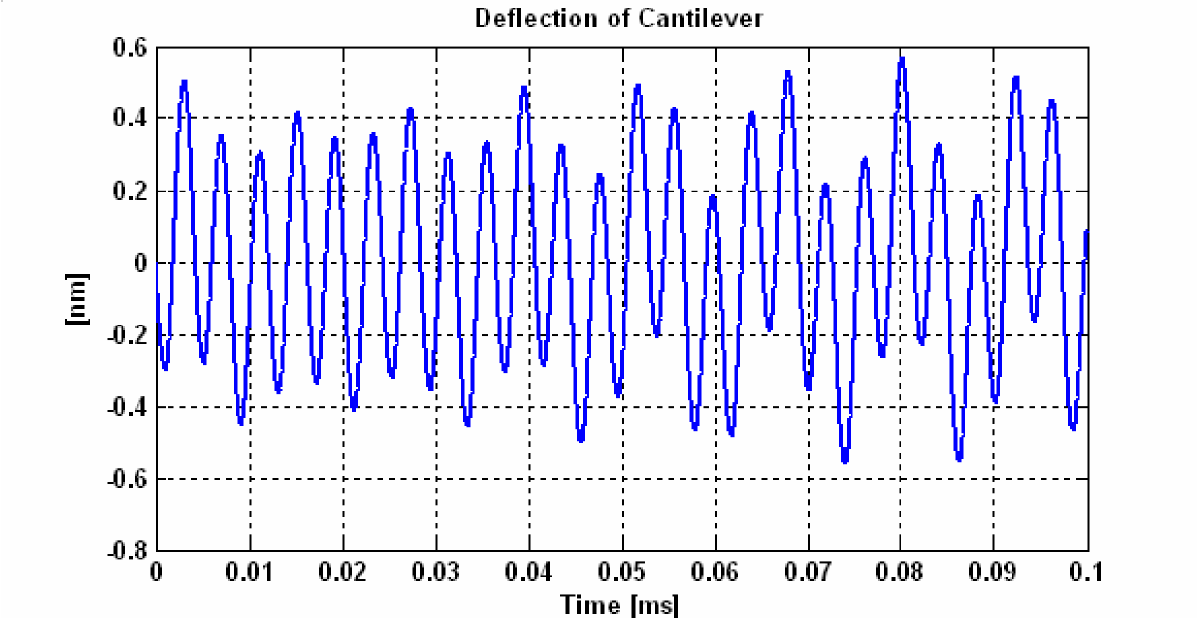

Fig. 5.21. Deflection of the cantilever actuator.

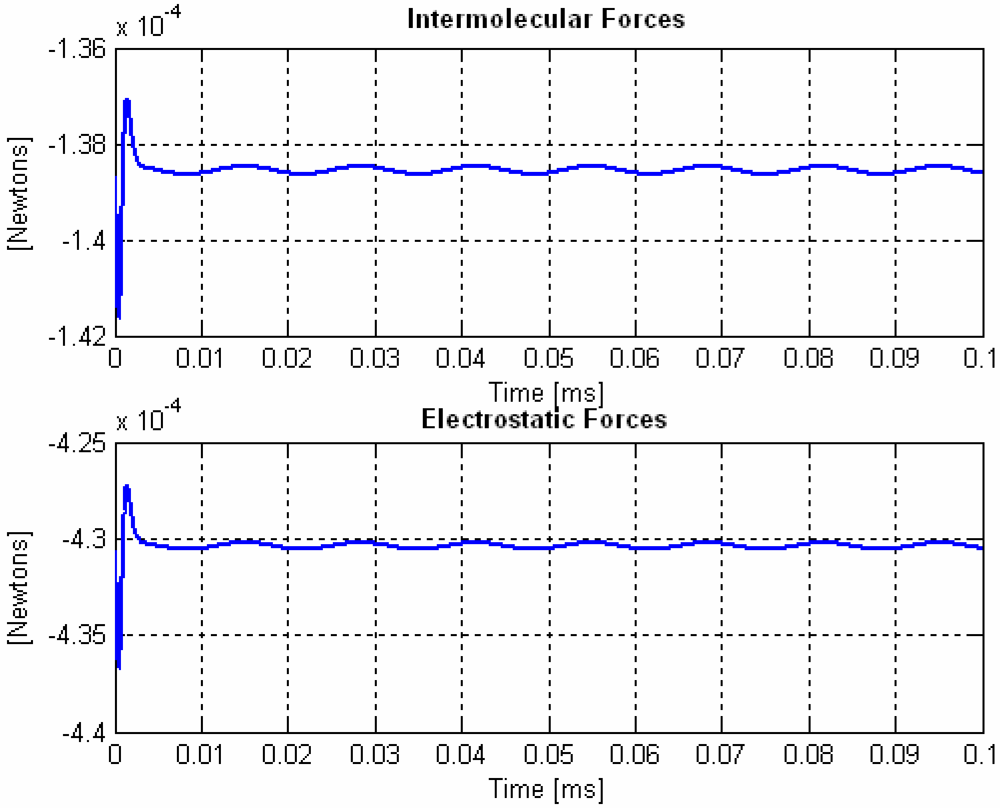

Fig. 5.22. The intermolecular and electrostatic forces (0.5V).

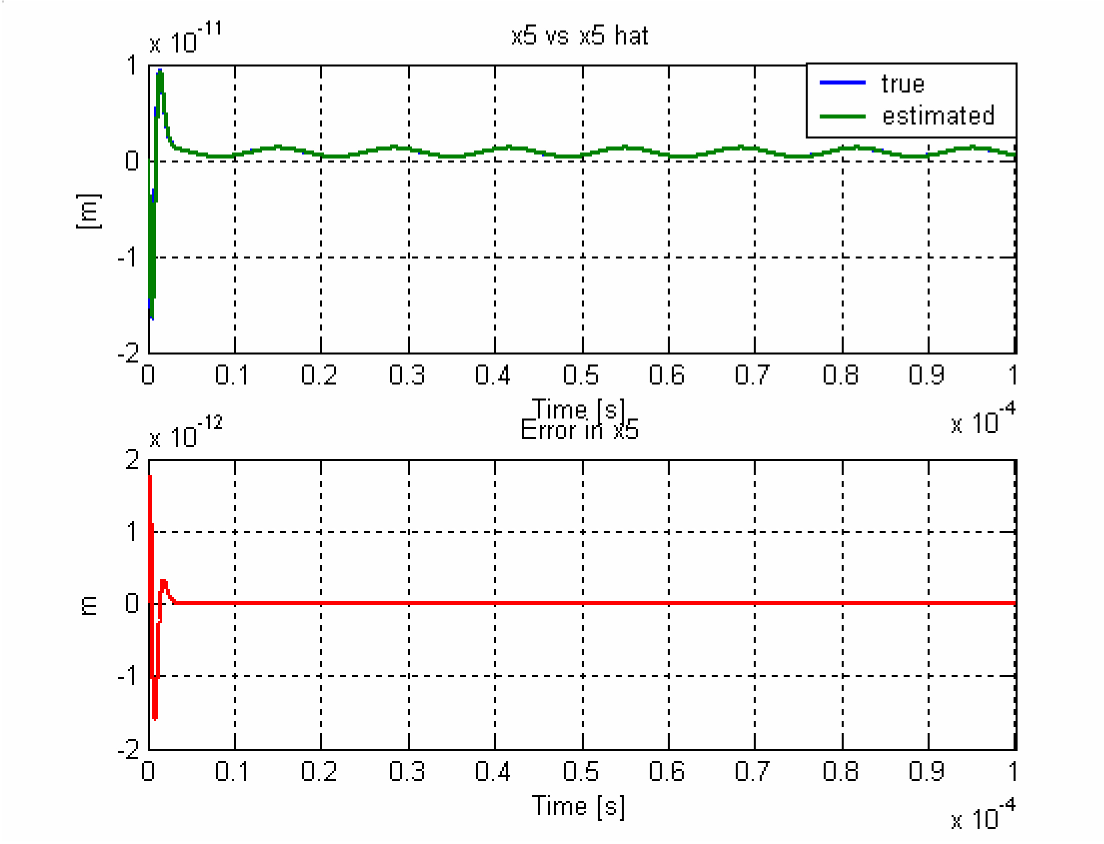

Fig. 5.23. True and estimated FHM (x_5).

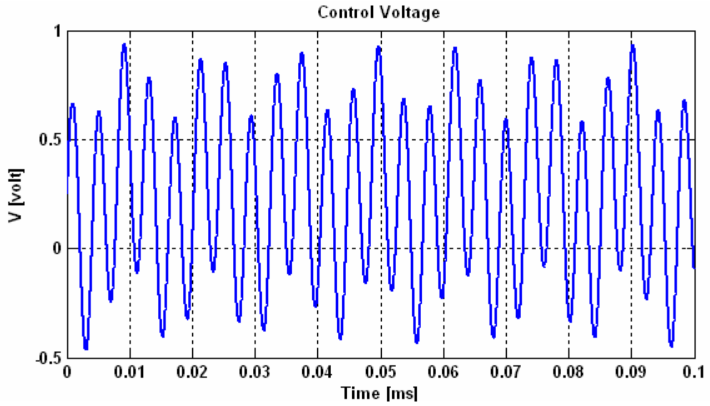

(a) Electrostatic potential 0 V

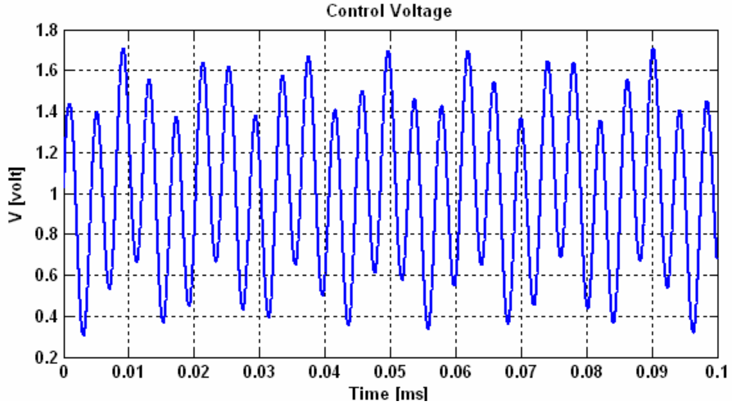

(b) Electrostatic potential 0.5 V

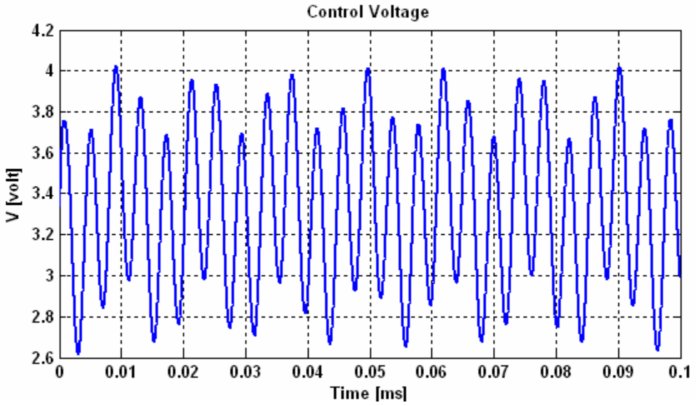

(c) Electrostatic potential 1 V

Fig. 5.24. Control voltages for different electrostatic potentials. The disk waviness wavelength is 0.2 mm.

CHAPTER 6

AIR BEARING EFFECTS ON ACTUATED THERMAL POLE-TIP PROTRUSION FOR HARD DISK DRIVES

Flying height (FH) control sliders with thermal actuation have been introduced recently in commercial products for compensating the static FH loss and reducing the risk of head-disk contacts. In the research reported here we investigated the effects of ABS designs on the thermal actuation. We created a 3-D finite element model of an entire slider with detailed read/write transducer structure, and then we conducted thermal-structural coupled-field analysis using velocity slip and temperature jump boundary conditions to formulate the heat transfer across the head-disk interface when a slider flies over a spinning disk. An iteration procedure was used to obtain the equilibrium solutions. Four ABS designs with distinct features were simulated. We defined five measures of merit, including protrusion rate, actuation efficiency, power consumption, pressure peak and temperature rise of the sensor, to evaluate the performance of thermal actuation. It is found that the effect of the pressure is more significant than that of the FH on the heat conduction from the slider to the disk. The efficiencies of three conventional designs decrease as the FHs are continuously reduced. A new ABS design, called “Scorpion III”, is presented and it demonstrates an overall enhancement, including virtually 100 percent efficiency with significantly less power consumption. Transient thermal analysis shows that it requires about 1-2 ms for the temperature to reach the steady-state values, and there is a trade-off between increasing the actuation bandwidth and decreasing the power consumption.

6.1 Introduction

With the increase of areal density in hard disk drives the physical spacing (or flying height, FH) between the read/write element and the surface of the disk has been continuously decreased. A spacing of about 2.5 nm is said to be required for a density of 1 Tbit/in^2. At such a low FH static losses of the FH due to manufacturing tolerance, ambient pressure changes and temperature variations can cause head-disk contact and result in data loss. Furthermore, slider disk contacts must be avoided during load/unload processes and operational shocks. The dynamic instability caused by FH modulations (FHMs) and nanoscale adhesion forces, such as electrostatic and intermolecular forces, should be minimized. Those challenges make a conventional air bearing surface (ABS) slider an unlikely choice for 1 Tbit/in^2. One potential solution is a FH adjustment or controlled slider that is capable of adjusting its gap FH. Due to their quick response and low power consumption piezoelectric materials have been proposed as active elements for adjusting the FH [1]-[8]. However, the requirements of the piezoelectric materials and the necessary modification of the slider design pose challenges in integration of the fabrication process and increase the manufacturing cost.

The concept of controlling gap FH by the thermal expansion of materials was demonstrated by Meyer *et al.* [9], in which a resistance heating element (heater) was deposited near the read/write elements and a temperature sensor was used for sensing an operating temperature of the slider body. Similarly, Kurita *et al.* developed an active head slider with a nano-thermal actuator [10]. They used a finite element method to calculate the temperature distribution and thermal protrusion of their slider. They found that the additional air pressure increase caused by the protrusion lifted the slider upward and the amount of FH reduction was 30 % less than the protrusion. In their study the distribution of the heat transfer coefficient on the ABS was assumed to be constant. However, the effect of heat conducted from the slider to the disk through the ABS is a strong function of both FH and air pressure distributions, and, hence, these two factors have to be considered in the model. Juang *et al.* [11] studied the actuation performance of an ABS slider with consideration of the effect of FH and pressure distributions. They found that even though the protruded area was relatively small there was still considerable air bearing coupling with the resulting actuation efficiency of only 63 %, which suggested that ABS played a key role in the actuation performance. Therefore, it is highly desirable to have a better understanding of the effects of the ABS on the thermal actuation and to provide design guidelines for improving the performance.

In this chapter we study the effects of the ABS on actuated thermal pole-tip protrusion by numerical simulation. A three-dimensional thermal-structural coupled field finite element model is created with detailed structures of read/write and heating elements. The cooling effect of the air bearing is included in the model as thermal boundary conditions. Steady-state and transient analyses of four ABSs with distinct features are presented. We found that a properly designed ABS can significantly improve the actuation efficiency and power consumption of a FH control slider with thermal actuation.

6.2 Numerical Modeling and Analysis

The temperature distribution and thermal deformation of a slider body with thermal actuation are determined by the configuration, dimensions and material properties of the read/write and heating elements and boundary conditions. The heat transfer boundary conditions depend on the flying state of the slider and hence the air bearing surfaces. In this study we kept the structure of the transducers the same and investigated the effect of ABS on actuation performance. We created a three-dimensional finite element model of an entire slider (length = 1.25 mm, width = 1.00 mm, thickness = 0.30 mm) with detailed read/write transducer structure as shown in Fig. 6.1. The slider has a single-layer 5-turn copper coil, a yoke width of 12 μm, and a write track width of 1 μm. The top and bottom poles are 1 μm thick. The top and bottom magnetic shields are 2 μm thick. The heating element has a thickness of 250 nm, and it is located between the coil and bottom pole. The photoresist layer, undercoat insulation layer and overcoat are also included in the model. The material properties and thickness of each layer are shown in Table 6.1. These values, in particular the thermal conductivity, are process-dependent, and we used the data published in various papers [12]-[15]. A series of thermal-structural coupled-field finite element analyses have been carried out using ANSYS, a commercial finite element package, to study the actuation performance of the thermal nanoactuator. The air bearing modeling was done using the CML Air Bearing Simulator, which solved the generalized Reynolds equation to obtain the steady-state flying attitude and pressure distribution.

At the head-disk interface heat is transferred from the slider to the disk through the air bearing cooling effect. The cooling effect of the air bearing plays a key role in this

3-D heat transfer problem. Chen *et al.* [16] found that the dominant factor of this effect was heat conduction. They applied the slip condition for the velocity and the jump condition for the temperature at the boundaries of the air bearing and obtained the heat transfer model as follows:

$$q(x,y) = -k\frac{T_s(x,y) - T_d}{h(x,y) + 2b\lambda(x,y)} + f(.) \tag{6.1}$$

where T_s and T_d are the temperatures of the slider and the disk, respectively; $b = 2(2 - \sigma_T)\gamma / \sigma_T(\gamma + 1)\,\mathrm{Pr}$; h is the FH (air bearing thickness) of the slider; the mean free path of the air under pressure p is $\lambda = \lambda_0 p_0/p$, while the thermal conductivity k is a very weak function of pressure.

Note that T_s, h and λ are functions of the coordinates, x and y. For air at $T = 300$ K and atmospheric pressure, the thermal conductivity $k = 0.0263$ W/m K, the mean free path $\lambda_0 = 65$ nm, and the Prandtl number $Pr = 0.7$. The specific heat ratio γ is 1.4 and the thermal accommodation coefficient σ_T is 0.9. We assume that the disk surface is kept at the ambient temperature $T_d = 25\ ^{o}$C. Since the first term of the right hand side is about 1-2 orders of magnitude larger than the other terms *f(.)* only this term is modeled in this study. Unlike the ABS, the dominant factor of heat transfer at the non-ABS surfaces of the slider is heat convection of a coefficient on the order of 100 W/m^2 K.

The numerical iteration approach developed in [11] is adopted in this chapter. We used the CML Air Bearing Simulator to obtain the nominal FH, pitch, roll and air pressure distribution of an ABS slider. Then we applied Eq. (6.1) to specify the thermal boundary condition at the ABS and calculated the temperature distribution of the slider body. The obtained temperature distribution was used then as the body load to solve the slider deformation and actuated pole-tip protrusion due to the temperature gradient and the mismatch of coefficient of thermal expansions of various materials. Since the thermal protrusion causes deformation of the ABS and hence changes the flying attitudes and the thermal boundary conditions, several iterations are required to achieve an equilibrium solution.

6.3 Results and Discussions

6.3.1 Four Air Bearing Designs

We study the actuation performances of four ABS designs that have distinct flying attitudes and pressure distributions as shown in Fig. 6.2. Their flying attitudes are summarized in Table 6.2. The first design, depicted in Fig. 6.2(a), is a five-pad design labeled CML-5nm. It was designed using an optimization algorithm for a nearly uniform 5-nm FH across the disk. The second design, labeled Slider A, is a three-pad design obtained from a commercial drive as shown in Fig. 6.2(b). It has three surfaces, each specifically designed to achieve the overall desired FH performance characteristics. The third and more complicated design is shown in Fig. 6.2(c) and labeled Slider B. This ABS was designed for sliders with thermal actuation, and, it has recently been implemented in commercial products. Figures 6.3(a)-(c) show the pressure profiles normalized by the ambient pressure generated under the CML-5nm, Slider A and Slider B, respectively. The sliders are mainly supported by the high pressure peaks generated by the central trailing pads, which are typically used in commercial products. The high peak pressure helps to maintain the stiffness of the air bearings. However when the thermal actuation is used to adjust the FH, the high peak pressure at the center trailing pad also corresponds to more molecules per unit volume to transport energy, and thus most of the power generated by the heating element is dissipated through the air bearing, which decreases the amount of thermal protrusion and increases the required heating power. Besides, the actuation efficiency is limited due to the strong counter effect of the air bearing push-back.

In order to increase the actuation efficiency and to reduce the power consumption we designed an ABS, named Scorpion III, as shown in Fig. 6.2(d). The pressure distributions exhibit a distinct pattern compared to conventional designs as shown in Fig. 6.3(d). Instead of being supporting by the center pressure peak the slider is primarily supported by the high pressures generated at the side rails. Scorpion III was found to exhibit an overall enhancement in performance, compared with several conventional ABS designs [17].

6.3.2 Steady-State Analysis

Fig. 6.4 shows the steady-state heat transfer film coefficients on the air bearing surfaces of the four designs obtained after several numerical iterations at a heating power of 20 mW. Only part of the ABS that is close to the trailing edge is plotted. The distances of the write gap and GMR sensor from the trailing edge are 33 and 36.5 μm, respectively. The disk linear speeds and skew angles are given in Table 6.2. It is seen that the heat transfer coefficients are not constant, and they are indeed strong functions of both the FH and air pressure distributions. The peak values are about 1.6, 1.2, 1.4, and 0.2 $MW/m^2.K$

for CML-5nm, Slider A, Slider B, and Scorpion, respectively. The value of the Scorpion ABS is about 83 % to 86 % less than those of Slider A and Slider B even though the FHs of the three designs are similar, which clearly indicates that the effect of the pressure is more significant than the FH effect.

Figs. 6.5 and 6.6 show the comparisons of the temperature rise and heat flux of the four designs at 20 mW, respectively. The maximum temperature rises are 2.78, 2.52, 3.21 and 7.8 K for CML-5nm, Slider A, Slider B and Scorpion, respectively. The Scorpion ABS has a higher temperature increase due to its relatively low heat flux whereas the temperature distribution of Slider B exhibits a different pattern from the others.

Using the temperature distributions as body loads in the finite element models, we carried out the static structural analysis to calculate the slider deformation. A comparison of the protrusion profiles is shown in Fig. 6.7. The maximum A-PTPs on the ABSs are found to be 3.86, 3.56, 4.54 and 6.86 nm for CML-5nm, Slider A, Slider B and Scorpion, respectively. As expected, the Scorpion slider achieves 51% more protrusion than the second highest one at the same heating power of 20 mW. Fig. 6.8 shows the protrusion profiles along the center line across the read/write elements, which indicates that the peaks of protrusions are located at the read/write elements as a result of the higher local temperature and higher coefficients of thermal expansion of the metal layers.

Fig. 6.9 shows the FH reductions as a function of the DC heating power. The results indicate that the FH reduction is not proportional to the power. Instead, quadratic expressions have been found to fit the calculated data points for all the ABSs. This nonlinearity is related to the fact that the air bearing becomes stiffer when the FH is reduced and the heat transfer across the air bearing also becomes more effective because of the increased pressure and reduced FH.

In order to evaluate the performance of thermal actuation we defined five measures of merit as follows:

1. Actuation efficiency (%): The ratio of FH reduction to A-PTP.
2. Power consumption (mW): The power required for lowering one unit of the FH.
3. Peak pressure increase (atm): The increase of pressure peak caused by the thermal protrusion.
4. Protrusion rate (nm/mW): The amount of protrusion per unit power.
5. Temperature rise of the sensor (K): The temperature rise of the GMR sensors as a function of FH.

Fig. 6.10 shows a comparison of the A-PTP as a function of the heating power. Scorpion exhibits an increase of 80 %, 104 %, and 63 % in the protrusion rate over CML-5nm, Slider A, and Slider B, respectively. Fig. 6.11 shows the actuation efficiency as a function of the FH for the four ABSs. It is noted that the efficiencies of CML-5nm, Slider A and Slider B monotonically decrease as the FHs are reduced by the thermal protrusions and the values range from 40 % to 60 %. However, Scorpion demonstrates virtually 100 percent efficiency which does not depend on the FH. The heating powers required for lowering the FHs are shown in Fig. 6.12. The Scorpion ABS requires remarkably less power for reducing the FH from 10 nm to 3 nm compared to the other designs. Another important parameter that has to be considered is the pressure increase due to the deformed ABS. Fig. 6.13 shows that the peak pressures of Slider A and Slider B are 84 and 149 *atm*, respectively, when the FHs are reduced to about 3 nm. Such high pressures may not be physical in reality and may cause adverse effects. Since the Scorpion slider is supported by the two side pressure peaks and the pressure underneath the center pad is relatively low, the thermal protrusion of the center pad does not affect the pressure distribution.

The temperature rise of the read/write elements is of great concern in the thermal nanoactuator. The read-back signal of GMR sensors can be significantly altered by thermal influences since their electrical resistance is temperature dependent. Fig. 6.14 shows the temperature rises of the sensors as a function of the FH. It is observed that Scorpion has less temperature rise at FHs over 5 nm compared to Slider A and Slider B. The temperatures of Slider A and Slider B decrease when the FHs are reduced to less than 5 nm due to the highly concentrated pressures.

6.3.3 Transient Analysis

The bandwidth of thermal actuation is of great importance because it determines the response time of the thermal protrusion to the heating power. A transient thermal study was conducted to investigate the bandwidth of the thermal protrusion when the slider flies over a disk. The power required for the first one nanometer FH reduction for each of the ABSs was applied from 0 to 2.5 ms and was turned off at 2.5 ms. The temperature changes of the GMR sensors were monitored as shown in Fig. 6.15. It requires about 1-2 ms for the read/write transducers to reach their steady-state values, corresponding to a bandwidth of 0.5-1 kHz. It is also seen that Scorpion has the least temperature rise and it takes longer to reach its steady-state value, which implies that a trade-off between increasing the bandwidth and decreasing the temperature rise of the sensors.

6.4 Conclusions

The effects of the ABS on thermal actuation have been studied by numerical simulation. A series of three-dimensional thermal-structural finite element analyses were conducted using velocity slip and temperature jump boundary conditions to formulate the heat transfer across the head-disk interface. An iteration procedure was used to obtain the equilibrium solutions. Four ABS designs with distinct features were simulated. In order to evaluate the performance of thermal actuation we defined five measures of merit, including protrusion rate, actuation efficiency, power consumption, pressure peak and temperature rise of the sensor. We found that the efficiencies of three conventional designs decrease as the FHs are continuously reduced. A new slider Scorpion, which meets all design and fabrication requirements, has been presented and exhibits an overall enhancement, including virtually 100 % efficiency with significantly less power consumption. Quadratic expressions have been found to best fit the curves of the FH reduction as a function of the heating power for all the designs.

Transient thermal analysis of the sliders in the flying conditions with a varying heating power showed that about 1-2 ms are required for the temperature to reach the steady-state values. It is found that Scorpion has the least temperature rise of the GMR sensor at the first one nanometer FH reduction but the response time was longer than the other three designs. Therefore, there is a trade-off between increasing the actuation bandwidth and decreasing the power consumption.

References

1. C. E. Yeack-Scranton, V. D. Khanna, K. F. Etzold, and A. P. Praino, “ An active slider for practical contact recording,” *IEEE Trans. Magn.,* vol. 26, pp. 2478-2483, 1990.
2. M. Kurita and K. Suzuki, “Flying-height adjustment technologies of magnetic head sliders,” *IEEE Trans. Magn.,* vol. 40, pp. 332-336, 2004.
3. K. Suzuki, R. Maeda, J. Chu, T. Kato, and M. Kurita, “An active head slider using a piezoelectric cantilever for in situ flying-height control,” *IEEE Trans. Magn.,* vol. 39, pp. 826-831, 2003.
4. N. Tagawa, K.-I. Kitamura, and A. Mori, “Design and fabrication of MEMS-based active slider using double-layered composite PZT thin film in hard disk drives,” *IEEE Trans. Magn.,* vol. 39, pp. 926-931, 2003.
5. L. Su, M. Kurita, J. Xu, K. Kato, K. Adachi, and Y. Miyake, “Static and dynamic characteristics of active-head sliders,” *Tribol. Intl.,* vol. 38, pp. 717-723, 2005.

6. J. Y. Juang and D. B. Bogy, “Controlled-flying proximity sliders for head-media spacing variation suppression in ultralow flying air bearings,” *IEEE Trans. Magn.,* vol. 41, pp. 3052-3054, 2005.
7. J. Y. Juang and D. B. Bogy, “Nonlinear compensator design for active sliders to suppress head-disk spacing modulation in hard disk drive,” *IEEE/ASME Trans. Mechatron.*, to be published.
8. J. Y. Juang, D. B. Bogy and C. S. Bhatia, “Numerical and experimental studies of an Al_2O_3-TiC slider with a piezoelectric nanoactuator,” *2006 ASME/JSME Joint Conf. on Micromechatronics for Information and Precision Equipment*, June 21-23, Santa Clara, CA.
9. D. W. Meyer, P. E. Kupinski, and J. C. Liu, “Slider with temperature responsive transducer positioning,” U. S. Patent 5,991,113, Nov. 23, 1999.
10. M. Kurita, T. Shiramatsu, K. Miyake, A. Kato, M. Soga, H. Tanaka, S. Saegusa and M. Suk, “Active flying-height control slider using MEMS thermal actuator,” *Microsyst. Technol.,* vol. 12, pp. 369-375, 2006.
11. J. Y. Juang, D. Chen, and D. B. Bogy, “Alternate air bearing slider designs for areal density of 1 Tbit/in^2,” *IEEE Trans. Magn*., vol. 42, pp. 241-246, 2006.
12. L. Pust, C. J. T. Rea, and S. Gangopadhyay, “Thermo-mechanical head performance,” *IEEE Trans. Magn.*, vol. 38, pp. 101-106, 2002.
13. Y. S. Ju, “Self-heating in thin-film magnetic recording heads due to write currents,” *IEEE Trans. Magn*., vol. 41, pp. 4443-4448, 2005.

14. Y. Yang, S. Shojaeizadeh, J. A. Bain, J. G. Zhu and M. Asheghi, "Detailed modeling of temperature rise in giant magnetoresistive sensor during an electrostatic discharge event," *J. Applied Physics*, vol. 95, pp. 6780-6782, 2004.

15. S. M. Lee and D. G. Cahill, "Thermal conductivity of sputtered oxide films,"*Physical Review B*, vol. 52, pp. 253-257, 1995.

16. L. Chen, D. B. Bogy, and B. Strom, "Thermal dependence of MR signal on slider flying state," *IEEE Trans. Magn*., vol. 36, no. 5, pp. 2486-2489, Sep. 2000.

17. J. Y. Juang and D. B. Bogy, "Design and analysis of a flying height control slider with thermal nanoactuator," Technical Chapter No. 2006-004, Computer Mechanics Lab., Department of Mechanical Engineering, University of California, Berkeley.

TABLE 6.1 Material Properties used in the FEA [13]-[16]

Layer and Material		Young's modulus (GPa)	Thermal conductivity (W/m.K)	Coefficient of thermal expansion (x 10^{-6}/ °C)	Specific heat (J/kg.K)	Poisson's ratio
Slider substrate	Al_2O_3-TiC	380	20	7.9	878	0.3
Under-coat (1.2 μm)	Al_2O_3	200	1.5	7.5	760	0.25
Shields (2.0 μm)	Ni-Fe	207	35	12.2	470	0.3
Bottom pole (1.0 μm)	Ni-Fe	207	35	12.2	470	0.3
Coil (2 μm)	Cu	120	395	16.5	390	0.33
Heater (250 nm)	Ni-Fe (thin layer)	207	30	12.2	470	0.3
Coil insulation (5 μm)	Photo-resist	7	0.19	51.0	1460	0.2
Top pole (1.0 μm)	Ni-Fe	207	35	12.2	470	0.3
Overcoat (39.7 μm)	Al_2O_3	200	1.5	7.5	760	0.25

TABLE 6.2 Comparison of Flying Attitudes at the MD

	FH (nm)	Pitch (μrad)	Roll (μrad)	Peak pressure (atm)	Linear velocity (m/s)	skew (°)
CML-5nm	5.3	220	0.9	18.9	17.3	9.10
Slider A	11.5	130	-1.2	23.4	37.5	-2.56
Slider B	12.0	115	2.4	21.0	18.0	-2.56
Scorpion III	10.5	124	-0.4	38.0	37.5	-2.56

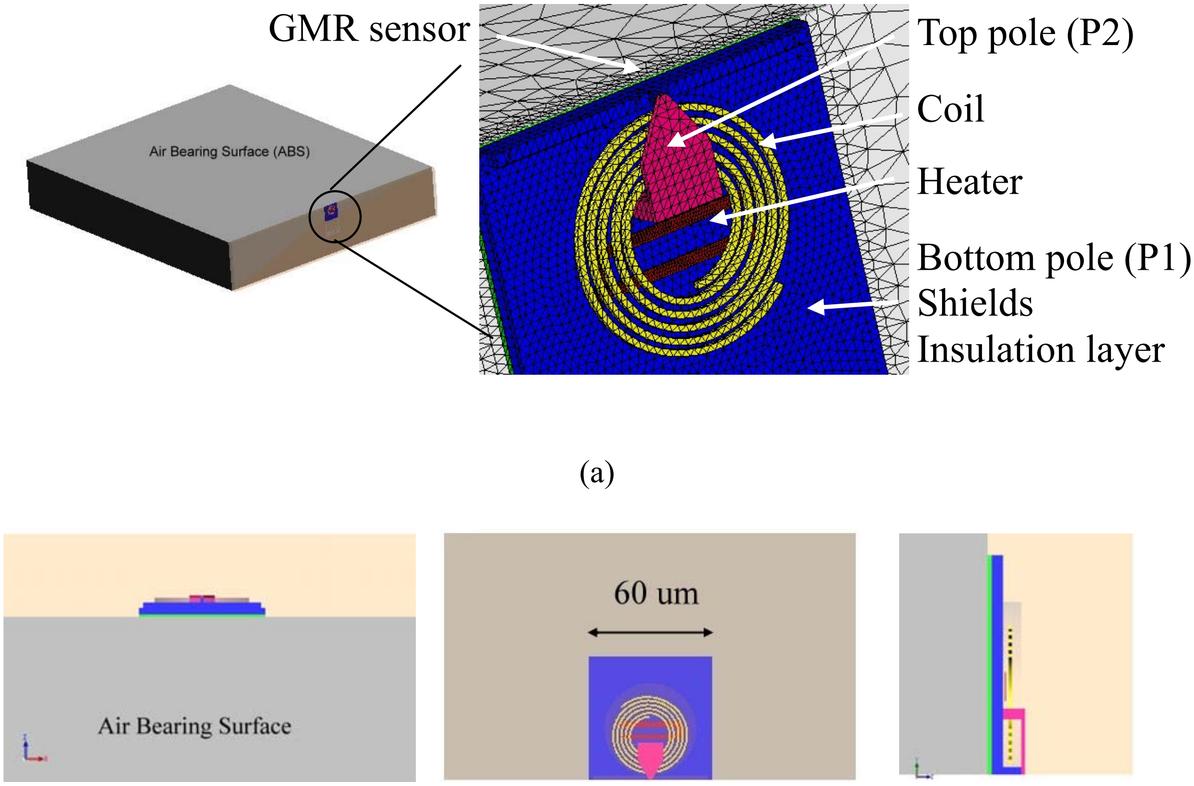

(a)

(b) (c) (d)

Fig. 6.1. The finite-element model of a FH control slider with thermal actuation. The overcoat and photoresist are not shown for a clear view of the read/write transducer. The protective carbon overcoat on the ABS and the pole-tip recession are not considered.

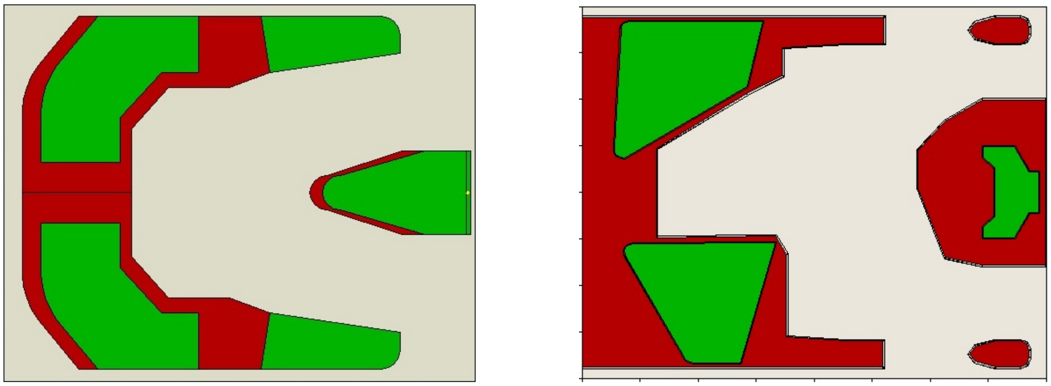

(a) CML-5nm (b) Slider A

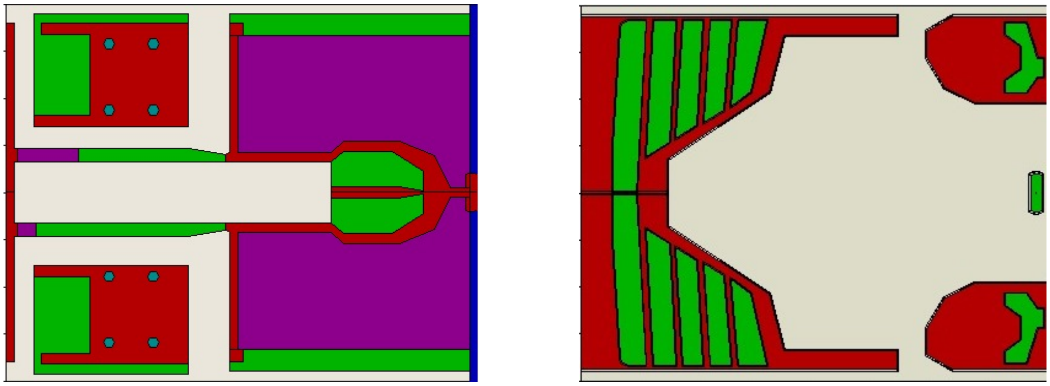

(c) Slider B (c) Scorpion III

Fig. 6.2. Four ABS designs used in this study (length: 1.25 mm; width: 1.00 mm). Different colors indicate different etching levels.

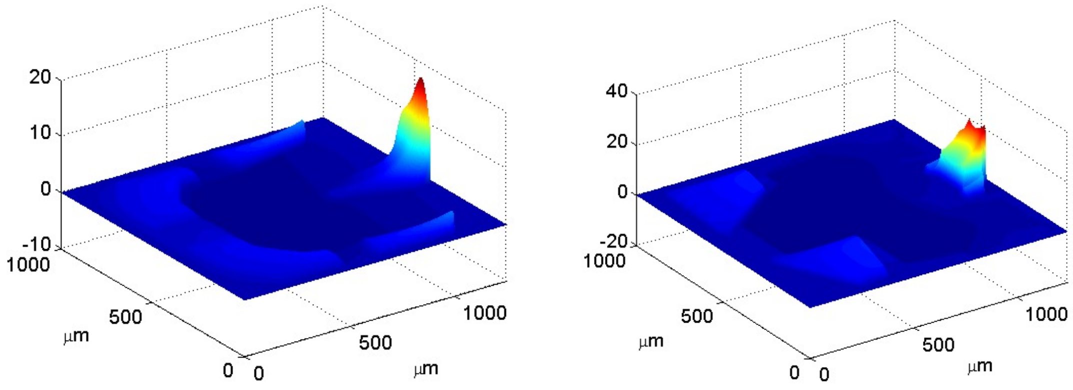

(a) CML-5nm (peak: 18.9 atm) (b) Slider A (peak: 23.4 atm)

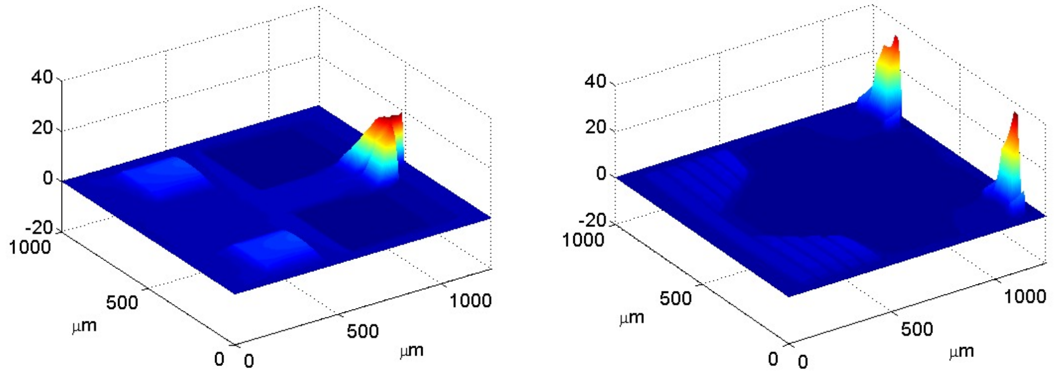

(c) Slider B (peak: 21.0 atm) (d) Scorpion III (peak: 38.0 atm)

Fig. 6.3. The air pressure distributions of the ABS sliders. The scale displayed is normalized to ambient pressure: $(p - p_a)/p_a$.

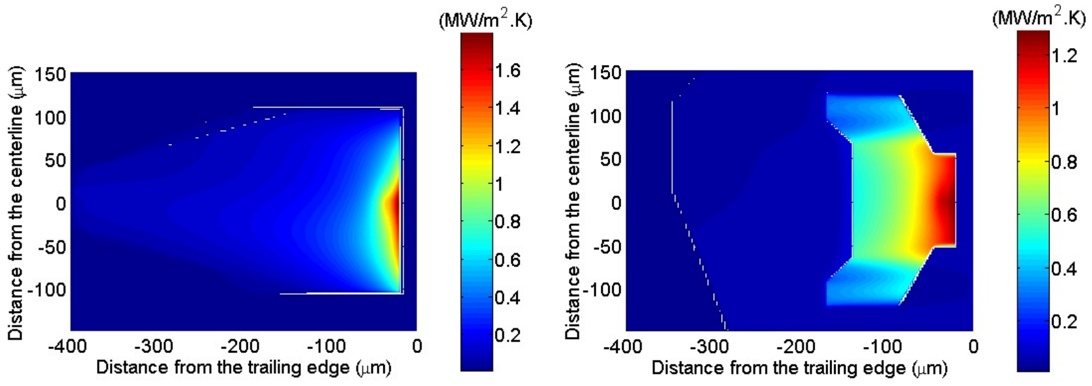

(a) CML-5nm (b) Slider A

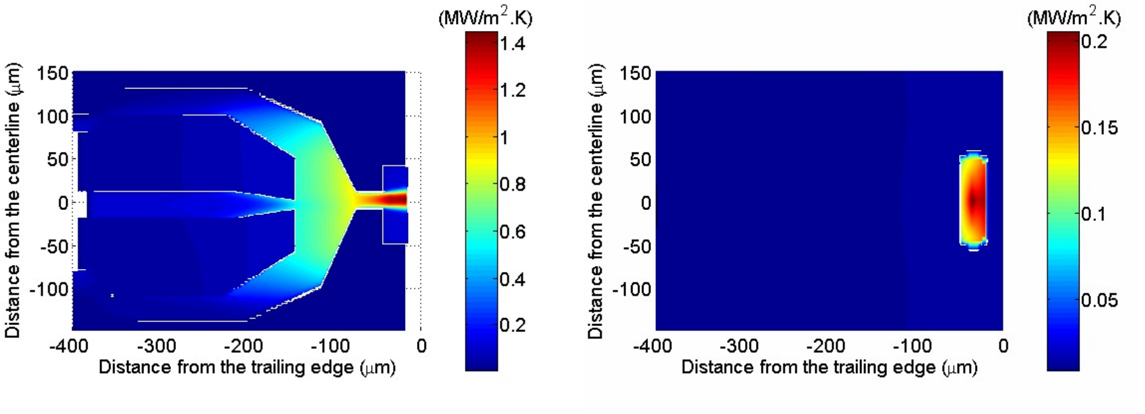

(c) Slider B (d) Scorpion

Fig. 6.4. The distributions of the heat transfer film coefficients on the air bearing surfaces at a heating power of 20 mW. Only part of the ABS that is close to the trailing edge is plotted. The distances of the write gap and the GMR sensor from the trailing edge are 33 and 36.5 μm, respectively.

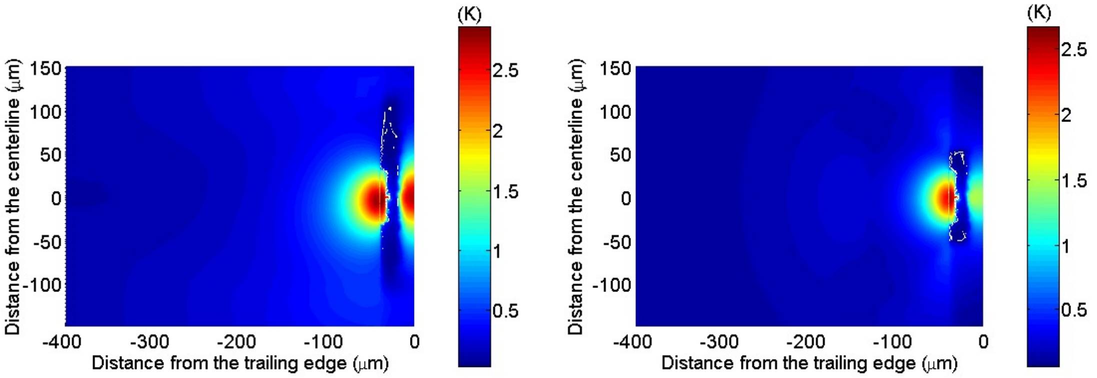

(a) CML-5nm (b) Slider A

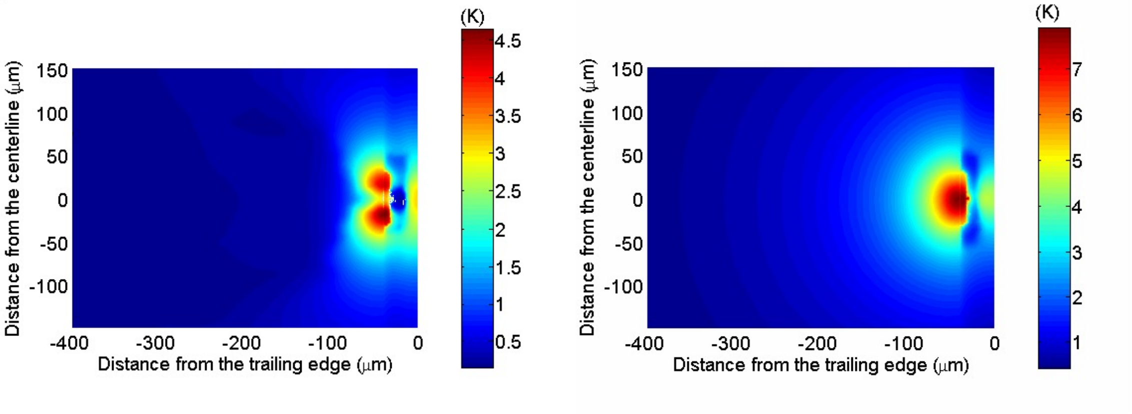

(c) Slider B (d) A-PTP

Fig. 6.5. The distributions of the temperature rises on the ABSs at a heating power of 20 mW.

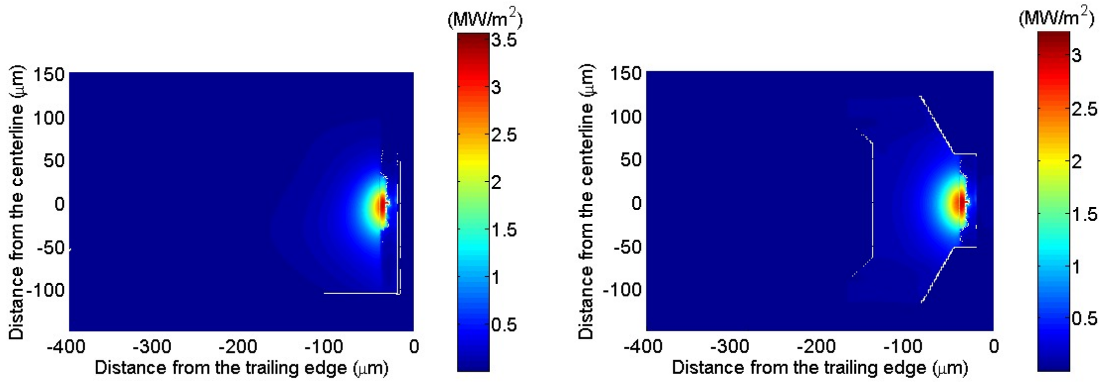

(a) CML-5nm (b) Slider A

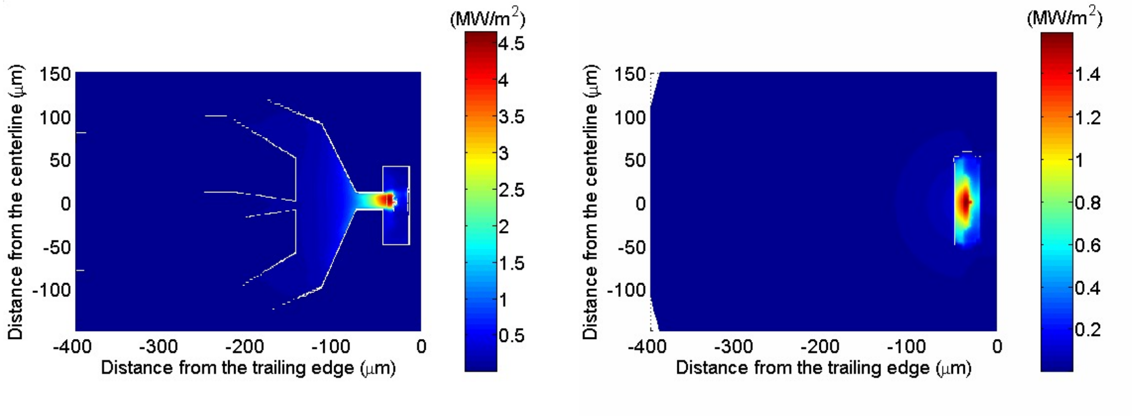

(c) Slider B (d) A-PTP

Fig. 6.6. The distributions of the heat flux on the ABSs at a heating power of 20 mW.

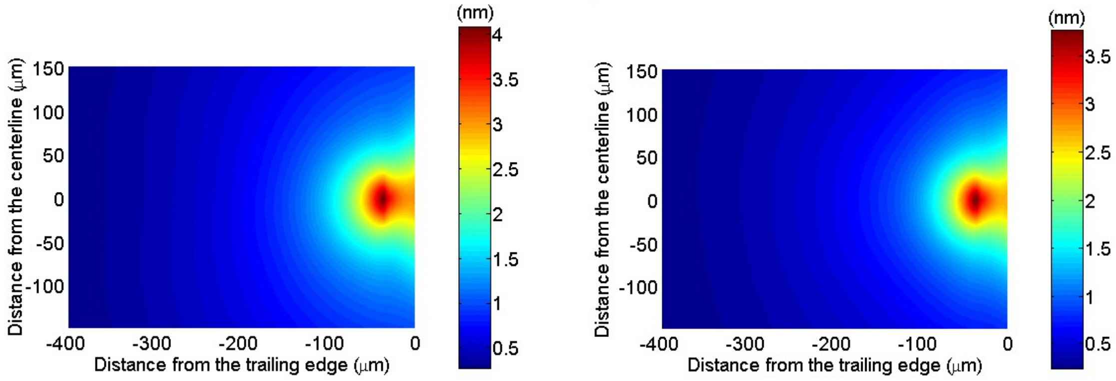

(a) CML-5nm (b) Slider A

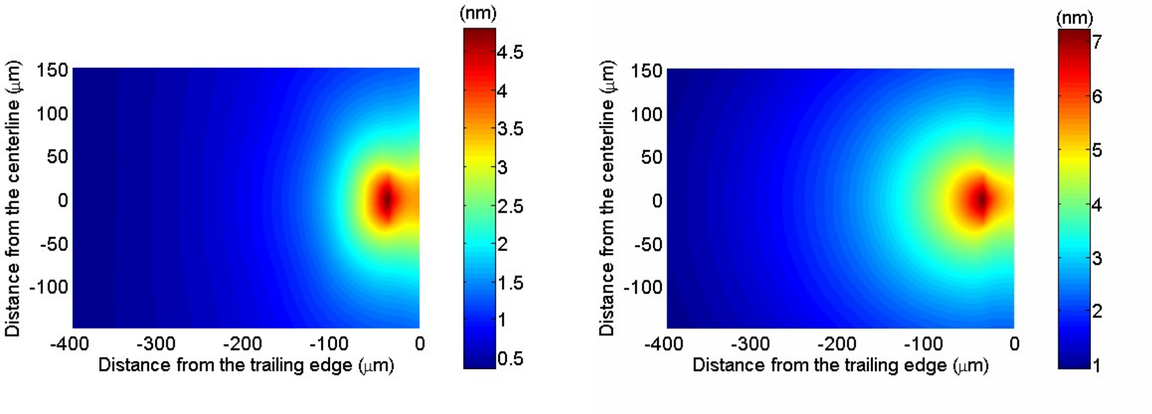

(c) Slider B (d) Scorpion

Fig. 6.7. The distributions of the A-PTP on the ABSs at a heating power of 20 mW.

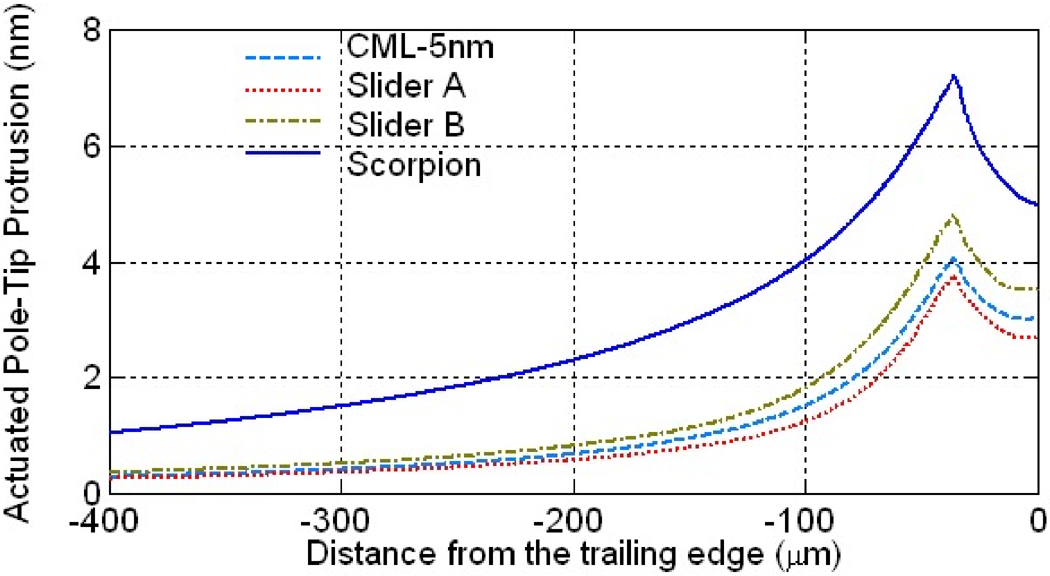

Fig. 6.8. Comparison of actuated thermal protrusion profiles of the four air bearings along the center line across the read/write element at a heating power of 20 mW.

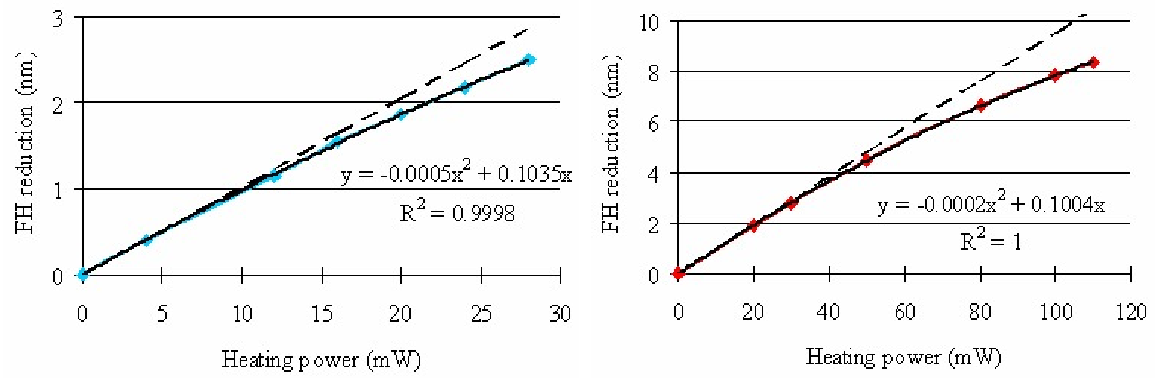

(a) CML-5nm (b) Slider A

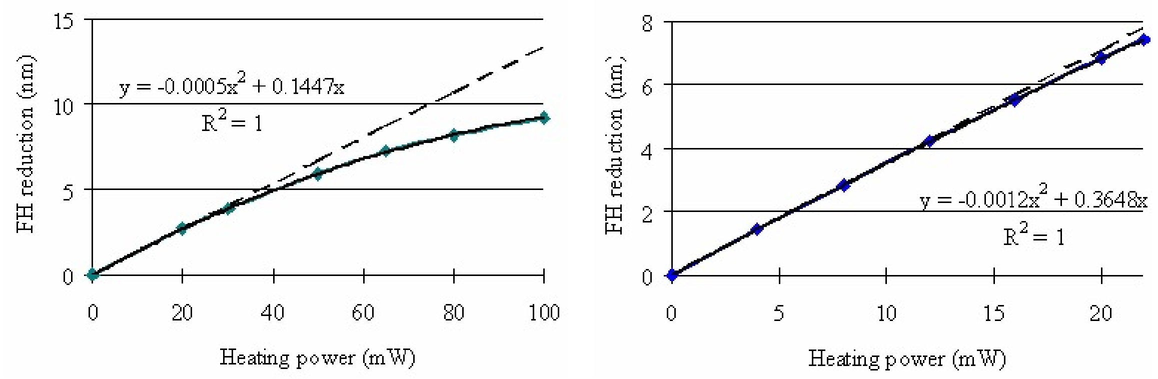

(c) Slider B (d) Scorpion

Fig. 6.9. The FH reductions as a function of heating power. The dash lines are the linear projections and the solid lines are quadratic fits to the data.

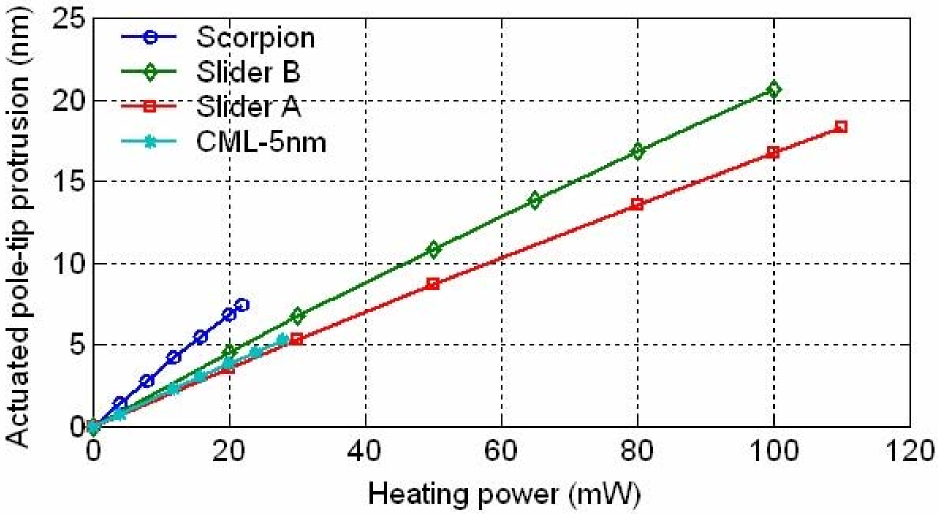

Fig. 6.10. A comparison of the A-PTP as a function of the heating power. The protrusion rates are about 0.19, 0.17, 0.21, and 0.34 nm/mW for CML-5nm, Slider A, Slider B, and Scorpion, respectively.

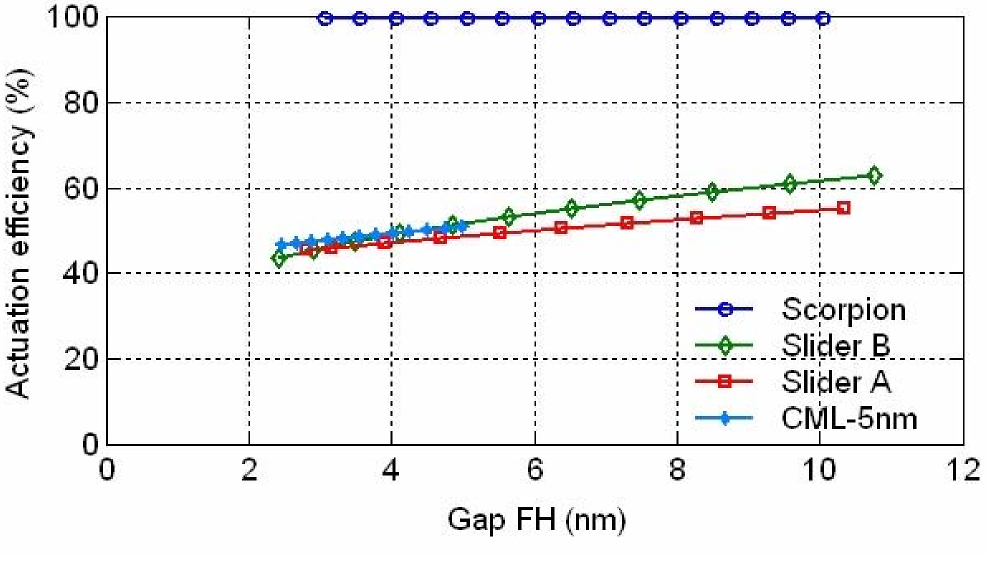

Fig. 6.11. A comparison of the efficiency as a function of the FH. The efficiencies of CML-5nm, Slider A and Slider B monotonically decrease as the FHs are reduced by the thermal protrusions and Scorpion demonstrates virtually 100 % efficiency.

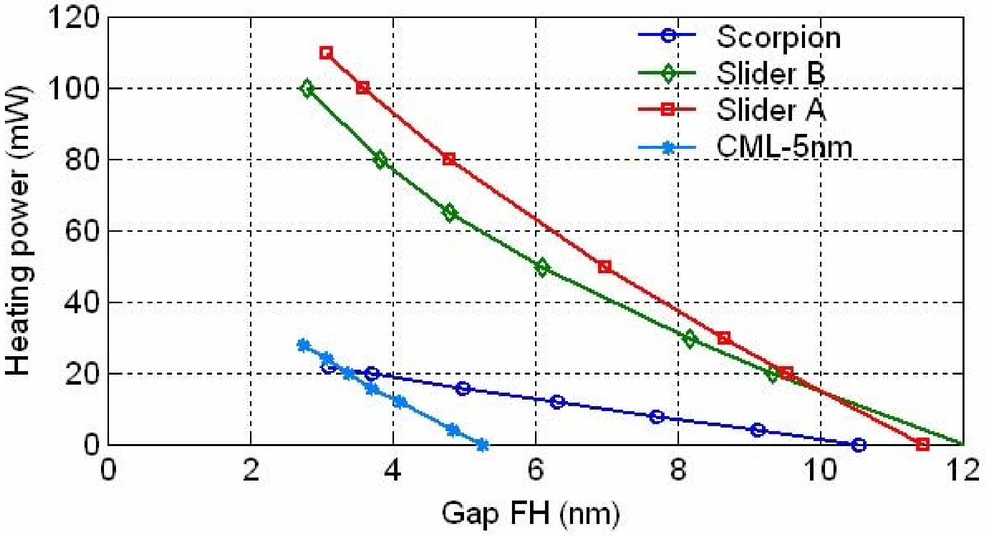

Fig. 6.12. The required heating power for reducing the FH.

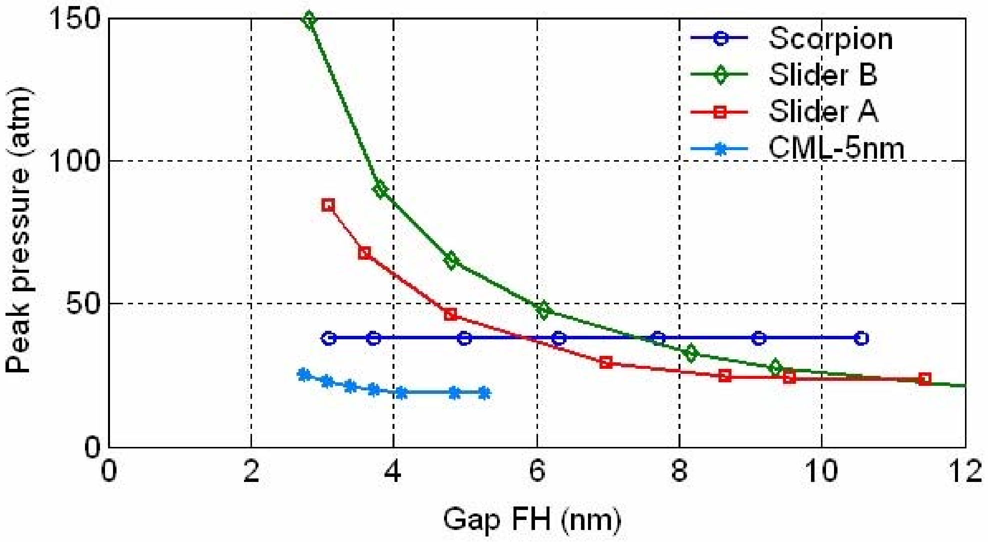

Fig. 6.13. A comparison of the peak pressures as functions of the FHs.

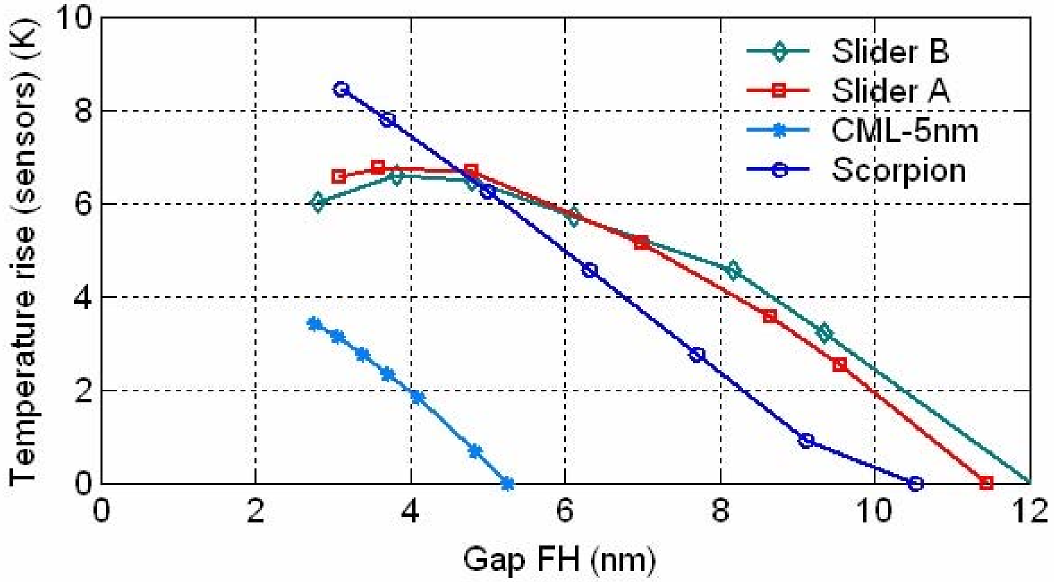

Fig. 6.14. The temperature rises of the sensors when the FHs are reduced by applying a heating power.

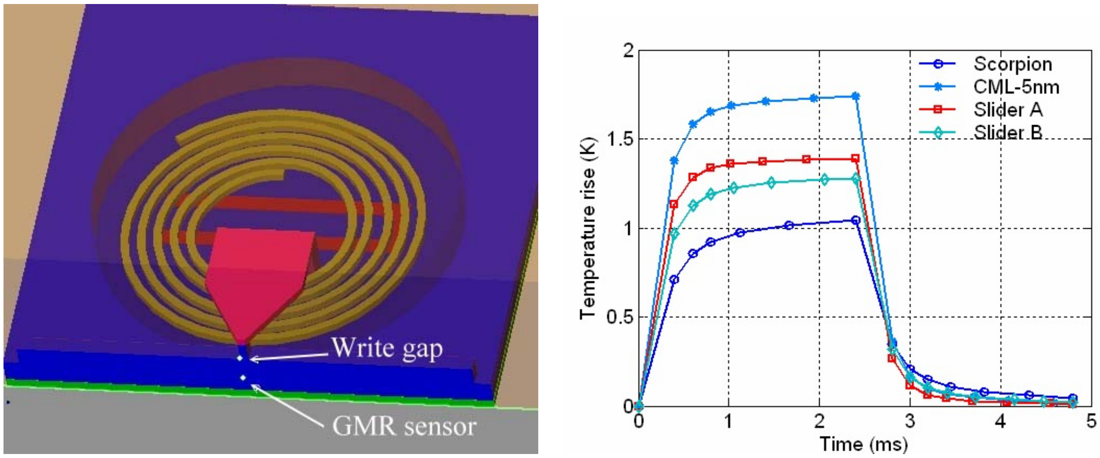

(a) (b)

Fig. 6.15. Transient temperature changes of the flying sliders with a varying heating power. The power required for the first one nanometer FH reduction for each of the ABSs was applied from 0 to 2.5 ms and was turned off at 2.5 ms.

CHAPTER 7
EFFECTS OF TRACK-SEEKING MOTION ON FLYING ATTITUDE OF ULTRALOW FLYING SLIDER

The flying height (FH) change during a track-seeking motion becomes of significant concern for ultralow flying sliders. The presence of nanoscale adhesion forces, such as intermolecular and electrostatic forces, can adversely decrease the FH and even cause head-disk impact. A quasi-static approximation of track-seeking motion is proposed here, which if sufficiently accurate can substantially decrease the computation time over that required for a dynamic analysis. The track-seeking performances of four different air bearing surface (ABS) designs are numerically investigated by the quasi-static approximation, and the results are compared with those computed by the CML Dynamic Simulator. The former gives good agreements with the latter but with much less computation effort. The effects of various factors causing FH changes are presented and compared quantitatively. The effective skew angle is found to be the dominant factor, but the inertia effect is also not negligible. Two designs, called Scorpion III and Scorpion IV, designed previously as active FH control sliders, are found to exhibit an enhancement in track-seeking performance, compared with two other conventional ABS designs.

7.1 Introduction

As the spacing between the slider and the disk decreases in hard disk drives the linear bit spacing of magnetic recording can decrease, resulting in a higher areal density.

A physical spacing (or gap flying height, gap FH) of less than 5 nm between the read/write element and the surface of the disk is required for ultrahigh density recording. For such ultralow flying sliders the changes in FH during track-seeking motions not only cause signal loss, but also significantly increase the risk of head-disk contact. Moreover, the presence of nanoscale adhesion forces, such as intermolecular and electrostatic forces, can cause dynamical instability. In order for a reliable head-disk interface to be maintained the FH change and contact between the slider and disk have to be avoided. Different ABS designs can perform quite differently during the track-seeking process. Therefore, the dynamic track-seeking performance of air bearing sliders is becoming of increasing importance. A better understanding of the factors that cause FH change should help improve the ABS design to achieve better track-seeking performance.

Cha *et al.* [1] studied the FH change during seek operation for TPC (transverse pressure contour) sliders. They suggested that at high seek velocities the skew angle effect dominates over the inertia effect, but there was no quantitative comparison between the cases with and without inertia effects due to the difficulty of measuring FH during track-seeking and the absence of proper dynamic simulators. Liu and Soh [2] experimentally investigated the effects of track-seeking velocity on air bearing skew angle, air flow speed and flying performance of TPC and Tri-pad sliders. The effects of the slider's inertia and acceleration were not considered. Chen and Bogy [3] carried out a numerical study of the track-seeking dynamics of the picosized TNPS and U sliders using the CML Dynamic Simulator. They found that the two sliders had distinct dynamic characteristics. The Dynamic Simulator included the inertia effect and provided more comprehensive simulations of track-seeking dynamics but it required much more computation time. In a recent paper by Dorius *et al.* [4], the gap FHs of a pico and femto slider were forced to drop about 20 and 10 %, respectively, during track seeking.

In this chapter we propose a quasi-static approximation of the track-seeking motion, which includes the effects of HGA inertia, effective skew angles and nanoscale adhesion forces in the HDI. We first compare the track-seeking simulations of four ABS designs by quasi-static approximation with those obtained using the CML Dynamic Simulator on a smooth disk surface. Then we quantitatively study the effects of various factors on the FH change.

7.2 Theoretical Background and Numerical Methods

7.2.1 Air Bearing Slider and Suspension Dynamics

The pressure distribution between the slider and the rotating disk can be described by the compressible Reynolds equation. The non-dimensionalized generalized Reynolds equation can be written as follows:

$$\frac{\partial}{\partial X}\left[\hat{Q}PH^3\frac{\partial P}{\partial X}-\Lambda_X PH\right]+\frac{\partial}{\partial Y}\left[\hat{Q}PH^3\frac{\partial P}{\partial Y}-\Lambda_Y PH\right]=\sigma\frac{\partial}{\partial T}\left[PH\right] \tag{7.1}$$

where $\Lambda_X = 6\mu UL/p_a h_m^2$ and $\Lambda_Y = 6\mu VL/p_a h_m^2$ are the bearing numbers in the x and y directions, $\sigma = 12\mu\omega L^2/p_a h_m^2$ is the squeeze number, μ is the viscosity, p_a is the ambient pressure, and $\hat{Q}$ is the Poiseuille flow factor.

The equations of motion of an air bearing slider flying over a rotating disk are:

$$
\begin{aligned}
m\ddot{z} &= F + \int_A (p - p_a) dA \\
I_\theta \ddot{\theta} &= M_\theta + \int_A (p - p_a)(x_g - x) dA \\
I_\phi \ddot{\phi} &= M_\phi + \int_A (p - p_a)(y_g - y) dA
\end{aligned}
\tag{7.2}
$$

where z, θ, and ϕ are the vertical displacement, pitch, and roll, respectively. I_θ and I_ϕ are the moments of inertia, x_g and y_g are the positions of the slider's center of gravity, and F, M_θ and M_ϕ are the force and moments exerted on the slider by the suspension. For track-seeking motions, M_θ and M_ϕ include the contribution of the inertia forces.

The CML Dynamic Air Bearing Simulator was developed to solve the generalized Reynolds equations (7.1) coupled with the dynamics of the slider body (7.2) and a lumped parameter suspension, where the suspension is represented by flexure stiffness and damping coefficients. By using the simulator, we can obtain the dynamic flying attitude of a slider during track-seeking motions. However, since the time step used in the dynamic simulation is usually on the order of 1×10^{-7} s, it requires considerable computation effort to conduct one track-seeking simulation with an average seeking time of 11 ms.

7.2.2 Qusai-Static Approximation of Track-seeking Motion

In order to reduce the computation effort of track-seeking simulations and quantitatively study the contribution of various factors on the FH change during track-seeking, we carried out a quasi-static approximation of the track-seeking motion. Instead of simultaneously solving Eq. (7.1) and (7.2) at each time step we solve Eq. (7.1) under static suspension loading with consideration of the seeking velocity and HGA inertia at different radial positions during track-seeking. The change of seeking velocity causes changes of skew angle and air flow speed and direction. The geometrical skew angle refers to the angle between the slider's longitudinal axis and the track direction. The effective skew angle is the angle between the slider's longitudinal direction and the relative disk velocity (or air flow velocity) which is the resultant vector of the disk track linear velocity and the slider's seeking velocity. As the seeking velocity increases the difference between the geometrical and effective skew angles increases.

The acceleration of the center of gravity of a slider during track-seeking can be expressed as

$$a = a_t e_t + a_n e_n = a_t e_t + \left(\omega^2 r\right) e_n \tag{7.3}$$

where a_t and a_n are the tangential and normal components, respectively. ω and r are the angular velocity of the arm and the arm length of the VCM actuator, respectively. The tangential component is also referred to as the seeking acceleration. Since the inertia effect of the suspension has minimal effect on the roll angle and FH, only the inertia of the slider is considered in this study. The additional torques exerted on the slider body due to these inertia forces can be written as

$$\Delta M_\theta = -m \cdot a_n \cdot \frac{h}{2}; \quad \Delta M_\phi = -m \cdot a_t \cdot \frac{h}{2} \tag{7.4}$$

where *m* and *h* are the mass and thickness of the slider.

7.3 Results and Discussions

7.3.1 Air Bearing Designs and Track-seeking Performances

In this chapter, we study the track-seeking performances of four ABS designs that incorporate subambient pressure regions. Their drive and air bearing specifications are summarized in Table 7.1. The first design, depicted in Fig. 7.1(a), is a five-pad design labeled ABS I. It was designed using an optimization algorithm [5] for a nearly uniform 5-nm FH across the disk. The region of pole-tip recession in the original design was removed for a more realistic calculation of the nanoscale adhesion forces in the HDI. The second and more complicated design is shown in Fig. 7.2(a) and labeled ABS II. Figures 7.1(b) and 2(b) show the pressure profiles normalized by the ambient pressure generated under the ABS I and ABS II sliders, respectively. The sliders are mainly supported by the high pressure peaks generated by the central trailing pads, which are typically used in commercial products. The third and fourth designs, named Scorpion III and Scorpion IV, were analyzed in Chapter 3 as actively controlled-FH sliders with thermal and piezoelectric nanoactuators, respectively. For a controlled-FH slider, the FH is about 10 nm in the off duty cycle (passive mode) and is reduced to ~2 nm during reading and writing (active mode) by applying either a current or a voltage to an active element, such as a resistive heating element or piezoelectric material. As shown in Figs. 7.3(a) and 7.4(a) the areas of their central trailing pads have been significantly reduced to increase the actuation efficiency. The pressure distributions exhibit distinct features compared to conventional designs as shown in Figs. 7.3(b) and 7.4(b). The high pressures generated at the side rails of Scorpion III and Scorpion IV support the sliders and help achieve high stiffness, especially in the roll direction, and constant roll angles over the disk. The increase of roll stiffness can effectively reduce variations of roll angle due to inertia forces during track-seeking motions. Therefore decrease in the minimum FH during these seek motions are held to a minimum. The features of the two ABS pads near the trailing edge of Scorpion III or Scorpion IV help generate high pressure and large negative force, which are expected to reduce the sensitivity of the FH to the change of skew angle. A summary of the flying attitudes, air bearing stiffness and negative forces at the MD is given in Table 7.2.

Figures 7.5 - 7.7 illustrate the track-seeking profiles used in this study. The maximum seeking acceleration is 637 m/s^2 (or 65 G) for all four of the ABS designs and the other parameters, such as velocity, radial position, geometrical and effective skews are determined by the length of the VCM actuator and the distance between the pivot and the center of the disk according to specifications of each product. The simulation starts with an outward seek that is followed by an inward seek, thus completing a full-stroke seeking loop. For the outward seeking process of ABS I, the slider is first accelerated to -2.548 m/s in 4 ms (the minus sign indicates that the direction of seek motion is from ID to OD), followed by 1 ms of constant velocity, then it is decelerated to zero velocity in 4 ms. During the seek the geometrical skew angle changes from -1.211 to 13.999 degrees. For the inward seek, we simply reverse the outward seeking process. Although the actual seeking profile in disk drives may be different from that shown in Fig. 7.5, the major characteristics of track-seeking motion are contained in the profiles used in this study.

Figures 7.8 – 7.11 illustrate comparisons of gap FHs, pitch and roll angles during the corresponding full-stroke seeking loop between dynamic simulations and the quasi-static approximations introduced here for the ABS I, ABS II, Scorpion III, and Scorpion IV sliders, respectively. It is seen that for all the designs the quasi-static approximations demonstrate good agreements with the dynamic simulations. The inertia effect is clearly seen in the roll and FH curves. It is noted that the Scorpion III and Scorpion IV sliders exhibit extremely small FH, pitch and roll variations caused by the track-seeking motion, which can significantly reduce the risk of head-disk contact during track-seeking motion.

7.3.2 Factors Causing FH Changes during Track-seeking Motion

To investigate the contribution of effective skew, inertia and air flow speed to the FH change during a track-seeking motion, we performed both outward and inward quasi-static simulations of the ABS I slider with different combinations of the various factors. Fig. 7.12(a) shows the minimum FH change when the slider moves from ID to OD with the acceleration profile described in Fig. 7.5(a). The curve labeled "Track-following" shows the FH without seeking. The curve labeled "with roll and pitch torques" includes the effects of tangential (roll torque) and normal acceleration (pitch torque), effective skew and air flow speed. This is used as a baseline for comparing the contributions of the factors. It is observed that the FH drops about 1.5 nm near the MD. The effect of effective skew angle on the FH drop is the difference between the curve “Track-following” and the curve “w/o inertia”. It is clearly seen that the skew angle change is the dominant factor that causes the FH change during track-seeking. The contributions of the other factors are shown in Fig. 7.12(b). The error is defined as the ratio of the FH difference to the baseline value. The result without the inertia effect has an error of 12 % near the radial position of 19 mm, which is attributed to the roll angle change. The effect of centrifugal forces caused by normal acceleration has an error of less than 5 % and the effect of the change of the air flow speed has an error of less than 2 %. Similarly, Fig. 7.13 shows the minimum FH change when the slider moves from OD to ID. In this case, the inertia effect is found to be comparable to the effect of skew angle change.

The FH changes as a function of skew angle for the ABS I, ABS II, Scorpion III and Scorpion IV sliders are shown in Figs. 7.14 and 7.15. It is seen that the FHs of Scorpion III and IV are quite insensitive to skew angle as compared with ABS I and ABS II. In Fig. 7.15, the minimum FH of Scorpion IV is reduced to 5 nm with a 4-nm actuation stroke.

In order to study the effect of intermolecular and electrostatic forces on the minimum FH during track-seeking motion we performed quasi-static simulations for ABS I and Scorpion IV with a 4-nm actuation stroke in the presence of these forces. The effect of intermolecular forces was included with a nominal value of the Hamaker constant ($A = 8.9\times10^{-20}$ J) and the electrostatic forces were added with different electrical potentials (V = 0, 0.3 and 0.6 V) between the slider and the disk. The minimum FHs of ABS I and Scorpion IV are shown in Fig. 7.16(a) and (b), respectively. A comparison of the FH drops under the influence of intermolecular forces and an electrical potential of 0.6 V is also illustrated in Fig. 7.16 (c). It is seen that the FH of ABS I drops over 30 % near the radial position of 19 mm while Scorpion IV exhibits a much smaller and more uniform FH drop of less than 10 %.

7.3 Conclusion

This chapter proposes a quasi-static approximation of the track-seeking motion, which includes the effects of HGA inertia, effective skew angles and nanoscale adhesion forces in the HDI. The track-seeking simulations of four ABS designs by the quasi-static approximation give good agreements with those by the CML Dynamic Simulator but with much less computation effort. A quantitative study of the effects of various factors on the minimum FH change during track-seeking shows that the effective skew angle is dominant but the inertia effect is not negligible. Intermolecular and electrostatic forces were found to add to the FH drop of ABS I during the track-seeking. However, even with an electrical potential of 0.6 V and intermolecular forces, the FH drop of Scorpion IV remains less than 10%. Even though the FH change and the adverse effect of these forces during track-seeking cannot be completely attenuated, a properly designed air bearing slider that decreases its sensitivity to skews, minimizes these forces and increases the roll stiffness can greatly enhance the track-seeking performance.

References

1. E. Cha, C. Chiang and J. J. K. Lee, "Flying height change during seek operation for TPC sliders," *IEEE Trans. Magn.,* vol. 31, pp. 2967-2969, 1995.
2. B. Liu and S. H. Soh, "Effects of seeking velocity on air bearing skew angle, air flow speed and flying performance of sliders with different ABS designs," *IEEE Trans. Magn.,* vol. 32, pp. 3693-3695, 1996.
3. L. S. Chen and D. B. Bogy, "A numerical study of the track-seeking dynamics of the 30% TNPS and U sliders on smooth and laser-textured disks," Technical Chapter No. 1998-007, Computer Mechanics Lab., Department of Mechanical Engineering, University of California, Berkeley.
4. L. Dorius, S. Bolasna, J. Kotla, R. Simmons, Y. Iihara, T. Matsumoto, A. Tobari, and H. Tsuchida, "Introduction of femto slider in mobile disk drives," *IEEE Trans. Magn.,* vol. 40, pp. 349-352, 2004.
5. H. Zhu and D. B. Bogy, "Hard disc drive air bearing design: modified DIRECT algorithm and its application to slider air bearing surface optimization," *Tribol. Intl.,* vol. 37, pp. 193-201, 2004.

TABLE 7.1 Air Bearing Specifications

	ABS I [a]	ABS II	Scorpion III [b]	Scorpion IV [c]
Form-Factor	Pico	Femco	Pico	Pico
Technology	N/A	Contact Start-Stop	Load/Unload	Load/Unload
Disk Speed (rpm)	7200	7200	15000	15000
Gram-Load (gf)	1.5	2.5	2.0	2.0
Crown (nm)	25.4	0	9.3	9.3
Camber (nm)	2.5	0	-2	-2
Etch Steps	2	4	2	3
Base Recess (μm)	2.5	4.75	1.7	1.7

TABLE 7.2 Comparison of Flying Attitudes and Air Bearing Stiffness at the MD

	FH (nm)	Pitch (μrad)	Roll (μrad)	k_z (gf/nm)	k_p (μN.m/μrad)	k_r (μN.m/μrad)	Negative force (gf)
ABS I	6.3	202	-0.6	0.178	0.537	0.059	-3.1
ABS II	12.3	104	3.5	0.176	0.404	0.031	-3.5
Scorpion III	10.4	124	-0.3	0.328	1.036	0.403	-4.7
Scorpion IV	9.8	109	-0.4	0.182	0.517	0.246	-3.1

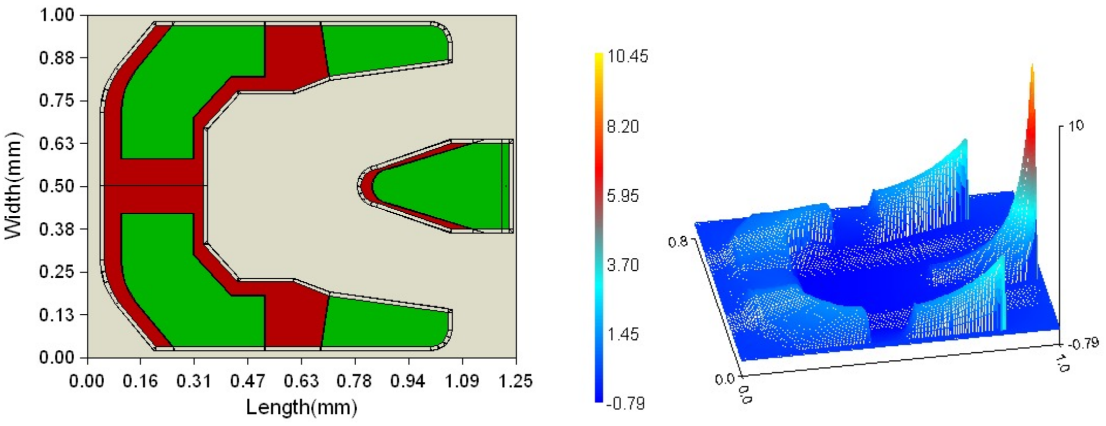

(a) (b)

Fig. 7.1. (a) Air bearing surface of a pico-slider, ABS I (1.25×1×0.3 mm); (b) Air bearing pressure profile at the MD (radial position: 21 mm, skew: 6.8248 °). The scale displayed is normalized to ambient pressure: *(p - p_a)/p_a*.

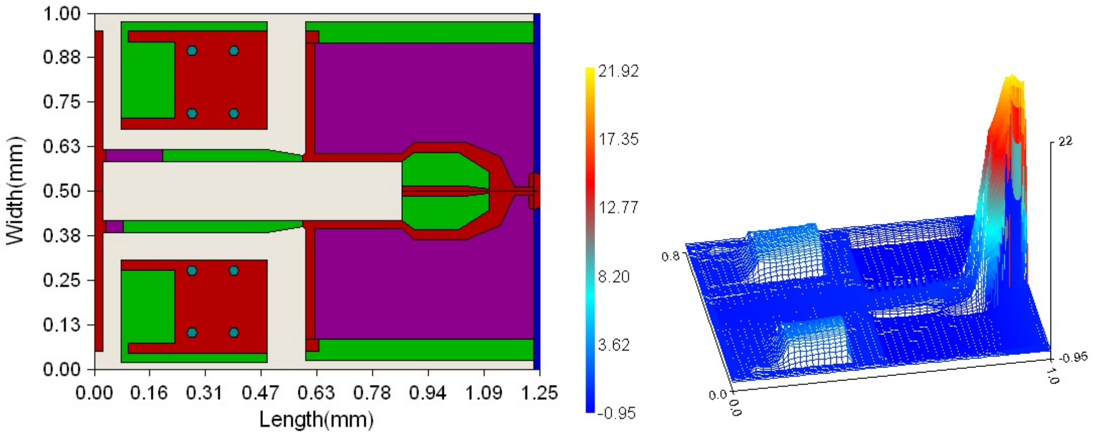

(a) (b)

Fig. 7.2. (a) Air bearing surface of a femco-slider (1.25×1×0.2 mm), ABS II; (b) Air bearing pressure profile at the MD (radial position: 31 mm, skew: 2.48 °).

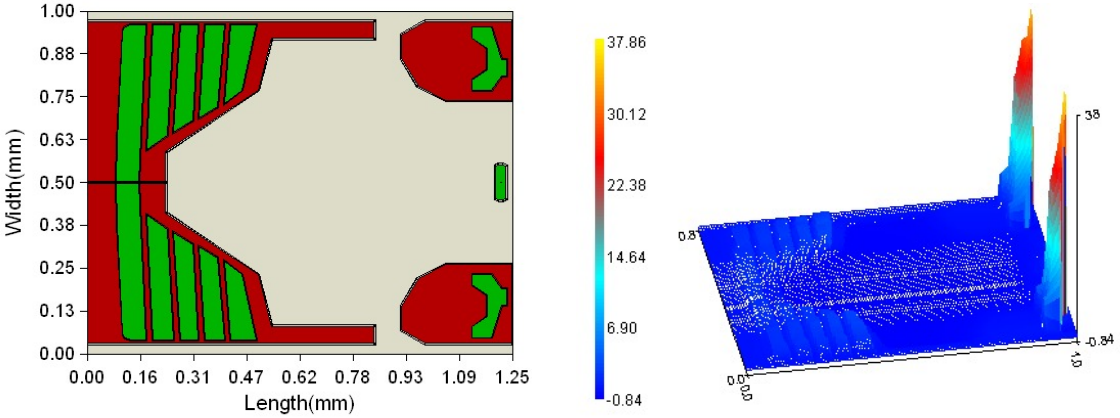

(a) (b)

Fig. 7.3. (a) Air bearing surface of a pico-slider, Scorpion III; (b) Air bearing pressure profile at the MD (radial position: 23.88 mm, skew: -2.56°).

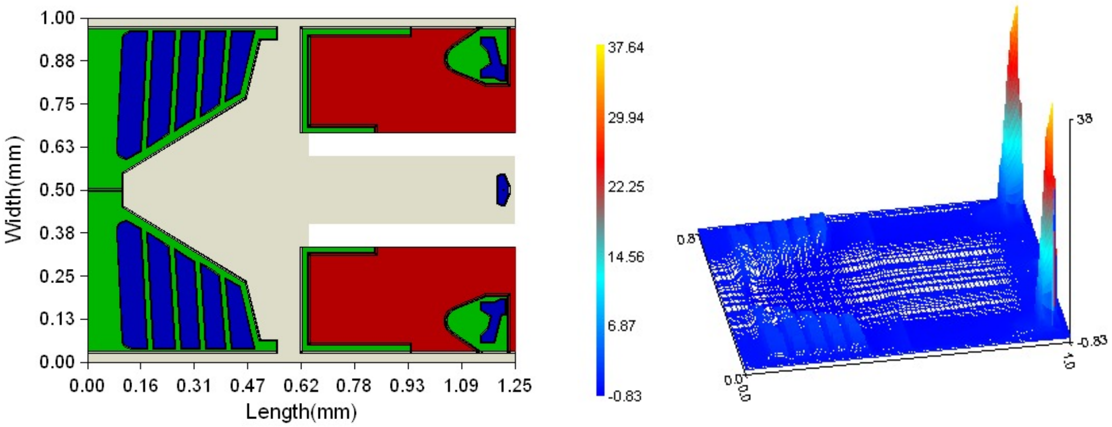

(a) (b)

Fig. 7.4. (a) Air bearing surface of a pico-slider, Scorpion IV; (b) Air bearing pressure profile at the MD (radial position: 23.88 mm, skew: -2.56°).

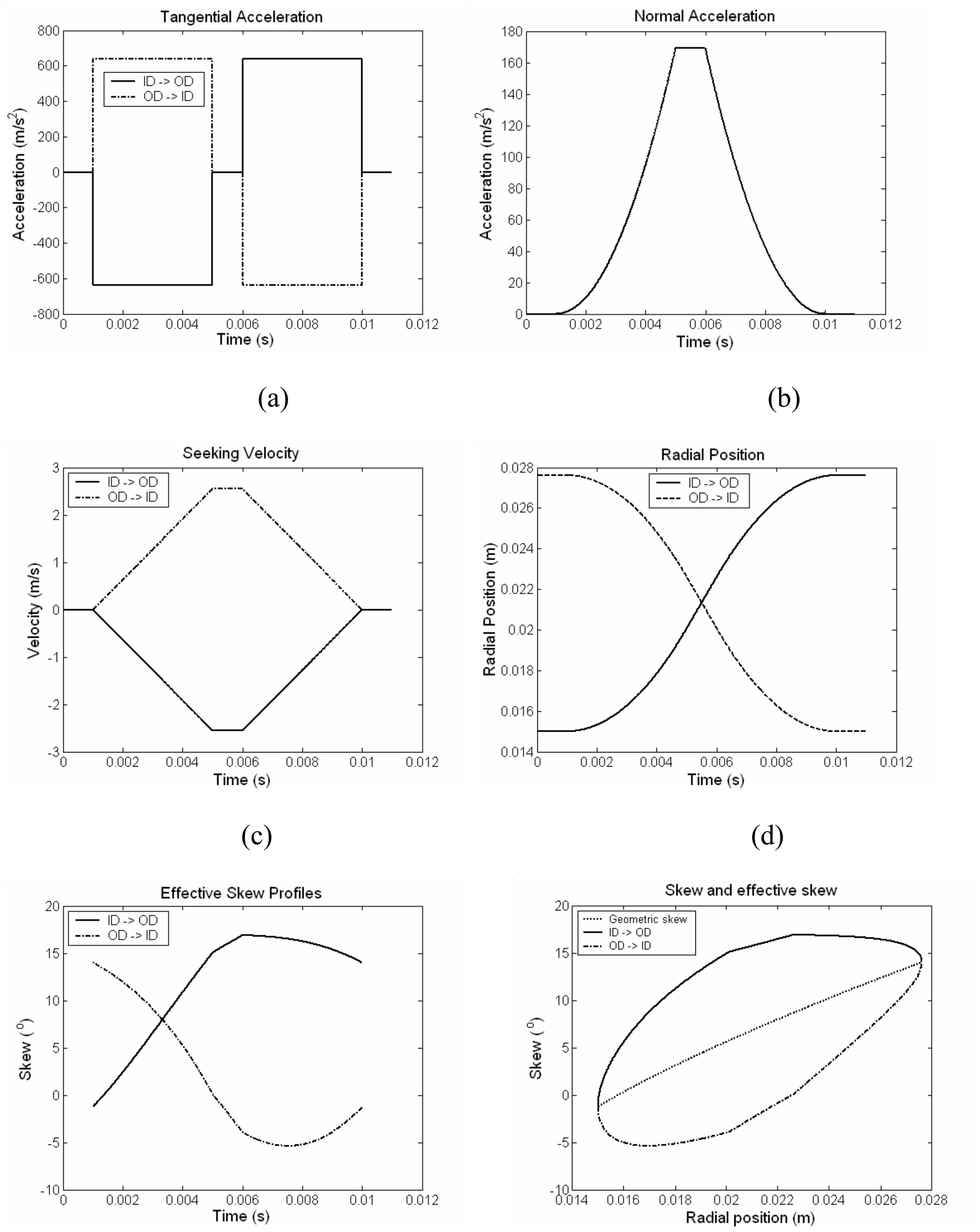

(a) (b)

(c) (d)

(e) (f)

Fig. 7.5. Track-seeking profiles for ABS I. The maximum acceleration is 637 m/s^2 (or 65 G).

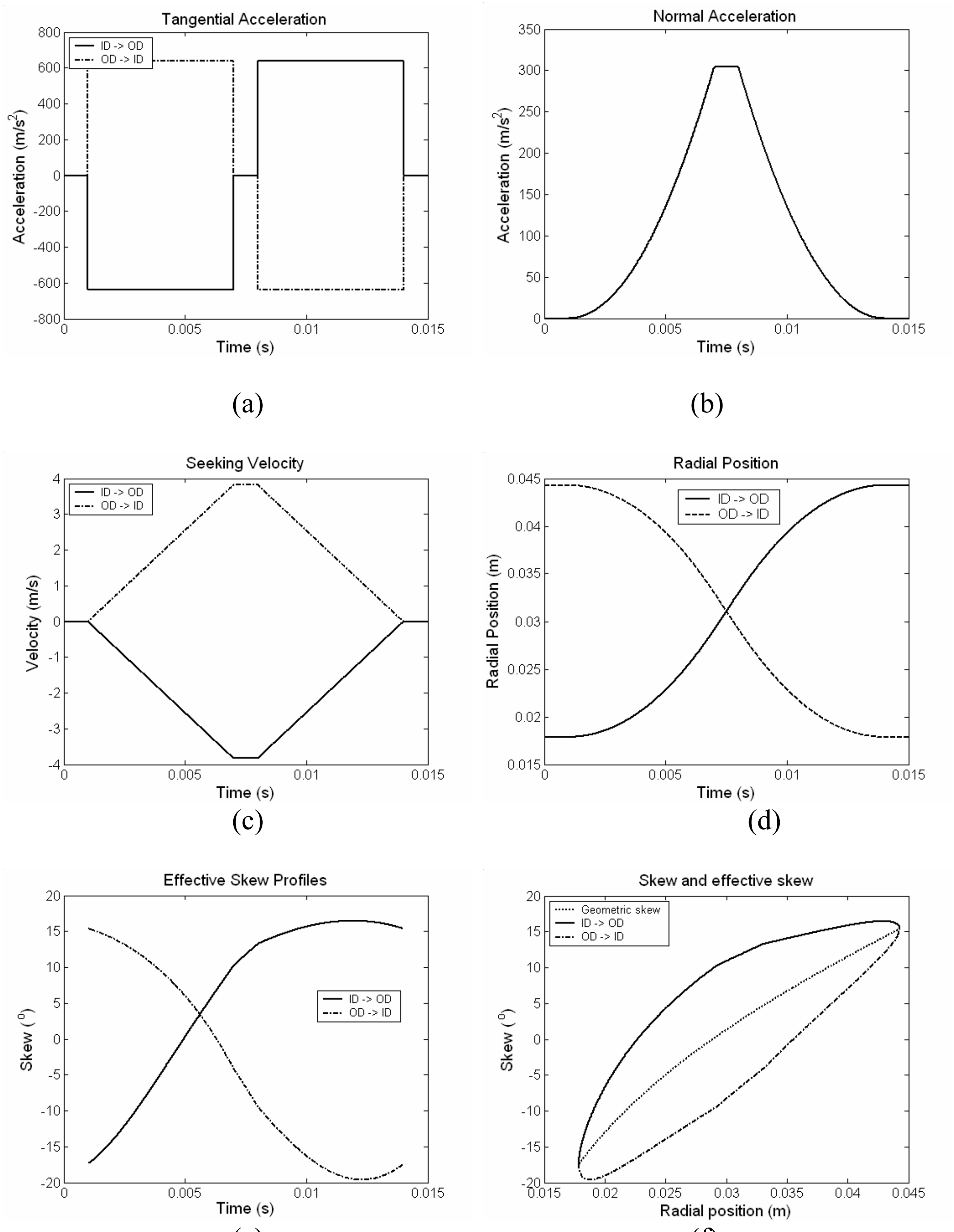

(a) (b)

(c) (d)

(e) (f)

Fig. 7.6. Track-seeking profiles for ABS II. The maximum acceleration is 65 G.

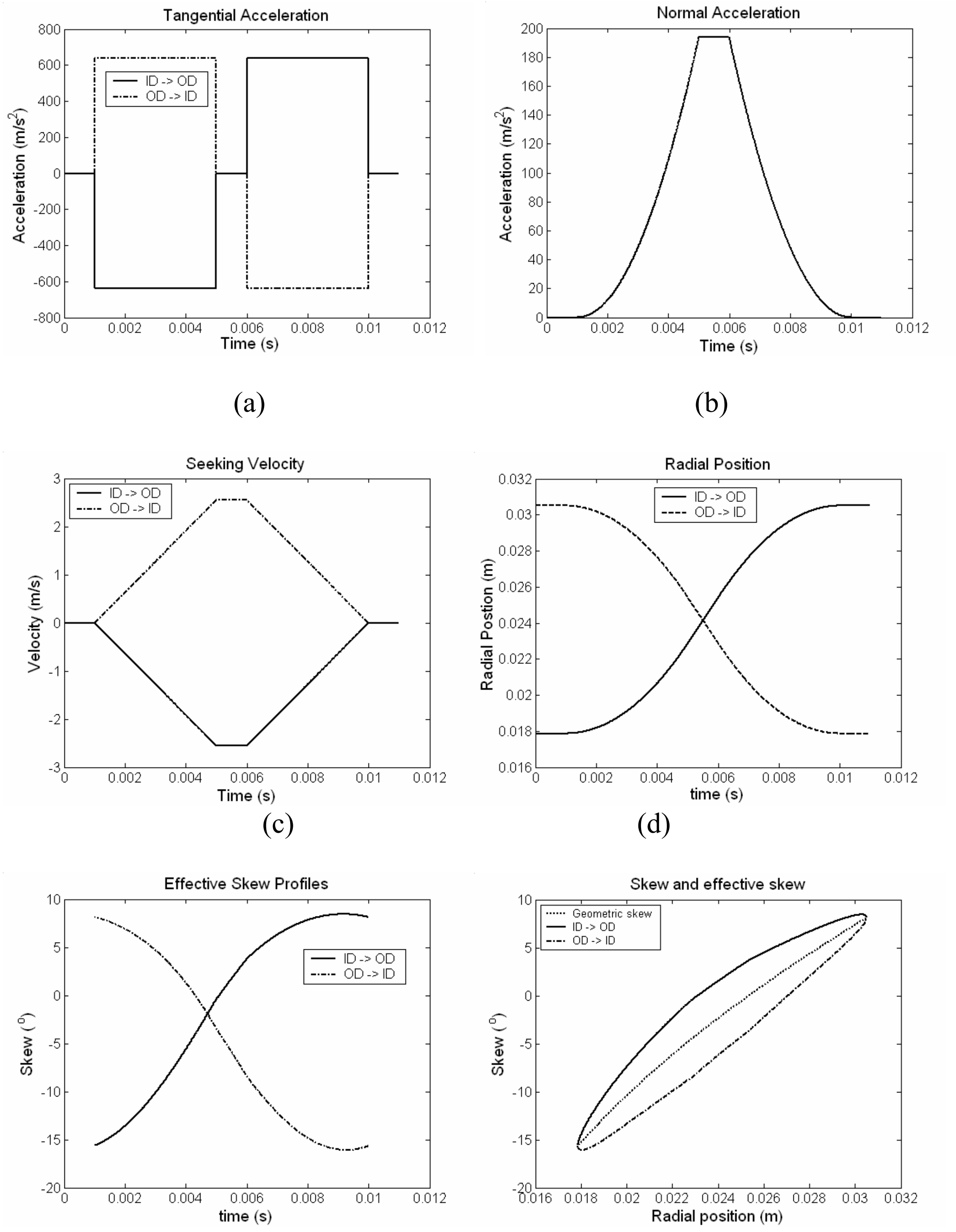

(a) (b)

(c) (d)

(e) (f)

Fig. 7.7. Track-seeking profiles for Scorpion III and IV. The maximum acceleration is 65 G.

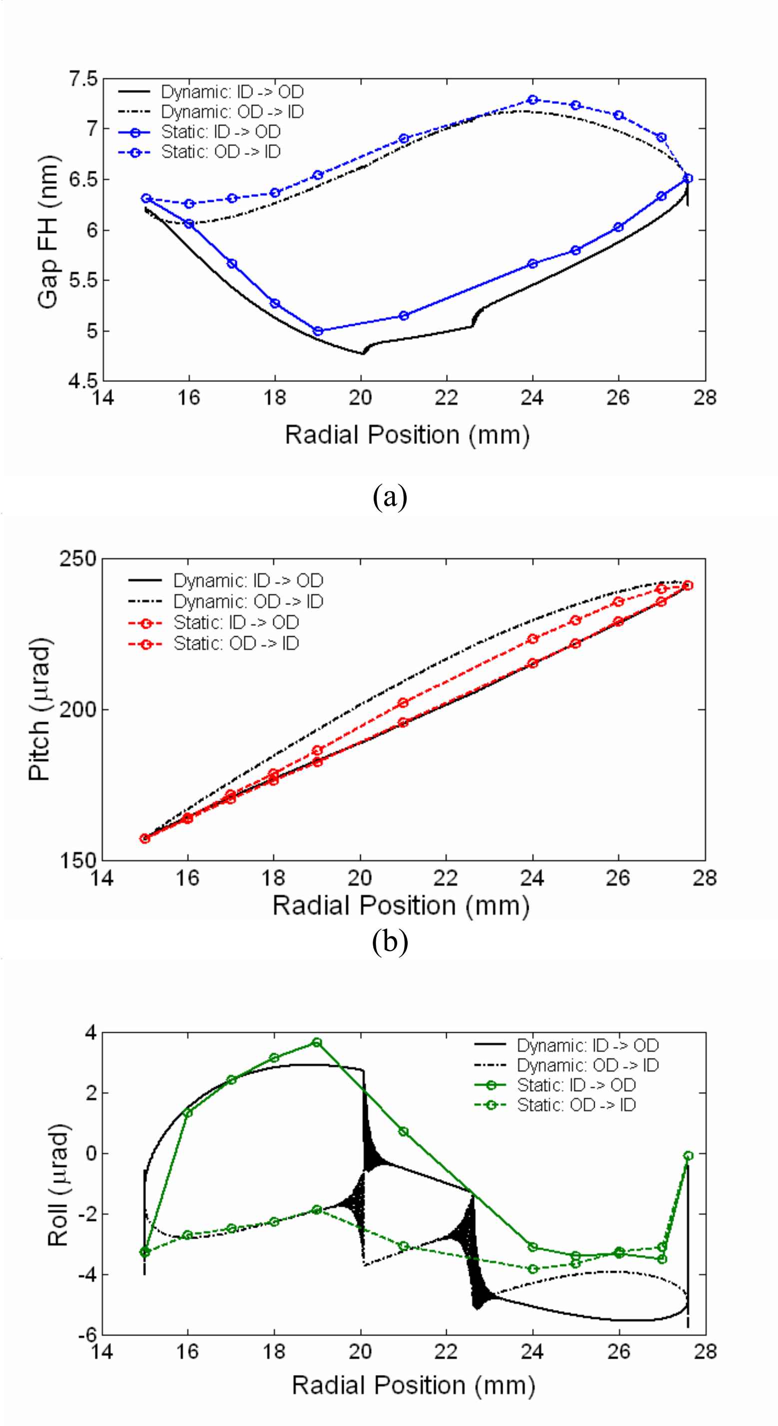

(a)

(b)

(c)

Fig. 7.8. Track-seeking performance of ABS I.

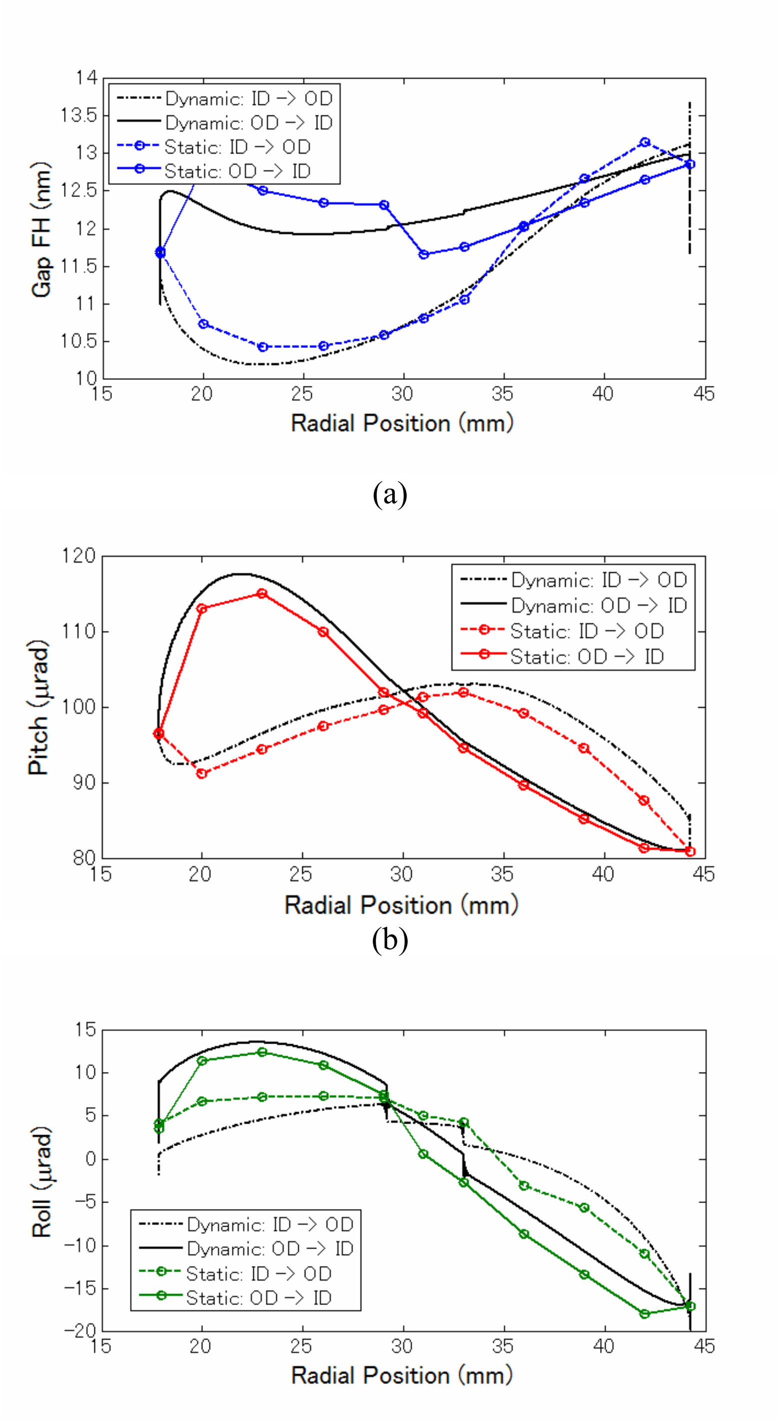

(a)

(b)

(c)

Fig. 7.9. Track-seeking performance of ABS II.

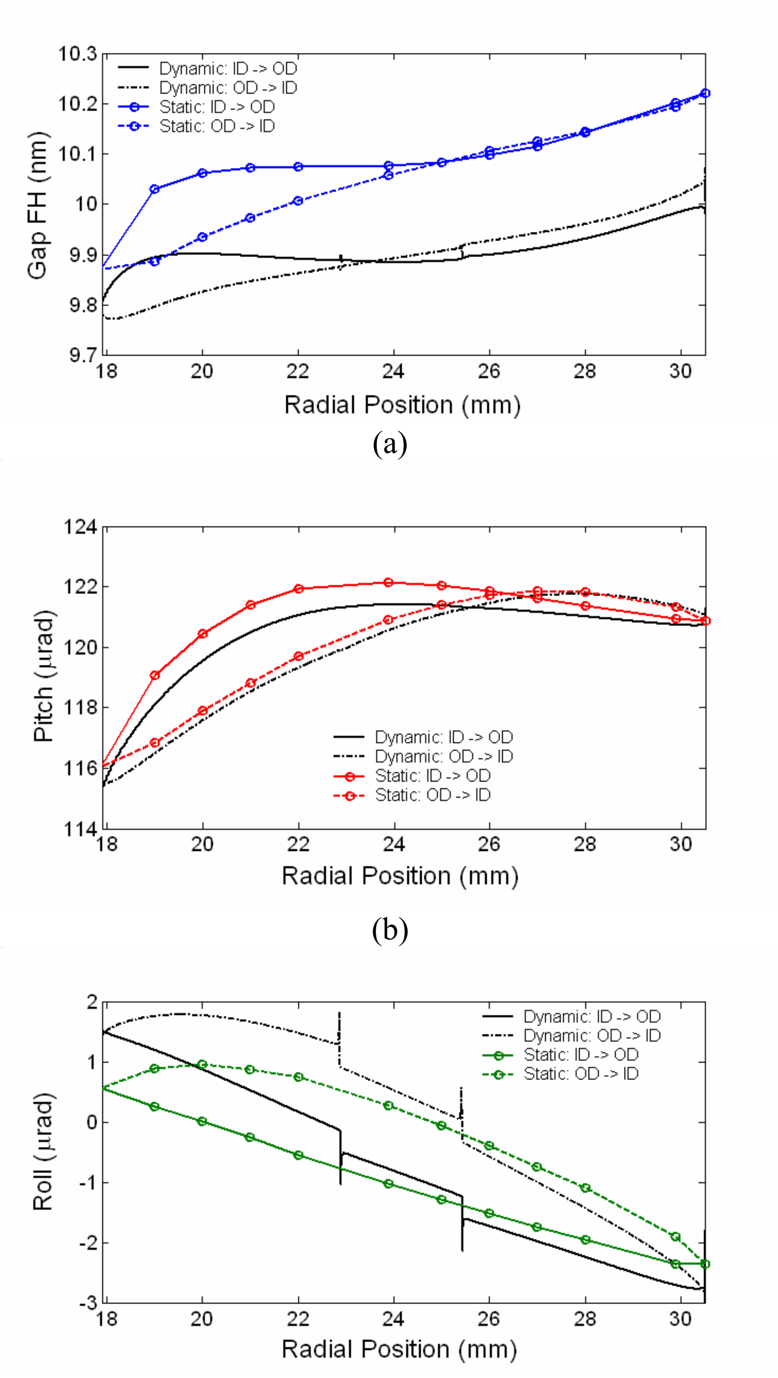

(a)

(b)

(c)

Fig. 7.10. Track-seeking performance of Scorpion III.

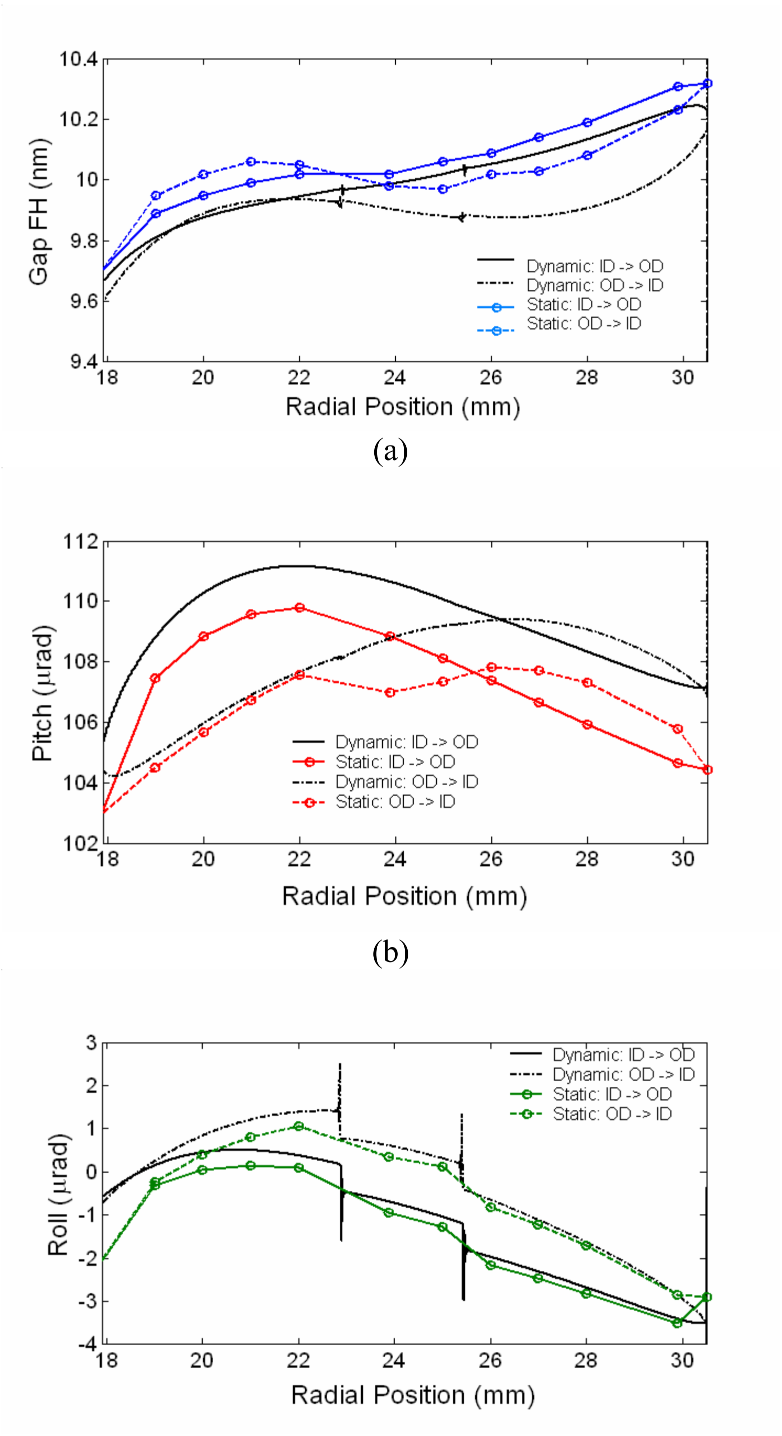

(a)

(b)

(c)

Fig. 7.11. Track-seeking performance of Scorpion IV.

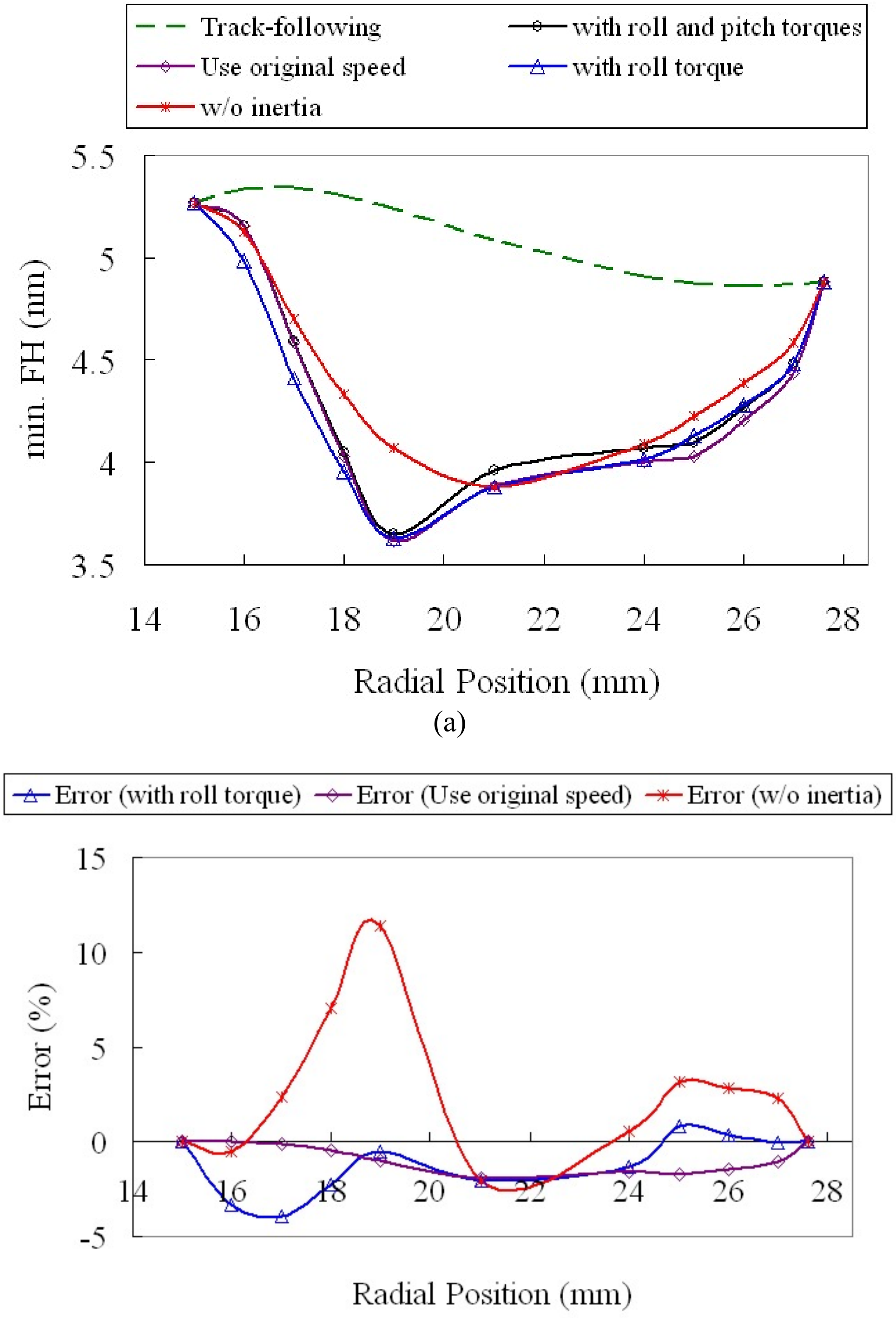

(a)

(b)

Fig. 7.12. Effects of the effective skew, inertia forces, and air flow speed on the FH changes of ABS I seeking from ID to OD. The error is calculated by subtracting the values of various curves from the baseline “with roll and pitch torques”.

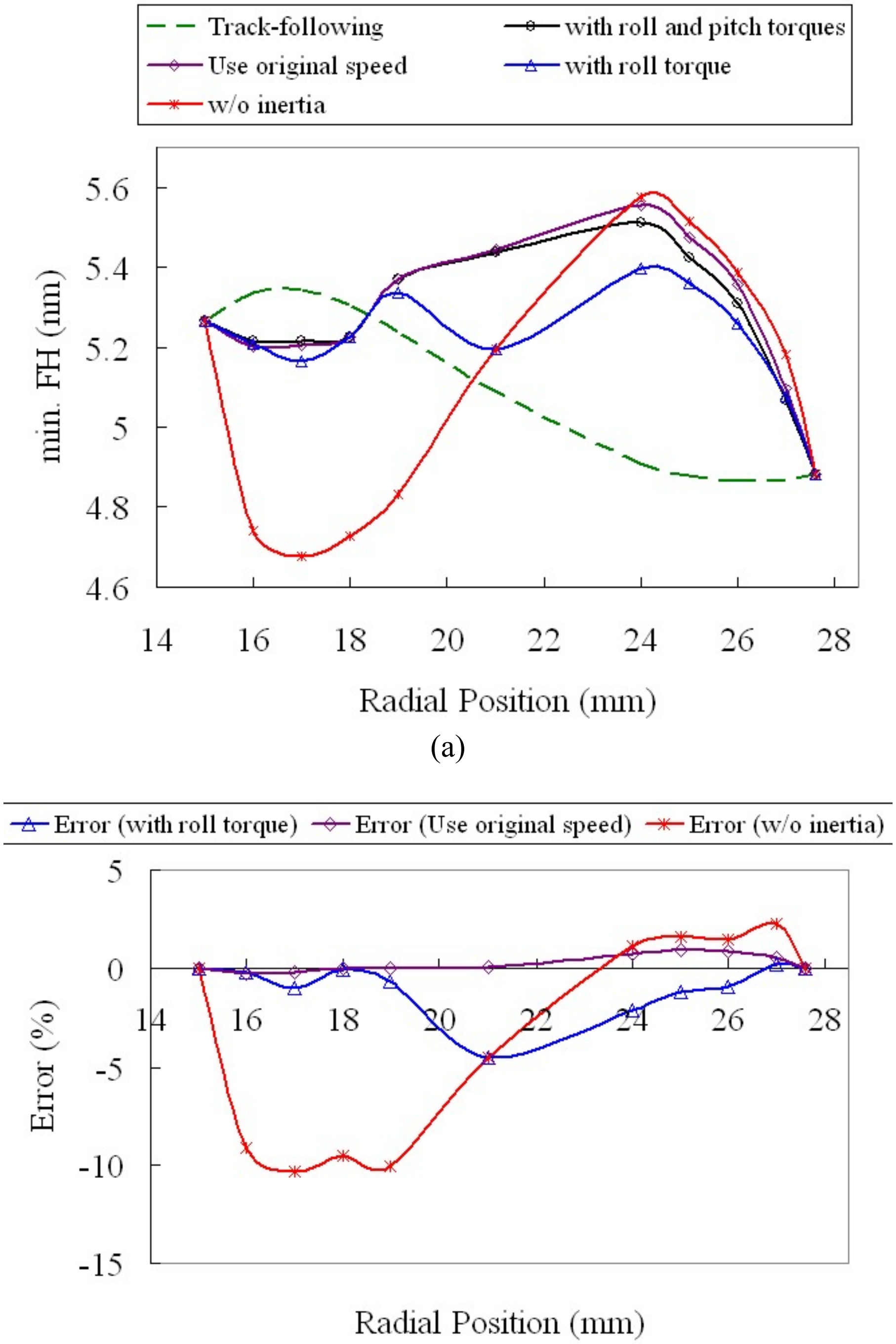

(a)

(b)

Fig. 7.13. Effects of the effective skew, inertia forces, and air flow speed on the FH changes of ABS I seeking from OD to ID.

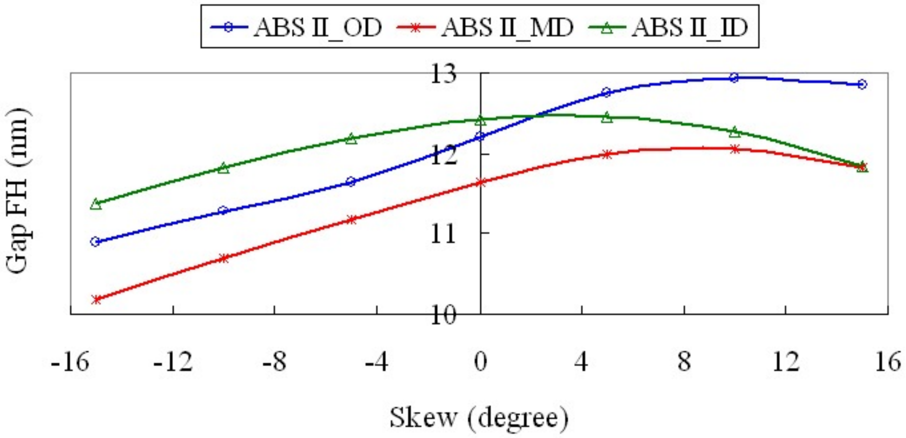

(a) ABS II

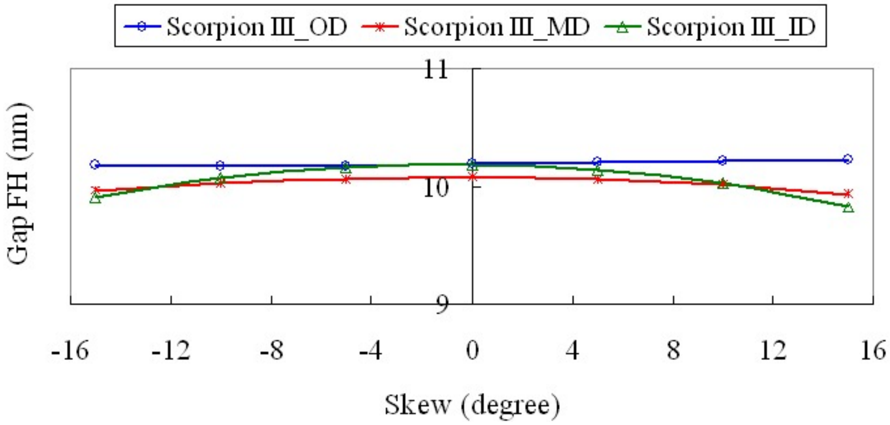

(b) Scorpion III

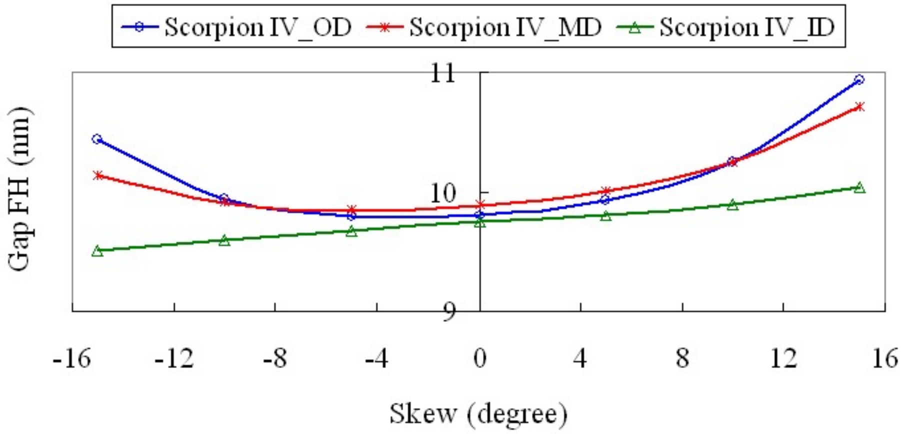

(c) Scorpion IV

Fig. 14. FH changes as a function of skew angle for (a) ABS II, (b) Scorpion III, and (c) Scorpion IV.

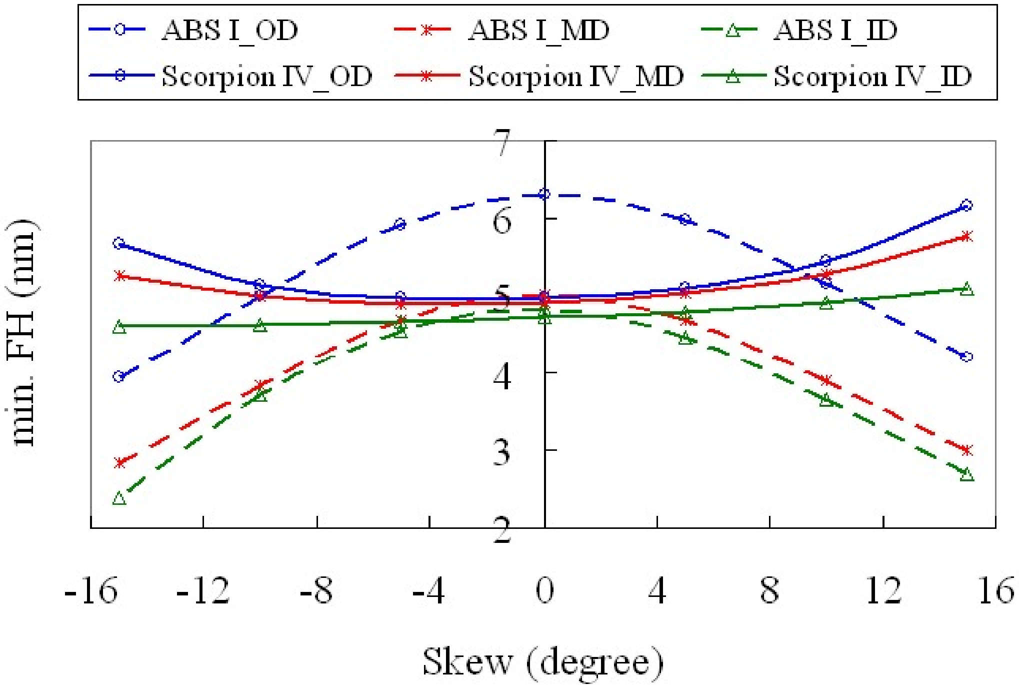

Fig. 7.15. A comparison of minimum FH changes as a function of skew angle between ABS I and Scorpion IV with a 4-nm actuation stroke.

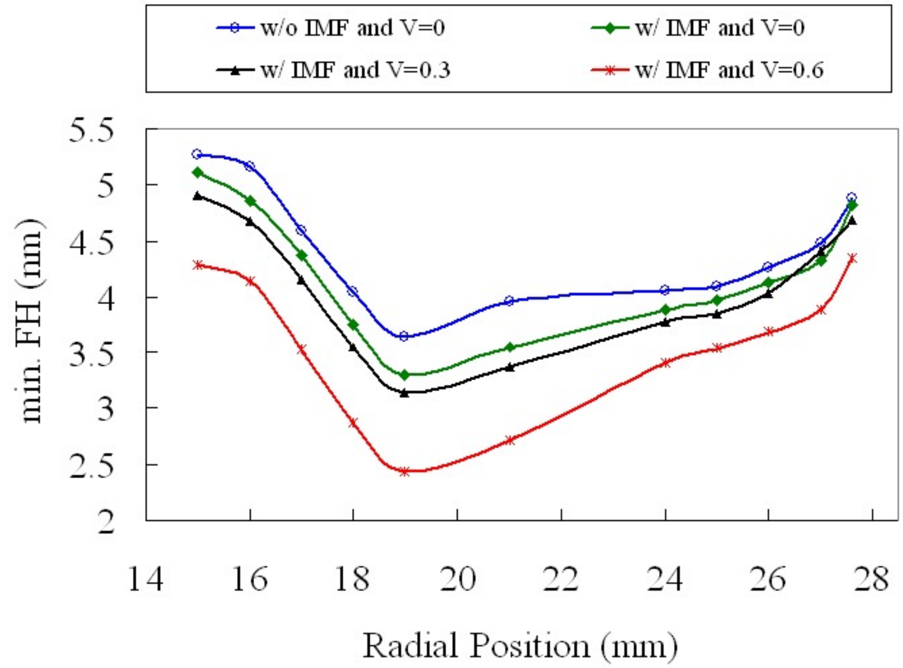

(a) ABS I

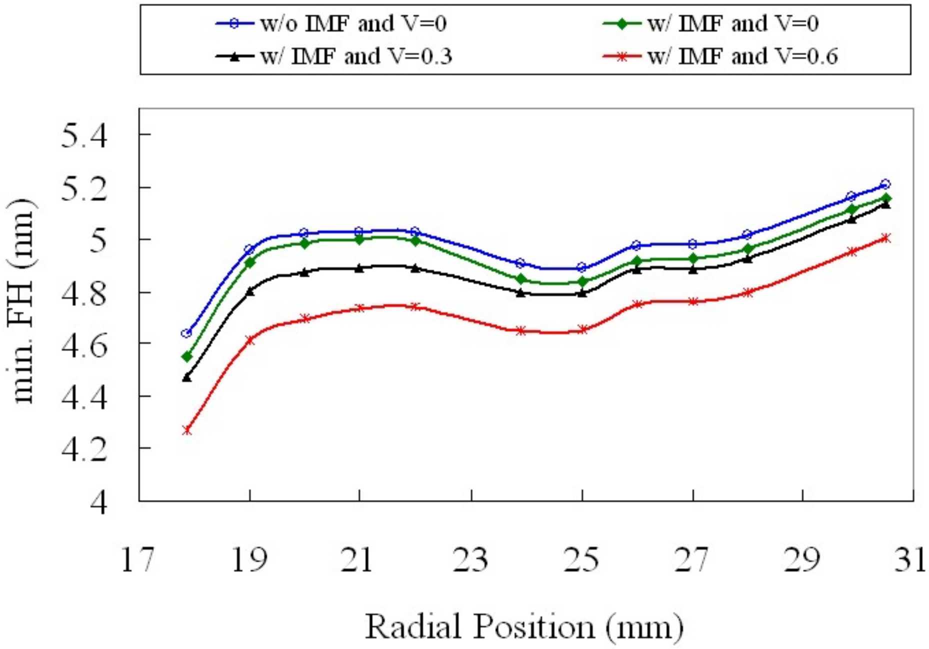

(b) Scorpion IV with a 4-nm actuation stroke

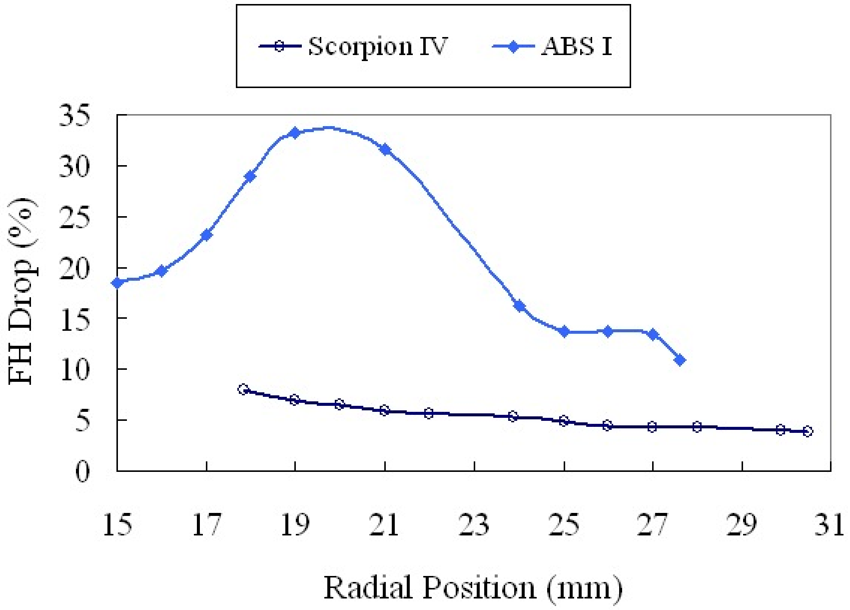

(c) with intermolecular forces and 0.6 V

Fig. 7.16. FH drops caused by the intermolecular and electrostatic forces during track-seeking motion (The Hamaker constant A = 8.9×10^{-20} J).

CHAPTER 8
SUMMARY AND CONCLUSIONS

One of the major technological challenges that still remains for achieving an areal density of 1 Tbit/in^2 is to obtain a reliable and robust head-disk interface with a FH of 2.5 nm. A stable and constant FH must also be sustained in the presence of altitude and temperature changes, manufacturing tolerance, and track-seeking motion. Furthermore, slider disk contacts must be avoided during load/unload processes and operational shocks. The dynamic instability caused by FH modulations (FHMs) and nanoscale adhesion forces, such as electrostatic and intermolecular forces should be minimized. These requirements have posed a tremendous challenge on the design of the next generation air bearing sliders.

The research presented in this dissertation is to study the feasibility of achieving the goal of 1 Tbit/in^2 by utilizing FH control sliders with thermal or piezoelectric nanoactuators. Emphasis is placed on understanding the new phenomena associated with actuation and controlling the FH for suppressing modulation and improving dynamic stability.

Chapter 2 presented two approaches, namely thermal and piezoelectric actuators, for minimizing the adhesion forces such as intermolecular and electrostatic forces and achieving a stable 2.5 nm FH. It was found that its quasi-static nature allowed thermal FH control sliders to compensate the static FH loss, but the inherent power-consuming thermal actuation limited the actuated pole-tip protrusion. The piezoelectric dynamic control slider showed the promising performance of higher bandwidth, larger actuated stroke and less power consumption. However, the requirement of piezoelectric materials and modification of the slider design poses challenges in integration of the fabrication process and increases the manufacturing cost.

In Chapter 3, two ABS designs, Scorpion III and Scorpion IV, for a FH control slider with a thermal and piezoelectric nanoactuator, respectively, were proposed to achieve virtually 100 percent actuation efficiency. A numerical study was conducted to investigate both the static and dynamic performances of the Scorpion sliders, such as uniformity of gap FH with near-zero roll over the entire disk, ultrahigh roll stiffness and damping, low nanoscale adhesion forces, uniform FH track-seeking motion, dynamic load/unload and FH modulation (FHM). The Scorpion sliders were found to exhibit an overall enhancement in performance, compared with several conventional ABS designs.

In Chapter 4, we designed and fabricated Al_2O_3-TiC sliders with the Scorpion ABS for achieving high actuation efficiency. We demonstrate an inexpensive and low-temperature approach for integrating piezoelectric materials in the fabrication of current Al_2O_3-TiC sliders. A bulk PZT sheet is bonded onto the back of row-bars and the sliders are separated by a standard dicing process. It requires no deep reactive-ion etching

(DRIE) or high temperature processes and is suitable for mass production. The fabricated prototype sliders were tested experimentally. The measured nonflying actuated stroke exhibited a linear relationship with the applied voltage with a rate of ~ 0.8 nm/V. The FHs of two different sliders, designed for the actuated center pad and actuated side pads scheme, were successfully reduced from 15.5 nm and 8.5 nm to contact with applied voltages of 20 V and 10 V, respectively, which demonstrated high actuation efficiency. The AE measurements showed clear spikes when the center pad was brought into contact with the disk by the actuator. The pattern of the AE signals during contact is different from the one observed in the conventional sliders during "touchdown-takeoff tests" where there was a pronounced increase in the AE amplitude upon contact. This is attributed to the sustained air bearing even when the intermittent contacts occur in the head-disk interface. It is also found that the dominant air bearing mode shifted from the first pitch to the second pitch as a result of the intermittent contacts. In addition, a track of considerable lube depletion and carbon wear was observed after the contact tests.

In Chapter 5, based on the concept that the FH of a portion of the slider that carries the read/write element can be adjusted by a piezoelectric actuator located between the slider and suspension and that the FH can be measured by use of a magnetic signal, a new 3-DOF analytic model and an observer-based nonlinear compensator were proposed to achieve ultra-low FH with minimum modulation under short range attractive forces. Numerical simulations showed that the FHM due to disk waviness was effectively controlled and reduced.

In Chapter 6, we investigated the effects of ABS designs on the thermal actuation. We created a 3-D finite element model of an entire slider with detailed read/write transducer structure and conducted thermal-structural coupled-field analysis using velocity slip and temperature jump boundary conditions to formulate the heat transfer across the head-disk interface when a slider flies over a spinning disk. An iteration procedure was used to obtain the equilibrium solutions. Four ABS designs with distinct features were simulated. We defined five measures of merit, including protrusion rate, actuation efficiency, power consumption, pressure peak and temperature rise of the sensor, to evaluate the performance of thermal actuation. It was found that the effect of the pressure was more significant than that of the FH on the heat conduction from the slider to the disk. The efficiencies of three conventional designs decreased as the FHs were continuously reduced. A new ABS design, called "Scorpion III", was presented and demonstrated an overall enhancement, including virtually 100 percent efficiency with significantly less power consumption. Transient thermal analysis showed that it required about 1-2 ms for the temperature to reach the steady-state values and there was a trade-off between increasing the actuation bandwidth and decreasing the power consumption.

In Chapter 7, a quasi-static approximation of track-seeking motion was proposed, which substantially decreased the computation time over that required for a dynamic analysis. The track-seeking performances of four different air bearing surface (ABS) designs were numerically investigated by the quasi-static approximation, and the results were compared with those computed by the CML Dynamic Simulator. The former gave good agreements with the latter but with much less computation effort. The effects of various factors causing FH changes were presented and compared quantitatively. The effective skew angle was found to be the dominant factor, but the inertia effect was also not negligible. The Scorpion designs were found to exhibit an enhancement in track-seeking performance, compared with two other conventional ABS designs.